



Virginia Commonwealth University
VCU Scholars Compass

Theses and Dissertations

Graduate School

2012

SOLVATION OF ORGANIC CATIONS IN THE GAS PHASE AND WITHIN MOLECULAR CLUSTERS

Ahmed Hamid
Virginia Commonwealth University

Follow this and additional works at: <https://scholarscompass.vcu.edu/etd>

 Part of the [Chemistry Commons](#)

© The Author

Downloaded from

<https://scholarscompass.vcu.edu/etd/323>

This Dissertation is brought to you for free and open access by the Graduate School at VCU Scholars Compass. It has been accepted for inclusion in Theses and Dissertations by an authorized administrator of VCU Scholars Compass. For more information, please contact libcompass@vcu.edu.

College of Humanities and Sciences

Virginia Commonwealth University

This is to certify that the dissertation prepared by Ahmed Mohamed Kotb Hamid entitled SOLVATION OF ORGANIC CATIONS IN THE GAS PHASE AND WITHIN MOLECULAR CLUSTERS has been approved by his committee as satisfactory completion of the thesis or dissertation requirement for the degree of Doctor of Philosophy

M. Samy El-Shall, Ph.D., Professor, Department of Chemistry, Research Adviser

James Turner, Ph.D., Professor, Department of Chemistry

Purusottam Jena, Ph.D., Professor, Department of Physics

Scott Gronert, Ph.D., Professor and Chair, Department of Chemistry

James Coleman, Ph.D., Dean, College of Humanities and Sciences

F. Douglas Boudinot, Ph.D., Dean of the School of Graduate Studies

April, 16th, 2012

© Ahmed Mohamed Kotb Hamid, 2012

All Rights Reserved

SOLVATION OF ORGANIC CATIONS IN THE GAS PHASE AND WITHIN
MOLECULAR CLUSTERS

A dissertation submitted in partial fulfillment of the requirements for the degree of doctor
of philosophy at Virginia Commonwealth University

by

AHMED MOHAMED KOTB HAMID

B.Sc., Alexandria University, Egypt, 2004

Director: M. SAMY EL-SHALL

Professor, Department of Chemistry

Virginia Commonwealth University

Richmond, Virginia

April, 2012

Acknowledgement

First of all, I have to admit that I am so blessed to have such a great family, all my family members have supported me in every step in my life. My brother, Mr. Nasser Hamid, has been my best example in life and always I am in his mind; he is my main supporter through my trip. My mom, Khadiga, my sister, Hala, and my brothers, Hany and Khaled, were always there for me and I feel safe because I have them in my life. In addition, I have been blessed again by joining Dr. Samy El-Shall's research group. Dr. El-Shall gave me a golden chance to pursue my graduate studies and discussions with him have significantly enriched my knowledge. Dr. El-Shall always has great research ideas and I have learnt how to be hard-worker and to think very systematically in his laboratory.

I am so grateful to my professors in faculty of Science, Alexandria, Egypt for the high quality education, great support and their precious recommendation letters. In particular, Dr. Adel N. Asaad who was my first academic advisor and he supported me greatly to pursue my dreams to get the best education and to never give up, I can't describe my appreciation to him by words. I am also so grateful to Drs. Yasser A. Hussein, Essam K. Ibrahim and Mamdouh S. Masoud for giving me their precious time and valuable advice. I can't forget the help I had through my application process from Ms. Rohayma Rateb, EducationUSA adviser who helped me since day one until I got accepted at VCU.

I am also so grateful for my former postdocs, Drs. Paul Momoh and Pramod Sharma. Dr. Momoh wasn't only the first one to introduce the gas-phase technology to me but also, he acts as my outstanding example and nice friend so I am following his footsteps. In addition, Dr. Sharma was a great postdoc, with him I have had very useful discussions and he has offered great technical help as well. I want to also thank Dr. Yehia Ibrahim for being such caring friend who supports me always with great advice. Moreover, I want to thank all my research group members for making my time at VCU to be very fruitful and enjoyable. Moreover, gas-phase group gave me great technical help and useful discussions, in particular, Dr. Abdel Rahman I. Soliman, with whom I have done many projects and got nice fruitful time working with him.

Table of Contents

Acknowledgement	ii
Table of Contents	iii
List of Figures	vi
List of Tables	xiv
Abstract	xix
Chapter 1: Introduction	1
Chapter 2: Experimental Setup	8
2.1. Vacuum System	8
2.2. Cluster formation	10
2.3. QMS-IM-QMS	12
2.3.1. Electron impact ionization	12
2.3.2. Quadrupole mass-filter	13
2.3.3. Drift cell	15
2.3.4. Electron multiplier detector	18
2.3.5. Ion energy and Injection energy	19
Chapter 3: Experimental Measurements	21
3.1. Mobility measurements and Structure determination	21
3.1.1. Mobility measurements	21
3.1.2. Structure determination	26
3.1.3. Theoretical methods of calculating mobilities and collision integrals	28
3.2. Thermochemistry measurements	30
3.3. Theoretical calculations	32
Chapter 4: Hydration of Pyrimidine Radical Cation and protonated pyrimidine cations	34
4.1. Introduction	34
4.2. Experimental Section	37
4.3. Theoretical calculations	38
4.4. Results and Discussion	38

4.4.1. Binary Pyrimidine-Water Clusters	38
4.4.2. Gas Phase Hydration of Pyrimidine Radical Cation	44
4.4.3. Gas Phase Hydration of Protonated Pyrimidine	59
4.5. Conclusions	70
Chapter 5: Sequential solvation of Protonated pyrimidine cation with methanol and acetonitrile molecules in the gas phase	71
5.1. Introduction	71
5.2. Mobility measurements and structure determination of the binary clusters	72
5.2.1. Mass-spectra of the binary pyrimidine-methanol and pyrimidine-acetonitrile clusters	72
5.2.2. Ion mobility measurements.....	74
5.3. Gas-Phase Thermochemical Equilibrium Measurements	78
5.3.1. Gas-Phase Solvation of Protonated Pyrimidine Cation by Methanol	78
5.3.2. Gas-Phase Solvation of Protonated Pyrimidine Cation by Acetonitrile.....	92
5.4. Conclusions	101
Chapter 6: Stepwise Solvation of Benzene ⁺ and Phenyl acetylene ⁺ Radical Cations by HCN molecules.....	103
6.1. Introduction	103
6.2. Stepwise Solvation of Benzene ⁺ by HCN and CH ₃ CN molecules.....	103
6.2.1. Experimental Section.....	104
6.2.2. Theoretical Calculations	106
6.2.3. Benzene ⁺ (HCN) _n Cluster System	107
6.2.4. Benzene ⁺ /CH ₃ CN reaction study.....	121
6.3. Stepwise Solvation of Phenyl acetylene ⁺ by HCN molecules in the gas- phase. Binding energies and structures of [Phenyl acetylene ⁺ (HCN) _n] clusters	133
6.3.1. Introduction.....	133
6.3.2. Experimental Section.....	133
6.3.3. Theoretical Calculations	134
6.3.4. Results and Discussion	134
6.4. Summary and Conclusions.....	147
Chapter 7: Sequential Association of HCN molecules with Pyridine ⁺ , Pyrimidine ⁺ and H ⁺ Pyridine. Binding Energies and Structures	150

7.1. Introduction	150
7.2. Experimental Section	151
7.3. Theoretical Calculations.....	153
7.4. Results and discussion	153
7.4.1. Solvation of Pyridine ⁺ and H ⁺ pyridine by HCN molecules.....	153
7.4.2. Solvation of Pyrimidine Radical cations by HCN molecules.....	175
7.5. Reaction of Acetylene radical cation and Hydrogen cyanide molecules in the gas phase	190
7.5.1. Introduction.....	190
7.5.2. Results and discussion.....	192
7.6. Summary and Conclusions.....	200
Chapter 8: Conclusions and future outlooks	201
List of References	204
Appendix A.....	212
Appendix B: Preliminary studies of Benzonitrile-water clusters	217
Ion mobility and collision cross sections of benzonitrile radical cation-water clusters	217
Thermochemistry studies of the hydration of Benzonitrile Radical Cation in the gas phase ..	224
Vita.....	229

List of Figures

- Figure 1.** Schematic diagram of the mass-selected ion mobility system at VCU: (1) pulsed nozzle (2) 3 mm skimmer (3) electron-impact ionizer (4) quadrupole mass filter (5) ions transport lenses stack 1 (Einzel Lenses 1, 2 and 3) (6) steering lens/ion gate (7) drift cell (8) to baratron (9) ions transport lenses stack 2 (Einzel Lenses 4, 5 and 6) (10) quadrupole mass filter (11) electron multiplier (detector) 9
- Figure 2.** The ion mobility system can be divided into four sections: the expansion, the ionization, the reaction and the detection parts..... 10
- Figure 3.** Schematic drawing of the ion volume (the ion region basket and filament) 13
- Figure 4.** Side view drawing of the drift cell. (1) Endcap (2) Reaction cell body (3) Entrance lens (lens B) (4) Tapered entrance lens (lens A) (5) Entrance orifice (0.25 mm) (6) Drift rings (7) Exit orifice (0.25 mm) (8) Tapered exit lens (lens C) (9) Cell body liquid nitrogen inlet (10) Baratron connector (11) Drift cell (12) Endcap liquid nitrogen inlet. Dimensions in inches..... 17
- Figure 5.** A simplified view for the mounting of the copper rings, the ceramic spacers and the tapered exit lens connected to the end cap..... 18
- Figure 6.** Electron impact (27 eV) mass-spectrum of pyrimidine clusters formed by supersonic beam expansion using 0.7% pyrimidine vapor in helium (5 atm) 40
- Figure 7.** Mass-spectrum resulting from injecting the pyrimidine radical cation in the RF-selection mode into the drift cell which contains 0.93 Torr of helium using injection energy of 13.4 eV (lab) and drift field of 4.6 V/cm. The temperature of the drift cell was 298 K. The sample mixture is composed of pyrimidine: water in a ratio of 1:2 41
- Figure 8.** ATDs of $[H^+pyrimidine (H_2O)]$ on varying the drift voltage from 10 to 21V . 42
- Figure 9.** DFT optimized structures done at the B3LYP/6-311++G(d,p) level of (a) Pyrimidine⁺ (b) Protonated pyrimidine $[H^+pyrimidine]$ (c) Protonated hydrated pyrimidine $[H^+pyrimidine (H_2O)]$ (d) Protonated pyrimidine dimer $[H^+pyrimidine_2]$. The experimental collision cross-sections and the calculated values obtained at room temperature are indicated. The interatomic distances are in Angstrom 43

- Figure 10.** Mass spectra resulting upon the injection of mass-selected pyrimidine radical cation into a mixture of H₂O mixed with helium gas using 12.7 eV (lab) as injection energy and 2.5 V/cm drift field. Drift cell temperature and pressure are indicated 45
- Figure 11. (Left)** ATDs of pyrimidine⁺ (H₂O)_n; n=1-3, collected when mass-selected pyrimidine⁺ is injected into the drift cell contains 0.21 of water vapor in a mixture with 0.22 Torr helium buffer gas at 268 K. **(Right)** ATDs of pyrimidine⁺ (H₂O)_n; n=3-5, collected when mass-selected pyrimidine⁺ is injected into the drift cell contains 0.19 Torr of water vapor in a mixture with 0.22 Torr of helium buffer gas at 243 K 49
- Figure 12.** van't Hoff plots of the established equilibria among pyrimidine⁺(H₂O)_n clusters; with n= 0-4 resulting from injecting pyrimidine radical cation in the mass-selected mode into the drift cell which has 0.24 Torr H₂O mixed with 0.23 Torr of helium gas using 12.7 eV injection energy and 2.5 V/cm drift field. Drift cell temperature was varied in the range of (238 K-283 K) 50
- Figure 13.** Charge transfer from pyrimidine radical cation to water cluster as hydration degree *n* evolves 59
- Figure 14.** Mass spectra resulting upon protonated pyrimidine cation (H⁺Py) injection into a mixture of water vapor (W) and helium gas using 13.9 eV (laboratory frame) injection energy and 2.2 V/cm drift field. Drift cell temperature and pressure are varied as indicated..... 60
- Figure 15. (Left)** ATDs of protonated pyrimidine cation (H⁺Py) and [H⁺pyrimidine (H₂O)] collected at 344 K and drift cell field of 2.5 V/cm. **(Right)** ATDs of [H⁺pyrimidine (H₂O)_n]; n=1-3, collected at 242 K and 2.5 V/cm as drift cell field 63
- Figure 16.** van't Hoff plots of the established equilibria among [H⁺pyrimidine.(H₂O)_n] clusters; with n= 0-3 resulting from injecting the mass-selected protonated pyrimidine cation into the drift cell which has 0.47 Torr H₂O mixed with 0.44 Torr of helium gas using 13.9 eV injection energy (lab) and 2.5 V/cm drift field. Drift cell temperature was varied in the range of (235 K-333 K) 64
- Figure 17.** Partial charge transfer from H⁺pyrimidine to (water)_n as a function of hydration degree *n* 69
- Figure 18.** Mass-spectrum resulting from injecting the protonated pyrimidine cation in the RF-selection mode into the drift cell which contains 0.83 Torr of helium using an injection energy of 13.9 eV (lab) and drift voltage of 4.6 V/cm. The temperature of the drift cell was 300 K. The sample mixture is composed of pyrimidine: methanol in a ratio of 1:2 73

- Figure 19.** Binary clusters of pyrimidine-acetonitrile resulting from injecting the pyrimidine radical cation in the RF-selection mode into the drift cell which contains 1.23 Torr of helium using injection energy of 13.9 eV (lab) and drift voltage of 4.0 V/cm. The temperature of the drift cell was 302 K. The sample mixture is composed of pyrimidine: acetonitrile in a ratio of 1:2..... 74
- Figure 20.** ATDs of $[H^+pyrimidine (CH_3OH)]$ on varying the drift voltage from 10 to 24V 75
- Figure 21.** ATDs of $[H^+pyrimidine (CH_3CN)]$ on varying the drift voltage from 22 to 28V resulting from injecting $[H^+pyrimidine (CH_3CN)]$ in the RF-mode using injection energy of 15 eV(laboratory frame). The measurement was done at 303 K 76
- Figure 22.** B3LYP/6-311++G(d,p) optimized structures of (a)Pyrimidine⁺ (b)Protonated pyrimidine $[H^+pyrimidine]$ (c) $[H^+pyrimidine (CH_3OH)]$ (c) $[H^+pyrimidine (CH_3CN)]$ (e) Protonated pyrimidine dimer $[H^+(Pyrimidine)_2]$. The experimental collision cross-sections and the calculated values are indicated for the room temperature measurements 77
- Figure 23.** Mass spectra resulting upon pyrimidine radical cation (Py⁺) injection via 12.7 eV (lab) injection energy and 2.2 V/cm drift field into a mixture of methanol (M) and helium gas. Drift cell temperature and total pressure are varied as indicated 79
- Figure 24.** (a) ATDs of $[H^+pyrimidine]$ and $[H^+pyrimidine (CH_3OH)]$ collected at 373 K and drift cell field of 2 V/cm (b) ATDs of $[H^+pyrimidine (CH_3OH)_n]$; n=1-3, collected at 264 K and 2.5 V/cm as drift cell field 83
- Figure 25.** van't Hoff plots of the established equilibria among $[H^+pyrimidine.(CH_3OH)_n]$ clusters; with n= 0-3 resulting from injecting pyrimidine radical cation into the drift cell which has 0.24 Torr CH₃OH mixed with 0.52 Torr of helium gas using 12.7 eV injection energy (lab) and 2.5 V/cm drift field. Drift cell temperature was varied between 249 K and 432 K 84
- Figure 26.** Partial charge transfer from $H^+pyrimidine$ to $(methanol)_n$ as a function of n . 91
- Figure 27.** Mass-spectra obtained upon injection of pyrimidine radical cations in the mass-selection mode, into a mixture of acetonitrile and helium yielded in exclusive formation of the protonated adducts; $[H^+pyrimidine.(CH_3CN)_{1-3}]$. Pressure and temperature are indicated..... 93

- Figure 28.** ATDs of H^+ pyrimidine $(\text{CH}_3\text{CN})_n$; $n=1-3$ obtained by injecting mass-selected pyrimidine radical cation into the drift cell contains 0.12 Torr CH_3CN mixed with 0.19 Torr of helium using 12 eV injection energy (lab. frame) and 2.5 V/cm drift field 95
- Figure 29.** van't-Hoff plots obtained as a result of injecting pyrimidine radical cation in the mass-selection mode into the drift cell contains 0.16 Torr of acetonitrile mixed with 0.19 Torr of helium using injection energy of 12 eV (lab. frame) and 2.5 V/cm drift field. The drift cell temperature was varied between 247 K and 303 K..... 96
- Figure 30.** Charge distribution on H^+ pyrimidine versus CH_3CN moiety as n increases 101
- Figure 31.** Mass-spectra resulting from injecting benzene radical cation in the mass-selection mode using injection energy of 13.8 eV (lab) into the drift cell which contains pure hydrogen cyanide gas and by applying a drift field of 4 V/cm. The drift cell temperature and pressure are varied as indicated..... 108
- Figure 32.** ATDs of benzene $(\text{HCN})_n$; $n=0-4$ collected upon injecting mass-selected benzene radical cations into the drift cell which contains hydrogen cyanide gas mixed with helium buffer gas using an injection energy of 13.8 eV (lab.) and by applying a drift field of 4 V/cm. **(Left)** ATDs matching of $n=0-2$, collected at 263 K. **(Right)** ATDs matching of $n=2-4$, collected at 210 K..... 110
- Figure 33.** van't- Hoff plots yielded by injecting benzene radical cations in the mass-selection mode into a mixture of hydrogen cyanide and helium gases using an injection energy of 14.4 eV (lab. frame) and by applying a drift field of 4 V/cm. The temperature of the reaction cell was varied between 187 K and 333 K..... 111
- Figure 34.** Mass-spectra obtained upon injecting benzene radical cation in the mass selection mode using injection energy of 16 eV (lab. frame) and 5 V/cm drift cell field. The reaction cell temperature and pressure are varied as indicated..... 122
- Figure 35.** van't-Hoff plots for the association equilibria (6.6) obtained by injecting mass-selected benzene radical cations C_6H_6^+ into pure acetonitrile (CH_3CN) vapor. The reaction cell temperature was varied between 234 K and 428 K. Thermochemical measured values are shown in Table 30..... 124
- Figure 36.** Charge distribution on both benzene $^+$ versus $(\text{HCN})_n$ as solvation degree n is proceeding..... 132
- Figure 37.** Mass-spectra resulting from injecting the phenyl acetylene radical cations into the drift cell containing different concentrations of hydrogen cyanide, the drift field is 4

V/cm while the injection energy was 14.4 eV (lab.). The drift cell temperature and pressure were varied as indicated..... 137

Figure 38. ATDs of [phenyl acetylene⁺ (HCN)_n] (**Left**) where n=0-2; collected at 293 K with the drift cell containing 0.25 Torr of hydrogen cyanide. (**Right**) where n=2-4; collected at 194 K with the drift cell containing 0.23 Torr of hydrogen cyanide. The cell field and the injection energy were maintained at 4 V/cm and 14.4 (lab.), respectively. 138

Figure 39. van't-Hoff plots for injecting C₈H₆⁺ into HCN gas using an injection energy of 12.4 eV (lab.) and applied field of 4 V/cm. The drift cell temperature was varied between 184 K and 298 K 139

Figure 40. Charge evolution as a function of solvation degree n which shows that the charge stays on phenyl acetylene⁺ in [phenyl acetylene⁺(HCN)_n] clusters..... 147

Figure 41. Mass-spectra resulting from injecting pyridine radical cation in the mass-selection mode using injection energy of 13.8 eV (lab) and on applying a drift field of 4 V/cm. The drift cell temperature and pressure are varied as indicated 156

Figure 42. ATDs of pyridine⁺ (HCN)_n; n=0-3 collected upon injecting mass-selected pyridine radical cations into the drift cell which contains hydrogen cyanide gas mixed with helium buffer gas using an injection energy of 13.8 eV (lab.) and by applying a drift field of 4 V/cm (**Left**) ATDs matching of n=0,1 collected at 263 K, the concentration of hydrogen cyanide was 0.27 Torr. (**Right**) ATDs matching of n=1-3, collected at 255 K, the concentration of hydrogen cyanide was 0.22 Torr 157

Figure 43. van't-Hoff plots for the association reaction yielding C₅H₅N⁺(HCN)_n; with n=1-4. The drift cell temperature was varied between 182 K and 322 K. The injection energy and drift field were maintained at 14 eV (laboratory frame) and 4 V/cm, respectively 158

Figure 44. Mass-spectra obtained upon injecting H⁺pyridine in the mass-selection mode into the drift cell using injection energy of 15.8 eV (laboratory frame) and by applying a weak electric field of 4 V/cm. The drift cell temperature and HCN concentrations are varied as indicated 167

Figure 45. van't-Hoff plots for the association reaction yielding C₅H₅NH⁺(HCN)_n; with n=1-4. The drift cell temperature was varied between 194 K and 364 K. The injection energy and drift field were maintained at 16 eV (laboratory frame) and 4 V/cm, respectively 168

- Figure 46.** Mass-spectra resulting from injecting the pyrimidine radical cations into the drift cell containing different concentrations of hydrogen cyanide. The applied drift field was 4V/cm while the injection energy was 12.4 eV (lab. frame). The drift cell temperature and pressure were varied as indicated 177
- Figure 47.** ATDs of [Pyrimidine⁺ (HCN)_n] (**Left**) where n=0-2; collected at 298 K with the drift cell containing 0.23 Torr of hydrogen cyanide. (**Right**) where n=2-4; collected at 213 K with the drift cell containing 0.16 Torr of hydrogen cyanide. The applied cell field and the injection energy were maintained at 4 V/cm and 12.4 (lab. frame), respectively 180
- Figure 48.** van't- Hoff plots for injecting pyrimidine radical cations into hydrogen cyanide (7.6) using an injection energy of 12.4 eV (lab.) and applied field of 4 V/cm. The drift cell temperature was varied between 184 K and 298 K..... 181
- Figure 49.** Mass-spectra obtained upon injecting acetylene radical cation in the mass-selection mode into the drift cell which contains a mixture of hydrogen cyanide (HCN) and helium buffer gas using injection energy of 11.8 eV(lab. frame) at room temperature and by applying a drift field of 6 V/cm 193
- Figure 50.** Mass-spectra resulting from the injection of acetylene radical cation (C₂H₂⁺) in the mass-selection mode into hydrogen cyanide gas mixed with helium buffer gas in the drift cell at different temperatures using injection energy of 11.8 eV(lab.) and by applying a drift field of 6V/cm 194
- Figure 51.** Mass-spectra obtained through thermochemistry measurements of association reaction (7.11) upon injecting acetylene radical cation in the mass-selection mode into a mixture of HCN and helium gases at different temperatures 196
- Figure 52.** ATDs matching of C₂H₂⁺(HCN)₂ and C₂H₂⁺(HCN)₃ obtained at 309 K by applying a drift field of 4 V/cm and using an injection energy of 11.8 eV(lab. frame)..... 197
- Figure 53.** van't-Hoff plot for reaction (7.11) obtained upon injecting acetylene radical cation into the drift cell which contains HCN and He mixture at different drift cell temperatures..... 198
- Figure 54.** A representative mass-spectrum obtained upon injecting hydrogen cyanide in the RF-mode after coexpansion of HCN and C₂H₂ (from 1% C₂H₂/He) at 335 K. The drift cell contains 4.4 Torr of helium buffer gas 199

- Figure 55.** Spectrum of phenyl acetylene clusters $(P_n)^+$ reacting with HCN molecules and different temperatures. They are obtained after injecting phenyl acetylene dimer in the RF-selection mode using 13 eV (lab. frame) injection energy 212
- Figure 56.** Spectrum of injecting protonated pyrimidine (H^+py) into pyrimidine vapor (py) in the mass-selection mode using 14 eV (lab. frame) injection energy 213
- Figure 57.** Mass-spectra for $H^+(HCN)_n$ clusters 214
- Figure 58.** Mass-spectra of thermal dissociation of benzonitrile dimer collected via injecting mass-selected benzonitrile dimer, BN_2 , into drift cell which has 0.89 Torr pure helium only using 9 eV injection energy (lab. frame) and 3V/cm as drift field 215
- Figure 59.** Mass-spectrum collected when the phenyllium cation ($P=C_6H_5^+$) was injected into 0.12 Torr water (W) only at 234 K at 12.9 eV injection energy (lab. frame) and 5 V/cm drift field 216
- Figure 60.** Mass-spectrum of mass-selected benzonitrile injected onto the drift cell contains 0.75 Torr of pure He using an injection energy of 14eV (lab.frame), the temperature of the drift cell=299 K, drift field=6V/cm..... 217
- Figure 61. (Top)** Arrival time distributions (ATDs) of benzonitrile monomer, $m/z=103$, the drift voltage was varied between 15 V and 33 V at 300 K with the drift cell contains 3.6 Torr of helium buffer gas **(Bottom)** The calculated structure of Benzonitrile using B3LYP/6-311++G(d,p) 218
- Figure 62.** A plot of the mean arrival time of benzonitrile as a function of P/V (Torr.V⁻¹), $R^2=0.9997$ 219
- Figure 63.** An example to Fitting of the experimental (open circles) to the transport theory (solid line). The measurement conditions were 300 K, 2.85 Torr and 5 V/cm 220
- Figure 64.** Mass-spectrum resulting from expanding both benzonitrile and water using He as a carrier gas, selecting **(Top)** Benzonitrile dimer in the RF-mode, the drift cell contains 0.76 Torr pure helium, the temperature of the drift cell=300 K, using 14 eV as injection energy (lab. frame) and 7 V/cm as drift field. **(Bottom)** Protonated hydrated benzonitrile trimer in the RF-mode, the drift cell contains 0.71 Torr pure helium, the temperature of the drift cell=301K, using 10 eV as injection energy (lab. frame) and 6 V/cm as drift field 221
- Figure 65. (Top)** The suggested structure of the protonated benzonitrile dimer, $[BN_2H^+]$. **(Middle)** Optimized structure for $[BN_2H(H_2O)^+]$. **(Bottom)** The suggested structure of the protonated hydrated benzonitrile dimer, $[BN_2H^+(H_2O)]$ 223

- Figure 66.** Mass-spectra obtained following injecting mass-selected benzonitrile monomer, BN^+ ($m/z=103$), into 0.90 Torr of pure water in a drift cell temperature range of 234 K and 302 K via 13.9 eV as injection energy, and 6V/cm as drift field. Drift cell temperatures are varied as indicated 224
- Figure 67.** ATDs of $[\text{BN}^+(\text{H}_2\text{O})_n]$ clusters obtained by injection of benzonitrile cation, BN^+ , at 14 eV injection energy and 6V/cm drift field into (**Left**) 0.78 Torr of pure water at 245 K and (**Right**) 0.84 Torr of pure water at 234 K 225
- Figure 68.** van't Hoff plots for the equilibria yielding $[\text{BN}^+(\text{H}_2\text{O})_n]$ for n values as indicated. The drift field was 4V/cm while the injection energy was 13.9 eV (lab. frame)226
- Figure 69.** B3LYP/6-311+G(d,p) structures of $[\text{Benzonitrile}^+(\text{H}_2\text{O})_n]$; $n=1-2$ 228

List of Tables

- Table 1.** Mobility and cross section values of pyrimidine and pyrimidine/water binary clusters at different drift cell temperatures 44
- Table 2.** Proton affinities of water clusters in comparison to that of pyrimidine 48
- Table 3.** Measured Thermochemistry ($-\Delta H_{n-1,n}^{\circ}$ and $-\Delta S_{n-1,n}^{\circ}$) of the formation of Pyrimidine $^{+} \cdot (H_2O)_n$ clusters; with n=1-4 for pyrimidine radical cation in comparison to the corresponding values of benzene, pyridine and protonated pyridine cations and the corresponding calculated binding energies..... 51
- Table 4.** Theoretically optimized structures using B3LYP/6-311++G(d,p) with NBO charge distribution of $C_4H_4N_2^{+}$, $H^{+}(C_4H_4N_2)$ and H_2O 54
- Table 5.** Theoretically optimized structures using B3LYP/6-311++G(d,p) of $C_4H_4N_2^{+}(H_2O)$. Distances are in Angstroms 55
- Table 6.** Theoretically optimized structures using B3LYP/6-311++G(d,p) of $C_4H_4N_2^{+}(H_2O)_2$. Distances are in Angstroms 56
- Table 7.** Theoretically optimized structures using B3LYP/6-311++G(d,p) of $C_4H_4N_2^{+}(H_2O)_3$. Distances are in Angstroms 57
- Table 8.** Theoretically optimized structures using B3LYP/6-311++G(d,p) of $C_4H_4N_2^{+}(H_2O)_4$. Distances are in Angstroms 58
- Table 9.** Measured Thermochemistry values ($-\Delta H_{n-1,n}^{\circ}$ and $-\Delta S_{n-1,n}^{\circ}$) of the formation of H^{+} pyrimidine. $(H_2O)_n$ clusters; with n=1-3 for protonated pyrimidine cation in comparison to the corresponding values of protonated pyridine cations and the calculated binding energy values 65
- Table 10.** Theoretically optimized structures using B3LYP/6-311++G(d,p) of $[H^{+}C_4H_4N_2(H_2O)_n]$; n=0-2. Distances are in Angstroms..... 67
- Table 11.** Theoretically optimized structures using B3LYP/6-311++G(d,p) of $[H^{+}C_4H_4N_2^{+}(H_2O)_3]$. Distances are in Angstroms..... 68

Table 12. Intracuster proton transfer in $[\text{H}^+\text{pyrimidine. (H}_2\text{O)}_n]$ from $\text{H}^+\text{pyrimidine}$ to water cluster as a function of hydration degree n	69
Table 13. Mobility and cross section values for various binary clusters obtained using pyrimidine/methanol and pyrimidine/acetonitrile solvent mixtures	78
Table 14. Proton affinities of methanol clusters in comparison to that of pyrimidine.....	82
Table 15. Binding energies and entropy changes from van't-Hoff plots (Figure 25) along with calculated binding energies using B3LYP/6-311++G(d,p)	85
Table 16. Theoretically optimized structures using B3LYP/6-311++G(d,p) with NBO charge distribution of $\text{H}^+(\text{C}_4\text{H}_4\text{N}_2)$, CH_3OH and CH_3CN	87
Table 17. Theoretically optimized structures using B3LYP/6-311++G(d,p) of $[\text{H}^+\text{C}_4\text{H}_4\text{N}_2(\text{CH}_3\text{OH})]$. Distances are in Angstroms.....	88
Table 18. Theoretically optimized structures using B3LYP/6-311++G(d,p) of $[\text{H}^+\text{C}_4\text{H}_4\text{N}_2(\text{CH}_3\text{OH})_2]$. Distances are in Angstroms.....	89
Table 19. Theoretically optimized structures using B3LYP/6-311++G(d,p) of $[\text{H}^+\text{C}_4\text{H}_4\text{N}_2(\text{CH}_3\text{OH})_3]$. Distances are in Angstroms.....	90
Table 20. Intracuster proton Transfer in $[\text{H}^+\text{pyrimidine. (CH}_3\text{OH)}_n]$ from $\text{H}^+\text{pyrimidine}$ to methanol	91
Table 21. Binding energies and entropy changes from van't-Hoff plots for $[\text{H}^+\text{Pyrimidine (CH}_3\text{CN)}_n]$ along with the corresponding calculated binding energies using B3LYP/6-311++G(d,p)	97
Table 22. Theoretically optimized structures using B3LYP/6-311++G(d,p) of $[\text{H}^+\text{C}_4\text{H}_4\text{N}_2(\text{CH}_3\text{CN})_n]$; $n=1,2$. Distances are in Angstroms.....	99
Table 23. Theoretically optimized structures using B3LYP/6-311++G(d,p) of $[\text{H}^+\text{C}_4\text{H}_4\text{N}_2(\text{CH}_3\text{CN})_3]$. Distances are in Angstroms.....	100
Table 24. Measured thermochemistry ($-\Delta H_{n-1,n}^\circ$ and $-\Delta S_{n-1,n}^\circ$) of the formation of $\text{C}_6\text{H}_6^+(\text{HCN})_n$ clusters; with $n=1-4$ and the corresponding calculated binding energy values at the B3LYP/6-311++G (d,p)	112
Table 25. Theoretically optimized structures using B3LYP/6-311++G(d,p) of $[\text{C}_6\text{H}_6^+(\text{HCN})]$	115

Table 26. Theoretically optimized structures using B3LYP/6-311++G(d,p) of $[\text{C}_6\text{H}_6^+(\text{HCN})_2]$	116
Table 27. Theoretically optimized structures using B3LYP/6-311++G(d,p) of $[\text{C}_6\text{H}_6^+(\text{HCN})_3]$	117
Table 28. Theoretically optimized structures using B3LYP/6-311++G(d,p) of $[\text{C}_6\text{H}_6^+(\text{HCN})_4]$	118
Table 29. $[\text{C}_6\text{H}_6^+(\text{HCN})]$ predicted structures at the M06-2X/6-311++G(d,p) level. Binding energies are corrected for ZPE and BSSE.....	120
Table 30. Measured Thermochemistry ($-\Delta H_{n-1,n}^\circ$ and $-\Delta S_{n-1,n}^\circ$) of the formation of $\text{C}_6\text{H}_6^+(\text{CH}_3\text{CN})_n$ cluster ions; with $n=1-3$ and the corresponding calculated binding energy values	125
Table 31. Theoretically optimized structures using B3LYP/6-311++G(d,p) of $[\text{C}_6\text{H}_6^+(\text{CH}_3\text{CN})]$	128
Table 32. Theoretically optimized structures using B3LYP/6-311++G(d,p) of $[\text{C}_6\text{H}_6^+(\text{CH}_3\text{CN})_2]$	129
Table 33. Theoretically optimized structures using B3LYP/6-311++G(d,p) of $[\text{C}_6\text{H}_6^+(\text{CH}_3\text{CN})_3]$	130
Table 34. $[\text{C}_6\text{H}_6^+(\text{HCN})]$ predicted structures at the M06-2X/6-311++G(d,p) level. Binding energies are corrected for ZPE and BSSE.....	131
Table 35. Measured Thermochemistry ($-\Delta H_{n-1,n}^\circ$ and $-\Delta S_{n-1,n}^\circ$) of the formation of phenyl acetylene. $(\text{HCN})_n$ clusters; with $n=1-4$ and the corresponding calculated binding energy values.....	140
Table 36. Structures of $[\text{C}_8\text{H}_6^+(\text{HCN})]$ calculated by DFT at the B3LYP/6-311++G (d,p) corrected for zero-point energies and basis-set super position errors. Energies are in kcal/mol. Distances are in Angstroms.....	143
Table 37. Structures of $[\text{C}_8\text{H}_6^+(\text{HCN})_2]$ calculated by DFT at the B3LYP/6-311++G (d,p) corrected for zero-point energies and basis-set super position errors. Energies are in kcal/mol. Distances are in Angstroms.....	144
Table 38. Structures of $[\text{C}_8\text{H}_6^+(\text{HCN})_3]$ calculated by DFT at the B3LYP/6-311++G (d,p) corrected for zero-point energies and basis-set super position errors. Energies are in kcal/mol. Distances are in Angstroms.....	145

- Table 39.** Structures of $[C_8H_6^+ (HCN)_4]$ calculated by DFT at the B3LYP/6-311++G (d,p) corrected for zero-point energies and basis-set super position errors. Energies are in kcal/mol. Distances are in Angstroms 146
- Table 40.** Thermochemistry values measured for the association reaction resulting in $C_5H_5N^+ (HCN)_n$; where $n=1-4$. The study was done in the drift cell temperature range of 182 K-322 K. The injection energy was 13.8 eV (lab. frame) while the applied drift field was 4 V/cm. Theoretically calculated binding energies are shown as well, from B3LYP/6-311++G(d,p) calculations 159
- Table 41.** Theoretically optimized structures using B3LYP/6-311++G(d,p) of $[C_5H_5N^+(HCN)]$. Distances are in Angstrom..... 163
- Table 42.** Theoretically optimized structures using B3LYP/6-311++G(d,p) of $[C_5H_5N^+(HCN)_2]$. Distances are in Angstroms 164
- Table 43.** Theoretically optimized structures using B3LYP/6-311++G(d,p) of $[C_5H_5N^+(HCN)_3]$. Distances are in Angstroms 165
- Table 44.** Theoretically optimized structures using B3LYP/6-311++G(d,p) of $[C_5H_5N^+(HCN)_4]$. Distances are in Angstroms 166
- Table 45.** Thermochemistry values measured for the association reaction resulting in $[C_5H_5NH^+ (HCN)_n]$; where $n=1-4$. The study was done in the drift cell temperature range of 194 K-364 K. The injection energy was 15.8 eV (lab. frame). The applied drift field was 4 V/cm. Theoretically calculated binding energies are shown as well, from B3LYP/6-311++G(d,p) 169
- Table 46.** Theoretically optimized structures using B3LYP/6-311++G(d,p) of $[C_5H_5NH^+(HCN)_n]$; $n=1,2$. Distances are in Angstroms 172
- Table 47.** Theoretically optimized structures using B3LYP/6-311++G(d,p) of $[C_5H_5NH^+(HCN)_3]$. Distances are in Angstroms 173
- Table 48.** Theoretically optimized structures using B3LYP/6-311++G(d,p) of $[C_5H_5NH^+(HCN)_4]$. Distances are in Angstroms 174
- Table 49.** Binding energy and entropy loss values for the association reaction (7.6) yielding 182
- Table 50.** Theoretically optimized structures using B3LYP/6-311++G(d,p) of $[C_4H_4N_2^+(HCN)]$. Distances are in Angstroms 186

- Table 51.** Theoretically optimized structures using B3LYP/6-311++G(d,p) of $[\text{C}_4\text{H}_4\text{N}_2^+(\text{HCN})_2]$. Distances are in Angstroms..... 187
- Table 52.** Theoretically optimized structures using B3LYP/6-311++G(d,p) of $[\text{C}_4\text{H}_4\text{N}_2^+(\text{HCN})_3]$. Distances are in Angstroms..... 188
- Table 53.** Theoretically optimized structures using B3LYP/6-311++G(d,p) of $[\text{C}_4\text{H}_4\text{N}_2^+(\text{HCN})_4]$. Distances are in Angstroms..... 189
- Table 54.** Comparison of the thermochemistry values obtained for formation of $\text{C}_4\text{H}_4\text{N}_2^+(\text{HCN})$ complex from two different sources..... 198
- Table 55.** Reduced mobilities of various benzonitrile-water binary clusters and their corresponding collision cross-section values. K_o results are expressed in $\text{cm}^2 \cdot \text{V}^{-1} \cdot \text{s}^{-1}$ while Ω values are expressed in \AA^2 units. Calculated results from Mobcal program using B3LYP/6-311++G (d,p) optimized structures..... 222
- Table 56.** Measured thermochemistry of benzonitrile⁺ (water)_n clusters along with the corresponding theoretical values..... 227

Abstract

SOLVATION OF ORGANIC CATIONS IN THE GAS PHASE AND WITHIN MOLECULAR CLUSTERS

Ahmed Mohamed Kotb Hamid, Ph.D.

A dissertation submitted in partial fulfillment of the requirements for the degree of Doctor of Philosophy at Virginia Commonwealth University

Virginia Commonwealth University, 2012

Director: M. SAMY EL-SHALL

Professor, Department of Chemistry

The role of the solvent in ionic and ion-molecule interactions is of fundamental importance in kinetics and thermodynamics of solution chemistry. However, the study of the ionic interactions in the presence of a large number of solvent molecules is very challenging. Therefore, the gas-phase is the appropriate medium to study such reactions on a molecular level

where the ion-solvent interaction can be examined by studying ions surrounded with a cluster of solvent molecules in the complete absence of the any interference caused by the bulk of the solvent.

In nature, organic ions can form hydrogen bonds with solvents. An insight into basic molecular interactions is required to be extracted from the gas phase energies and structures of the solvated organic ions. Therefore, the stepwise hydration experiments of benzene⁺, C₃H₃⁺, acetylene⁺, pyridine⁺, 2-fluoropyridine⁺, phenyl acetylene⁺ and acetylene dimer⁺ have been investigated using quadrupole mass-selected ion mobility mass spectrometer. Thus, these systems can be considered as prototypical models for understanding the molecular aspects leading to hydrophobic hydration in the condensed phase.

Two routes of the investigation of ion-molecule interactions are considered in this dissertation. The first route is concerned with injecting the same ion into various solvents to study the nature and strength of the ion-solvent interactions when protonated pyrimidine cation interacts with water, methanol and acetonitrile molecules. Association and proton transfer reactions were observed. On the other hand, the second route involves the injection of various ions into the same solvent where the interactions of hydrogen cyanide (HCN) molecules with different ions. Benzene, phenyl acetylene, pyridine, protonated pyridine, and pyrimidine ions were investigated. All the investigated ions exhibited hydrogen bonding with the hydrogen cyanide molecules with variable strength depending on the charge distribution on the specified ion as well as the nature of interaction.

Additionally, ion mobility structural methods were utilized to investigate structures of binary clusters formed by supersonic expansion of mixed vapors. The structures can be identified by comparing the experimentally measured collision cross section values with those predicted from DFT computations.

Chapter 1: Introduction

Supersonic molecular beams have been employed to study molecular clusters of various kinds, ranging from van der Waals complexes to metals and fullerenes.¹⁻⁶ Supersonic expansion experiments provide suitable means for the formation of various molecular clusters of different sizes. Therefore, they can promote molecular level studies that can be used as model systems for the macroscopic phenomena.⁶⁻⁸ Cold gas phase clusters allow the identification of lowest energy configurations of the various solute-(solvent)_n systems such as hydrogen bonded complexes. The lowest energy configuration in hydrogen bonded complexes is usually the one that maximizes the extent of the hydrogen bonding.^{6,9,10}

The role of the solvent in ionic and ion-molecule interactions is of fundamental importance in the kinetics and thermodynamics of reactions in solution chemistry.¹¹⁻¹³ Ion-solvent interactions influence the stability, reactivity and dynamics of the ionic species in solution phase; they affect charge transfer and ion association reactions.^{5,14,15} However, the understanding of the ionic interactions in the presence of a large number of solvent molecules is challenging.¹⁶⁻¹⁹ Therefore, it is more informative to study the impact of solvation on an ion in a solvent free environment where the ions are “naked” or in a microsolvated environment and a controlled number of solvent molecules exists.^{7,14,17,20} Thus, the gas-phase is the appropriate medium to study such reactions on a molecular level where ion-solvent interaction can be examined where ions surrounded with a specific number of solvent molecules in the complete absence of the interference from complex bulk phenomena.^{7,8,14} Gas-phase mass-spectrometry has developed as one of the most informative and accurate tools for the investigation of ion structures, energetics and reactivity.²¹⁻²³ Thus, the investigation studies of cluster ions can bridge

the gap between the gas and condensed phases.^{7,14,15} By comparing the condensed-phase and the gas-phase properties, and thus the real solvent effects can be readily understood and quantified.^{24,25} With the capability to control the amount of solvent molecules, it is easy to investigate the dependence of the ionic chemical and physical properties on the stepwise solvation process.³

Ion-molecule interaction is one of the most-studied subjects in the gas-phase where the solvent effects are completely removed using various spectroscopic and ion mobility mass spectrometric techniques.^{14,15,18} The solvation and microsolvation of aliphatic and aromatic carbocations by polar molecules have attracted attention in recent years because of their importance in many chemical, biological and physical phenomena.^{26,27} In fact, ion-molecule reactions present a common route that leads to the formation of polycyclic aromatic hydrocarbons (PAHs) which were detected in the interstellar medium.²⁸ PAHs are believed to be responsible for unidentified infrared bands, and to be intermediates in soot formation processes.²⁸⁻³⁰ Although our studies are directly applied to positive cluster ions, cluster growth trends can be applied to neutral systems since as the cluster size increases, binding energies for ionic clusters will approach those of the neutral clusters.^{5,26} In fact, the evolution of the physical properties of ions in bulk solution can be obtained from the trends in ion-solvent interactions in clusters of controlled sizes and compositions.^{5,7,14}

Results from ion-equilibria measurements in solution recorded in the form of acid-base dissociation constants, stability constants of ion-ligand complexes, etc represent the most valuable source of numerical data available to chemists.³¹ Similarly valuable information is available via gas-phase measurements.^{7,14} Gas-phase ion equilibrium measurements have been expanded rapidly since firstly introduced in the 1960s by P. Kebarle and his coworkers, and they

became the most abundant and reliable sources for thermochemical data of ions.^{15,17,32-38} Equilibrium measurements have often been used to measure the binding energies and upon comparing the measured values with those predicted through theoretical calculations of low energy structures, lowest energy structures can be identified.^{18,20,35} These measurements have been employed to examine biologically interesting systems, such as amino acids and mononucleotides through investigating their interactions with water molecules.^{15,36,37,39}

Using quadrupole mass-selected ion mobility system, the ion of interest is pre-selected according to its mass-to-charge ratio by a mass-filter and then injected into the reaction cell where the neutral gas exists. The products are then determined using mass-filter scanning.^{33,40,41} Thus, this apparatus can be utilized to follow the energetics of most of the ion-molecule reactions through thermochemistry measurements of successive equilibrium steps. In addition, the rate constants can be measured for irreversible faster reactions.⁴² Therefore, it can be used in probing the molecular interactions and energy transfer.^{43,44} Moreover, the ion mobility mass-spectrometer can be used to study weakly-bound clusters. For instance, it has been used to study the interactions of H_3O^+ reactions with N_2 , H_2 and CO molecules with no interference from the strongly bound $\text{H}_3\text{O}^+(\text{H}_2\text{O})_n$ clusters.⁴⁵

Organic ions can form hydrogen bonds with solvents in nature.^{18,46} Hydrogen bonding interactions involving ionized aromatics are important in radiation chemistry, electrochemistry, polymerization in aqueous solvents and in astrochemical environments.⁴⁷ Since water is nature's solvent, it usually exhibits strong solvent effects on reactions.^{14,15,24,38} An insight into basic molecular interactions is required to be extracted from the gas phase energies and structures of the hydrated organic ions.^{18,20} In fact, the stepwise hydration of these ions can provide useful correlation to the factors that determine hydrophobic and hydrophilic hydration in macroscopic

systems. Therefore, the stepwise hydrations of benzene⁺, C₃H₃⁺, acetylene⁺, pyridine⁺, 2-fluoropyridine⁺, phenyl acetylene⁺ and acetylene dimer⁺ have been investigated in our laboratory.^{17-20,48} Organic ions can interact with water molecules either by relatively weak carbon-based CH^{δ+}---O hydrogen bonds, for instance, benzene⁺ and the C₃H₃⁺ ions, or via stronger hydrogen bonds, such as in protonated pyridine cation where the NH⁺---O hydrogen bonds can be formed.^{17,32,33} Thus, these systems can be considered as prototypical models for understanding the molecular aspects leading to hydrophobic hydration in the condensed phase.⁴⁹ For example, hydration of acetylene cations provided evidence of involvement of water molecules in the formation of simple alcohols in space.⁴²

Ion mobility spectrometry is a well-established analytical technique that has been utilized to analyze various chemical species including explosives, drugs, chemical warfare agents in ambient conditions.^{50,51} Moreover, ion mobility spectrometry instruments have been developed to be portable, fieldable, fully automated and commercialized devices for public uses like security gates in airports and military security.⁵² The mobility of an ion is a measure of how rapidly it moves through a buffer gas under the influence of a weak drift field. The mobility of a polyatomic ion depends mainly on its average collision cross-section which in turn depends on its geometry.^{41,53,54} Therefore, ion mobility measurements can distinguish different geometries of structural conformers, especially in systems with a diverse population of conformers.^{4,53-55} Ion mobility measurements of hydrated ionic clusters can provide valuable information about their structures.^{43,44,54,56-58} Mobility measurements supported by collision induced dissociation and thermochemistry measurements have been utilized to establish that the acetylene trimer cation can efficiently isomerize to the benzene cyclic structure.^{59,60}

Molecular computation technique utilizing, e.g. Density Functional Theory (DFT), helps to understand and support the experimental measurements.^{61,62} Recent advances in computational techniques and the development of highly advanced *ab-initio* and DFT electronic calculations enabled chemists to provide a powerful complement to the experimental results.^{63,64} The time-independent nature of theoretical computational methods and their accuracy features provide ideal means to study the structures and reaction enthalpies of the hydrogen bonded complexes.^{6,65} Moreover, theoretical computations can be used not only to evaluate the ion-solvent interaction energy but also, to predict the solvent-solvent interaction energies.¹⁵ In addition, theoretical computations have been employed to examine the solvent impact on the activation energy barriers. For example, it was predicted that water molecules can reduce the activation barriers significantly in the tautomerization of purine.⁶⁶

The organization of this dissertation is as follows: chapters two and three are primarily focused on the details of the experimental setup and the various measurements that were used in this work. Chapter four deals with the hydrations of pyrimidine and protonated pyrimidine cations in the gas phase and also, it provides a structure study of the binary pyrimidine-water clusters. In chapter five, the results from thermochemistry measurements of the solvation of protonated pyrimidine by methanol and acetonitrile molecules are presented. The obtained thermochemistry values and structures are compared with those obtained from hydration experiments. In chapter six, the solvations of benzene radical cation with several HCN and CH₃CN in the gas phase are examined. Moreover, the solvation of phenyl acetylene radical cation by HCN molecules under temperature and pressure controlled conditions is presented in chapter six as well. The solvation experiments of various nitrogen containing cations are presented in chapter seven where the solvation studies of pyridine, protonated pyridine and

pyrimidine cations by several HCN molecules are presented. The dissertation's conclusions and possible future research aspects are then presented in chapter eight.

Two routes of the investigation of ion-molecule interactions are considered in this dissertation. The first route is relies on injecting the same ion into various solvents to study the nature and strength of its interaction with different solvents. This study is presented in chapters four and five. In this study, a comparison of the hydration behavior of pyrimidine radical cation, a biologically significant ion, with the hydration of its corresponding protonated cation is presented and discussed. Chapter five extends the hydration study to other solvents such as, methanol and acetonitrile. Moreover, proton transfer from organic cations by polar solvent clusters resulting in protonated solvent clusters was investigated experimentally and theoretically. This reaction was found to be not only size dependent but also, it is related to the solvent cluster molecules interaction with the specified cation and with each other. The solvent molecules are required to form an aggregate of higher proton affinity than the resulting radical formed after the proton transfer to be able to abstract the H-atom from the aromatic cation.

To date, astronomers and molecular astrophysicists have identified and spectroscopically characterized more than 100 gaseous interstellar molecules.⁶⁷ Among them, the gaseous hydrogen cyanide (HCN) molecule and its metastable isomer (HNC) are thought to be ubiquitous in both cold, dark molecular clouds and in some comets.⁶⁸ HCN has received great attention from biochemists as well, because of its possible role in the synthesis of prebiotic compounds.⁶⁸⁻⁷⁶ It was reported by Matthews and co-workers that HCN molecule can act as a precursor for the formation of a mixture of amino acids through reaction of its oligomers with water. Moreover, they accounted for the presence of protein/nucleic acid ancestors on the early Earth to the presence of hydrogen cyanide polymers.⁷⁷ Therefore, the second investigation route involves the

injection of different ions into the same solvent (HCN) as presented in chapters six and seven. The different investigated ions include benzene, phenyl acetylene, pyridine, protonated pyridine, and pyrimidine. All the investigated ions showed hydrogen bonding interaction with HCN molecules, with variable strength depending on the charge distribution on the specified ion as well as the nature of the interaction forces.

In addition, ion mobility was utilized to obtain structural information of binary clusters formed via supersonic expansion of mixed vapors. Binary clusters are of particular interest not only because they simulate multicomponent systems but also, investigating them can clarify the structures of hydrogen bonded networks about a protonated ion.⁷⁸ The structures can be then identified through comparing the experimentally measured cross section values with those predicted using DFT computations.

Chapter 2: Experimental Setup

The experiments were conducted using Virginia Commonwealth University quadrupole mass-selected ion mobility quadrupole mass-spectrometer (QMS-IM-QMS) that consists of four stainless steel chambers. The QMS-IM-QMS with all the details is shown in Figure 1 and Figure 2 and it is explained in details in the following sections.^{20,34,40,79-83}

2.1. Vacuum System

The first chamber is the source chamber where the formation of neutral clusters occurs. The first chamber is pumped down using a Varian VHS-6 diffusion pump with pumping speed of 3000 L/s (He), which is in turn backed by an Edward E2M-30 mechanical pump. The typical pressure is $\sim 10^{-5}$ Torr during the experiment.

The second chamber hosts an electron-impact ionizer which is followed by a co-axial quadrupole mass-filter. This chamber is pumped down via an Edward Diffstak 160/700 M diffusion pump which is backed by an Edward E2M-40 mechanical pump. The typical pressure during the experiment is $\sim 10^{-6}$ Torr.

The third chamber houses two stacks of transport einzel lenses and the drift cell (reaction cell). The third chamber is pumped down by an Edwards Diffstak 250/2000 P, which is backed by an E2M-40 Edwards mechanical pump. Typical pressure during the experiment is $\sim 10^{-5}$ Torr.

The fourth chamber houses another electron impact ionizer coupled to the second quadrupole mass-spectrometer followed by an off-axis collision dynode electron multiplier detector. This chamber is pumped down by an Edwards Diffstak 160/700 M diffusion pump, which is backed by the same Edwards E2M-40 that backs the second chamber diffusion pump. The pressure in the fourth chamber is $\sim 10^{-7}$ Torr during the experiment. Pyrex iridium ion gauges are used to measure the pressure in all the chambers.

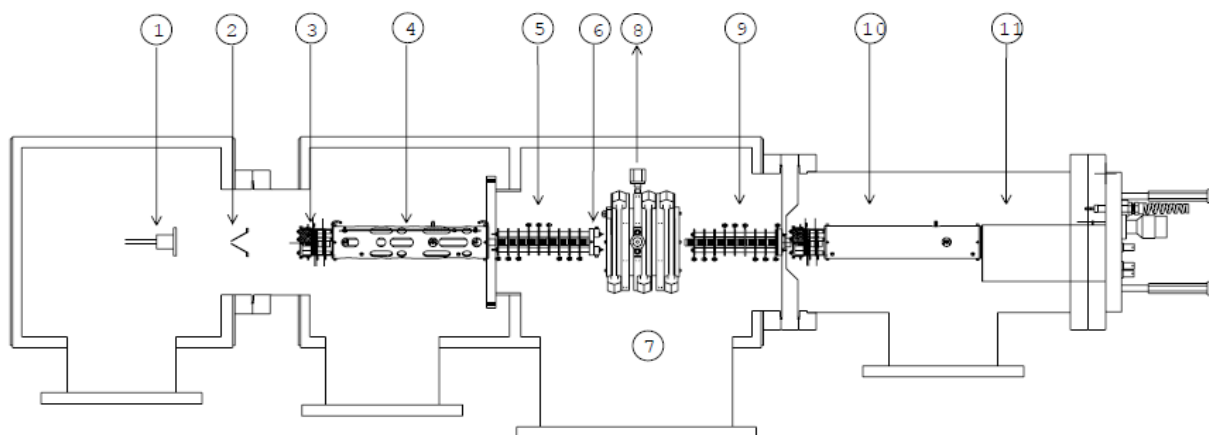


Figure 1. Schematic diagram of the mass-selected ion mobility system at VCU: (1) pulsed nozzle (2) 3 mm skimmer (3) electron-impact ionizer (4) quadrupole mass filter (5) ions transport lenses stack 1 (Einzel Lenses 1, 2 and 3) (6) steering lens/ion gate (7) drift cell (8) to baratron (9) ions transport lenses stack 2 (Einzel Lenses 4, 5 and 6) (10) quadrupole mass filter (11) electron multiplier (detector)

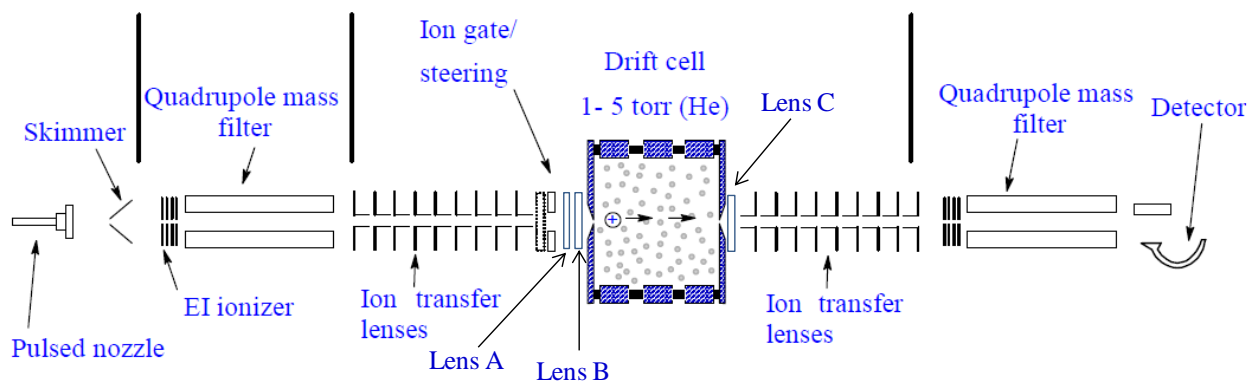


Figure 2. The ion mobility system can be divided into four sections: the expansion, the ionization, the reaction and the detection parts

2.2. Cluster formation

Clusters are defined as assemblies of atoms and molecules sometimes attached to ions, range from as few as two or three atoms to several thousands.⁸⁴ Clusters properties lie between those of the gas and the bulk condensed state. Therefore, clusters are referred to as the fifth state of matter.⁸⁵

Intermolecular forces are attractive cohesive forces which tend to order the molecules and repulsive thermal forces which tend to disorder them. At very low temperatures accompanying the supersonic adiabatic expansion, thermal forces decrease and cohesive forces dominate.⁸⁴ The clusters' formation is carried out through an adiabatic supersonic expansion process. The expansion of 3-5 atm of the carrier gas, helium or argon, seeded with ~0.5-4% sample's vapor occurs through a pulsed conical nozzle (500 μm diameter) in pulses of 200-300 μs duration at repetition rates of 30-100 Hz into a low pressure region (10^{-6} to 10^{-7} Torr).

Continuous flow is used often in this work whenever clustering is unfavorable and only atomic or molecular ion is being investigated. However, the life time of the ionization filament is

shortened in the continuous flow regime in comparison to the pulsed flow. The nozzle flange used for continuous flow has 250 μm orifice diameter, and there will be no delay for the gate from the nozzle in that case.

If C_p is the heat capacity of the expanding gas at source temperature (T_o), and T_I is the beam temperature, then the energy balance of an ideal gas is given by:⁸⁶

$$C_p T_o = C_p T_I + \frac{mu^2}{2} \quad (2.1)$$

where m is the mass of the expanding gas, and u is the supersonic velocity of the cluster beam. Since mu^2 is positive, T_I is lower than the source temperature T_o . The temperature decrease can be quantified by equation (2.2):

$$T_I - T_o = T_I \left\{ \left(\frac{P_I}{P_o} \right)^{\frac{\gamma-1}{\gamma}} - 1 \right\} \quad (2.2)$$

where P_o is the source pressure, P_I is the cluster beam pressure, and γ is the heat capacity ratio;

$\gamma = \frac{C_p}{C_v}$.⁸⁷ It was found that the clusters' temperature is ~ 30 K.³⁵ This cooling promotes

condensation that molecular beams of clusters with weak van der Waals forces can be formed.

The size of clusters can be predicted using Hagena parameter, Γ^* , which in turn is defined using equation (2.3):⁸⁸

$$\Gamma^* = k \frac{\left(\frac{d}{\tan \alpha} \right)^{0.85}}{T_o^{2.3}} P_o \quad (2.3)$$

where d is the nozzle diameter (mm), α is half of the expansion angle ($\alpha < 45^\circ$ for supersonic while $\alpha = 45^\circ$ for sonic expansion regimes). P_o and T_o are the pre-expansion pressure and temperature in mbar and Kelvin, respectively. k represents a bond formation parameter, which

represents the intermolecular bond strengths. Clustering generally begins when $\Gamma^* > 100-300$. The cluster size (the number of atoms per cluster, N_c) was found to be directly proportional to $\Gamma^{*2.0-2.5}$.⁸⁹

The formed molecular beam is enriched in the larger clusters in its centerline due to the preferential diffusive migration of light atoms, such as carrier gas atoms, radially away from the beam axis.⁹⁰ This effect is enhanced by using a 3 mm diameter cone-like skimmer which skims the preformed cluster jet into a unidirectional molecular cluster beam.^{90,91} Moreover, skimmer acts as a conductance limit that maintains the pressure of the second chamber to be in 10^{-7} Torr level, which is safe level for both the electron impact ionizer and the quadrupole mass filter.

2.3. QMS-IM-QMS

2.3.1. Electron impact ionization

The neutral molecular beam is ionized by an axial electron-impact ionizer (Extrel, CMS).^{92,93} Ionization occurs in the ionizing volume (ion region basket) shown in Figure 3. The ionizing electrons are emitted from a pre-heated tungsten filament.⁹⁴ Mesh filament shield is used to increase the pumping efficiency by reducing the number of possible collisions with background gases. Thermionic emission of electrons occurs as a result of heating the Tungsten filament to 1873-2973 K using an emission current of 0.05-5.0 mA. By applying electrostatic field, the free electrons are extracted from the filament and accelerated into the ionization volume.⁹⁵ These electrons abstract an electron from an atomic or molecular orbital of the analyte following the equation (2.4):^{94,96}



The electron energy is usually in the range of 50-80 eV, which should be enough to ionize all the organic compounds.⁹² Moreover, the ion yield is at maximum at electron energy of 50-70 eV range where the ionizer sensitivity gets close to a maximum. However, excessive electron energy can cause significant fragmentation of the parent ions. High electron energies are utilized if the fragment study is of experimental interest so the fragment ion can be mass-selected and injected into the drift cell for structure and reactivity studies. The ions are then transported into the quadrupole entrance using several electrostatic lenses.

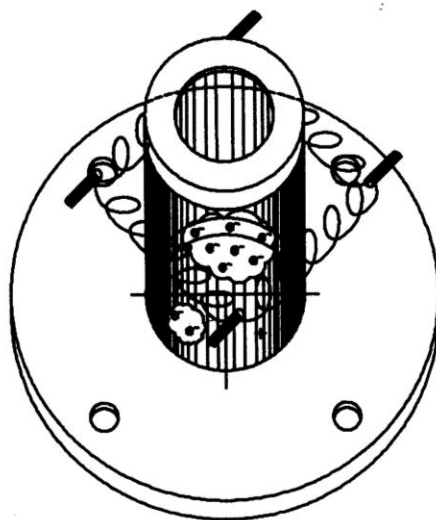


Figure 3. Schematic drawing of the ion volume (the ion region basket and filament)

2.3.2. Quadrupole mass-filter

The quadrupole ($3/8" \times 7.88"$, 10-4000 amu) tri-mass filter (Extrel, CMS) is made of four parallel stainless steel poles of circular cross section, in which the opposite pairs are electrically connected. Fluctuating electric field is applied to the rods in specific strength and frequency which affects the ions' path.^{97,98} The quadrupole mass filter operates with the superposition of uniform RF and DC voltages. Both of the applied DC and RF voltages depend on the mass to

charge ratio (m/z) of the ions. Therefore, with proper selection of them, ions of a given (m/z) will have stable trajectories and oscillate about the z -axis and pass through the mass-filter to the other end while others won't.⁹⁹ The quadrupole rods diameter is 9.5 mm while the RF frequency used is 880 kHz, which can reach up to 4000 amu. It has pre and post filters which are short stub rods before and after the main rods. The pre and post filters are employed to collimate the ions coming into and exiting from the main rods, respectively to improve the abundance sensitivity. Moreover, the pre-filter is preceded by an entrance lens which steers the ions into the quadrupole filter in order to enhance the signal intensity. The ions of interest are selected according to their (m/z) ratio using the first quadrupole mass-filter, which can work in either resolved (RF-DC) mode or the integral (RF only) mode according to the abundance of the ions. (RF-DC) mode is preferred in case of strong signals since it allows the ion of interest to pass exclusively, while in case of weak signals, (RF only) mode is used.

In the resolved RF-DC mode, the mass-selection mode, ions of the wrong masses are deflected by the quadrupole mass filter while those of pre-selected masses are allowed to pass through the mass-filter and eventually injected onto the drift cell.¹⁰⁰ The ions are transported out of the quadrupole to the third chamber through the exit lens. The exit lens has a small acceleration applied voltage (up to $\pm 100V$) to enhance the quadrupole sensitivity.

Resolution of the mass-filter depends on the number of oscillations (n) that the transversing ion experiences in the mass-filter. The value of n depends on the time length that ions spend in the quadrupole field. Thus, the number of oscillations depends upon the ion entrance velocity and the length of the quadrupole rods.¹⁰¹ Ion entrance velocity depends on the ion energy. Therefore, the resolution increases when the ions enter the mass-filter in moderate speeds. Therefore, the ion energy was maintained in the 10-30 eV range. If the ions enter the

quadrupole mass-filter with higher energies, poor resolution and poor peak shapes will be obtained.¹⁰² For higher energy sources, floating of the quadrupole housing is a necessity to help the quadrupole to handle the highly energetic ions. The housing quadrupole can be floated via a voltage up to ± 100 V.¹⁰² Moreover, polebias voltage which is a DC-voltage applied to the z-axis of the quadrupole rods is usually applied in such way the ion energy is kept in the favorable range.

2.3.3. Drift cell

The ion beam is transported and focused by the first stack composed of three einzel lenses to be eventually injected onto the drift cell. An ion gate is present following the first stack of the einzel lenses. The ion gate consists of two sets of steering lenses. The ion gate is made of two half circles Nickel plates. One half of each set is biased to the third einzel lens while the other half is connected to a separate power supply which is connected to an external pulse generator (DEI, PVX-4140). The gate opens when both the half circles of the vertical steering lenses have the same sign while it closes when they have opposite signs. The steering lenses chop the ion beam into 10-50- μ s-wide packets to be injected to the drift cell. The zero time is set at the middle of the ion gate so that the reaction time can be measured. The reaction time is represented as the time taken by the ions to reach from the ion gate to the detector.^{48,80}

The drift cell consists of two major pieces, the reaction cell body ($3.50'' \times 3.50'' \times 2.14''$) and the cell endcap ($3.50'' \times 3.50'' \times 0.40''$), as shown in Figure 4 and Figure 5.^{35,79} The drift cell was designed by Dr. P. Kemper.¹⁰³ The endcap is separated from the cell body by an insulating ceramic ring. Both pieces are made of oxygen free high conductivity copper; with an exceptionally high melting point of 1360 K. The entrance plate has a 0.254 mm orifice which is the same as the exit aperture. Two entrance lenses separated by ceramic spacers, lenses A and B,

where A is a cone taper lens, are mounted on the exterior entrance of the cell-body. Lenses A and B are utilized to focus the ions into the drift cell entrance aperture. Both lenses use separate voltage supplies. In addition, another taper lens, lens C, (exit lens) is mounted on the exterior of the endcap. Lens C has a separate voltage supply and is insulated from the endcap by ceramic spacers. The drift cell is heated by tantalum wires running inside ceramic tubes which are inserted into the cell body. The cell body and endcap parts are heated separately. The maximum operational temperature is approximately 773 K. The lowest attainable temperature is 78 K, the temperature of liquid nitrogen used for cooling. Four temperature controllers are used to keep constant temperature within ± 1 K. Heating of the drift cell is controlled by two controllers (Omega type CN3251). Cooling is controlled by two temperature controllers (Omega type CNi3233) coupled to On/Off solenoid valves, each for a cell piece cooling.

Voltage supply for the ionizer lenses, entrance and exit plates, as well as all sets of einzel lenses is provided by an ABB Extrel power supply and remote controlled using Merlin controlling program (Extrel, CMS). Inert and/or reacting gas is supplied to the cell through a stainless steel tube (with ceramic breakers for insulation). Flow rates are controlled by two mass flow controllers (MKS 1479A) which are capable of maintaining cell pressure accuracy of ± 1 mTorr. The helium buffer gas and the reactant gas molecules in the drift cell flow out of the drift cell through the entrance and exit apertures of the cell. Complete thermalization of the injected ions takes place through the collisions with the escaping drift cell gas molecules at the drift cell entrance aperture.^{42,45,80,82}

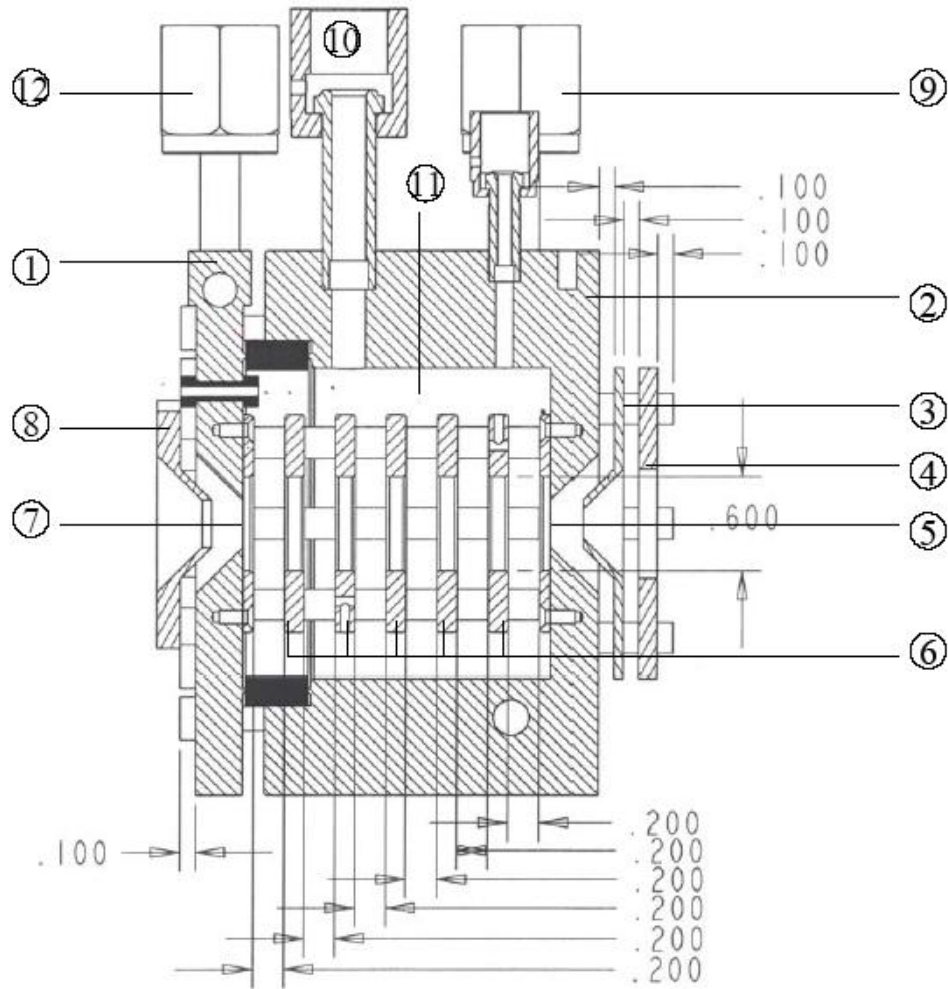


Figure 4. Side view drawing of the drift cell. (1) Endcap (2) Reaction cell body (3) Entrance lens (lens B) (4) Tapered entrance lens (lens A) (5) Entrance orifice (0.25 mm) (6) Drift rings (7) Exit orifice (0.25 mm) (8) Tapered exit lens (lens C) (9) Cell body liquid nitrogen inlet (10) Baratron connector (11) Drift cell (12) Endcap liquid nitrogen inlet. Dimensions in inches

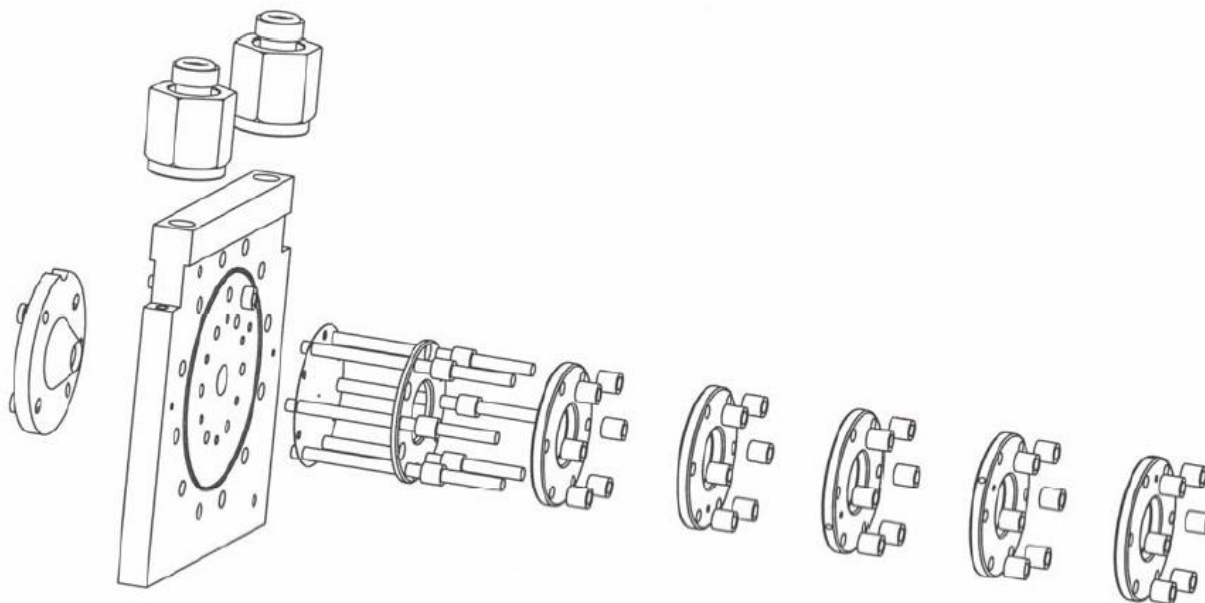


Figure 5. A simplified view for the mounting of the copper rings, the ceramic spacers and the tapered exit lens connected to the end cap

The unreacted as well as the product ions exit from the drift cell are guided and focused via the second set of einzel lenses, composed of three lenses, into the fourth chamber. The ions are analyzed and detected by the second mass-filter and electron multiplier detector, respectively. The second mass-filter can work in either fixed (m/z) ion mode or the scan mode. The fixed ion is used to get arrival time distributions (ATDs) of individual reactant or product ions. The scan mode is employed to monitor the intensity change of all the ions exiting from the drift cell. The intensity of an ion is obtained as a function of time after its injection into the drift cell through the integration of the area under the ATD peaks.^{42,60}

2.3.4. Electron multiplier detector

Pulse counting electron multiplier detector with conversion dynode (De-Tech; 402A-H) is then used to detect the product ions. The positive ions strike the conversion dynode surface

which is set at very high negative voltage of ~5 kV, and electrons are evolved and accelerated to the multiplier tube. The multiplier tube has appropriate applied positive voltage which depends upon the abundance of the signal and the age of the multiplier tube. The current signal is then amplified to higher levels by using counting pre-amplifier (MTS-100). Since signal comes from multielectron process while noise comes solely from single electron process, a discriminator is utilized to improve the signal to noise ratio. The counting pre-amplifier (MTS-100) has an adjustable discriminator.

2.3.5. Ion energy and Injection energy

The axial kinetic energy of the ions in the quadrupole mass filter is determined by the difference of the total voltage applied to the ion region and the axial potential of the four poles, the polebias voltage. The polebias voltage is DC voltage (± 200 V) applied to the quadrupole z-axis to speed up or slow down the ions prior to entering the quadrupole field. Therefore, the actual energy of the ions seen by the quadrupole mass-filter can be calculated using equation (2.5):

$$\text{Ion energy} = \text{Ion region voltage} + \text{Floating quadrupole voltage} - \text{polebias voltage} \quad (2.5)$$

The ion kinetic energy is maintained in the 10-30 eV range. In fact, if the ions are going too fast, the mass filter won't have enough time to decide whether to pass or reject them. Moreover, fast ions can cause bad quadrupole resolution and lumpy peak shapes.⁹²

The injection energy of the ions is the energy that ions have when injected into the drift cell. The injection energy should be only slightly higher than the energy required to get the ions into the drift cell against the drift gas outflow to not affect the time-resolved measurements. Injection energy (laboratory frame) can be determined from equation (2.6):

$$\text{Injection energy} = \text{Ion region voltage} + \text{Floating quadrupole voltage} - \text{Drift cell entrance plate applied voltage} \quad (2.6)$$

The product dissociation by collisions is avoided by low acceleration energy between the cell exit and the second quadrupole. Therefore, the energy difference between the drift cell exit and the polebias of the second quadrupole is kept in the 3-12 eV range.

Chapter 3: Experimental Measurements

In this chapter, the experimental measurements that are employed throughout the rest of the dissertation are discussed in detail. Several clarifying examples are presented in Appendix B.

3.1. Mobility measurements and Structure determination

3.1.1. Mobility measurements

Ion mobility spectrometry is a well-established analytical technique that has been utilized to analyze various chemical species including explosives, drugs, and chemical warfare agents in the ambient conditions.^{4,50-52,104} The mobility of gas phase ions is a measure of how rapidly they move through buffer gas under the influence of a weak uniform electric field.^{4,53,55} Therefore, ion mobility measurements provide a direct and accurate way of measuring the collision cross-sections of the mass-selected ions in buffer gas. The motion of the ions through a buffer gas under the influence of an externally applied weak electric field depends only upon the ion's collision cross-section with the buffer gas. The collision cross-section is directly related to the geometric shapes of the ions.^{16,44,81,86} Thus, mobility measurements can be used to separate isomers with different geometries.² Moreover, ion mobility mass spectrometry can be utilized for structural characterization of various conformers. Recently, this technique has been utilized to examine the effect of the binding of various alkali metals to gramicidin A in the resulting conformers.⁵⁴

In our experiment, ions subjected to an electric field are accelerated along the electric field direction axis. However, when the drift cell contains helium buffer gas atoms, the ions get decelerated by the frictional force with the buffer gas atoms. If the ions stay in the drift cell for enough time and the electric field is uniform throughout the whole drift cell, equilibrium state is reached. Under these conditions, ions move in a constant velocity, which is called drift velocity, \vec{v}_d .¹⁰⁵

The cluster ions of interest are mass-selected by the first quadrupole mass filter, focused and injected into the drift cell which contains homogeneous pressure of helium buffer gas. The injection energy is maintained only slightly higher than that required to introduce the ions into the drift cell against the buffer gas outflow. The ions are thermalized at the entrance of the drift cell through collisions with buffer gas atoms escaping from the cell entrance orifice. The ions are accelerated by applying a uniform drift field while the friction forces resulting from collisions with helium atoms decelerate them, causing the ions to move with a constant drift velocity. The mobility, K , of an ion is defined as the velocity at which the ions drift through the buffer gas, \vec{v}_d , divided by the electric field across the drift region, \vec{E} , as in equation (3.1):⁸¹

$$K = \frac{\vec{v}_d}{\vec{E}} \quad (3.1)$$

Since the drift velocity, \vec{v}_d , is inversely proportional to the buffer gas number density, N , the mobility, K , is also inversely proportional to N . Therefore, the mobility is often expressed in terms of reduced mobility, K_o , rather than K . where $K_o \propto NK$, as shown in equation (3.2):³⁸

$$K_o = \frac{P}{P_o} \frac{T_o}{T} K \quad (3.2)$$

where P is the pressure in Torr and T is the temperature in Kelvin. P_o and T_o are the STP values which are 760 Torr and 273.15 K, respectively.

Equations (3.1) and (3.2) can be combined and rearranged to give: ¹⁰⁶

$$t_d = \left(\frac{l^2 \cdot 273.15}{T \cdot 760} \frac{1}{K_o} \right) \frac{P}{V} + t_o \quad (3.3)$$

where t_d is the measured mean arrival time of the drifting ion packet taken at the peak maximum, l is the drift length (5 cm long for our drift cell), V is the potential difference across the drift cell and t_o is the time the ion spends outside the drift cell before reaching the detector.

All the mobility measurements should be carried out in the low-field limit where the ion's drift velocity is small compared to the thermal velocity and the ion mobility is independent of the field strength. In fact, the reduced mobility, K_o , can be obtained from the slope of the plot of t_d versus (P/V) . Arrival time (t_d) is measured at different drift cell voltages at constant buffer gas pressure or at different buffer gas pressures at constant applied voltage. It is easier to follow the former route for ion mobility measurements.

The resolution of the ion mobility instrument can be measured from equation (3.4):³⁸

$$resolution = \frac{t}{\Delta t} = \frac{L}{\Delta x} = \sqrt{\frac{\pi V e}{4 k_B T}} \quad (3.4)$$

Therefore, the resolution of an ion mobility instrument can be directly enhanced by using longer drift tubes, where resolution is directly proportional to the drift length, L . Moreover, according to equation (3.4), the resolution is enhanced at higher drift voltages and lower temperatures. The resolution, in practice depends on the pulse width, Δt_o . The gate width can be adjusted in our

experiment via adjusting the gate width, short pulses are always recommended for higher resolution results.

However, to substantially increase the drift voltage for resolution enhancement, the buffer gas density, N , should be increased to avoid arc formation.¹⁰⁷ Moreover, high buffer gas density ensures complete thermalization of gas ions at the cell entrance aperture and prevents the neutral molecules from getting into the drift cell.⁴ In fact, the field intensity can be expressed using (E/N) parameter where E is the electric field and N is the buffer gas number density.¹⁰⁶ In other words, E/N parameter represents the energy gain from the drift field E and low field conditions are present when $E/N < 6$ Td. E/N is expressed in units of Townsend (Td); where $1\text{Td} = 10^{-17} \text{ V}\cdot\text{cm}^2$. At low field conditions, the ion drift velocity is small compared to the thermal velocity. Under these conditions, ion mobility is independent on field strength.⁸¹ Mobility measurements are made by injecting a narrow pulse of ions into the drift cell which is filled with 2 to 5 Torr of buffer gas. The ion gate located just prior to the cell entrance chops the pulse to narrow, 30-50- μs -wide packets which enter the drift cell.⁷⁹

Since the temporal spread of ions in the ion mobility experiment depends on ion gate width, thermal diffusion and space charge effects, maximum resolving power of the instrument is attained by minimizing the gate width. However, very tiny gate width would result in very low signal levels. Therefore, a compromise between the signal intensity levels with the resolving power is required. The injection energies used in all the experiments are slightly above the minimum energies required to introduce the ions into the cell against the helium flow. Below the used injection energies, no ions would be able to pass through the counter flow of helium and transmitted into the cell. In contrast, if the injection energy was very high, the measured mobility constant will be overestimated since the ions will get deep into the drift cell and the arrival time

will be shorter than the accurate value. The injection energy was maintained at 12-16 eV (laboratory frame). As the ions are injected into the drift cell, the injection energy is dissipated in collisions with the helium buffer gas escaping from the drift cell entrance orifice. Inside the drift cell, the ions will suffer from two opposing forces, the friction decelerating forces as a result of the collisions of the ions with helium atoms and the applied field accelerating force.⁴ Upon exiting the cell, the ions are collected and refocused into the second quadrupole for analysis and detection. The signal is collected on a multichannel scalar with (2 μ s/channel resolution) with the zero time for data acquisition set to the midpoint of the ion gate trigger. Mobility is determined according to equation (3.3), by plotting t_d versus P/V , a straight line should be obtained. In other words, the applied drift cell voltage is varied at constant buffer gas pressure and temperature and the ATDs are collected at the corresponding voltages. The slope of the linear plot is inversely proportional to the reduced mobility, K_o , and the intercept represents the time spent within the second quadrupole before the detection of the ions (t_o).^{34,108} The straight line shows that the mobility is independent of the drift field so, low-field conditions are satisfied.^{4,109}

Low-field limit conditions are satisfied when:¹⁰⁸⁻¹¹⁰

(1) Ions are in thermal equilibrium with the buffer gas. (2) Thermal velocity obtained from collisions with buffer gas molecules is higher than that obtained from the applied field. This condition was satisfied in our measurements. At very high applied field, the effective temperature (T_{eff}) was only 9% higher than the buffer gas temperature (T_g) which changed the measured reduced mobility by less than 2%. T_{eff} can be measured using equation (3.5), which divides T_{eff} into two sources, first is the thermal temperature (T_g) and the second is the drift field effect additional temperature.

$$T_{eff} = T_g + \frac{M_b v_d^2}{3k_B} \quad (3.5)$$

where M_b is the drift gas mass and v_d is the drift velocity and k_B is Boltzmann constant. (3) Velocity distribution is nearly maxwellian. Non-Gaussian shape of the arrival time distortion by the drift cell exit aperture can be corrected by the relation:

$$t_d(\text{corrected}) = t_{obs} + \frac{4D}{v_d^2} \quad (3.6)$$

where t_{obs} is the observed arrival time at the peak maximum, $t_d(\text{corrected})$ is the corrected arrival time and D is the diffusion coefficient. The diffusion coefficient can be correlated to the measured mobility under low field conditions by Einstein equation (3.7):¹⁰⁹

$$D = D_L = D_T = K \frac{k_B T}{ze} \quad (3.7)$$

where K is the mobility constant, k_B is the Boltzmann constant and ze is the number of charges times the elementary charge e ; $e = 1.60 \times 10^{-19}$ Coulombs.

3.1.2. Structure determination

Ionic collision cross section is a measure of the size of the ion and it can be directly obtained from ion mobility measurements; using equation (3.8). Collision cross section information is very important for structural and conformational studies in particular for biopolymers.³⁸

The measured reduced mobility can be related to the collision cross-section, Ω , via the following equation: ¹⁰⁵

$$K_o = \frac{3ze}{16N_o} \left(\frac{2\pi}{k_B T} \right)^{(1/2)} \left[\frac{1}{\mu^{1/2} \Omega^{(1,1)}} \right] \quad (3.8)$$

where K_o is the reduced mobility constant, z is the number of elementary charges, e is the electron charge $=1.6 \times 10^{-19}$ C, N_o is the buffer gas number density, k_B is Boltzmann constant, and μ is the reduced mass. This relation indicates that difference in the ions' mobilities is a function of ions' cross section in the buffer gas, its mass and its charge. In other words, the separation of molecular conformations through ion mobility experiments requires obvious differences in their sizes and/or shapes which lead to noticeable differences in their collision cross sections for their interaction with the buffer gas atoms.^{1,111} Ions with open geometries undergo more collisions with the buffer gas and thus they will have larger collision cross sections and hence travel slower than compact ones, and reach the detector at longer arrival times than those of compact isomers.¹¹²

The ATDs can be calculated via transport theory for a short packet of ions injected into cylindrical drift tube with an entrance aperture of area a using equation (3.9):^{81,82}

$$\phi(t) = \frac{sae^{-\alpha t}}{4\sqrt{\pi D_L t}} \left(v_d + \frac{l}{t} \right) \left(1 - \exp\left(-\frac{r_o^2}{4D_T t} \right) \right) \exp\left(-\frac{(l - v_d t)^2}{4D_L t} \right) \quad (3.9)$$

The ions are introduced in the form of thin disk of radius r_o and uniform surface density s . α represents the reaction frequency which can account for the loss of ions as a result of reactions with the drift gas. In fact, α is usually set to zero as helium is unreactive. D_L and D_T are the longitudinal and transverse diffusion coefficients. In case of single isomers, the collected ATDs match with those calculated by the transport theory under a particular set of conditions of

drift cell voltage, temperature and pressure. Moreover, this can confirm that the center of the arrival time peak represents the actual drift time of the Gaussian peak.²

3.1.3. Theoretical methods of calculating mobilities and collision integrals

Structural characterization can be performed through the comparison of the measured reduced mobility and collision cross section values with those of the calculated structures through various methods implemented in the Mobcal program using the input from *ab-initio* and DFT theoretical calculation functionals.^{19,58,79} These methods simulate the collisions among the injected ions and the buffer gas atoms. They apply various interaction potentials, namely, exact hard sphere, projection approximation and trajectory methods.

3.1.3.1. Exact hard sphere approximation

This procedure employs the hard sphere potential for the interaction of the ions with helium atoms where both the ion and the neutral collision partners are considered as hard spheres.¹¹³ This method considers the collision cross section to be equal to the sum of the two van der Waals radii of the colliding atoms, as shown in equation (3.10):¹¹⁴

$$\Omega^{(1,1)} = \sigma_{HS} \quad (3.10)$$

It neglects the long range interactions between the polyatomic ion and buffer gas atoms and multiple scattering. However, this potential will be suitable at high temperatures and for convex polyatomic ions.¹¹⁴

3.1.3.2. Projection Approximation

This method utilizes the 12,6,4-interaction potential and it considers the long-range ion-induced dipole attractive interaction effects.¹¹³ Moreover, temperature-dependence was taken into the account rather than the hard-sphere model which yields temperature independent

collision cross section values. Higher collision cross section values were predicted at low temperatures due to the long range attractive interaction of the ions' individual atoms and the bath gas atoms.¹¹³ However, this model shows asymptotic behavior at large R values.¹¹³ The model employs the interaction potential described by equation (3.11):

$$V(R) = \frac{n\varepsilon}{n(3+\gamma) - 12(1+\gamma)} \left[\frac{12}{n} (1+\gamma) \left(\frac{r}{R}\right)^n - 4\gamma \left(\frac{r}{R}\right)^6 - 3(1-\gamma) \left(\frac{r}{R}\right)^4 \right] \quad (3.11)$$

In which, R is the distance between a specific atom in the polyatomic ion and a helium atom. R is obtained (as shown below in equation (3.12)) from tabulated values of collision integrals of atom-atom collisions ($\Omega^{(1,1)}(T)$).¹¹⁵ n is the exponent that describes the ion-neutral repulsion (taken at 12 as it is commonly used for Lennard-Jones potentials), ε is the depth of the potential well, r is the position of the potential well while γ is a ratio that defines the relative contributions of R^{-6} and R^{-4} terms.

$$R_{coll.} = (\Omega(T)^{(1,1)} / \pi)^{1/2} \quad (3.12)$$

For simplicity, potential energy $V(r)$ is presented as the sum of $V_{n,6}(R)$ and $V_4(R)$ as shown in equation (3.13), where $V_4(R)$ can be defined using equation (3.14) and $V_{n,6}(R)$ is defined using equation (3.15). The best fit to the experimental collision integrals is used to predict the ε_{LJ} and r that best describe the interaction system. Thus, $V_{n,6}(R)$ is completely defined, and γ can be obtained by substitution in equation (3.11).

$$V(r) = V_{n,6}(R) + V_4(R) \quad (3.13)$$

$$V_4(R) = -\frac{q^2\alpha}{2R^4} \quad (3.14)$$

$$V_{n,6}(R) = \varepsilon_{LJ} \left[\left(\frac{r_{LJ}}{R} \right)^{12} - 2 \left(\frac{r_{LJ}}{R} \right)^6 \right] \quad (3.15)$$

The molecule is projected randomly into a plane in space and circles corresponding to the collision radii are drawn in the plane. Then points are picked randomly in that plane within a square with area A, if the point falls within a circle, it is considered a hit. Collision cross section of that projection can be then obtained using equation (3.16).

$$\Omega = \frac{\text{\# of hits}}{\text{Total \# of trials}} \times A_{\text{rectangle}} \quad (3.16)$$

3.1.3.3. Trajectory calculation

This procedure uses a potential composed of (12-6) Lennard-Jones and long-range (ion-induced dipole) potentials.¹¹⁶ The collision integrals are evaluated from the scattering angle and from the angle between the trajectory before and after a collision between the ion and a buffer gas atom. This method gives the most reliable estimates among the three methods, especially when long range attractive interaction gets more significant and in multiple scattering cases. However, this method is very tedious and computationally expensive process.

3.2. Thermochemistry measurements

Tandem IMS instrument can be used to bridge the gap between the solution and the solvent-free environments on utilizing volatile solvents introduced onto the reaction cell.^{23,25,73} The guided-ion mass spectrometry can be used efficiently to elucidate thermochemical measurements.¹¹⁷ The ions of interest are mass-selected via the first quadrupole mass-filter, and then injected in 30-50- μ s-wide pulses. Low electric field is usually utilized to ensure insignificant collisional heating and enough time to reach equilibrium.³⁸ Upon injecting the ions

onto the drift cell, the high number of collisions, at least 10^4 , with the drift cell gas quickly establishes an equilibrium state between the injected ion and product cluster ion. The concentrations of both the reactant and product ions are measured via measuring the intensity of the selected ATD of the ion of interest by integrating the area under the ATDs peaks.^{20,32}

For the following hydration study of an ion A^+ :



When the equilibrium is established, a constant ratio of the integrated intensity of the product to the reactant is maintained when the drift voltage is varied at constant pressure and temperature. This indicates equilibrium establishment regardless the reaction time.³⁵ In addition, ATDs of the reactant and product ions are identical indicating equal residence times. Once the equilibrium conditions are well-established, the equilibrium constant, K_{eq} , can be measured using equation (3.18):

$$K_{eq} = \frac{I[A^+.(H_2O)_n] \times 760}{I[A^+.(H_2O)_{n-1}] \cdot P_{H_2O}} \quad (3.18)$$

where $I[A^+.(H_2O)_{n-1}]$, $I[A^+.(H_2O)_n]$ are the integrated intensities of ATD of the reactant and product cluster ions, respectively and P_{H_2O} is the pressure of water, in Torr.

Hence, by using the well-defined concepts of thermodynamics,⁴³

$$\Delta G^\circ = \Delta H^\circ - T\Delta S^\circ \quad (3.19)$$

$$\Delta G^\circ = -RT \ln K_{eq} \quad (3.20)$$

From them, the following relation can be obtained;

$$R \ln K_{eq} = \frac{-\Delta H^\circ}{T} + \Delta S^\circ \quad (3.21)$$

Using equation (3.21), van't Hoff plots can be obtained by plotting $R \ln K_{eq}$ as a function of $1000/T$. A straight line is obtained whose slope represents the enthalpy (ΔH°) while the intercept represents the entropy change of the clustering reaction (ΔS°).

3.3. Theoretical calculations

The cooperative impacts of experiment and theory extracted from ion mobility and equilibrium studies provide important insights into the energetic and structural information of organic ions.^{38,39} In fact, binding energy calculations can be used to validate the calculation methods.⁶ *ab-initio* calculations have been utilized at the level of the second order Moller-Plesset (MP2) while density functional theory (DFT) calculations have been used at the B3LYP and M06-2X levels using Gaussian 03 and Gaussian 09 packages, respectively.^{118,119} These calculation levels have been widely used efficiently in the literature and showed strong reliability.^{66,120,121} All the geometry optimizations and energy calculations were performed using 6-311++G(d,p) basis sets which includes d-type and p- type polarization functions on non-hydrogen and hydrogen atoms, respectively with all the electrons are included.¹²¹ Moreover, vibrational analysis was used to verify the lack of any imaginary frequencies.⁶⁶ Frequency calculations have been performed for all the optimized geometries at the same level of theory to obtain the zero point vibrational energy (ZPVE). Therefore, all the calculated energies are corrected for ZPVE. Moreover, the counterpoise method has been used to correct the calculated energies for the basis-set superposition error (BSSE) using counterpoise regime supplied in

Gaussian program package.^{118,122} Moreover, total spin $\langle s^2 \rangle$ value was 0.75-0.77 which illustrates the lack of spin contamination for open shell ions.^{62,123}

Chapter 4: Hydration of Pyrimidine Radical Cation and protonated pyrimidine cations

4.1. Introduction

Hydrogen bonding interactions involving ionized aromatics are important in radiation chemistry, electrochemistry, polymerization in aqueous solvents, astrochemistry, and in protein folding.^{15,22,37,74,124-126} Therefore, an insight into basic molecular interactions is required to be extracted from the gas phase energies and structures of the hydrated organic ions since gas phase studies can probe elementary reactions under well-defined conditions unperturbed by external factors that dominate in the condensed phase reactions.^{18,20,84,127} In fact, the microhydration, or the stepwise addition of water molecules one unit at a time to the ion of the interest can provide useful correlation to the factors that determine hydrophobic and hydrophilic hydration in macroscopic systems.^{37,128} Organic ions can interact with water molecules by either relatively weak carbon-based $\text{CH}^{\delta+} \cdots \text{O}$ hydrogen bonds, such as benzene⁺ and the C_3H_3^+ ions, or via stronger hydrogen bonds, such as in protonated pyridine where the $\text{NH}^+ \cdots \text{O}$ hydrogen bonds are formed.^{17,33,48} Thus, these systems can be considered as prototypical models for understanding the molecular aspects leading to hydrophobic interactions in the condensed phase.⁴⁹

Deoxyribonucleic acid (DNA) is at the heart of the molecular biology science, cell biology, and genetics.^{37,129} Each DNA strand is composed of repeating nucleotide units.¹²⁹ Each nucleotide is composed of a deoxyribose sugar, a phosphate group and a nucleobase.¹²⁹ Nucleobases have either purine or pyrimidine nitrogen bases.^{130,131} In the living organisms, DNA molecules interact very strongly with water molecules.²⁴ This interaction catalyzes the

conversion of A-helix to B-helix form.^{37,132} In fact, hydrogen bonding modulates recognition of DNA and RNA bases.¹³³

Pyrimidine ($C_4H_4N_2$) represents the main constituent of cytosine and thymine DNA nucleotides^{62,134} It possesses two different proton acceptor sites: the ring π -cloud and the lone pairs of the heteroatoms.^{62,134,135} Therefore, pyrimidine solvation can be regarded as a prototype for the solvation of heterocyclic aromatic rings containing nitrogen heteroatoms. The hydrogen-bonded clusters resulting from supersonic expansion of the pyrimidine/water and pyrimidine/methanol mixtures have been investigated experimentally using laser photoionization time of flight mass spectrometry technique.^{62,134} Moreover, the resultant structures have been depicted using theoretical calculations at the B3LYP/6-31+G(d,p) and B3LYP/6-311++G(d,p) levels.^{62,134,136-138}

Although pyrimidine and its derivatives were studied long time ago,¹³⁹ they are still interesting for researchers due to their great biological significance.¹⁴⁰⁻¹⁴² Damaged DNA bases differ in structure and features from normal nucleobases. Hence, they intervene with gene expression and replication, leading to aging, carcinogenesis, and cell death.¹³³ In fact, the formation of pyrimidine dimers is the most frequent damage induced by the UV portion of the sunlight and they distort the DNA helical structure. Moreover, if DNA contains a pyrimidine dimer that can't be repaired, replication and transcription are blocked at that site.^{142,143} The molecular structures of pyrimidine and its protonated analogs have been studied in the gas phase using quadrupole mass spectrometry to locate the lowest energy protonation site.¹³¹ Therefore, it is of fundamental interest to study the solvation of pyrimidine and its protonated species with polar solvents, such as water, methanol, and acetonitrile in the gas phase. In fact, pyrimidine has been detected in the meteorites as well as purine bases and amino acids.¹⁴⁴ Therefore, the

interaction of pyrimidine with the other abundant molecules in the space is of fundamental interest. The possibility of formation of the RNA uracil nucleotide through the reaction of pyrimidine with two water molecules under space conditions of low density and low temperatures was verified.¹⁴⁴

In the present study, we examine the gas phase stepwise hydration of the pyrimidine radical cations by 1-4 H₂O molecules and for comparison, the stepwise hydration of protonated pyrimidine by 1-3 H₂O molecules is reported as well. Two kinds of hydrogen bonds can be formed through the interaction of the water molecules with the pyrimidine cations, NH^{δ+}---O, or CH^{δ+}---O bonds. Thermochemical equilibrium measurements using the mass-selected ion mobility technique in combination with (DFT) functionals are employed to determine the solvation sites and to locate the lowest energy isomers. These measurements can provide useful information about the individual binding energies of the hydrated cations. Moreover, they provide a basis for comparing pyrimidine and protonated pyrimidine in their interaction with water molecules.

The binary clusters of pyridazine and pyrimidine radical cations with both water and methanol have been extensively studied using time of flight mass-spectrometer employing multiphoton ionization techniques coupled with ab-initio calculations.^{62,134,145,146} Therefore, it is of fundamental interest to examine the structures of the binary clusters of pyrimidine/water formed through co-expansion of their mixed vapors. Binary clusters can be of interest not only because they simulate multicomponent systems but also, investigating them can clarify the structures of hydrogen bonded networks about a protonated ion.⁷⁸ The structures can be then identified by comparing the measured collision cross sections of these clusters with the

corresponding values of the theoretically predicted structures using sufficiently high levels of the theory.^{41,147,148}

4.2. Experimental Section

Supersonic beam expansion of ~0.5-2% pyrimidine vapor (Aldrich, 99% purity) seeded in 3-4 atm of helium carrier gas, helium in case of pyrimidine⁺ study. 10% hydrogen in helium is used for the study of protonated pyrimidine cation (H⁺pyrimidine). A pulsed conical nozzle (500 μm diameter) in pulses of 200-300 μs duration at repetition rates of 50-100 Hz is used. The neutral cluster beam is ionized by an axial electron-impact ionizer using 50-70 eV electron energy. The pyrimidine⁺ or the H⁺pyrimidine ions are mass-selected via the first quadrupole mass-filter, which is operated in either (RF-DC) or (RF only) mode depending on ion intensity signal. The ion beam is injected into the drift cell in 30-50-μs-wide packets using injection energies of (10-13 eV, laboratory frame). The used injection energies are slightly above the required energies to introduce the injected ions against the counter flow of the gas escaping from the drift cell entrance aperture. Four temperature controllers are used to keep constant temperature within ± 1 K.

The drift cell contains the reactant, water vapor either alone or in a mixture with helium buffer gas in the binding energy measurements while it contains only helium during mobility measurements. After the ions exit the drift cell, they are guided and focused to the second mass-filter. The second mass filter can be operated either in a fixed (m/z) ion mode to obtain arrival time distributions (ATDs) of the reactant and product ions, or in a scan mode to monitor the intensity change of all the ions exiting from the drift cell.

4.3. Theoretical calculations

Although the accuracy of the density functional methods for the study of the hydrogen-bonded compounds is questionable, the hybrid three parameter B3LYP method provides comparable results to the reliable second order Moller-Plesset perturbation theory (MP2) ones.^{62,149} Therefore, hybrid (DFT) calculations were carried out using Gaussian 03 software packet at the level of the B3LYP/6-311++G (d,p) to get the optimized structures.¹¹⁹ Frequency calculations and ZPVE corrections have been performed for all the optimized geometries at the same level of theory. Moreover, due to the significance of the basis-set superposition error (BSSE) in evaluating the hydrogen bonding energies, the counterpoise method has been employed to correct the calculated energies for the BSSE.^{62,122,134} This level of the theory was sufficient for our computational jobs as the binding energies agree with the corresponding measured values within the experimental uncertainty. Moreover, the Mobcal program has been used for the mobility and cross-section calculations using the trajectory method. Trajectory method employs a potential composed of Lennard-Jones and ion-induced dipole interactions.⁵⁸

4.4. Results and Discussion

4.4.1. Binary Pyrimidine-Water Clusters

4.4.1.1. Mass-Spectra of the binary clusters

Mixed clusters of pyrimidine and pyridazine with both water and methanol have been extensively studied both theoretically and experimentally using photoionization technique employing a time-of-flight mass spectrometer.^{62,134,145,146} In the previous studies, a strong dominance of the protonated mixed clusters has been observed while their unprotonated analogues weren't detected.^{62,134} Figure 6 shows a typical mass-spectrum obtained using electron

impact ionization of neutral pyrimidine clusters which were formed by supersonic expansion in vacuum. In addition to protonated pyrimidine clusters, protonated pyrimidine-water clusters have been observed as a result of the presence of trace water in the carrier gas. Supersonic expansion of pyrimidine/water mixture is introduced by passing the helium carrier gas through a bubbler containing a mixture of pyrimidine and water in a 1 : 2 ratio. This method appeared to be an efficient route to obtain mixed binary clusters of pyrimidine/water as shown in Figure 7.¹⁵⁰ No obvious magic number clusters were observed which agrees with previously reported results.^{62,134} The proton in protonated hydrated pyrimidine cation $[H^+PyW]$ is expected to reside on the pyrimidine rather than on the water because the proton affinity of pyrimidine is higher than that of water (see Table 2).^{3,31} In fact, the observation of protonated pyrimidine cation $[H^+Py]$ in the spectrum shows that the proton resides on the pyrimidine.³

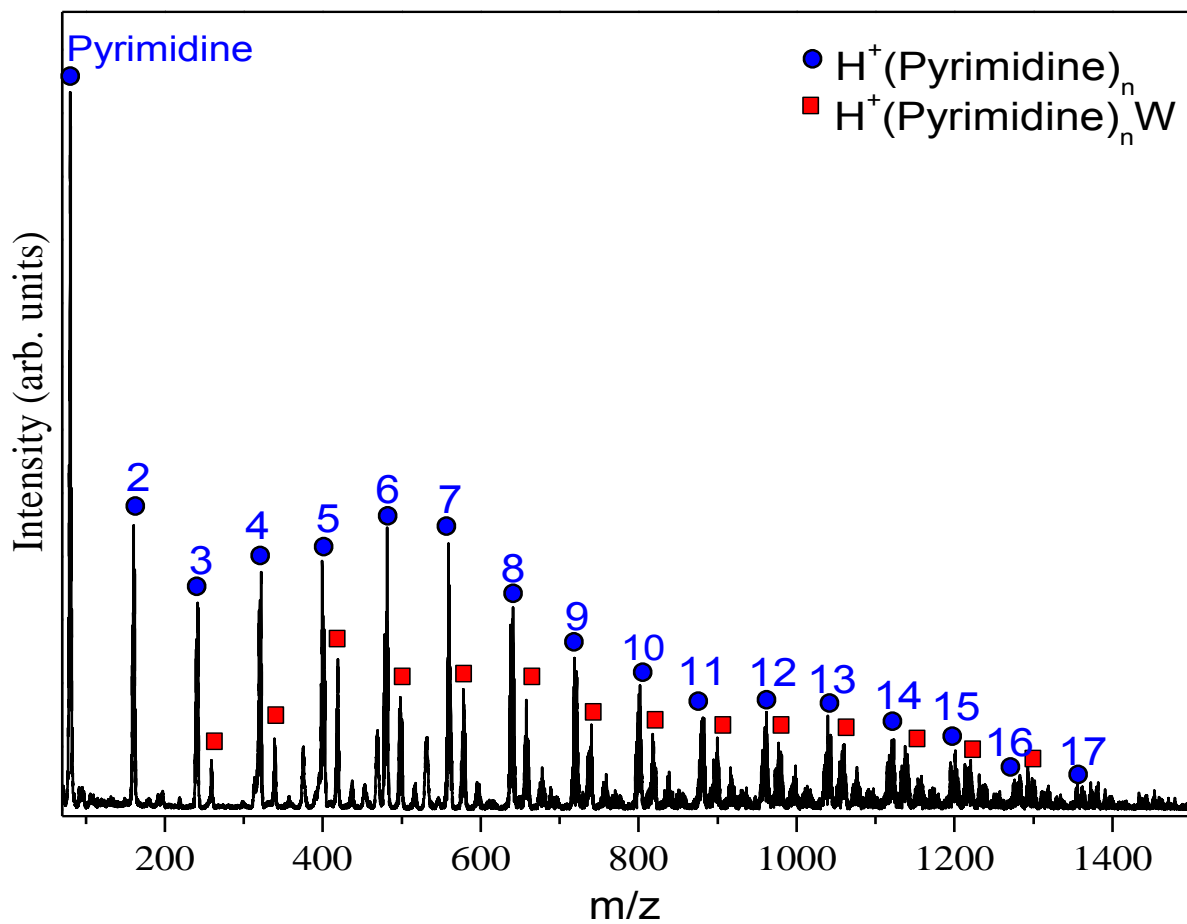


Figure 6. Electron impact (27 eV) mass-spectrum of pyrimidine clusters formed by supersonic beam expansion using 0.7% pyrimidine vapor in helium (5 atm)

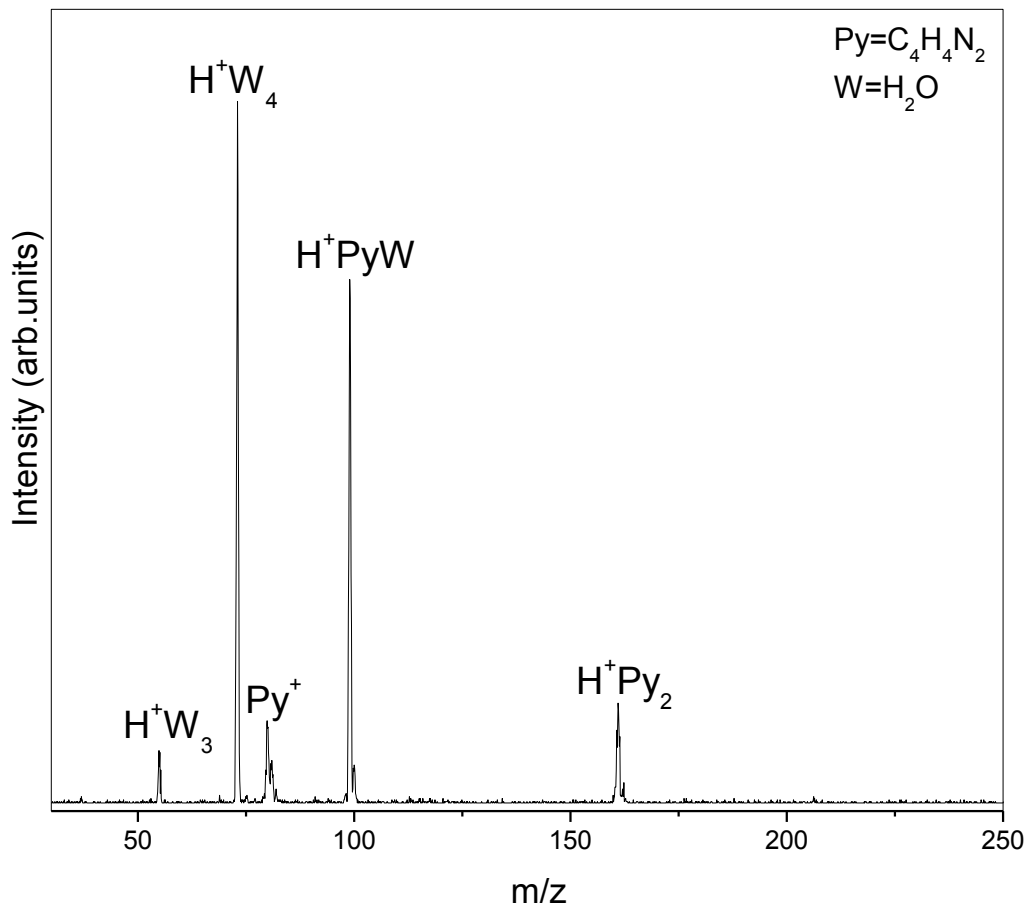


Figure 7. Mass-spectrum resulting from injecting the pyrimidine radical cation in the RF-selection mode into the drift cell which contains 0.93 Torr of helium using injection energy of 13.4 eV (lab) and drift field of 4.6 V/cm. The temperature of the drift cell was 298 K. The sample mixture is composed of pyrimidine: water in a ratio of 1:2

4.4.1.2. Ion mobility measurements

The reduced mobilities of the observed clusters, K_o , were measured as explained in the section 3.1. Figure 8 illustrates a typical example of ATDs of the protonated pyrimidine-water cluster $[H^+pyrimidine.(H_2O)]$ at different applied drift cell voltages. Table 1 has the reduced mobilities and their corresponding collision cross-section values in addition to the calculated values using the trajectory method of the DFT-structures shown in Figure 9. The protonated

pyrimidine dimer ($[\text{H}^+\text{Pyrimidine}]_2$) appeared to have a relative exceptional stability with respect to its non-protonated analogue ($[\text{Pyrimidine}^+]_2$), which was not observed, as shown in Figure 7. This observation can be attributed to the formation of a stable structure for the protonated dimer as shown in Figure 9d. ($[\text{H}^+\text{Pyrimidine}]_2$) is predicted to have T-shaped proton bound structure.

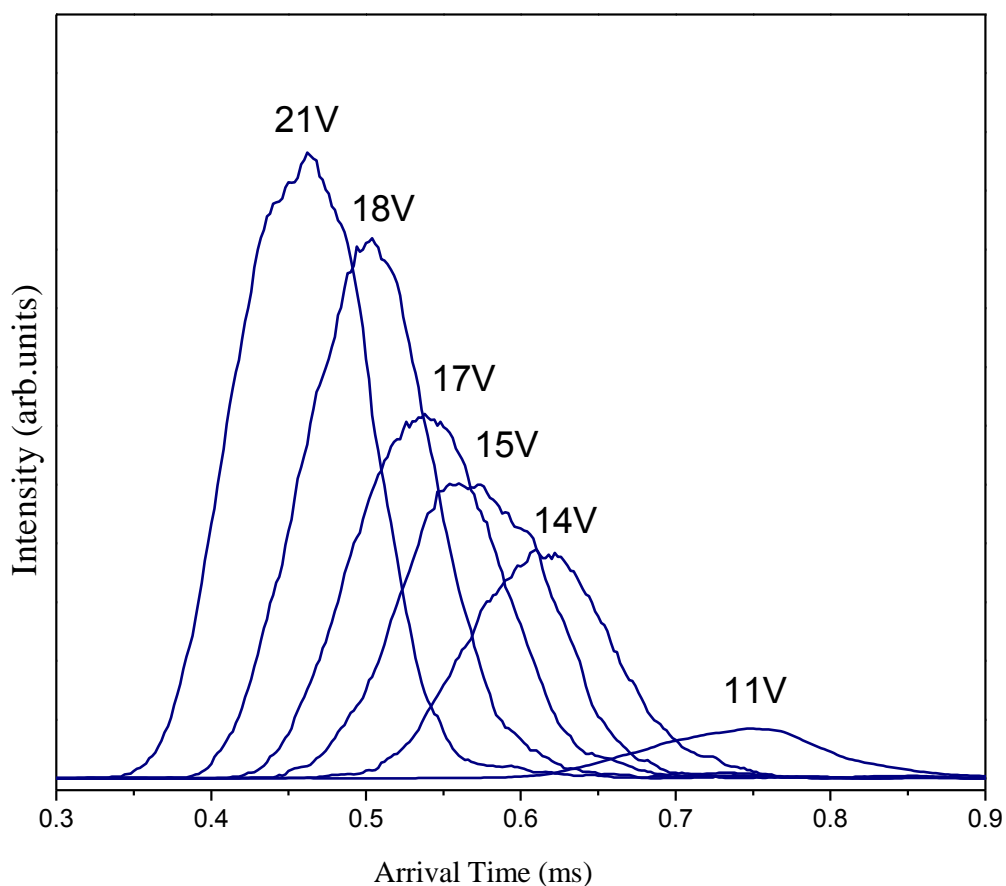


Figure 8. ATDs of $[\text{H}^+\text{pyrimidine}(\text{H}_2\text{O})]$ on varying the drift voltage from 10 to 21V

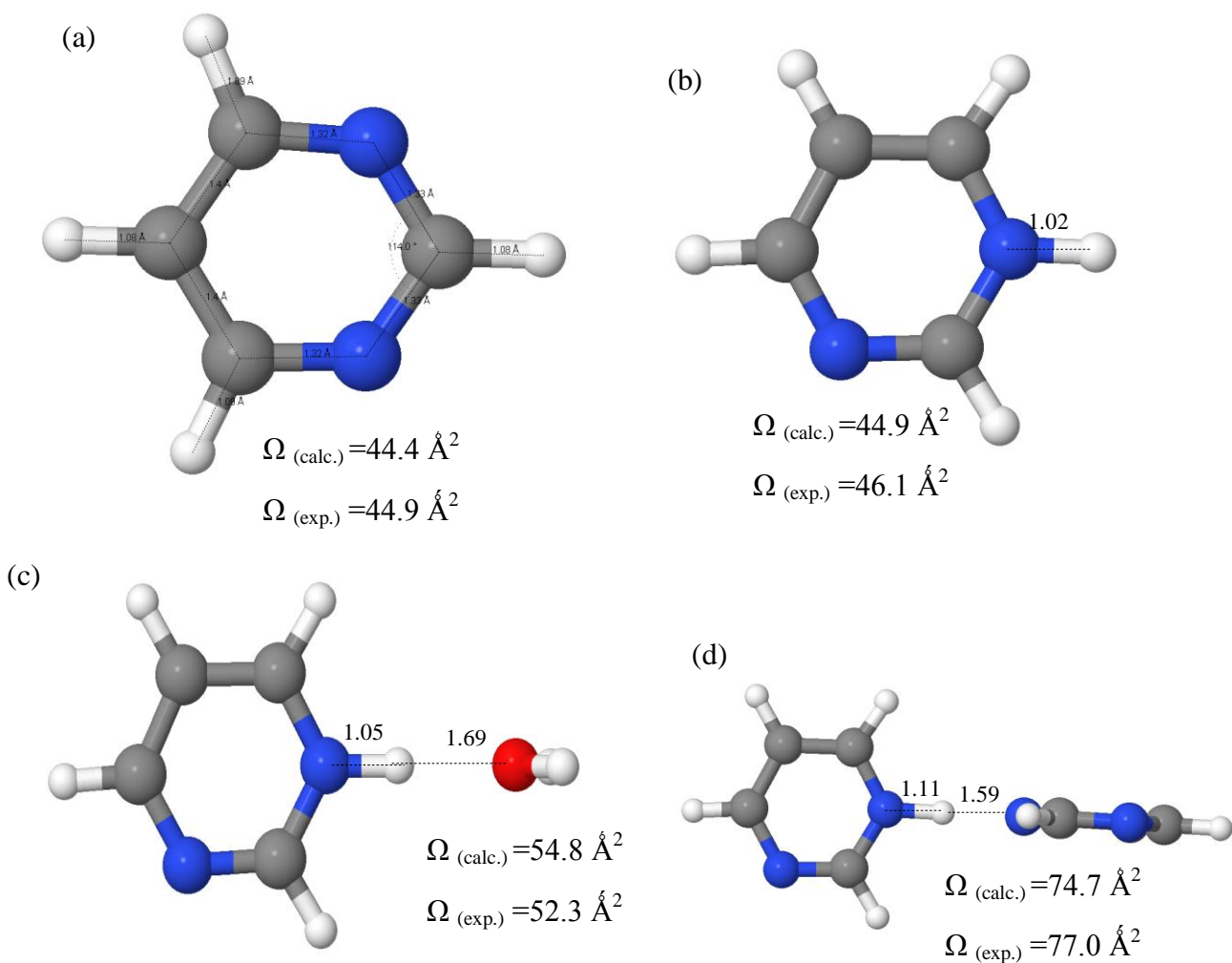


Figure 9. DFT optimized structures done at the B3LYP/6-311++G(d,p) level of (a) Pyrimidine⁺ (b) Protonated pyrimidine [H⁺pyrimidine] (c) Protonated hydrated pyrimidine [H⁺pyrimidine (H₂O)] (d) Protonated pyrimidine dimer [H⁺pyrimidine₂]. The experimental collision cross-sections and the calculated values obtained at room temperature are indicated. The interatomic distances are in Angstrom

Cluster ion	T (K)	$K_{0(\text{exp.})}^a$	$\Omega_{(\text{exp.})}^b$	$K_{0(\text{cal.})}^{*,a}$	$\Omega_{(\text{cal.})}^{*,b}$
Pyrimidine	299	12.20	44.9	12.34	44.4
H ⁺ Pyrimidine	301	11.85	46.1	12.16	44.9
H ⁺ Pyrimidine(H ₂ O)	300	10.40	52.3	9.93	54.8
H ⁺ (Pyrimidine) ₂	300	7.02	77.0	7.20	74.9
H ⁺ (Pyrimidine) ₂	225	8.05	82.8	7.92	78.8

^a K_0 in $\text{cm}^2 \cdot \text{V}^{-1} \cdot \text{s}^{-1}$ ^b Ω in \AA^2 * Calculated by DFT (B3LYP/6-311++G(d,p))

Table 1. Mobility and cross section values of pyrimidine and pyrimidine/water binary clusters at different drift cell temperatures

4.4.2. Gas Phase Hydration of Pyrimidine Radical Cation

4.4.2.1. Mass Spectra

Pyrimidine⁺ ions were injected into the drift cell containing a mixture of water vapor and helium at various drift cell temperatures; between 283 K and 238 K. The lowest attainable temperature was 238 K before the freezing of water.²⁰ Complete thermalization of the injected ions was ensured through collisions with the drift gas escaping through the entrance aperture of the cell.⁴² The resultant mass-spectra are shown in Figure 10. At 285 K, [Pyrimidine⁺(H₂O)_n]; n=1-2 are the major observed products. At 238 K, protonated water clusters, [H⁺.(H₂O)_m]; m=5-9, become the major observed products in addition to the [Pyrimidine⁺(H₂O)_n]; n=2-5. In

addition, the hydrated pyrimidine series is shifted to higher additions at lower drift cell temperatures, following the usual clustering trend.

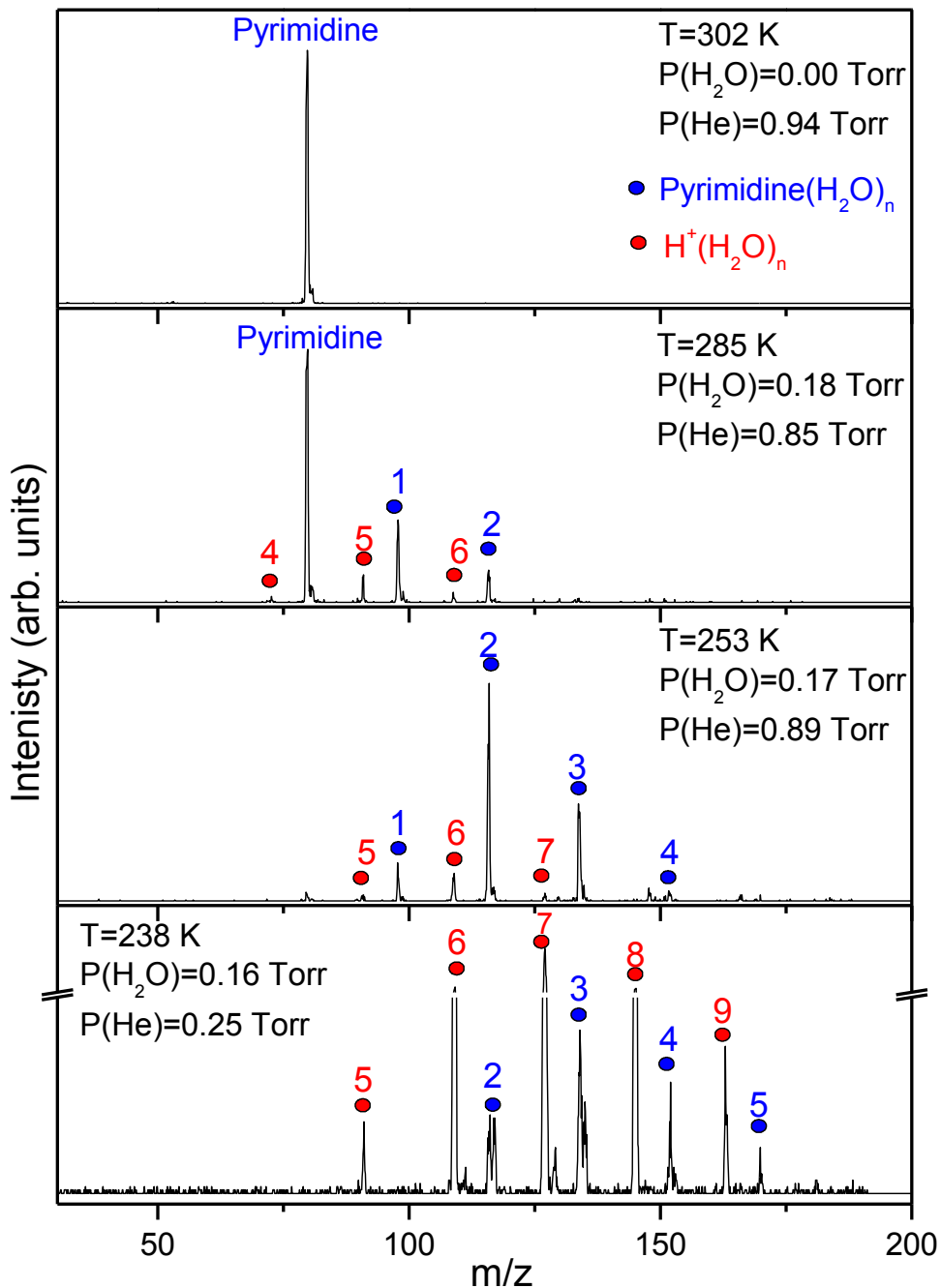
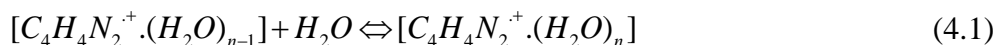


Figure 10. Mass spectra resulting upon the injection of mass-selected pyrimidine radical cation into a mixture of H₂O mixed with helium gas using 12.7 eV (lab) as injection energy and 2.5 V/cm drift field. Drift cell temperature and pressure are indicated

The high number of collisions, at least 10^5 , with the reactant mixture quickly establishes equilibria among the injected ions and hydrated product ions. The concentrations of both the reactant and product ions are measured using the integrated intensity of the selected ATD of the ion of interest. When the equilibrium is established, a constant ratio of the integrated intensity of the product to the reactant is maintained at constant pressure and temperature which indicates that the measured equilibrium constant is independent on the residence time. The residence time is controlled by the applied drift field. In addition, ATDs of the reactant ions and the hydrated product ions identical indicating equal residence times.

The equilibrium constant, K_{eq} , of the stepwise hydration reaction of pyrimidine⁺ (4.1) can be measured using equation (4.2).

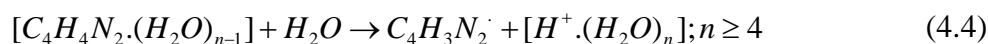


$$K_{eq} = \frac{I[C_4H_4N_2^+.(H_2O)_n] \times 760}{I[C_4H_4N_2^+.(H_2O)_{n-1}] \cdot P_{H_2O}} \quad (4.2)$$

where $I[C_4H_4N_2^+.(H_2O)_{n-1}]$, $I[C_4H_4N_2^+.(H_2O)_n]$ are the integrated intensities of ATDs of the reactant and product cluster ions of the association reaction (4.1), respectively and P_{H_2O} is the pressure of water, in Torr. The equilibrium constant, K_{eq} , was measured at different temperatures and from van't-Hoff equation (4.3), ΔH° and ΔS° values are obtained from the slope and intercept, respectively. van't-Hoff plots are obtained by plotting $R \ln K_{eq}$ versus $1000/T$, where T is the drift cell temperature, in Kelvin.

$$R \ln K_{eq} = \frac{-\Delta H^\circ}{T} + \Delta S^\circ \quad (4.3)$$

Arrival time distributions shown in Figure 11 illustrate identical arrival times of $[\text{Pyrimidine}^+(\text{H}_2\text{O})_n]$; with $n=1-5$, which in turn indicate the equilibrium establishment under our experimental conditions. However, ATDs of the formed hydrated pyrimidine are divided into two separate groups. The $[\text{Pyrimidine}^+(\text{H}_2\text{O})_n]$ with $n=1-3$ have equal arrival times while $[\text{Pyrimidine}^+(\text{H}_2\text{O})_n]$ with $n=3-5$ have equal but longer arrival times. The division of ATDs into two groups can be attributed to the disappearance of the small cluster ions at lower drift cell temperatures. Moreover, protonated water clusters $[\text{H}^+(\text{H}_2\text{O})_n]$; $n \geq 4$ have been observed as can be seen in the mass-spectra displayed in Figure 10. Their formation can be attributed to the dissociative proton transfer reaction as shown in equation (4.4):



This reaction is the major source of the observed protonated water cluster series in Figure 10 and it has been observed before in the hydration of benzene radical cation.^{10,20,33} The proton transfer reaction exhibits a critical cluster size dependence at $n \geq 4$ which can be rationalized by the proton affinity of $(\text{H}_2\text{O})_4$ relative to that of the $\text{C}_4\text{H}_3\text{N}_2$ radical, as shown in Table 2.^{9,31}

Cluster	Proton Affinity (kcal/mol)
H ₂ O	165±1
(H ₂ O) ₂	197±1
(H ₂ O) ₃	206±1
(H ₂ O) ₄	215±1
(H ₂ O) ₅	216±1
Pyrimidine	212±1
C ₄ H ₃ N ₂	206*

* Calculated by B3LYP/6-311++G(d,p)

Table 2. Proton affinities of water clusters in comparison to that of pyrimidine

4.4.2.2. Thermochemistry measurements and structural implications

The equilibrium constants of the stepwise hydration reaction (4.1) were measured at different temperatures yielding van't-Hoff plots as can be seen in Figure 12. From van't-Hoff plots, the binding energies and entropy changes were obtained and summarized below in Table 3. The binding energies follow the usual decreasing trend as the degree of hydration increases. This can be attributed to the decrease in ion-dipole interaction as the number of water molecules increases.²² Moreover, the entropy loss decreases as n increases which is expected for more and more weakly bound solvent molecules. In fact, the largest entropy loss is expected for the first

step as a result of significant loss in the degrees of freedom of both the ion and the ligand.²² Moreover, both the binding energy and the measured entropy loss values agree with the expected values for hydrogen bonds.²² For comparison, thermochemical values of the hydration of benzene, pyridine and protonated pyridine cations are shown as well.^{17,20,33}

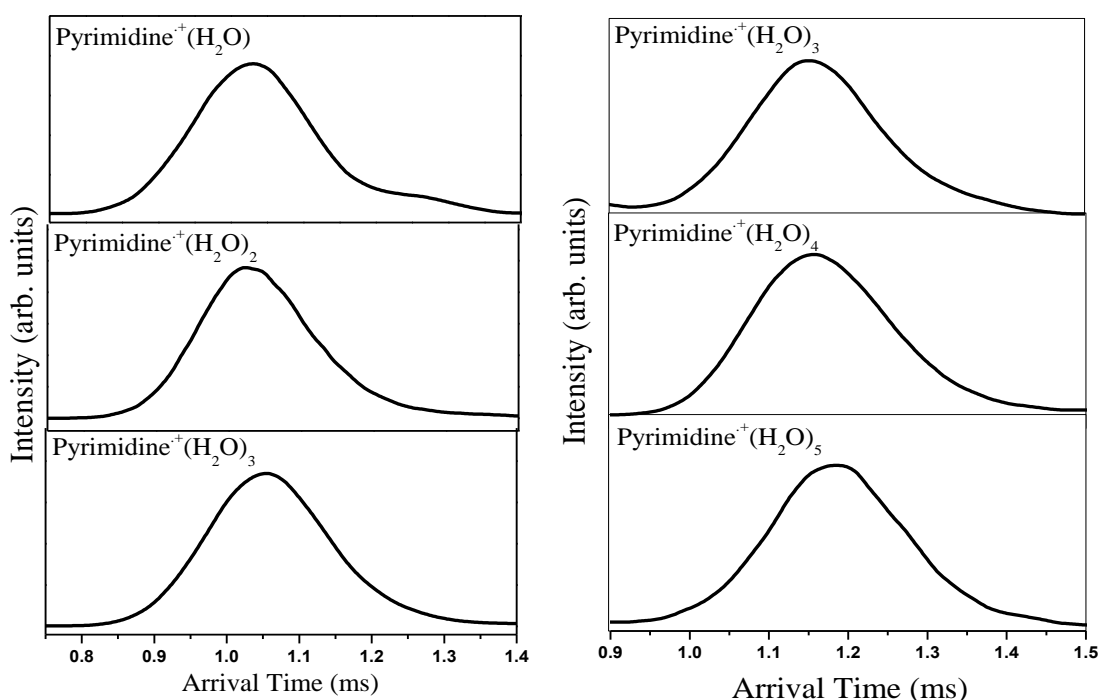


Figure 11. (Left) ATDs of pyrimidine⁺ (H₂O)_n; n=1-3, collected when mass-selected pyrimidine⁺ is injected into the drift cell contains 0.21 of water vapor in a mixture with 0.22 Torr helium buffer gas at 268 K. (Right) ATDs of pyrimidine⁺ (H₂O)_n; n=3-5, collected when mass-selected pyrimidine⁺ is injected into the drift cell contains 0.19 Torr of water vapor in a mixture with 0.22 Torr of helium buffer gas at 243 K

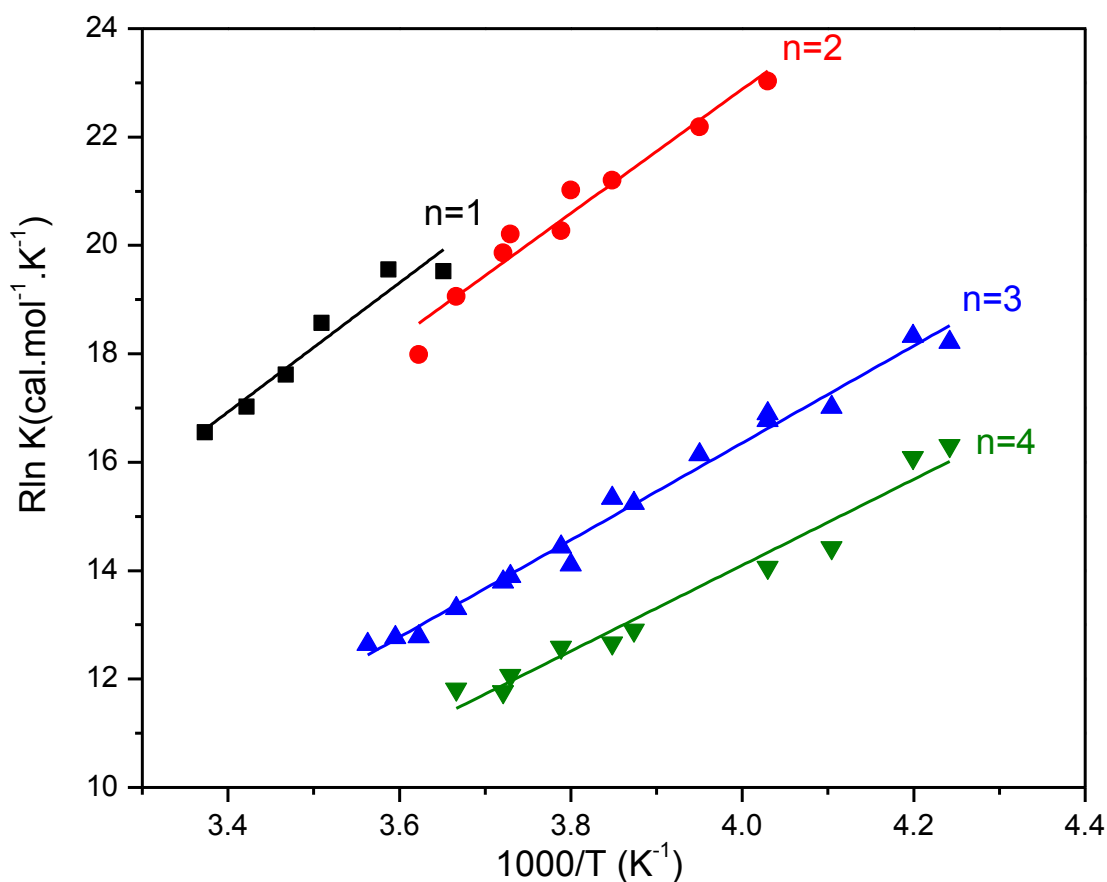


Figure 12. van't Hoff plots of the established equilibria among pyrimidine⁺(H₂O)_n clusters; with n= 0-4 resulting from injecting pyrimidine radical cation in the mass-selected mode into the drift cell which has 0.24 Torr H₂O mixed with 0.23 Torr of helium gas using 12.7 eV injection energy and 2.5 V/cm drift field. Drift cell temperature was varied in the range of (238 K-283 K)

	Pyrimidine ⁺				Pyridine ⁺ ^d		PyridineH ⁺ ^d		Benzene ⁺ ^e	
n	-ΔH ^o ^a	-ΔS ^o ^b	BE ^c	BE ^{c,*}	-ΔH ^o ^a	-ΔS ^o ^b	-ΔH ^o ^a	-ΔS ^o ^b	-ΔH ^o ^a	-ΔS ^o ^b
1	11.9	23.6	10.7	9.9	15.2	33.1	15.6	27.0	9.0	19.5
2	11.4	22.9	9.9	8.8	9.9	19.0	11.5	26.0	8.0	18.9
3	9.0	19.5	9.1	8.2	8.8	20.2	6.9	17.1	8.0	
4	7.9	17.6	9.0	7.4	7.1	15.3			10.3	22.4

^a ΔH^o_{n-1,n} units are kcal/mol, ^b ΔS^o_{n-1,n} units are cal/mol.K, ^c Binding energy calculated by B3LYP/6-311++G(d,p) (^{*} with BSSE correction included), ^d Ref(Pyridine)¹⁷ and ^e Ref (Benzene)^{20,33}

Table 3. Measured Thermochemistry (-ΔH^o_{n-1,n} and -ΔS^o_{n-1,n}) of the formation of Pyrimidine⁺.(H₂O)_n clusters; with n=1-4 for pyrimidine radical cation in comparison to the corresponding values of benzene, pyridine and protonated pyridine cations and the corresponding calculated binding energies

Pyrimidine⁺ can bind to water molecules via two different types of hydrogen bonds. One via CH^{δ+}---O hydrogen bonds, which would be relatively weak as reported in benzene⁺ hydration example.^{20,33} It can bind also via NH⁺---O hydrogen bonds, which would be stronger than the former case; similar to the protonated pyridine hydration example.¹⁷ On comparing the experimentally measured values, reported in Table 3, it can be noticed that pyrimidine thermochemical values are more similar to the benzene⁺ example rather than the pyridine⁺ case. Pyridine⁺ shows similar hydration pattern to that of H⁺pyridine. So, it was concluded the

distonic ions are formed in $[\text{pyrimidine}^+(\text{H}_2\text{O})_n]$.¹⁵¹ In particular, the first added water molecule shows a weaker binding to the pyrimidine than to the pyridine cation. This suggests that the first hydration site does not involve the N-site but rather C-H sites. This observation suggests that the formation of distonic pyrimidine ion in the pyrimidine.H₂O complex can be ruled out.

4.4.2.3. Theoretical calculations and structures

Density functional theory (DFT) was employed at the B3LYP/6-311++G(d,p) level to calculate the total energies and to optimize the structures of $[\text{pyrimidine}^+(\text{H}_2\text{O})_n]$ ions.¹⁵²⁻¹⁵⁴ From the thermochemistry comparisons of pyrimidine⁺ with both benzene⁺ and pyridine⁺, the first water molecule binds more weakly to the pyrimidine cation than the corresponding one in the pyridine cation case. Thus, the most likely hydration site is not expected to the N-site but rather C-H sites. This can be attributed to the charge localization on the aromatic H-atoms is higher than the charge on N-atoms. Therefore, NBO distribution of charges on pyrimidine⁺, H⁺pyrimidine and H₂O is shown below in Table 4. The charge distribution perceives that the water interaction with pyrimidine⁺ will be through the O-atom to H₂ which has a charge number of +0.27 which is a little higher than that assigned for H₁ which has +0.25. Moreover, partial charge transfer from the ion to the water moiety can occur as shown in Figure 13. As shown in Table 3, the predicted binding energies using B3LYP/6-311++G(d,p) agree well with the experimental values.

The lowest energy isomer of $[\text{pyrimidine}^+(\text{H}_2\text{O})]$ predicted by B3LYP/6-311+G(d,p) level calculations is listed as (1-a) in Table 5. (1-a) structure has a bifurcated structure which has the O-atom of water molecule bound to two aromatic hydrogen atoms through 1.92 Å and 3.70 Å hydrogen bonds. This bifurcated structure of (1-a) resembles the predicted structure of $[\text{C}_6\text{H}_6^+(\text{H}_2\text{O})]$.^{20,33} Structure (1-b) is predicted to be 0.4 kcal/mol less stable than (1-a) structure

and it has simple 1.93 Å hydrogen bond formation with the H₁-atom. The third isomer listed in Table 5 is (1-c) which has a single hydrogen bond with the pyrimidine⁺ (H₃) of 2.00 Å length and 9.5 kcal/mol binding energy.

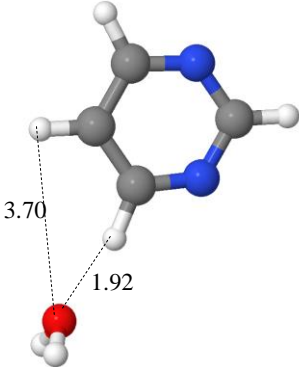
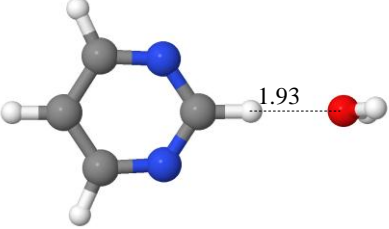
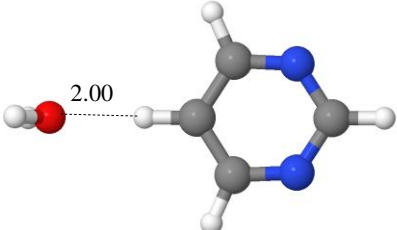
The optimized structures of the [pyrimidine⁺(H₂O)₂] isomers are displayed in Table 6. Structure (2-a) is the lowest energy isomer; it has external hydration pattern in which the two water molecules are connected by a hydrogen bond. The newly formed bond is predicted to be of 1.78 Å length and 9.9 kcal/mol binding energy. The internal hydration structures (2-b) and (2-c) are 0.3 and 0.5 kcal/mol higher in energy, respectively than (2-a). Structure (2-b) has a symmetric geometry with the two water molecules forming bifurcated structure with the aromatic H-atoms of the pyrimidine ion core. Structure (2-c) has the second water molecule to hydrogen bond with H₁-atom through 1.96 Å and 9.4 kcal/mol binding energy.

Table 7 displays the lowest energy structures predicted at the B3LYP/6-311++G(d,p) level of [pyrimidine⁺(H₂O)₃]. The lowest energy structure [pyrimidine⁺(H₂O)₃] is (3-a). (3-a) has third water molecule to bind to the pyrimidine ion core through two aromatic hydrogen bonds forming a bifurcated structure. (3-a) isomer shows 9.1 kcal/mol binding energy for the third water molecule. (3-b) is the second stable structure for [pyrimidine⁺(H₂O)₃]. It has the third water molecule to be hydrogen bonded through 1.97 Å bond to H₁ which results in a binding energy of 9.1 kcal/mol. The third stable structure in the [pyrimidine⁺(H₂O)₃] list has the structure shown in (3-c) of Table 7. Structure (3-c) expresses external hydration pattern in which the three water molecules are hydrogen bonded to each other forming a symmetric structure. Interestingly, (3-c) was predicted to be only 0.2 kcal/mol less stable than (3-a) at the B3LYP/6-311++G(d,p) level of the theory.

The three lowest energy isomers predicted for [pyrimidine⁺(H₂O)₄] are shown below (see Table 8). (4-a) has the lowest energy. Isomer (4-a) has external hydration pattern which elucidates the hydrogen abstraction process by the water clusters to form [H⁺(H₂O)_n], which starts to be formed at n=4. However, internally hydrated structures [(4-b) and (4-c)] are only 0.2 kcal/mol and 0.6 kcal/mol higher in energy than (4-a), respectively; (see Table 8)

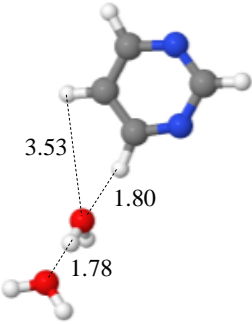
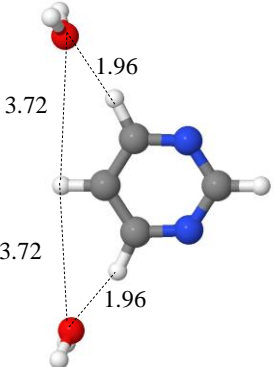
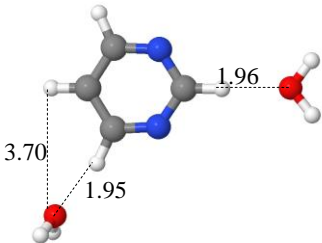
Name	Optimized Structure	Total Charge
C ₄ H ₄ N ₂ ⁺		1.0
H ⁺ C ₄ H ₄ N ₂		1.0
H ₂ O		0.0

Table 4. Theoretically optimized structures using B3LYP/6-311++G(d,p) with NBO charge distribution of C₄H₄N₂⁺, H⁺(C₄H₄N₂) and H₂O

Name	Optimized Structure	Relative Energy ^a	Binding energy ^b
1-a		0.0	10.7 (*9.9)
1-b		0.4	10.3 (*9.5)
1-c		1.2	9.5 (*8.8)

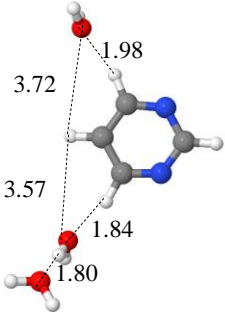
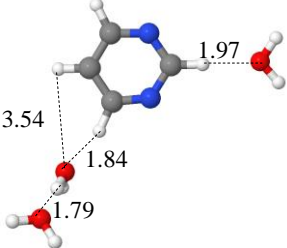
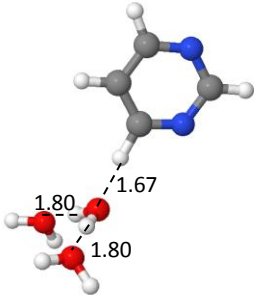
^a in kcal/mol (corrected for ZPE) ^b in kcal/mol *(corrected for ZPE and BSSE)

Table 5. Theoretically optimized structures using B3LYP/6-311++G(d,p) of C₄H₄N₂⁺(H₂O). Distances are in Angstroms

Name	Optimized Structure	Relative Energy ^a	Binding energy ^b
2-a		0.0	9.9 (*8.8)
2-b		0.3	9.6 (*8.8)
2-c		0.5	9.4 (*8.7)

^a in kcal/mol (corrected for ZPE) ^b in kcal/mol *(corrected for ZPE and BSSE)

Table 6. Theoretically optimized structures using B3LYP/6-311++G(d,p) of $C_4H_4N_2^+(H_2O)_2$. Distances are in Angstroms

Name	Optimized Structure	Relative Energy ^a	Binding energy ^b
3-a		0.0	9.1 (*8.1)
3-b		0.0	9.1 (*8.2)
3-c		0.2	8.9 (*7.6)

^a in kcal/mol (corrected for ZPE) ^b in kcal/mol *(corrected for ZPE and BSSE)

Table 7. Theoretically optimized structures using B3LYP/6-311++G(d,p) of $C_4H_4N_2^+(H_2O)_3$. Distances are in Angstroms

Name	Optimized Structure	Relative Energy ^a	Binding energy ^b
4-a		0.0	9.0 (*7.4)
4-b		0.2	8.8 (*7.8)
4-c		0.6	8.4 (*7.5)

^a in kcal/mol (corrected for ZPE) ^b in kcal/mol *(corrected for ZPE and BSSE)

Table 8. Theoretically optimized structures using B3LYP/6-311++G(d,p) of $C_4H_4N_2^+(H_2O)_4$. Distances are in Angstroms

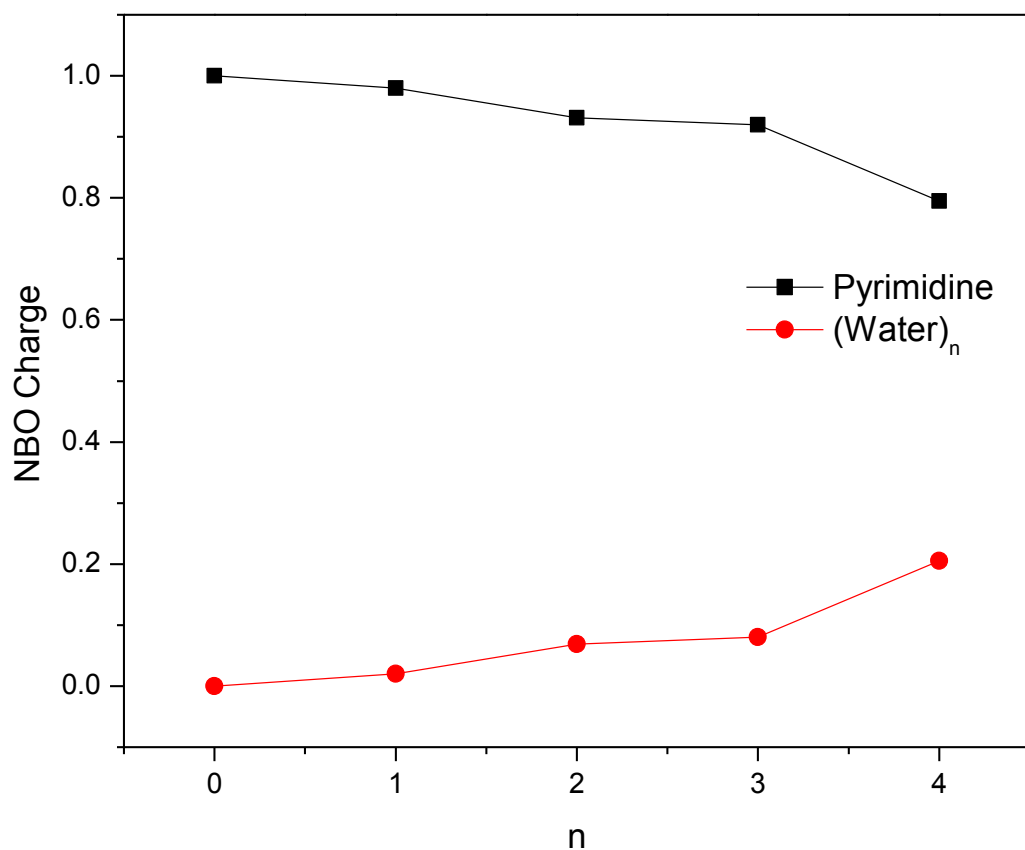


Figure 13. Charge transfer from pyrimidine radical cation to water cluster as hydration degree n evolves

4.4.3. Gas Phase Hydration of Protonated Pyrimidine

4.4.3.1. Mass-spectra

Figure 14 displays the mass-spectra resulting upon injecting the protonated pyrimidine into the drift cell which contains a mixture of water vapor and helium gas at various drift cell temperatures. The temperature is varied between 300 K and 235 K, which is the lowest attainable temperature before water freezing. 10% H_2 in He was used as a carrier gas to generate the protonated pyrimidine cation. At 300 K, $[H^+pyrimidine.(H_2O)]$ was the only observed product

while at 235 K, the hydrated protonated pyrimidine series is shifted to higher additions, following the usual clustering trends.

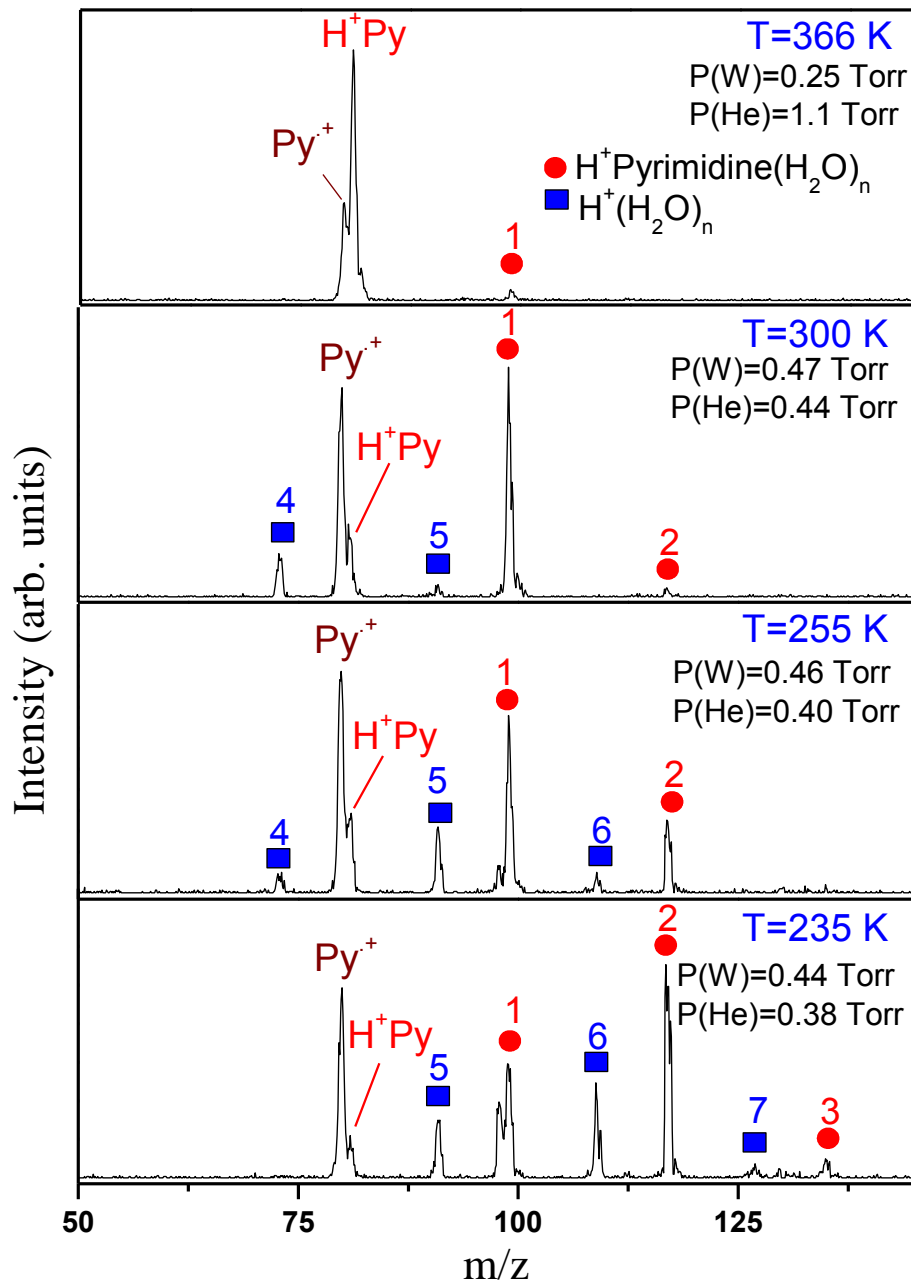
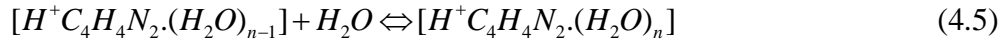


Figure 14. Mass spectra resulting upon protonated pyrimidine cation (H^+Py) injection into a mixture of water vapor (W) and helium gas using 13.9 eV (laboratory frame) injection energy and 2.2 V/cm drift field. Drift cell temperature and pressure are varied as indicated

4.4.3.2. Thermochemical Measurements

The high number of collisions, at least 10^5 , with the drift cell gas quickly establishes equilibria among the injected ions and their hydrated product ions. The concentrations of both the reactant and product ions are measured using the integrated intensity of the selected ATD of the ion of interest. When the equilibrium is established, a constant ratio of the integrated intensity of the product to the reactant ion is maintained at constant pressure and temperature. This indicates that the measured equilibrium constant is independent on the reaction time which is controlled by the applied drift field. In addition, identical ATDs of the reactant ions and the hydrated product ions are indicating equal residence times.

The equilibrium constant, K_{eq} , of the stepwise hydration reaction of H^+ pyrimidine (4.5) can be measured using equation (4.6):



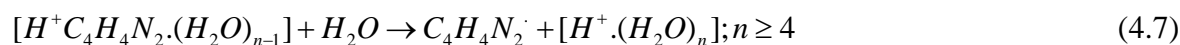
$$K_{eq} = \frac{I[H^+C_4H_4N_2.(H_2O)_n] \times 760}{I[H^+C_4H_4N_2.(H_2O)_{n-1}] \cdot P_{H_2O}} \quad (4.6)$$

where $I[H^+C_4H_4N_2.(H_2O)_{n-1}]$, $I[H^+C_4H_4N_2.(H_2O)_n]$ are the integrated intensities of ATDs of the reactant and product cluster ions of the association reaction (4.5), respectively and P_{H_2O} is the pressure of water, in Torr. The equilibrium constant, K_{eq} , is measured at different temperatures and from van't-Hoff equation (4.3), ΔH° and ΔS° values are obtained from the slope and intercept, respectively. van't-Hoff plots are obtained by plotting $R \ln K_{eq}$ versus $1000/T$, where T is the drift cell temperature, in Kelvin.

Arrival time distributions shown in Figure 15 illustrate identical arrival times of $[H^+Pyrimidine.(H_2O)_n]$; with $n=0-3$. This matching indicates the equilibria establishments under

our experimental conditions. However, ATDs of the formed hydrated pyrimidine are divided into two separate groups; in each an equilibrium state was established. The division of the ATDs into two groups occurs as a result of disappearance of the small clusters at low temperatures.

On the other hand, the formation of the observed protonated water clusters (see Figure 14) can be attributed to the dissociative proton transfer reaction as shown in equation (4.7):^{20,33}



The proton transfer reaction represents critical cluster size dependence which can be rationalized by the proton affinities of the water clusters versus that of pyrimidine as shown in Table 2. As for reaction (4.7) to become feasible, a minimal number of four water molecules is required in order to extract the proton from the aromatic cation. These results agree excellently with the previously reported DFT calculations which investigated the proton transfer process quantitatively. These theoretical studies followed the electron density motion among the relevant subunits and showed the gradual movement of the proton from the pyrimidine to the water subunit side.⁶²

The equilibrium constants of the stepwise hydration reaction (4.5) were measured at different temperatures yielding van't-Hoff plots shown in Figure 16 as explained in the experimental section. From van't-Hoff plots depicted in Figure 16. The binding energies ($-\Delta H^\circ$) and entropy changes (ΔS°) of the stepwise hydration steps were obtained and summarized below in Table 9, which also includes the theoretically calculated corresponding values. The binding energies follow the usual decreasing trend as the degree of hydration increases due to the repulsion among the water molecules and charge delocalization.²² For comparison, thermochemical values of the hydration of protonated pyridine cations are shown as well.¹⁷ It also worth noting that the calculated binding energies are in good agreement with their

corresponding measured values within the experimental uncertainty (± 1 kcal/mol) which elucidates the sufficiency of the employed calculation level.

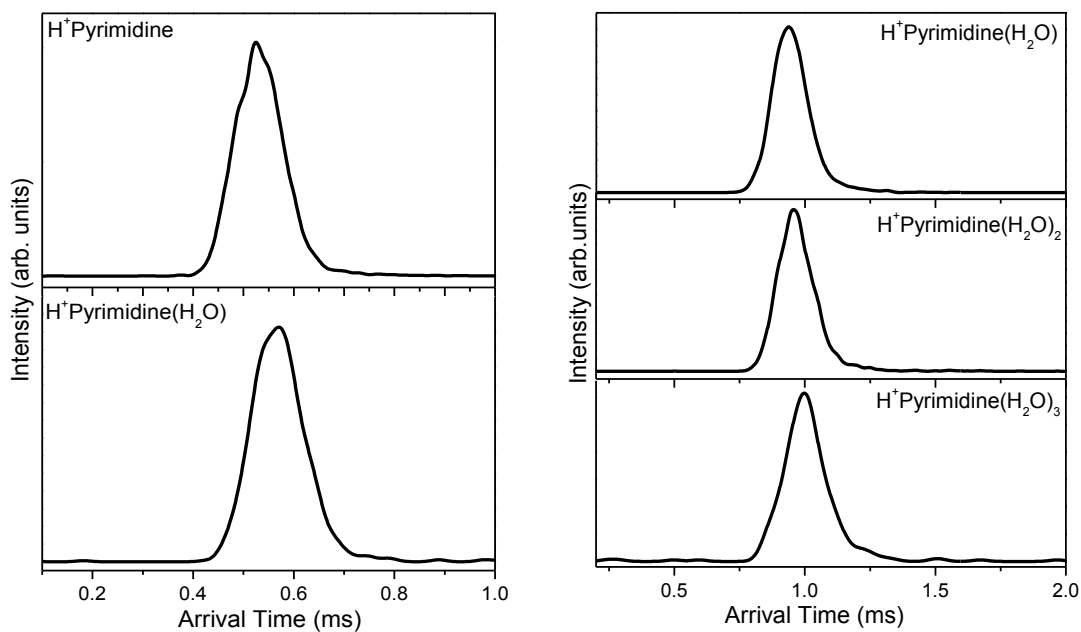


Figure 15. (Left) ATDs of protonated pyrimidine cation (H^+Py) and [H^+ pyrimidine (H_2O)] collected at 344 K and drift cell field of 2.5 V/cm. (Right) ATDs of [H^+ pyrimidine (H_2O) $_n$]; $n=1-3$, collected at 242 K and 2.5 V/cm as drift cell field

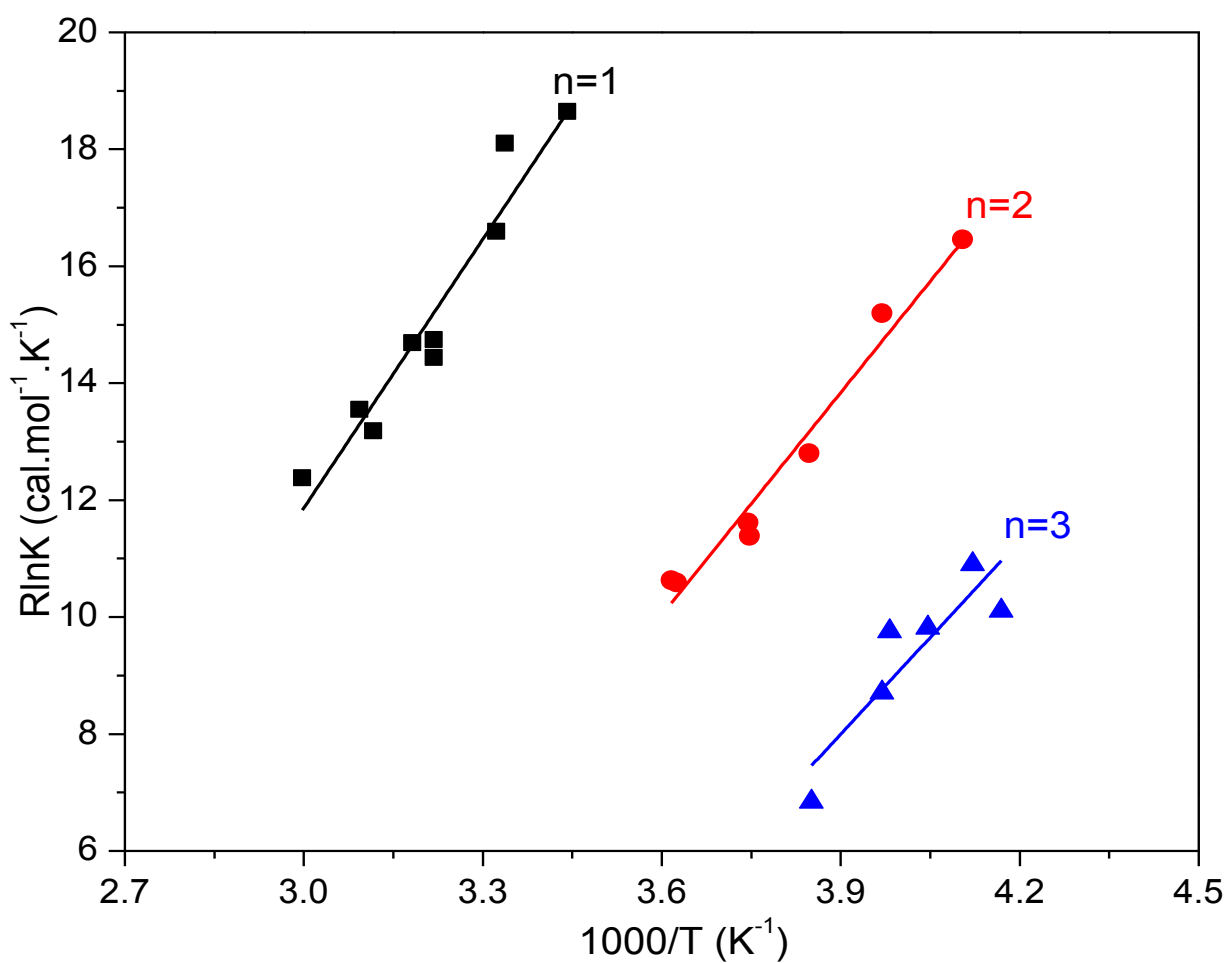


Figure 16. van't Hoff plots of the established equilibria among $[\text{H}^+\text{pyrimidine} \cdot (\text{H}_2\text{O})_n]$ clusters; with $n=0-3$ resulting from injecting the mass-selected protonated pyrimidine cation into the drift cell which has 0.47 Torr H_2O mixed with 0.44 Torr of helium gas using 13.9 eV injection energy (lab) and 2.5 V/cm drift field. Drift cell temperature was varied in the range of (235 K-333 K)

n	Protonated Pyrimidine				Protonated Pyridine ^d	
	$-\Delta H^{\circ a}$	$-\Delta S^{\circ b}$	BE ^c		$-\Delta H^{\circ a}$	$-\Delta S^{\circ b}$
1	15.3	34.1	17.1	*(16.0)	15.6	27.0
2	12.7	35.6	12.2	*(11.1)	11.5	26.0
3	11.0	34.9	10.5	*(9.5)	6.9	17.1

^a $\Delta H^{\circ}_{n-1,n}$ units are kcal/mol, ^b $\Delta S^{\circ}_{n-1,n}$ units are cal/mol.K, ^c Binding energy calculated by B3LYP/6-311++G(d,p) (* with BSSE correction), and ^d Ref. (Pyridine)¹⁷.

Table 9. Measured Thermochemistry values ($-\Delta H^{\circ}_{n-1,n}$ and $-\Delta S^{\circ}_{n-1,n}$) of the formation of H^+ pyrimidine.(H₂O)_n clusters; with n=1-3 for protonated pyrimidine cation in comparison to the corresponding values of protonated pyridine cations and the calculated binding energy values

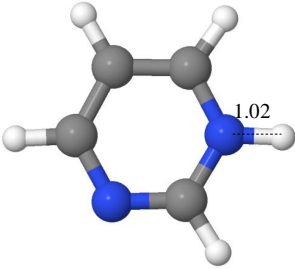
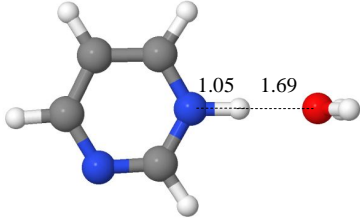
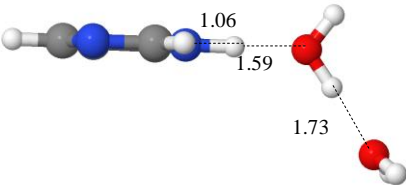
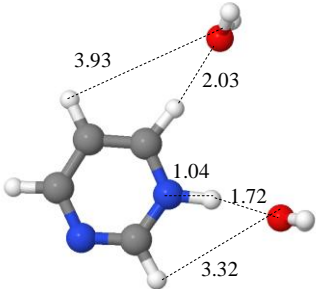
4.4.3.3. Theoretically calculated structures

H^+ pyrimidine can bind to water molecules via two different types of hydrogen bonds. One via $CH^{\delta+} \cdots O$ hydrogen bonds, which would be relatively weak as reported in benzene⁺ hydration example^{20,33} or via $NH^{\delta+} \cdots O$ hydrogen bonds, which are stronger similar to the hydration of the protonated pyridine.¹⁷ By checking the experimentally measured values, reported in Table 9, it can be noticed that the protonated pyrimidine binding energy values are very similar to the protonated pyridine example especially in the first two additions. This implies a strong similarity in the resultant structures in both cases. This can be explained by the similarity in the charge distribution in their optimized structures. The charge distribution in protonated pyrimidine, shown in Table 4, shows more localized charge on the proton (H₄) which

resembles the example of the protonated pyridine as the protonation occurs exclusively on the N-atom.^{17,135} Moreover, our calculation results agree excellently with previous high level calculation studies in locating the lowest energy protonated isomer.^{17,131,151} In fact as shown in Table 10, in the lowest energy [H^+ pyrimidine (H_2O)], the water molecule is attached to the NH via a $\text{NH}^+\cdots\text{O}$ hydrogen bond which simulates the hydration pattern of protonated pyridine cations.^{17,131,151} Structure (1-a) has a 1.69 Å hydrogen bond with 17.1 kcal/mol binding energy. This accounts for the binding energy similarity between the hydrated pyrimidine with the protonated pyridine. The second water molecule binds to the first water molecule by a 1.73 Å hydrogen bond forming a linear chain while the first hydrogen bond shortens to be 1.59 Å, see (2-a) in Table 10. Moreover, when two water molecules bind to the H^+ pyrimidine through internal hydration pattern, the optimized structure (2-b) was found to be 3.6 kcal/mol higher in energy than (2-a) at the B3LYP/6-311++G(d,p).

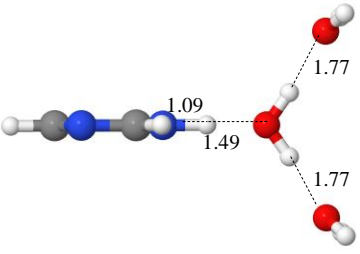
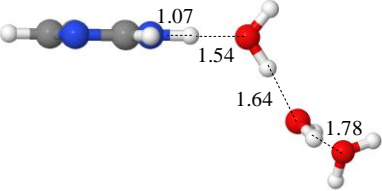
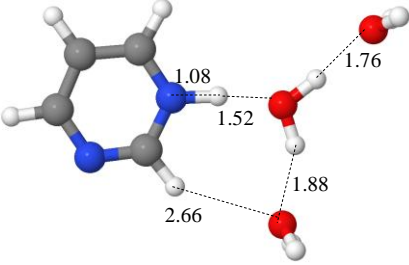
The third water molecule binds to the first one by 1.77 Å hydrogen bond; forming the symmetric structure, shown in Table 11 as (3-a). Therefore, external hydration pattern seems to be more energetically favorable; which can explain the proton transfer from the protonated pyrimidine cation to the water moiety, explained in detail in Table 12. Proton transfer process from the pyrimidine moiety to the water cluster can be depicted in the N \cdots H bond length versus H \cdots W one, as appears in Tables 10 and 11. As the number of added water molecules (n) increases, the former bond weakens while the later one strengthens as can be pointed out from the structures shown below. This eventually leads to the protonated water clusters formation noticed in Figure 14. Moreover, two additional less stable structures are considered, namely, (3-b) and (3-c). In fact, structures (3-a) through (3-c) present external hydration pattern. Moreover,

slow partial charge transfer is accompanying the hydration of H^+ pyrimidine cation with the increasing number of water molecules n as shown in Figure 17.

Name	Optimized Structure	Relative Energy ^a	Binding energy ^b
H^+ py		0.0	
1-a		0.0	17.1 (*16.0)
2-a		0.0	12.2 (*11.1)
2-b		3.6	8.6 (*7.8)

^a in kcal/mol (corrected for ZPE) ^b in kcal/mol *(corrected for ZPE and BSSE)

Table 10. Theoretically optimized structures using B3LYP/6-311++G(d,p) of $[H^+C_4H_4N_2(H_2O)_n]$; $n=0-2$. Distances are in Angstroms

Name	Optimized Structure	Relative Energy ^a	Binding energy ^b
3-a		0.0	10.5 (*9.5)
3-b		0.7	9.8 (*8.8)
3-c		1.0	9.5 (*8.5)

^a in kcal/mol (corrected for ZPE) ^b in kcal/mol *(corrected for ZPE and BSSE)

Table 11. Theoretically optimized structures using B3LYP/6-311++G(d,p) of $[\text{H}^+\text{C}_4\text{H}_4\text{N}_2^+(\text{H}_2\text{O})_3]$. Distances are in Angstroms

n	N---H ₄ (Å)	O---H ₄ (Å)
0	1.02	∞
1	1.05	1.69
2	1.06	1.59
3	1.09	1.49

Table 12. Intracuster proton transfer in [H⁺pyrimidine. (H₂O)_n] from H⁺pyrimidine to water cluster as a function of hydration degree *n*.

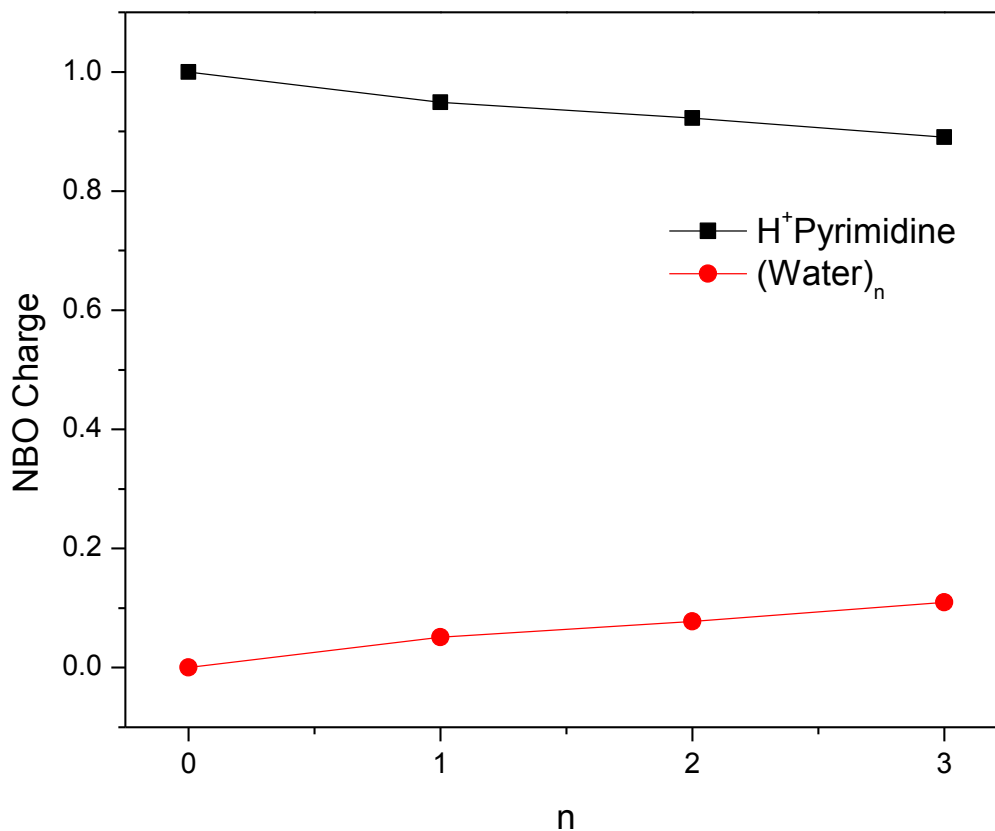


Figure 17. Partial charge transfer from H⁺pyrimidine to (water)_n as a function of hydration degree *n*

4.5. Conclusions

Using ion mobility measurements, structures of the binary pyrimidine-water have been identified. Moreover, it was observed that the protonated species are more predominant over their corresponding unprotonated ions. This observation is consistent with the previously reported results which investigated the proton transfer reactions in these clusters.^{62,145,146}

Equilibrium measurements have been used to investigate the hydration of pyrimidine radical cation on a molecular level. Stepwise association of water molecules onto the injected mass-selected pyrimidine⁺ results in the formation of [pyrimidine⁺(H₂O)_n]; with n=1-5. Thermochemistry measurements and theoretical calculations verified the similarity of the pyrimidine⁺ hydration to that of benzene⁺ rather than pyridine⁺. In both the pyrimidine⁺ and benzene⁺ hydration studies, hydrogen bonding with the aromatic H-atoms was observed. For comparison, the thermochemistry of stepwise hydration of the protonated pyrimidine using hydration equilibrium measurements is reported. Comparing the hydration of the protonated pyrimidine with the protonated pyridine suggests a strong similarity in the hydrated structures of H⁺pyrimidine with those of H⁺pyridine. In both cases, the hydrated structures involve NH⁺---O bonds. In fact, theoretical calculations identified the protonation site to be on the N-atom similar to the H⁺pyridine example.¹⁷

In addition, we have attributed the observed series of protonated water clusters to dissociative proton transfer reactions previously reported in the hydration of the benzene⁺.³³

Chapter 5: Sequential solvation of Protonated pyrimidine cation with methanol and acetonitrile molecules in the gas phase

5.1. Introduction

The replacement of water (H_2O) with Methanol (CH_3OH) in the H^+ pyrimidine(solvent)_n clusters probes the distinct hydrogen bonding properties of the two solvents. The loss of half the hydrogen bonding hydrogen atoms in methanol (CH_3OH) relative to H_2O can be expected to promote the chain-like growth over the cyclic hydrogen bonded structures common for water clusters. On the other hand, the presence of acetonitrile (CH_3CN) in the H^+ pyrimidine(CH_3CN)_n clusters should show blocked structures that prevent the formation of extended hydrogen bonded chains.⁷⁸

Moreover, both of CH_3OH and CH_3CN have higher proton affinities than H_2O ; 186 kcal/mol for CH_3CN , 180 kcal/mol for CH_3OH versus 165 kcal/mol for H_2O .³¹ The dipole moments of H_2O (1.85 D) is slightly higher than that of CH_3OH (1.69 D).³¹ This would lead to different intermolecular interaction preference toward hydrogen bonded interactions over the charge-dipole ones in the H^+ pyrimidine(CH_3OH)_n clusters.⁹ Acetonitrile, in addition to having higher proton affinity than both water and methanol, it has distinctly higher dipole moment than both of them as well (3.92 D).¹⁵⁵

In the present study, the gas phase stepwise solvations of protonated pyrimidine by 1-3 CH_3OH , and CH_3CN molecules are examined. Two kinds of hydrogen bonds can be formed through the interaction of the methanol and acetonitrile molecules with the protonated pyrimidine, $\text{NH}^{\delta+} \cdots \text{O}$, or $\text{CH}^{\delta+} \cdots \text{O}$ bonds in case of methanol while $\text{NH}^{\delta+} \cdots \text{N}$, or $\text{CH}^{\delta+} \cdots \text{N}$

bonds in case of acetonitrile. These systems are studied by employing the thermochemical equilibrium measurements using the mass-selected ion mobility technique in combination with (DFT) computational methods to determine the solvation sites and to locate the lowest energy isomers.¹⁵⁶ Such studies provide useful information about the individual binding energies and structures of the solvated cations. Moreover, it provides a basis for comparing CH₃OH and CH₃CN with H₂O in their hydrogen bonding affinities to the protonated pyrimidine cation.

5.2. Mobility measurements and structure determination of the binary clusters

5.2.1. Mass-spectra of the binary pyrimidine-methanol and pyrimidine-acetonitrile clusters

Supersonic expansion of a mixture of pyrimidine/solvent introduced by passing helium carrier gas through a glass bubbler contains a mixture of liquid pyrimidine and methanol or acetonitrile in a ratio of 1 to 2. This appeared to be an efficient route to get mixed binary clusters of pyrimidine/methanol as shown in Figure 18 while the binary clusters of pyrimidine/acetonitrile are shown in Figure 19.¹⁵⁰

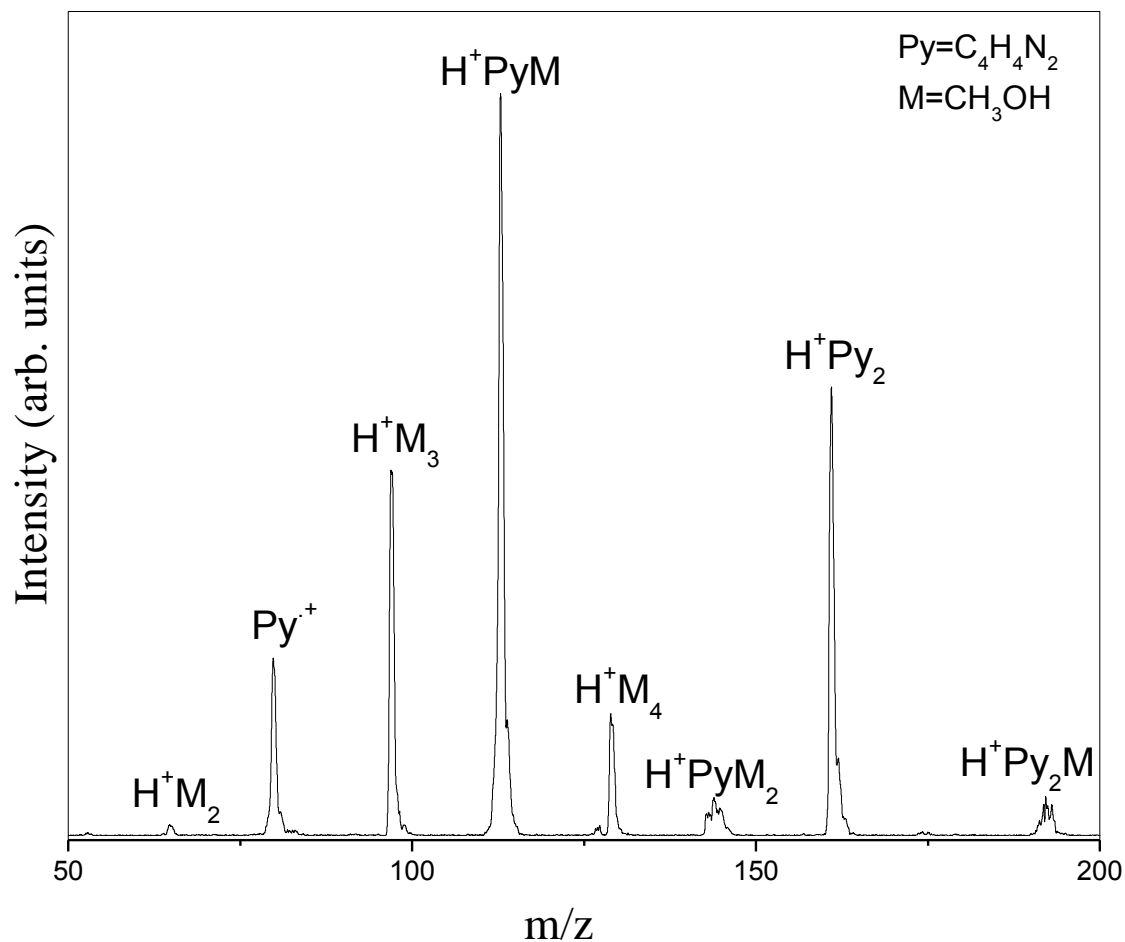


Figure 18. Mass-spectrum resulting from injecting the protonated pyrimidine cation in the RF-selection mode into the drift cell which contains 0.83 Torr of helium using an injection energy of 13.9 eV (lab) and drift voltage of 4.6 V/cm. The temperature of the drift cell was 300 K. The sample mixture is composed of pyrimidine: methanol in a ratio of 1:2

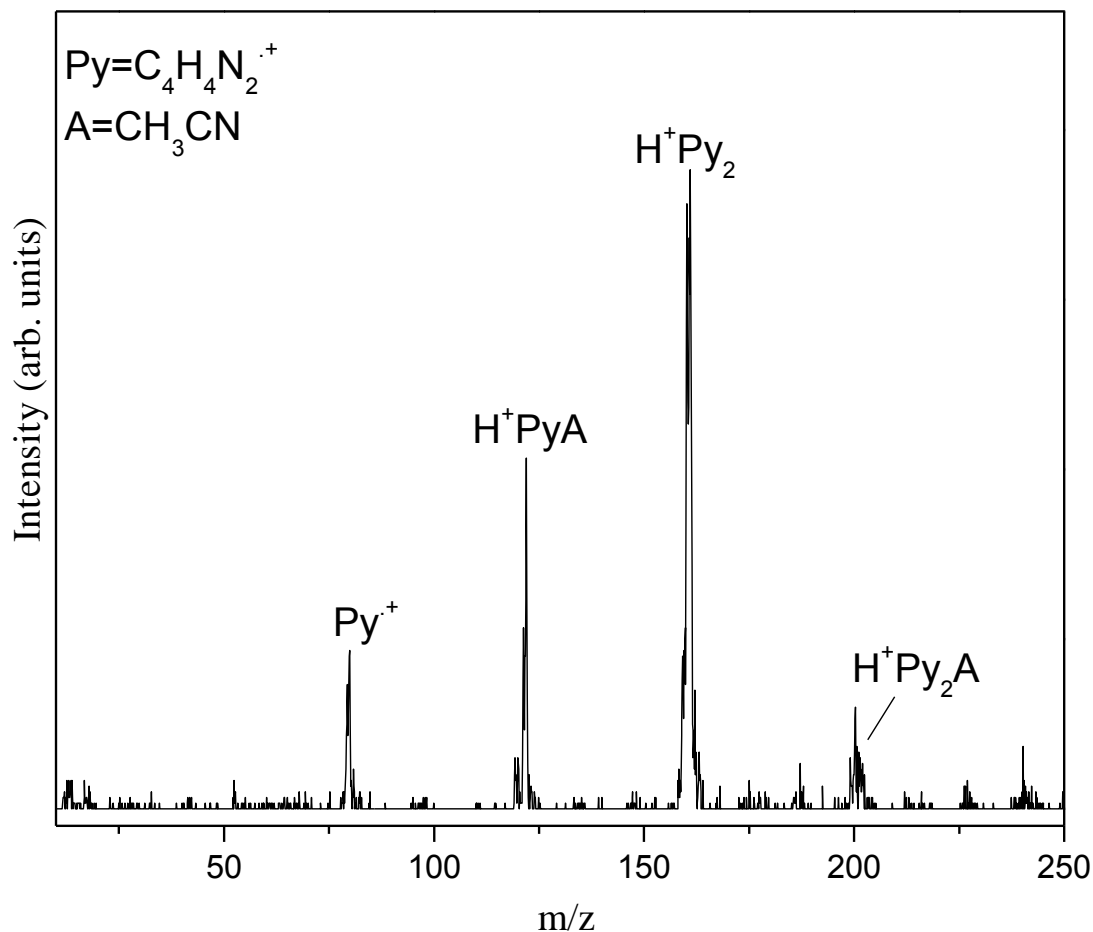


Figure 19. Binary clusters of pyrimidine-acetonitrile resulting from injecting the pyrimidine radical cation in the RF-selection mode into the drift cell which contains 1.23 Torr of helium using injection energy of 13.9 eV (lab) and drift voltage of 4.0 V/cm. The temperature of the drift cell was 302 K. The sample mixture is composed of pyrimidine: acetonitrile in a ratio of 1:2

5.2.2. Ion mobility measurements

The reduced mobility constants of the observed clusters were measured under low field conditions ($E/N < 5.1$ Td) at 300 K using 14 eV (lab. Frame) as injection energy. Figure 20 illustrates typical examples of ATDs of the protonated pyrimidine solvated by a single methanol molecule at different applied drift cell voltages. Figure 21 illustrates the ATDs of protonated pyrimidine solvated by a single acetonitrile molecule at different applied drift cell voltages. The

reduced mobilities and their corresponding collision cross-section values are tabulated in Table 13 in addition to those calculated via the trajectory method of the lowest energy DFT-structures shown below in Figure 22. Moreover, the protonated pyrimidine dimer (H^+Py_2) appeared to have relative exceptional stability with respect to its non-protonated analogue (Py_2^+). Pyrimidine dimer (Py_2^+) was not observed in cases of water, methanol, or acetonitrile mixed clusters. This observation can be rationalized to a stable structure for the protonated species (see Figure 22e).

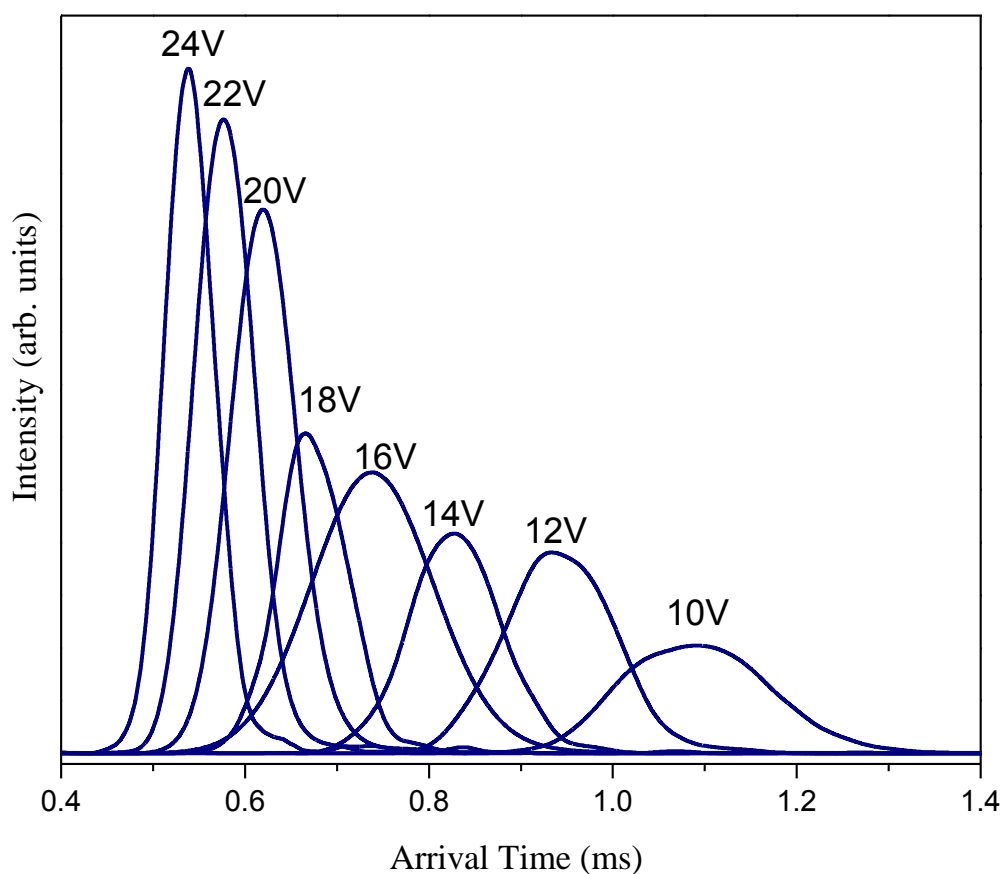


Figure 20. ATDs of $[\text{H}^+\text{pyrimidine} (\text{CH}_3\text{OH})]$ on varying the drift voltage from 10 to 24V

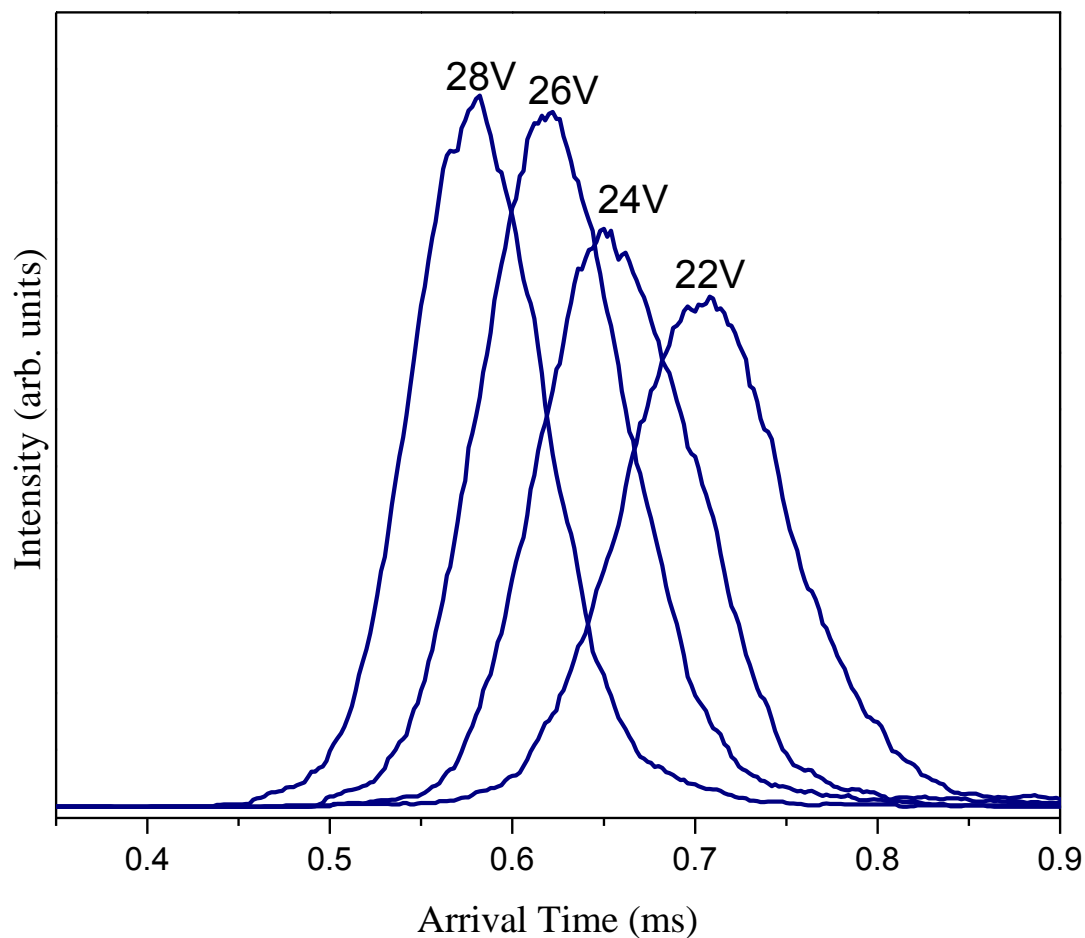


Figure 21. ATDs of $[H^+ \text{pyrimidine (CH}_3\text{CN)}]$ on varying the drift voltage from 22 to 28V resulting from injecting $[H^+ \text{pyrimidine (CH}_3\text{CN)}]$ in the RF-mode using injection energy of 15 eV(laboratory frame). The measurement was done at 303 K

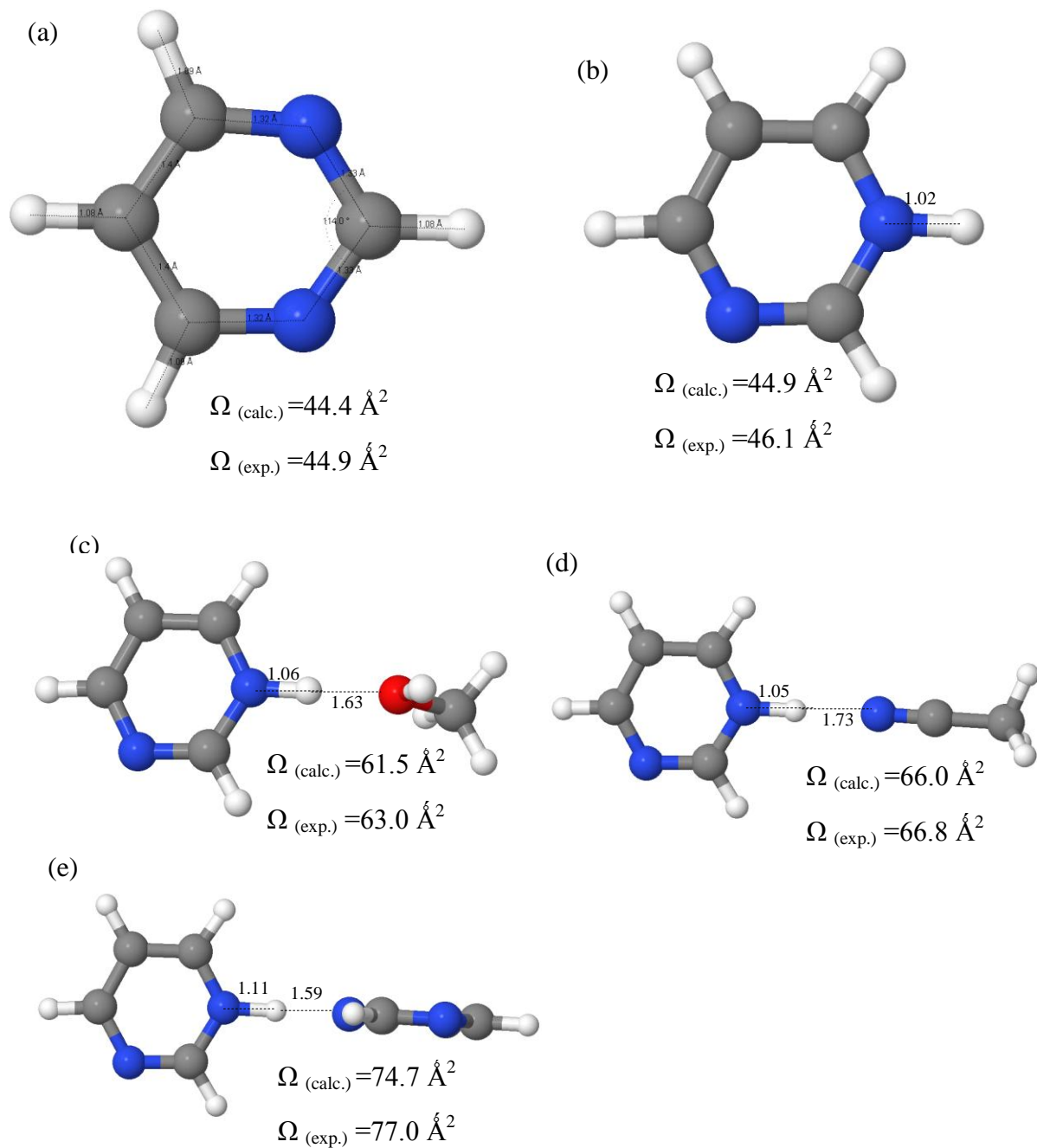


Figure 22. B3LYP/6-311++G(d,p) optimized structures of (a)Pyrimidine⁺ (b)Protonated pyrimidine [H⁺pyrimidine] (c)[H⁺pyrimidine (CH₃OH)] (c)[H⁺pyrimidine (CH₃CN)] (e) Protonated pyrimidine dimer [H⁺(Pyrimidine)₂]. The experimental collision cross-sections and the calculated values are indicated for the room temperature measurements

Cluster ion	T (K)	$K_{0(\text{exp.})}^{\text{a}}$	$\Omega_{(\text{exp.})}^{\text{b}}$	$K_{0(\text{cal.})}^{*,\text{a}}$	$\Omega_{(\text{cal.})}^{*,\text{b}}$
Pyrimidine	299	12.20	44.9	12.34	44.4
H ⁺ Pyrimidine	301	11.85	46.1	12.16	44.9
H ⁺ Pyrimidine(CH ₃ OH)	300	8.62	63.0	8.84	61.5
H ⁺ Pyrimidine(CH ₃ CN)	302	8.09	66.8	8.18	66.0
H ⁺ (Pyrimidine) ₂	300	7.02	77.0	7.20	74.9
H ⁺ (Pyrimidine) ₂	225	8.05	82.8	7.92	78.8

^a K_0 in $\text{cm}^2 \cdot \text{V}^{-1} \cdot \text{s}^{-1}$ ^b Ω in \AA^2 * Calculated by DFT (B3LYP/6-311++G(d,p))

Table 13. Mobility and cross section values for various binary clusters obtained using pyrimidine/methanol and pyrimidine/acetonitrile solvent mixtures

5.3. Gas-Phase Thermochemical Equilibrium Measurements

5.3.1. Gas-Phase Solvation of Protonated Pyrimidine Cation by Methanol

On injecting pyrimidine radical cation into the drift cell containing a gas mixture of methanol vapor and helium gas, only the protonated series; [H⁺pyrimidine (CH₃OH)_n]; with n=0-3 could be observed as shown below in Figure 23. The protonation of the injected pyrimidine occurs exclusively even at very low concentrations of methanol and very short residence times.

This implies that proton transfer reaction is very fast which can be rationalized to the fact that the proton affinity of pyrimidine is higher than that of methanol by about 30 kcal/mol.^{22,31}

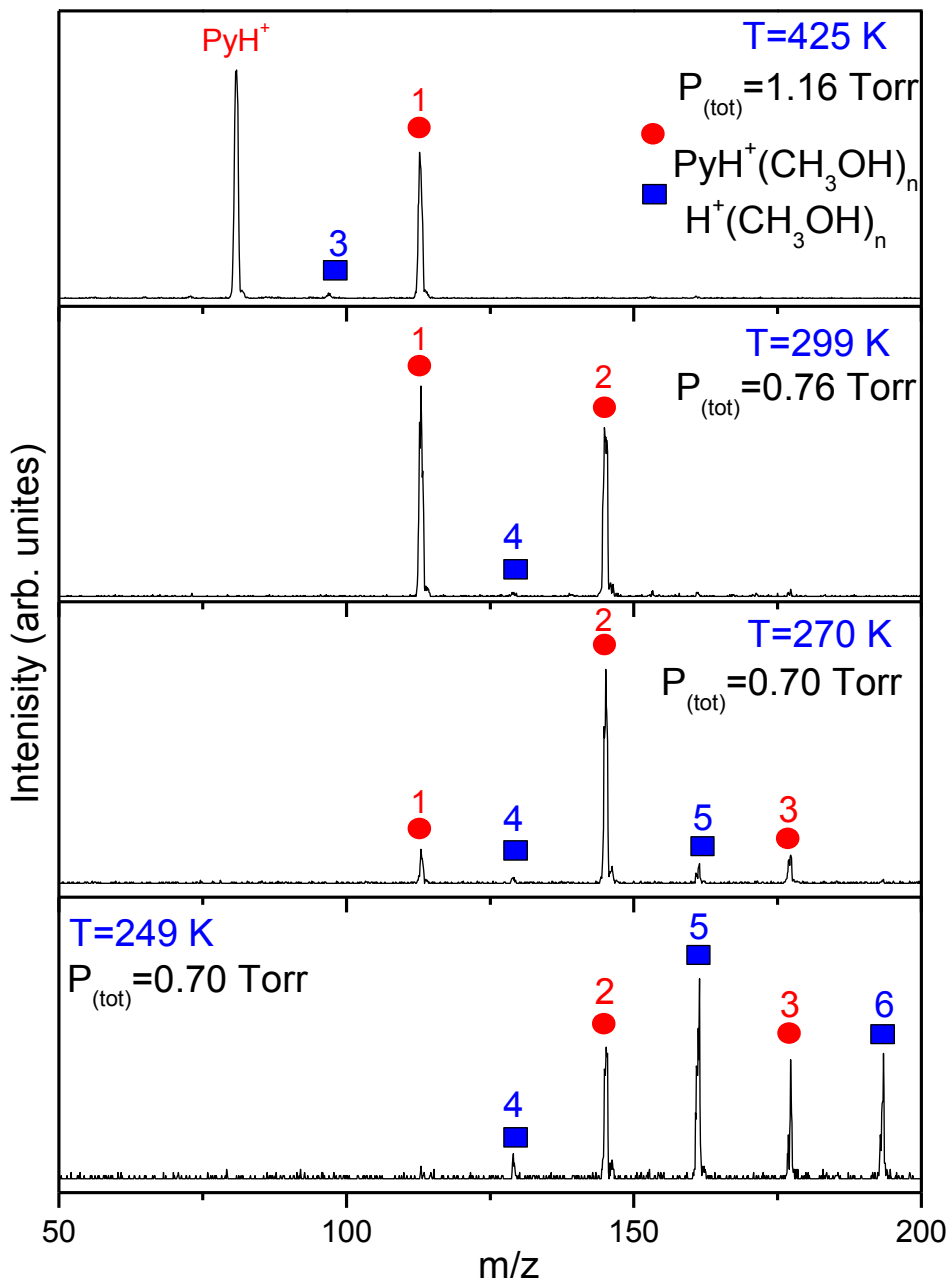
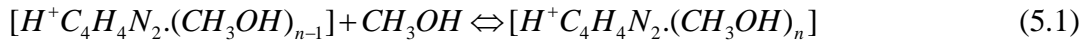


Figure 23. Mass spectra resulting upon pyrimidine radical cation ($\text{Py}^{\cdot+}$) injection via 12.7 eV (lab) injection energy and 2.2 V/cm drift field into a mixture of methanol (M) and helium gas. Drift cell temperature and total pressure are varied as indicated

5.3.1.1. Thermochemistry measurements and structural implications

Injecting the mass-selected pyrimidine radical cation into the drift cell under mild conditions of weak drift field of 2.5 V/cm, and low injection energy of 13 eV (laboratory frame) helps to lengthen the residence times in the drift cell. Therefore, the number of collisions is increased dramatically which enhances the establishment of equilibrium. The high number of collisions, at least 10^5 , with the drift cell gas quickly establishes equilibria among the injected ions and their solvated product ions. The concentrations of both the reactant and product ions are measured using the integrated intensity of the selected ATD of the ion of interest. When the equilibrium is established, a constant ratio of the integrated intensity of the product to the reactant is maintained at constant pressure and temperature. This indicates that the measured equilibrium constant is independent on the reaction time which is controlled through the applied drift field. In addition, ATDs of the reactant ions and the solvated product ions are identical indicating equal residence times.

The equilibrium constant, K_{eq} , of the stepwise association reaction of methanol molecules with H^+ pyrimidine (5.1) can be measured using equation (5.2):



$$K_{eq} = \frac{I[H^+C_4H_4N_2.(CH_3OH)_n] \times 760}{I[H^+C_4H_4N_2.(CH_3OH)_{n-1}] \cdot P_{CH_3OH}} \quad (5.2)$$

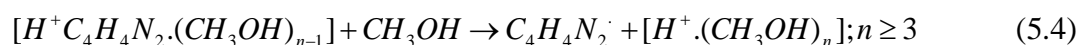
$$R \ln K_{eq} = \frac{-\Delta H^\circ}{T} + \Delta S^\circ \quad (5.3)$$

where $I[H^+C_4H_4N_2.(CH_3OH)_{n-1}]$, $I[H^+C_4H_4N_2.(CH_3OH)_n]$ are the integrated intensities of ATDs of the reactant and product cluster ions of the association reaction (5.1), respectively and

P_{CH_3OH} is the pressure of methanol, in Torr. The equilibrium constant, K_{eq} , is measured at different temperatures and from van't-Hoff equation (5.3), ΔH° and ΔS° values are obtained from the slope and intercept, respectively. van't-Hoff plots are obtained by plotting $R \ln K_{eq}$ versus $1000/T$, where T is the drift cell temperature in Kelvin.

Arrival time distributions shown in Figure 24 illustrate identical arrival times of $[H^+Pyrimidine.(CH_3OH)_n]$; with $n=0-3$. This matching indicates the equilibria establishments under our experimental conditions. However, ATDs of the formed solvated pyrimidine are divided into two separate groups; in each an equilibrium state was established.

On the other hand, the formation of the observed protonated methanol clusters; with $n=3-6$ (see Figure 23) can be attributed to the dissociative proton transfer reaction previously observed in the H^+ pyrimidine hydration example, Figure 14, according to equation (5.4):^{20,33}



The proton transfer reaction (5.4) exhibits critical cluster size dependence at $n \geq 3$ which can be rationalized by the proton affinities of the solvent clusters as shown in Table 14.^{31,150} For reaction (5.4) to become feasible, a minimal number of three methanol molecules is needed in order to extract the proton from the protonated pyrimidine cation yielding protonated methanol cluster and pyrimidine radical. These results agree well with the previously reported DFT calculations which investigated the proton transfer process quantitatively by following the electron density motion among the relevant subunits and showed the gradual movement of the proton from the pyrimidine to the methanol subunit side.⁶²

Cluster	Proton Affinity (kcal/mol)
CH ₃ OH	182±1
(CH ₃ OH) ₂	211±1
(CH ₃ OH) ₃	224±1
(CH ₃ OH) ₄	231±1
(CH ₃ OH) ₅	234±1
Pyrimidine	212±1

Table 14. Proton affinities of methanol clusters in comparison to that of pyrimidine

Equilibrium constants have been measured over a wide range of drift cell temperatures which yields the van't-Hoff plots. The experimental values of binding energies and entropy changes are obtained from the slope and intercept, respectively of van't-Hoff plots shown in Figure 25. Equilibrium was confirmed to be established under our conditions by obtaining identically matching ATDs of the reactants and products as shown in Figure 24. The resulting values are shown in Table 15 along with the corresponding calculated values. The calculated binding energies match well with the experimental measurements within the uncertainty range for the first two additions. The predicted binding energy for the third step is 2 kcal/mol less than the experimentally measured binding energy which can be attributed to that the level of calculations could not locate the lowest energy structure of $[H^+C_4H_4N_2.(CH_3OH)_3]$.

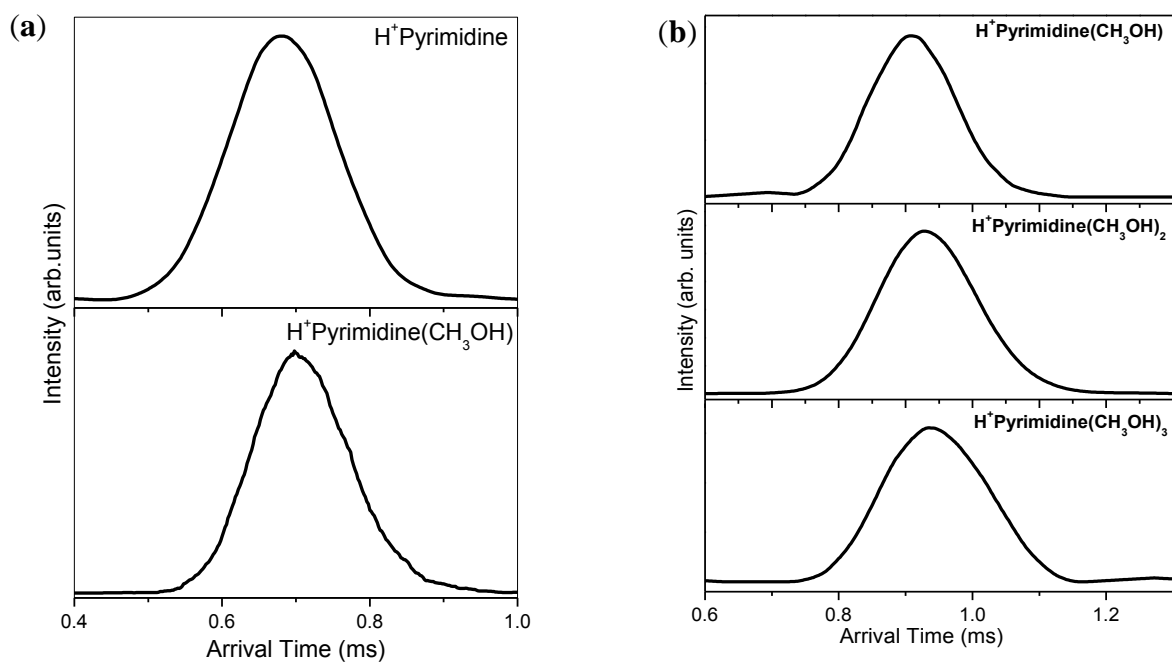


Figure 24. (a) ATDs of [H⁺pyrimidine] and [H⁺pyrimidine (CH₃OH)] collected at 373 K and drift cell field of 2 V/cm (b) ATDs of [H⁺pyrimidine (CH₃OH)_n]; n=1-3, collected at 264 K and 2.5 V/cm as drift cell field

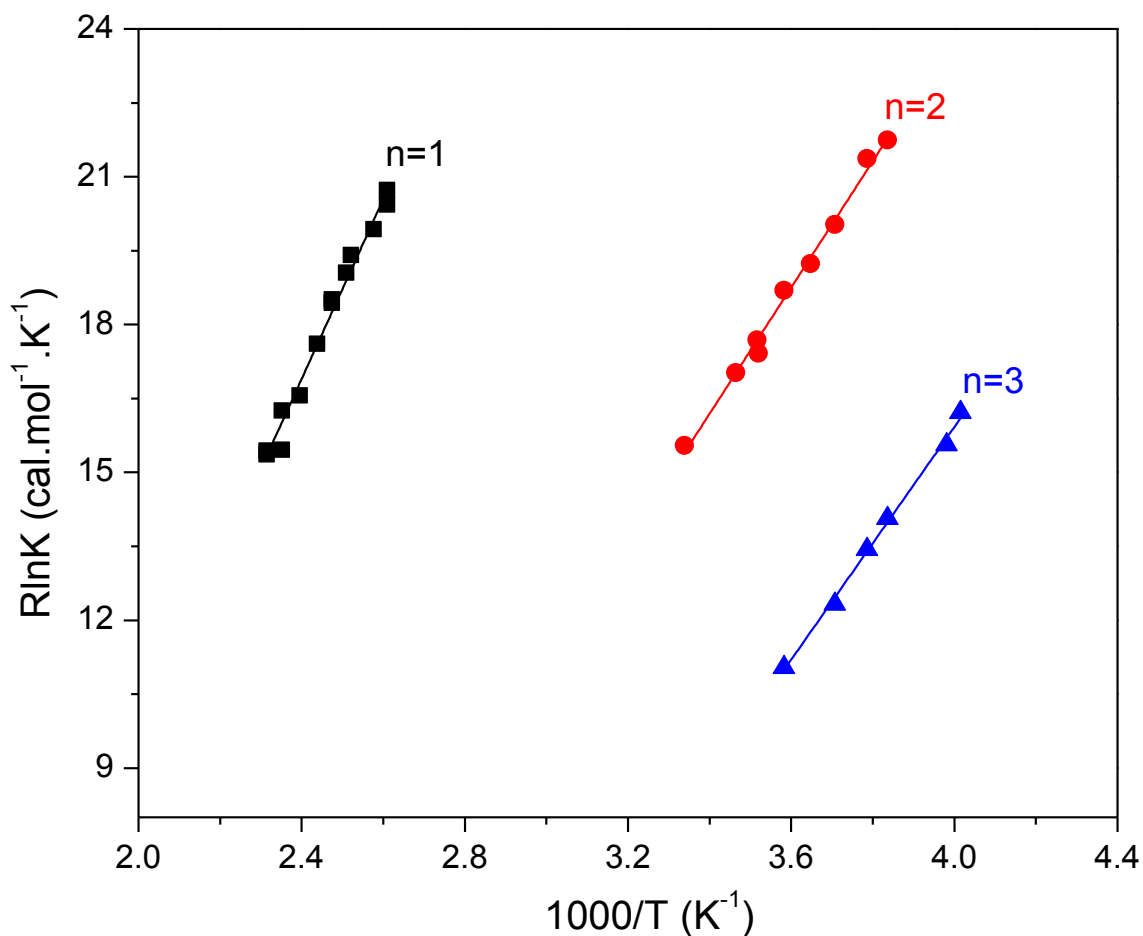


Figure 25. van't Hoff plots of the established equilibria among $[H^+pyrimidine.(CH_3OH)_n]$ clusters; with $n= 0-3$ resulting from injecting pyrimidine radical cation into the drift cell which has 0.24 Torr CH_3OH mixed with 0.52 Torr of helium gas using 12.7 eV injection energy (lab) and 2.5 V/cm drift field. Drift cell temperature was varied between 249 K and 432 K

n	$-\Delta H^{\circ a}$	$-\Delta S^{\circ b}$	BE ^c	
1	18.2	26.9	19.4	* (18.0)
2	12.8	27.4	13.3	* (12.7)
3	11.8	31.3	9.9	* (8.8)

^a $\Delta H^{\circ}_{n-1,n}$ units are kcal/mol, ^b $\Delta S^{\circ}_{n-1,n}$ units are cal/mol.K, and ^c Binding energy calculated by B3LYP/6-311++G(d,p) (* with BSSE correction).

Table 15. Binding energies and entropy changes from van't-Hoff plots (Figure 25) along with calculated binding energies using B3LYP/6-311++G(d,p)

5.3.1.2. Theoretical calculations

Methanol binds to the protonated pyrimidine core by relatively stronger hydrogen bond of 1.63 Å than the water example, as displayed in Table 17 as (1-a). However, (1-b) structure has a bifurcated structure in which the O-atom of methanol is hydrogen bonded to two CH- aromatic hydrogen atoms. (1-b) structure was predicted to lie at 10.3 kcal/mol higher in energy than (1-a).

The second methanol molecule binds to the first by 1.70 Å hydrogen bond favoring external solvation pattern while the first hydrogen bond shortens to 1.52 Å; see structure (2-a) in Table 18. (2-b) structure was predicted at B3LYP/6-311++G(d,p) to be 4.3 kcal/mol higher in energy than (2-a). Isomer (2-c) showed internally solvated structure. However it is 5.4 kcal/mol less stable than (2-a).

The third methanol molecule binds to the second one by a weaker 1.85 Å hydrogen bond and forms a cyclic solvent structure with the pyrimidine ring through the formation of a new hydrogen bond to an aromatic hydrogen atom of 2.36 Å; as displayed as structure (3-a) in Table 19. This cyclic structure (3-a) supports the large entropy loss observed in the third step (31.3 cal/mol. K). (3-b) structure was predicted to be at 2.0 kcal/mol higher in energy than (3-a). Structure (3-b) has the second methanol molecule to be hydrogen bonded to an aromatic hydrogen atom. Structure (3-c) isomer has a very similar structure to that of (3-b) with the new methanol molecule is hydrogen bonded to another H-atom. (3-c) is predicted to be 2.5 kcal/mol higher in energy than (3-a).

5.3.1.3. Proton transfer

Table 20 shows quantitative transfer of the proton from the H⁺pyrimidine to the methanol cluster resulting in eventual release of pyrimidine radical and H⁺(CH₃OH)_n with n≥3. These results show the N—H bond is stretched while O—H bond is shortened with the solvation degree *n* increase. The N—H bond was stretched from 1.02 Å to 1.06 Å at *n*=1 and to 1.08 Å at *n*=2 and further lengthened to 1.09 Å at *n*=3, while the O—H hydrogen bond was shortened from 1.63 Å to 1.52 Å and eventually to 1.49 Å as *n* increases from 1 to 3. Moreover, the ionic charge moves from the H⁺pyrimidine partially as the number of attached methanol molecules increase, as can be seen from Figure 26.

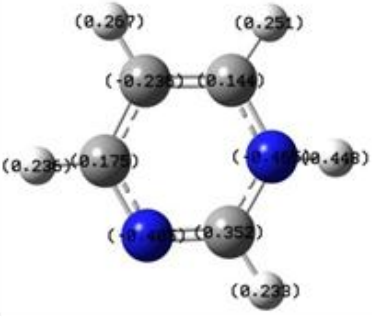
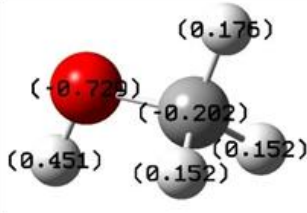
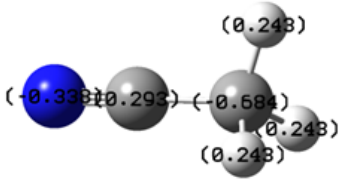
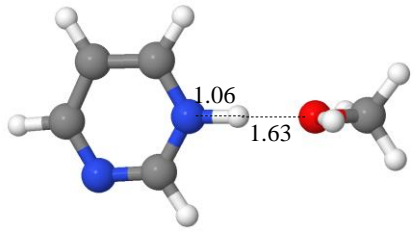
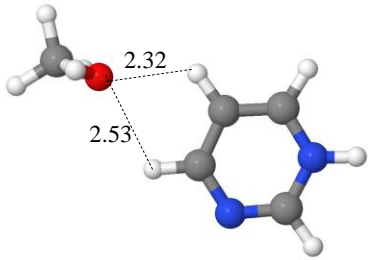
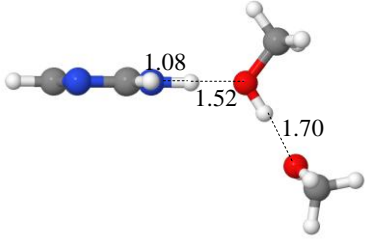
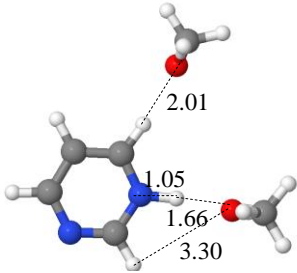
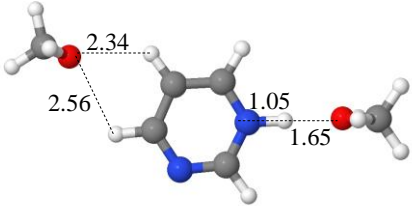
Name	Optimized Structure	Total Charge
$H^+C_4H_4N_2$		1.0
CH_3OH		0.0
CH_3CN		0.0

Table 16. Theoretically optimized structures using B3LYP/6-311++G(d,p) with NBO charge distribution of $H^+(C_4H_4N_2)$, CH_3OH and CH_3CN

Name	Optimized Structure	Relative Energy ^a	Binding energy ^b
1-a		0.0	19.4 (*18.0)
1-b		10.3	9.1 (*8.6)

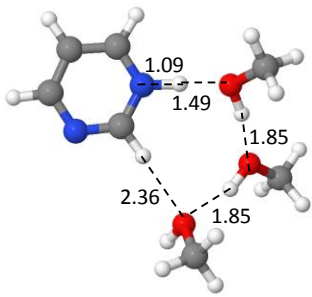
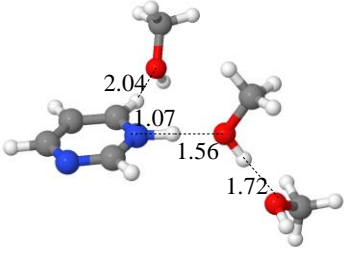
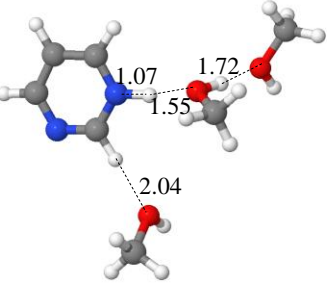
^a in kcal/mol (corrected for ZPE) ^b in kcal/mol *(corrected for ZPE and BSSE)

Table 17. Theoretically optimized structures using B3LYP/6-311++G(d,p) of $[\text{H}^+\text{C}_4\text{H}_4\text{N}_2(\text{CH}_3\text{OH})]$. Distances are in Angstroms

Name	Optimized Structure	Relative Energy ^a	Binding energy ^b
2-a		0.0	13.3 (*12.7)
2-b		4.3	9.0 (*8.9)
2-c		5.4	7.9 (*7.9)

^a in kcal/mol (corrected for ZPE) ^b in kcal/mol* (corrected for ZPE and BSSE)

Table 18. Theoretically optimized structures using B3LYP/6-311++G(d,p) of $[\text{H}^+\text{C}_4\text{H}_4\text{N}_2(\text{CH}_3\text{OH})_2]$. Distances are in Angstroms

Name	Optimized Structure	Relative Energy ^a	Binding energy ^b
3-a		0.0	9.9 (*8.8)
3-b		2.0	7.9 (*7.5)
3-c		2.5	7.4 (*6.8)

^a in kcal/mol (corrected for ZPE) ^b in kcal/mol *(corrected for ZPE and BSSE)

Table 19. Theoretically optimized structures using B3LYP/6-311++G(d,p) of $[H^+C_4H_4N_2(CH_3OH)_3]$. Distances are in Angstroms

n	N---H ₄ (Å)	O---H ₄ (Å)
0	1.02	∞
1	1.06	1.63
2	1.08	1.52
3	1.09	1.49

Table 20. Intracluster proton Transfer in [H⁺pyrimidine. (CH₃OH)_n] from H⁺pyrimidine to methanol

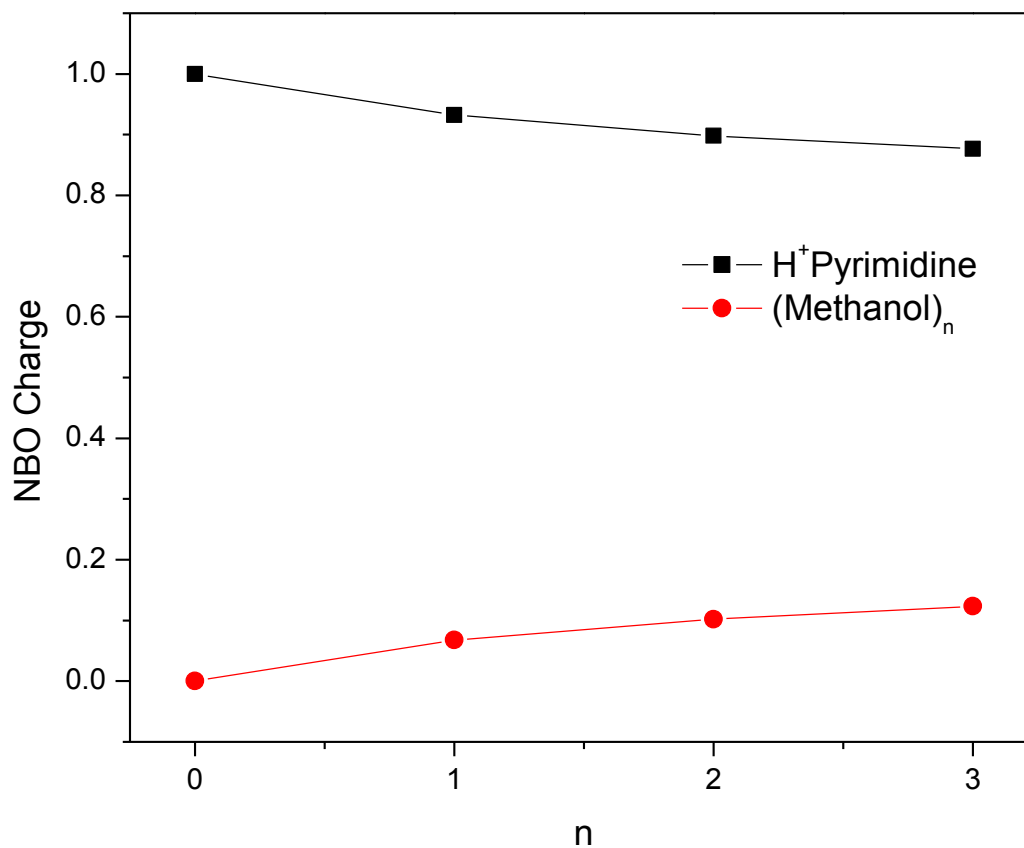


Figure 26. Partial charge transfer from H⁺pyrimidine to (methanol)_n as a function of n

5.3.2. Gas-Phase Solvation of Protonated Pyrimidine Cation by Acetonitrile

Acetonitrile is extensively used as an aprotic organic solvent in various processes in chemical industries. It is also widely involved in research laboratories for amino acid separation, synthesis of DNA and peptide sequencing.⁷⁵ Moreover, acetonitrile (CH_3CN) was found to be present in the stratosphere in the form of protonated hydrates.⁷⁸ Injection of pyrimidine radical cations in the mass-selected mode, into a mixture of acetonitrile and helium yielded in exclusive formation of the protonated adducts; $[\text{H}^+\text{pyrimidine}(\text{CH}_3\text{CN})_n]$ where $n=1-3$, The formation of protonated adducts seen in Figure 27 can be attributed to the proton affinity difference which is 25 kcal/mol. This behavior is similar to the methanol example, however, no protonated acetonitrile clusters were observed.

Recently, clustering studies has been done on protonated amino acids with CH_3CN and H_2O molecules which showed higher solvation power of acetonitrile versus water. This behavior has been ascribed to the larger electrostatic factors of acetonitrile.³¹ The dipole moment and polarizability of CH_3CN are 3.92 D and 4.45 \AA^3 , respectively.¹⁵⁷ The dipole moment and polarizability of water are 1.85 D and 1.45 \AA^3 , respectively.¹⁵⁷

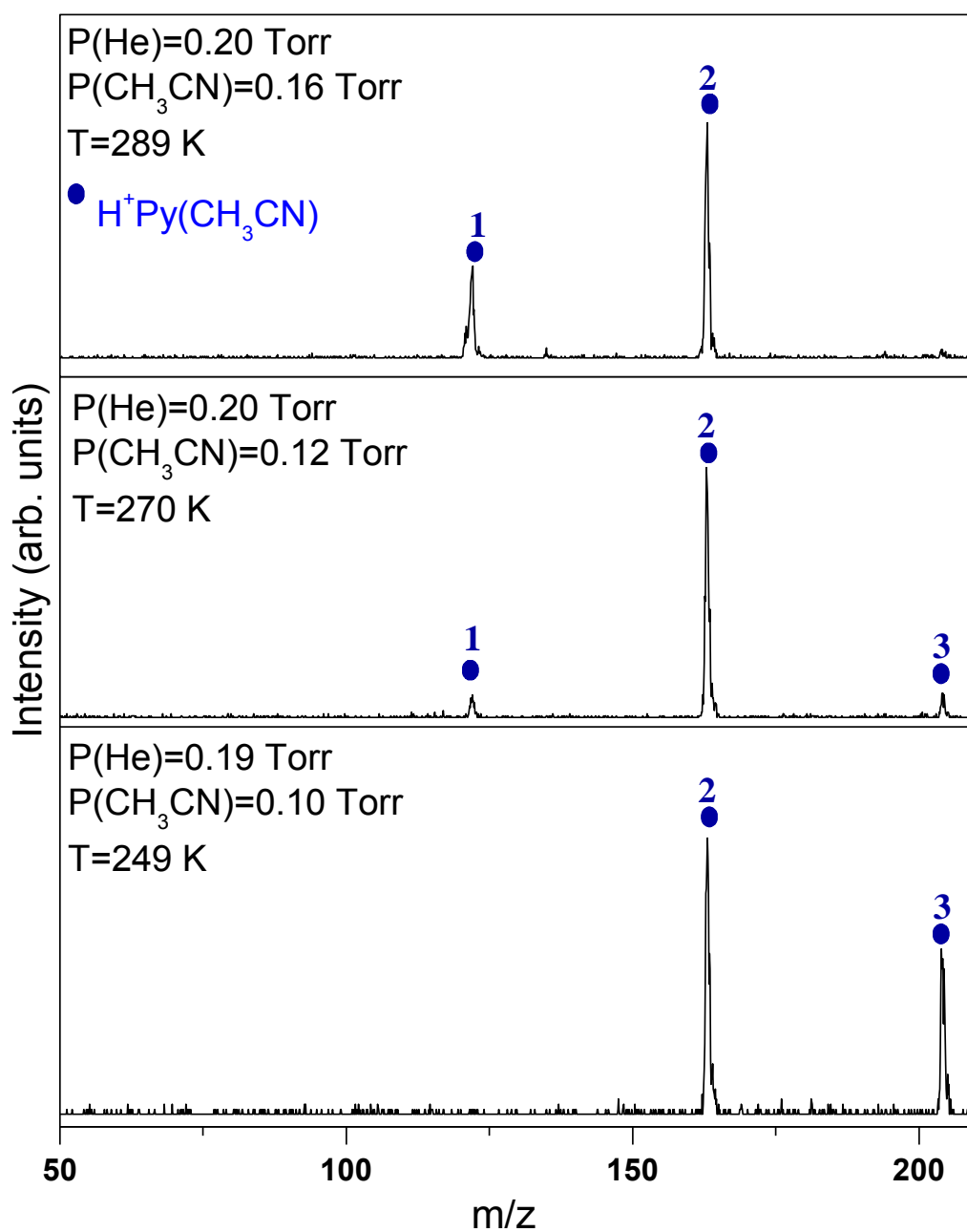
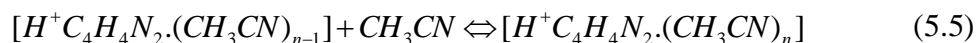


Figure 27. Mass-spectra obtained upon injection of pyrimidine radical cations in the mass-selection mode, into a mixture of acetonitrile and helium yielded in exclusive formation of the protonated adducts; [H⁺pyrimidine.(CH₃CN)₁₋₃]. Pressure and temperature are indicated

5.3.2.1. Thermochemistry measurements and structural implications

The reaction investigated in the present study was the stepwise association of acetonitrile molecules to protonated pyrimidine at different temperature according to equation (5.5):



The equilibrium constant, K_{eq} , of the stepwise association reaction of acetonitrile molecules with H^+ pyrimidine (5.5) can be measured using equation (5.6):

$$K_{eq} = \frac{I[H^+C_4H_4N_2.(CH_3CN)_n] \times 760}{I[H^+C_4H_4N_2.(CH_3CN)_{n-1}] \cdot P_{CH_3CN}} \quad (5.6)$$

where $I[H^+C_4H_4N_2.(CH_3CN)_{n-1}]$, $I[H^+C_4H_4N_2.(CH_3CN)_n]$ are the integrated intensities of ATDs of the reactant and product cluster ions of the association reaction (5.5), respectively and P_{CH_3CN} is the pressure of acetonitrile, in Torr. The equilibrium constant, K_{eq} , was measured at different temperatures and from van't-Hoff equation (5.3), ΔH° and ΔS° values were obtained from the slope and intercept, respectively. van't-Hoff plots of H^+ pyrimidine(CH_3CN)_n; n=1-3 are shown below in Figure 29.

Arrival time distributions shown in Figure 28 illustrate identical arrival times of $[H^+$ pyrimidine(CH_3CN)_n]; with n=1-3. This matching indicates the equilibria establishments under our experimental conditions. The H^+ pyrimidine(CH_3CN)/ H^+ pyrimidine equilibrium wasn't established under our conditions. This study probably has required higher temperatures ranges than the highest temperature used here, namely, 303 K.

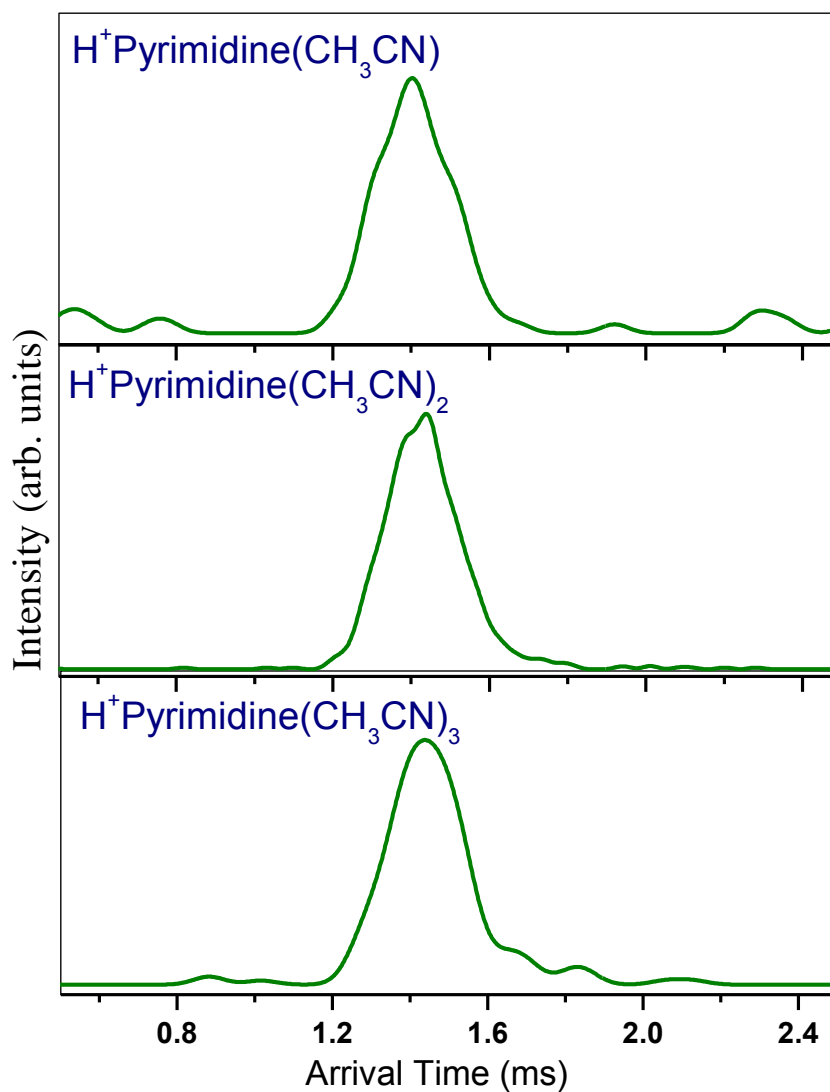


Figure 28. ATDs of $\text{H}^+\text{pyrimidine}(\text{CH}_3\text{CN})_n$; $n=1-3$ obtained by injecting mass-selected pyrimidine radical cation into the drift cell contains 0.12 Torr CH_3CN mixed with 0.19 Torr of helium using 12 eV injection energy (lab. frame) and 2.5 V/cm drift field

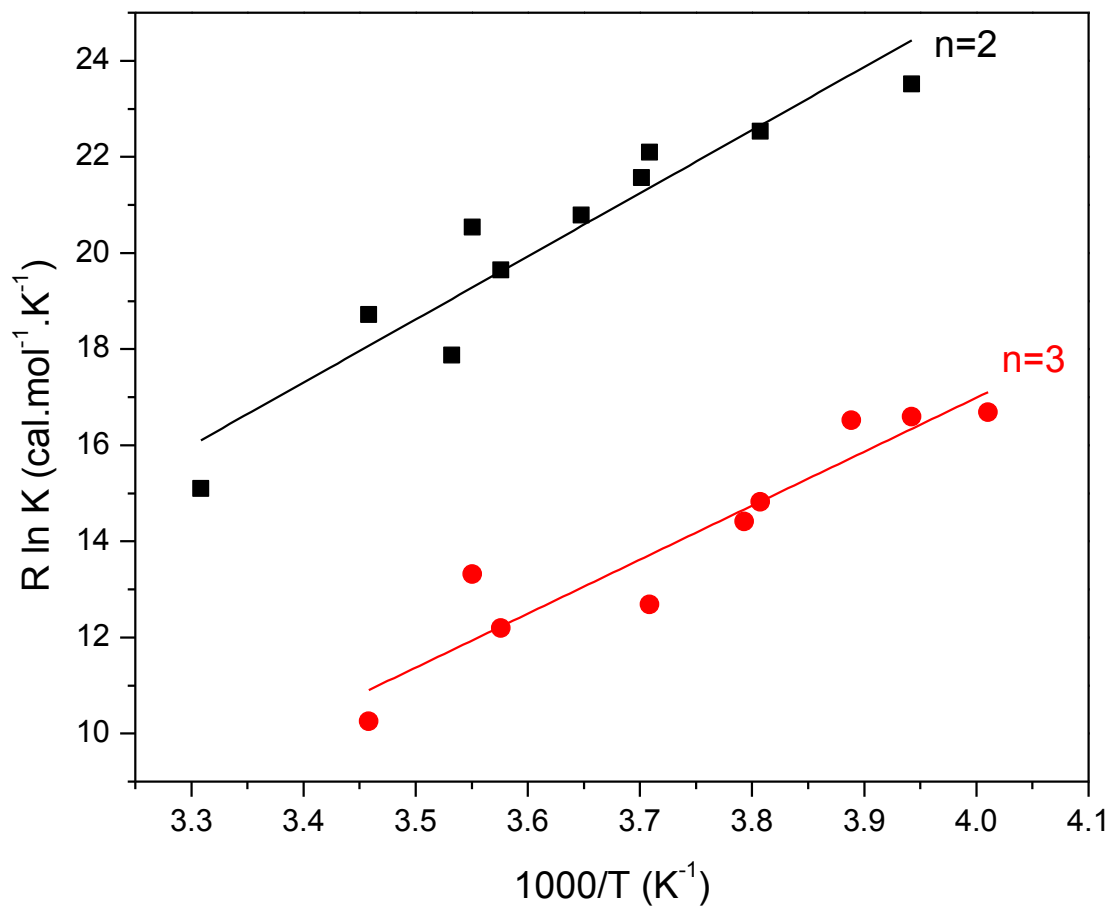


Figure 29. van't-Hoff plots obtained as a result of injecting pyrimidine radical cation in the mass-selection mode into the drift cell contains 0.16 Torr of acetonitrile mixed with 0.19 Torr of helium using injection energy of 12 eV(lab. frame) and 2.5 V/cm drift field. The drift cell temperature was varied between 247 K and 303 K

n	$-\Delta H^\circ$ ^a	$-\Delta S^\circ$ ^b	BE ^c	
1	N/A	N/A	22.8	* (22.5)
2	13.1	27.3	11.0	* (10.8)
3	11.2	27.9	8.9	* (8.7)

^a $\Delta H^\circ_{n-1,n}$ units are kcal/mol, ^b $\Delta S^\circ_{n-1,n}$ units are cal/mol.K, and ^c Binding energy calculated by B3LYP/6-311++G(d,p) (* with BSSE correction).

Table 21. Binding energies and entropy changes from van't-Hoff plots for $[H^+Pyrimidine(CH_3CN)_n]$ along with the corresponding calculated binding energies using B3LYP/6-311++G(d,p)

5.3.2.2. Theoretical calculations

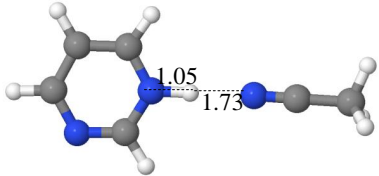
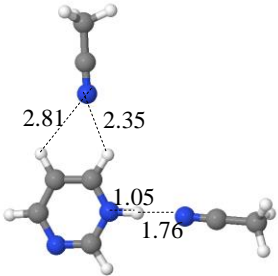
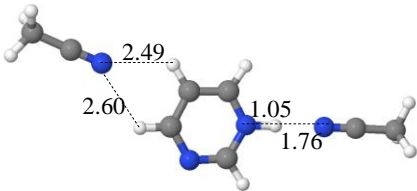
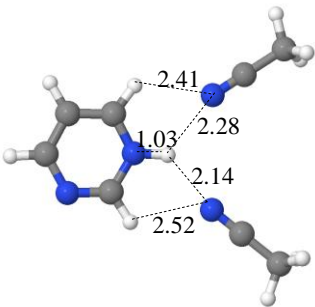
B3LYP/6-311++G(d,p) level of DFT was used to examine the structures and the corresponding binding energies. First acetonitrile binds exclusively to the proton of the H^+ pyrimidine cation through a hydrogen bond of 1.73 Å. The corresponding corrected predicted binding energy of $[H^+pyrimidine(CH_3CN)]$ was 22.5 kcal/mol.

The second acetonitrile molecule prefers internal solvation pattern. This behavior is different from the hydration as well as the methanol solvation examples, both showed preference of external solvation over the internal solvation in the second step. This can be attributed to the acetonitrile blocked structure which suppresses the probabilities of formation of extended structure with acetonitrile molecules hydrogen bonded to each other.⁷⁸ Structure (2-a) has the second CH_3CN molecule hydrogen bonded through bifurcated structure through 2.35 Å and 2.81

Å hydrogen bonds to two aromatic hydrogen atoms. Structure (2-b) has a similar structure but it was predicted to be 0.9 kcal/mol higher in energy than (2-a). However, the third most stable structure (2-c) is degenerate with (2-b). In (2-c), both the CH₃CN molecules are forming bifurcated structures, as shown in Table 22.

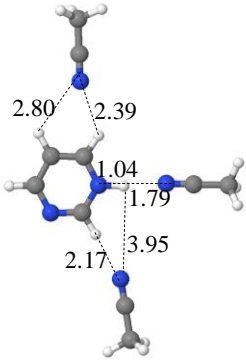
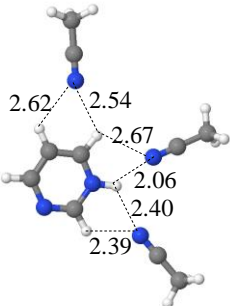
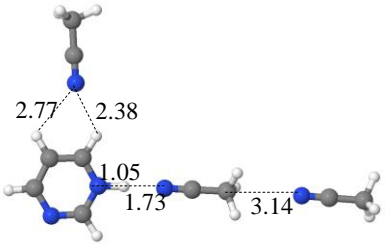
The most stable structure predicted for [H⁺pyrimidine(CH₃CN)₃] has the structure (3-a) shown in Table 23. Structure (3-a) has an asymmetric structure in which two CH₃CN molecules are forming bifurcated hydrogen bonds with aromatic hydrogen atoms while the third is hydrogen bonded to the H⁺pyrimidine cation 's proton. The (3-b) structure was predicted to be 0.6 kcal/mol higher in energy than (3-a) and it shows that the three CH₃CN molecules are forming bifurcated hydrogen bonds with aromatic hydrogen atoms. The third most stable structure of [H⁺pyrimidine(CH₃CN)₃] (3-c) has the third CH₃CN hydrogen bonded to the first one via a weak hydrogen bond of 3.14 Å. The third CH₃CN molecule in (3-c) shows predicted binding energy of 6.6 kcal/mol. Therefore, all three lowest energy structures of [H⁺pyrimidine(CH₃CN)₃] are predicted to have internal solvation geometries so the lack of the protonated acetonitrile clusters can be explained.

In addition, partial charge transfer from the aromatic cation to (CH₃CN)_n moiety as *n* increases is shown in Figure 30. The charge transfer pattern shows that most of the positive ion (~90%) stays focused on the ionic core.

Name	Optimized Structure	Relative Energy ^a	Binding energy ^b
1-a		0.0	22.8 (*22.5)
2-a		0.0	11.0 (*10.8)
2-b		0.9	10.1 (*9.9)
2-c		0.9	10.1 (*9.8)

^a in kcal/mol (corrected for ZPE) ^b in kcal/mol *(corrected for ZPE and BSSE)

Table 22. Theoretically optimized structures using B3LYP/6-311++G(d,p) of $[H^+C_4H_4N_2(CH_3CN)_n]$; n=1,2. Distances are in Angstroms

Name	Optimized Structure	Relative Energy ^a	Binding energy ^b
3-a		0.0	8.9(*8.7)
3-b		0.6	8.3 (*8.0)
3-c		2.3	6.6 (*6.4)

^a in kcal/mol (corrected for ZPE) ^b in kcal/mol *(corrected for ZPE and BSSE)

Table 23. Theoretically optimized structures using B3LYP/6-311++G(d,p) of $[H^+C_4H_4N_2(CH_3CN)_3]$. Distances are in Angstroms

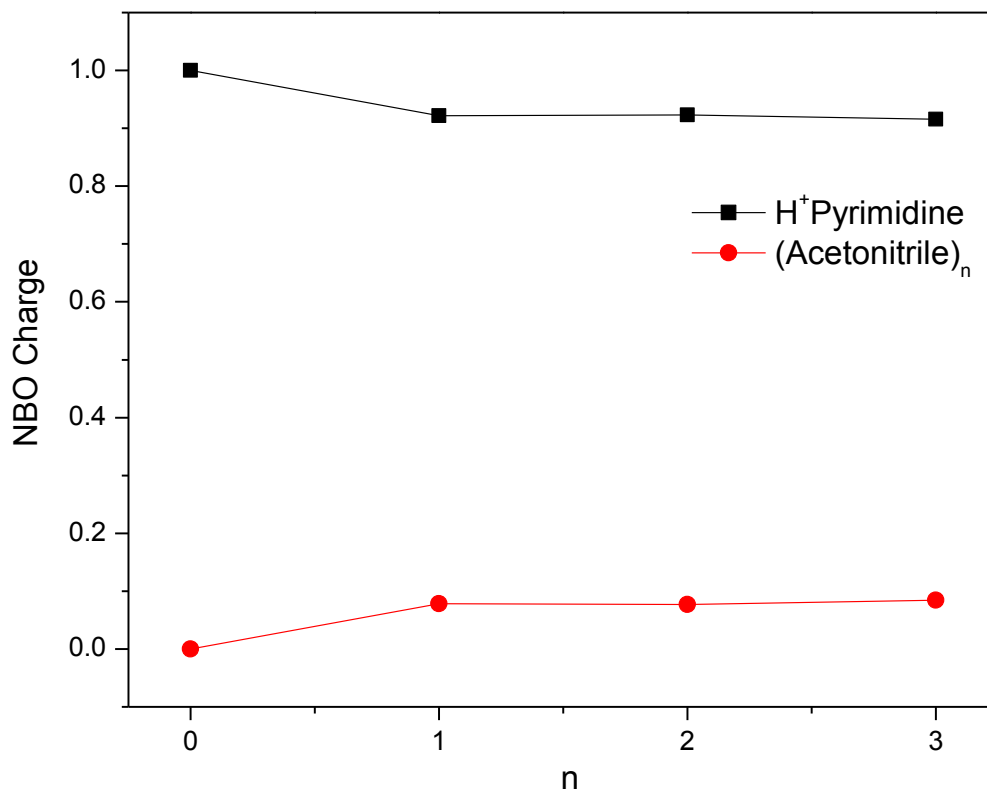


Figure 30. Charge distribution on H⁺pyrimidine versus CH₃CN moiety as n increases

5.4. Conclusions

Preferential binding of CH₃CN to H⁺pyrimidine over H₂O and CH₃OH can be attributed to the difference in the proton affinities in which acetonitrile is about 6 kcal/mol higher than methanol and 21 kcal/mol higher than water. Theoretically calculated structures show preferential external solvation as all the low energy structures of [H⁺pyrimidine.(H₂O)_n] and [H⁺pyrimidine.(CH₃OH)_n] are exclusively externally solvated. In addition, the calculated binding energies are in good agreement with the experiment.

In addition, we have attributed the observed series of protonated methanol clusters to the dissociative proton transfer reactions previously reported in the hydration of the benzene^{+.33}

Moreover, this reaction wasn't observed with acetonitrile, which has been attributed to the blocked structure of acetonitrile which prevents the formation of linear solvent cluster structure. This can be seen clearly in the theoretical calculated structures of $[H^+ \text{pyrimidine}(\text{CH}_3\text{CN})_n]$ by B3LYP/6-311++G(d,p) level.

Chapter 6: Stepwise Solvation of Benzene^{•+} and Phenyl acetylene^{•+} Radical Cations by HCN molecules

6.1. Introduction

To date, astronomers and molecular astrophysicists have identified and spectroscopically characterized more than 100 gaseous interstellar molecules.⁶⁷ Among them, the gaseous hydrogen cyanide (HCN) molecule and its metastable isomer (HNC) are thought to be ubiquitous in both cold, dark molecular clouds and in some comets.⁶⁸ The HCN formation in the titan atmosphere was initiated by the dissociation of the nitrogen and methane.^{74,158}

HCN molecule has received great attention from biochemists as well⁶⁹⁻⁷¹ because of its possible role in the synthesis of prebiotic compounds, such as amino acids, peptides, and purine bases.^{68,72-76} It was reported by Matthews and co-workers that HCN can act as a precursor for the formation of a mixture of amino acids through reaction of its oligomers with water.⁷⁷ Moreover, they accounted for the presence of protein/nucleic acid ancestors on the early Earth to the presence of hydrogen cyanide polymers.⁷⁷ Recently, Terlouw and coworkers carried out extensive theoretical studies of hydrogen cyanide dimer and trimer to investigate their structures and to locate their global minima.^{159,160} Moreover, they studied the formation of pyrimidine and its isomers from reactions of HCN with C₃H₃N^{•+} isomers.^{161,162}

6.2. Stepwise Solvation of Benzene^{•+} by HCN and CH₃CN molecules

The formation of the complex polycyclic aromatic nitrogen containing hydrocarbons (PANHs) was theoretically predicted to be feasible through the reaction of benzene radical cation and hydrogen cyanide molecules.¹⁶³ This reaction was theoretically predicted to be initiated via

an aromatic hydrogen atom abstraction from benzene; forming phenyl cation which further interacts with HCN molecules.¹⁶³ Therefore, the interaction of aromatic organic cations with hydrogen cyanide is of fundamental experimental and theoretical importance.

In this work, the stepwise solvation of benzene radical cations on a molecular level by several HCN molecules is reported. Thermochemical equilibrium measurements have been utilized to measure the enthalpy and entropy changes accompanying the individual solvation steps yielding benzene⁺ (HCN)_n; with n =1- 4.¹⁶⁴

Acetonitrile (CH₃CN) is extensively used as an aprotic organic solvent in various processes in chemical industries. It is also widely involved in research laboratories for amino acid separation, synthesis of DNA and peptide sequencing.⁷⁵ Thus, for comparison purposes, solvation of benzene radical cation by acetonitrile (CH₃CN) was investigated using thermochemistry equilibrium measurements. Enthalpy and entropy changes are measured experimentally for benzene (CH₃CN)_n; where n=1-3, the results are then compared with those experimentally measured and theoretically predicted for the benzene (HCN)_n.¹⁶⁴

6.2.1. Experimental Section

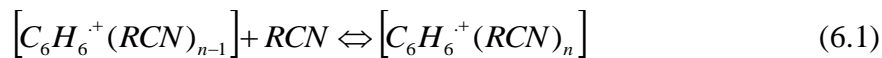
The molecular ions of benzene (C₆H₆⁺) are formed by electron impact ionization using electron energy of 60-70 eV following the supersonic adiabatic expansion. The supersonic expansion of 40 psi (2.8 bar) of ultra high pure helium seeded with about 1-4% benzene vapor. The expansion occurs through a pulsed supersonic nozzle (500 μm) to the source chamber which has 10⁻⁷ mbar background pressure. C₆H₆⁺ ions are mass-selected by the first quadrupole mass-filter and injected in (30-50 μs pulses) into the drift cell. The drift cell contains the neutral HCN gas or CH₃CN vapor (sigma-Aldrich, 99.9%) mostly in a mixture with helium buffer gas.⁷³ The

temperature of the drift cell can be controlled better than ± 1 K using four temperature controllers. The pressure can be controlled in the drift cell by using mass flow controllers (MKS # 1479A) within ± 1 mTorr, and monitored using a baratron (MKS-626A).

The product and unreacted ions were then scanned using the second quadrupole mass-filter and detected by electron multiplier detector. Arrival time distributions (ATDs) of the ions were collected by monitoring their intensities as a function of time.

HCN is prepared by firstly adding 8 g of sodium cyanide (NaCN) (Sigma-Aldrich, 97%) into a 500 ml stainless steel bubbler. The bubbler is tightly closed and evacuated off air under liquid nitrogen temperature. Then 4 ml of ultra high pure sulfuric acid (H_2SO_4) (Aldrich, 99.999%) are added through a 4 cm stainless steel tube extension of the inlet valve of the bubbler. Then, the sulfuric acid is allowed to get into the bubbler as a result of pressure difference and to react with the sodium cyanide salt. HCN evolves when the bubbler is allowed to warm up to room temperature.¹⁶⁴ The pressure in the HCN line is monitored by a baratron (MKS-626A).

For the following association reaction:



where $R=H, CH_3$ for HCN and CH_3CN , respectively.

Equilibrium establishment is verified when:

(1) A constant ratio of the integrated intensity of the product to the reactant ions is maintained when the residence time is varied at constant pressure and temperature. This confirms the equilibrium establishment regardless the reaction time.

(2) ATDs of the reactant and product ions are identical indicating equal residence times.

If the equilibrium conditions are well-established, the equilibrium constant, K_{eq} , can be measured using equation (6.2):

$$K_{eq} = \frac{[C_6H_6^+.(RCN)_n]}{[C_6H_6^+.(RCN)_{n-1}][RCN]} = \frac{I[C_6H_6^+.(RCN)_n]}{I[C_6H_6^+.(RCN)_{n-1}].P_{RCN}} \quad (6.2)$$

$$R \ln K_{eq} = \frac{-\Delta H^\circ}{T} + \Delta S^\circ \quad (6.3)$$

where $I[C_6H_6^+.(RCN)_{n-1}]$, $I[C_6H_6^+.(RCN)_n]$ are the integrated intensities of ATDs of the reactant and product cluster ions, respectively and P_{RCN} is the pressure of HCN or CH_3CN in atmosphere. The equilibrium constant, K_{eq} , is measured at different drift cell temperatures and from van't-Hoff plots (equation (6.3)), ΔH° and ΔS° values are obtained from the slope and intercept, respectively. The measured values are at least three measurements average.

6.2.2. Theoretical Calculations

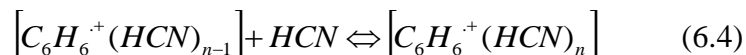
Density functional theory (DFT) calculations have been employed at the B3LYP and M06-2X levels using Gaussian 03 and Gaussian 09 packages, respectively.^{118,119} DFT calculations at these calculation levels have been widely used efficiently in the literature and showed great reliability.^{123,165} All the geometry optimizations and energy calculations were performed using a 6-311++G(d,p) basis set. Frequency calculations have been performed for all the optimized geometries at the same levels of theory to obtain the zero point vibrational energy (ZPVE) and to verify the absence of any imaginary frequencies. Therefore, all the calculated energies are corrected for ZPVE. In addition, total spin $\langle s^2 \rangle = 0.75-0.76$ which confirms the lack

of any spin contamination.⁶² Moreover, the counterpoise method has been used to correct the calculated energies for the basis-set superposition error (BSSE).¹²²

6.2.3. Benzene⁺(HCN)_n Cluster System

6.2.3.1. Mass-Spectra

Figure 31 displays a comparison of the product distributions after injecting C₆H₆⁺ into (0.08-0.11) Torr of pure HCN gas at different temperatures between 298 K and 175 K. The study was stopped at 175 K because it is the lowest achievable temperature before freezing of HCN.¹⁶⁴ At 298 K, the main observed ions were C₆H₆⁺(HCN)_n; where n =0-2. At lower temperatures, the population is shifted to higher clusters, following the usual association trends. The main observed products at 175 K were C₆H₆⁺(HCN)_n; n=3,4. These ions are formed according to the association reaction (6.4):



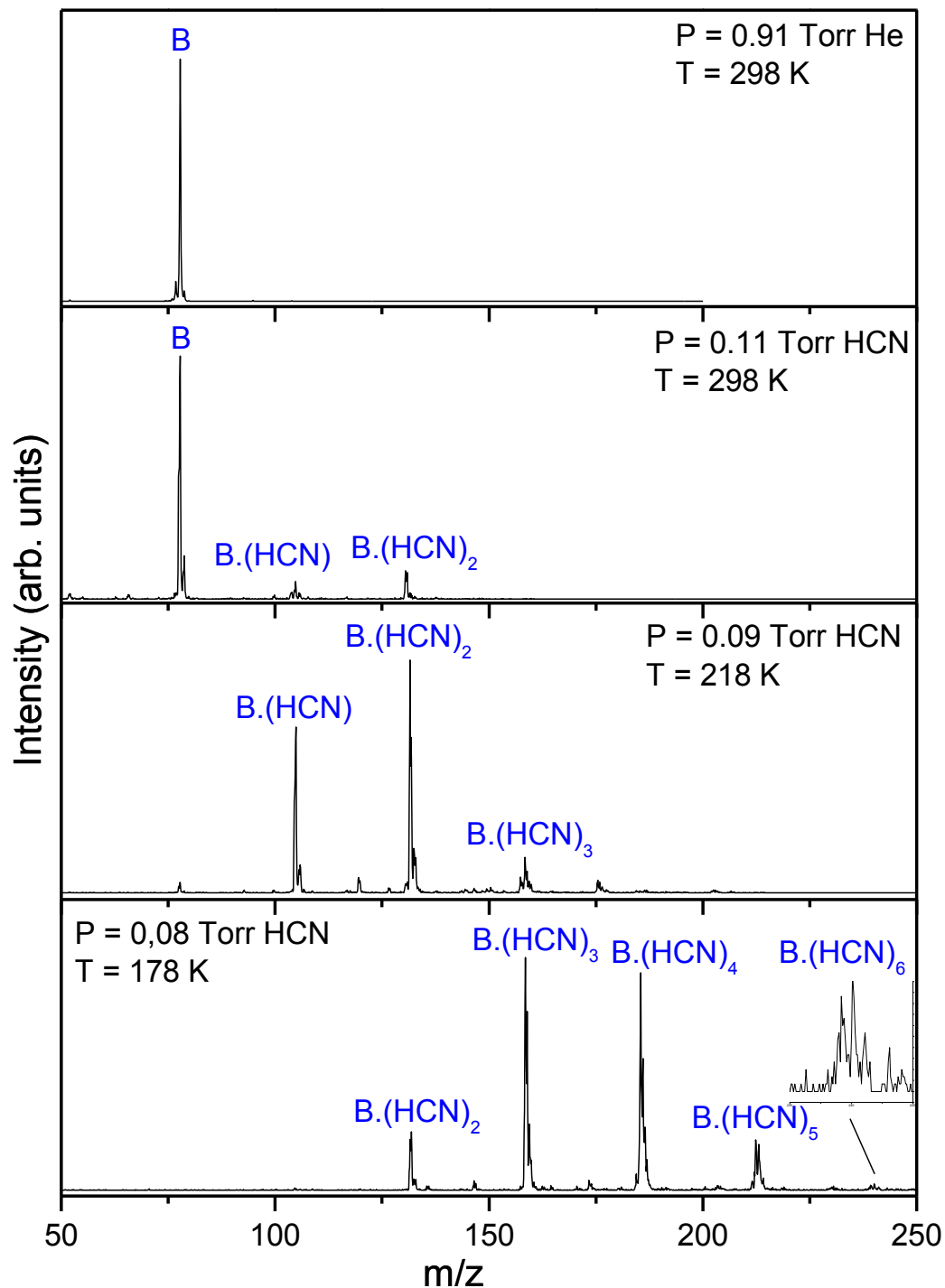


Figure 31. Mass-spectra resulting from injecting benzene radical cation in the mass-selection mode using injection energy of 13.8 eV (lab) into the drift cell which contains pure hydrogen cyanide gas and by applying a drift field of 4 V/cm. The drift cell temperature and pressure are varied as indicated

6.2.3.2. Thermochemistry measurements and structural implications:

Thermochemical studies were done upon injecting the mass-selected $C_6H_6^+$ using 14 eV injection energy into a mixture of HCN and He gases in the reaction cell upon applying weak field of 4 V/cm. The displayed ATDs illustrated in Figure 32 show very good matching among the reactant and product cations. Therefore, they are in equilibrium state. ATDs are displayed in two sets as the bigger cluster ions were observed after partial disappearance of the smaller ones as can be seen in Figure 31.

Equilibrium constants, K_{eq} , were measured at different temperatures using equation (6.5), which yielded van't-Hoff plots shown in Figure 33. van't-Hoff plots resulted in ΔH° and ΔS° values obtained from the slope and intercept, respectively.

$$K_{eq} = \frac{I[C_6H_6^+(HCN)_n]}{I[C_6H_6^+(HCN)_{n-1}] \cdot P_{HCN}} \quad (6.5)$$

where $I[C_6H_6^+(HCN)_{n-1}]$, $I[C_6H_6^+(HCN)_n]$ are the integrated intensities of ATDs of the reactant and product cluster ions, respectively and P_{HCN} is the pressure of HCN, in atmosphere.

Table 24 provides the experimentally measured ΔH° and ΔS° . The consecutive binding energies follow the usual decreasing trends. This behavior is expected for association reactions as a result of charge delocalization and the repulsion among added HCN molecules.²² Moreover, the entropy loss values (18-22 cal/mol. K) are expected for hydrogen bonds formation where internal rotation and low frequency vibrations are retained.²² Theoretically calculated values were found to match the experimental results excellently. Thus, we consider the B3LYP/6-311++G(d,p) calculation level to be satisfactory for our computation jobs.

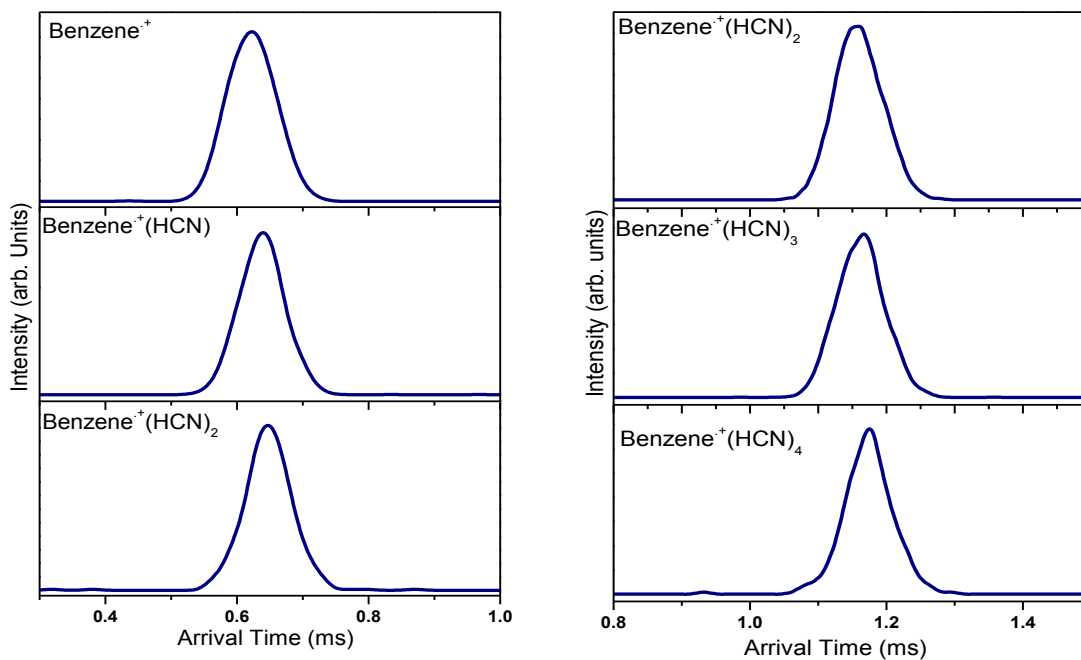


Figure 32. ATDs of benzene (HCN)_n; n=0-4 collected upon injecting mass-selected benzene radical cations into the drift cell which contains hydrogen cyanide gas mixed with helium buffer gas using an injection energy of 13.8 eV (lab.) and by applying a drift field of 4 V/cm. (**Left**) ATDs matching of n=0-2, collected at 263 K. (**Right**) ATDs matching of n=2-4, collected at 210 K

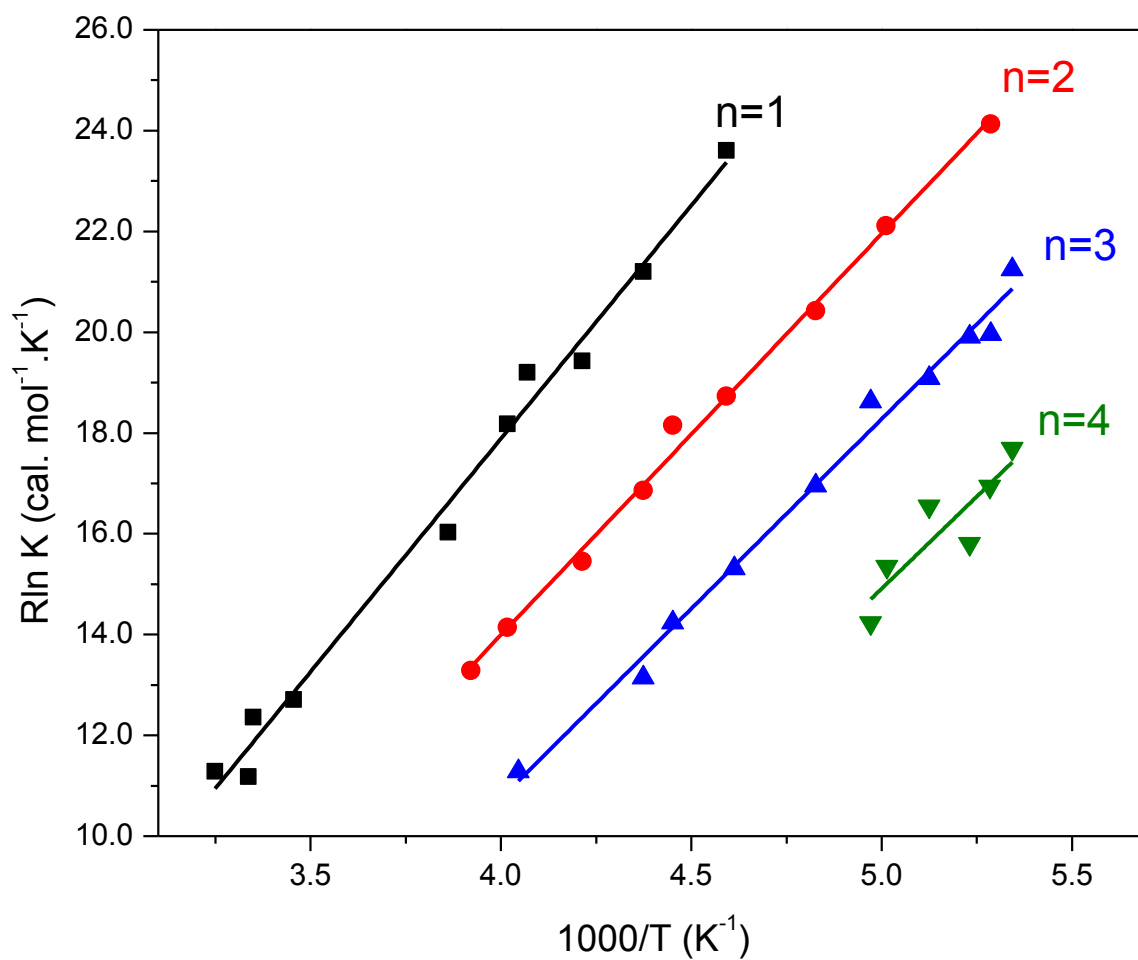


Figure 33. van't- Hoff plots yielded by injecting benzene radical cations in the mass-selection mode into a mixture of hydrogen cyanide and helium gases using an injection energy of 14.4 eV (lab. frame) and by applying a drift field of 4 V/cm. The temperature of the reaction cell was varied between 187 K and 333 K.

n	$-\Delta H^{\circ a}$	$-\Delta S^{\circ b}$	BE ^c	BE ^d
1	9.2	19.1	9.4	9.2
2	8.0	17.8	8.2	7.8
3	7.5	19.4	7.5	7.3
4	7.3	21.7	7.3	7.1

^a $\Delta H^{\circ}_{n-1,n}$ units are kcal/mol, ^b $\Delta S^{\circ}_{n-1,n}$ units are cal/mol. K, ^c Binding energy calculated by B3LYP/6-311++G(d,p); units are kcal/mol (corrected for ZPE), and ^d Binding energy calculated by B3LYP/6-311++G(d,p); units are kcal/mol (with BSSE counterpoise correction included).

Table 24. Measured thermochemistry ($-\Delta H^{\circ}_{n-1,n}$ and $-\Delta S^{\circ}_{n-1,n}$) of the formation of $C_6H_6^+.(HCN)_n$ clusters; with $n=1-4$ and the corresponding calculated binding energy values at the B3LYP/6-311++G (d,p)

6.2.3.3. Theoretical Calculations of the solvated benzene radical cations by HCN molecules

6.2.3.3.1. B3LYP/6-311++G(d,p) level calculations

Tables (25-28) display the optimized structures of the most stable solvated benzene isomers, $C_6H_6^+(HCN)_n$ ($n=1-4$), calculated by the hybrid DFT B3LYP method, using the standard basis-set of 6-311++G(d,p). Moreover, Table 24 displays the resulting binding energies of the lowest energy isomers corrected for (ZPVE) and for (BSSE).¹²² It is obvious that the theoretically calculated binding energy values are indistinguishable from the experimental ones within the experimental accuracy ($\Delta H^{\circ}_{n-1,n} \pm 1.0$ kcal mol⁻¹). Therefore, we consider this level of theory to be enough for our computational jobs.

C₆H₆⁺(HCN): The lowest energy isomer has a bifurcated structure with HCN bonding to two CH hydrogen atoms by 2.5 Å and 2.6 Å bonds as shown in Table 25. This geometry is very similar to that previously predicted for C₆H₆⁺(H₂O). As depicted in Table 24, its corrected binding energy is indistinguishable from the experimentally measured value. The second most stable isomer (1-b) shown in Table 25 is about 0.4 kcal/ mol higher in energy than (1-a). This structure shows the HCN molecule's nitrogen atom bonding to an aromatic hydrogen atom via a hydrogen bond of 2.2 Å forming a planar complex. The third most stable isomer (1-c) is degenerate with (1-b). It shows the HCN molecule to be nearly perpendicular to the benzene cation plane by 76.5° angle and binds to an aromatic carbon by 2.7 Å bond, as shown in Table 25.

C₆H₆⁺(HCN)₂: Upon addition of the second HCN molecule at the B3LYP/6-311++G(d,p) level, the lowest energy isomer (2-a) shows external solvation where the second HCN molecule binds to the first one rather than binding to the C₆H₆⁺ core ion. As shown in Table 26, the second HCN molecule binds to the first one by a 2.1 Å hydrogen bond forming a linear chain.

The second most stable isomer (2-b) shown in Table 26 is only about 0.1 kcal/mol higher in energy than (2-a). Interestingly, it shows internal solvation in which both of HCN molecules are hydrogen bonded to the C₆H₆⁺ aromatic hydrogen atoms. The second HCN molecule binds to an aromatic CH hydrogen atom by 2.2 Å bond.

The third most stable isomer (2-c) is 0.2 kcal/ mol less stable than (2-a). As shown in Table 26, internal solvation pattern is again employed in (2-c). However, (2-c) shows a bifurcated structure in which the second HCN molecule is bound to aromatic hydrogen atoms by 2.4 Å and 2.8 Å.

$C_6H_6^+(HCN)_3$: The third HCN molecule addition shows preference for the internal solvation, see structure (3-a) in Table 27. In (3-a), the third HCN molecule's nitrogen atom binds to an aromatic hydrogen atom by 2.2 Å hydrogen bond. This behavior is very similar to $C_6H_6^+(H_2O)_n$ example in which internal hydration was preferred starting at $C_6H_6^+(H_2O)_3$.

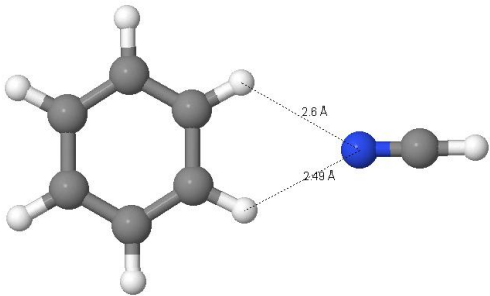
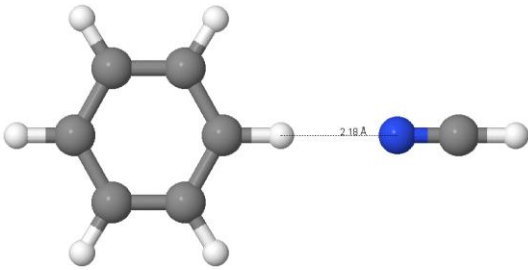
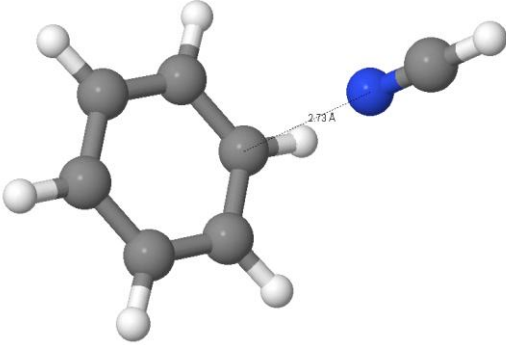
The second most stable isomer (3-b) shows external solvation pattern where the three HCN molecules form a linear cluster as displayed in Table 27. This structure is predicted to be 0.7 kcal/ mol higher in energy than (3-a). The third HCN molecule is hydrogen bonded to the second HCN molecule by 2.1 Å hydrogen bond.

(3-c) shows internal solvation where the third HCN molecule adds to CH aromatic hydrogen by a 2.3 Å hydrogen bond. This isomer is 0.9 kcal/ mol higher in energy than (3-a).

$C_6H_6^+(HCN)_4$: The addition of four HCN molecules to $C_6H_6^+$ showed dominance of the internal solvation pattern as shown in Table 28. (4-a) is the most stable $C_6H_6^+(HCN)_4$ isomer; it has two HCN molecules bound to the core $C_6H_6^+$ from each side. The fourth HCN molecule binds to the third by a 2.1 Å hydrogen bond.

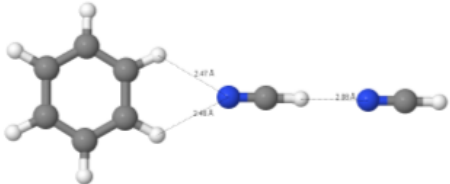
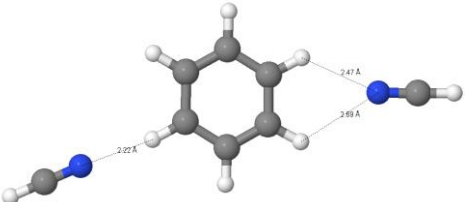
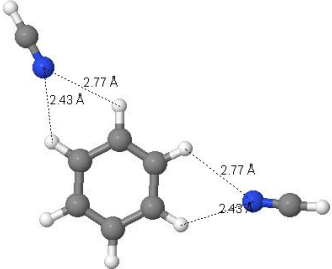
(4-b) is the second most stable isomer; it is 0.4 kcal/mol higher in energy than the lowest energy isomer, (4-a). As displayed in Table 28, (4-b) has a sort of symmetric structure, in which the fourth HCN molecule binds to $C_6H_6^+$ aromatic hydrogen atom by a 2.3 Å bond.

(4-c) is the third most stable isomer. It is less stable than (4-a) by 0.6 kcal/mol. It shows three HCN molecules hydrogen bonded to each other forming a linear cluster chain from one side while having the fourth molecule binds to an aromatic CH hydrogen atom by 2.2 Å hydrogen bond.

Name	Optimized Structure	Relative Energy ^a	Binding energy ^b
1-a		0.0	9.4 (*9.2)
1-b		0.4	9.0 (*8.8)
1-c		0.4	9.0 (*8.5)

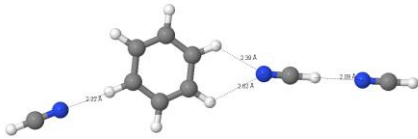
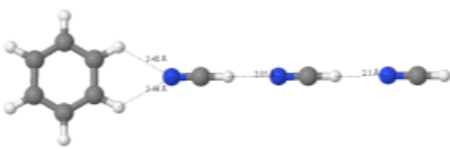
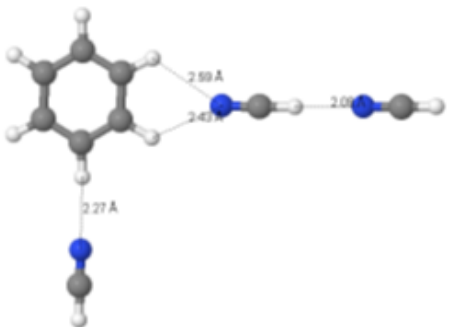
^a in kcal/mol (corrected for ZPE) ^b in kcal/mol *(corrected for ZPE and BSSE)

Table 25. Theoretically optimized structures using B3LYP/6-311++G(d,p) of $[C_6H_6^+(HCN)]$

Name	Optimized Structure	Relative Energy ^a	Binding energy ^b
2-a		0.0	8.2 (*7.8)
2-b		0.1	8.1 (*7.6)
2-c		0.2	8.0 (*7.6)

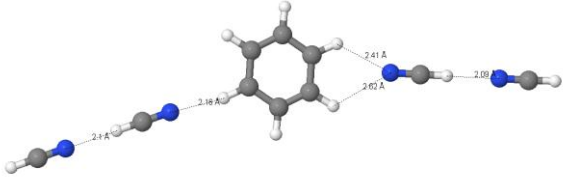
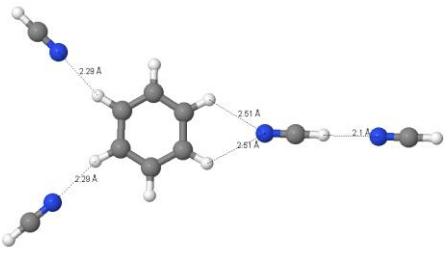
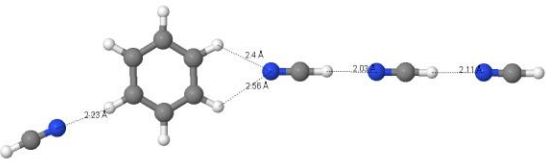
^a in kcal/mol (corrected for ZPE) ^b in kcal/mol *(corrected for ZPE and BSSE)

Table 26. Theoretically optimized structures using B3LYP/6-311++G(d,p) of $[C_6H_6^+(HCN)_2]$

Name	Optimized Structure	Relative Energy ^a	Binding energy ^b
3-a		0.0	7.5 (*7.3)
3-b		0.7	6.8 (*6.6)
3-c		0.8	6.6 (*7.1)

^a in kcal/mol (corrected for ZPE) ^b in kcal/mol *(corrected for ZPE and BSSE)

Table 27. Theoretically optimized structures using B3LYP/6-311++G(d,p) of $[C_6H_6^+(HCN)_3]$

Name	Optimized Structure	Relative Energy ^a	Binding energy ^b
4-a		0.0	7.3 (*7.1)
4-b		0.4	6.9 (*6.7)
4-c		0.6	6.7 (*6.5)

^a in kcal/mol (corrected for ZPE) ^b in kcal/mol *(corrected for ZPE and BSSE)

Table 28. Theoretically optimized structures using B3LYP/6-311++G(d,p) of $[C_6H_6^+(HCN)_4]$

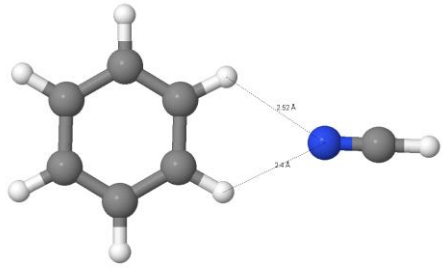
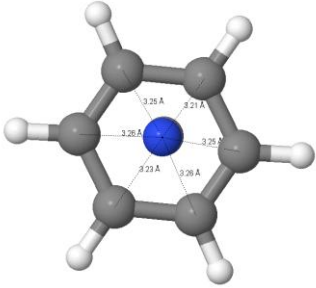
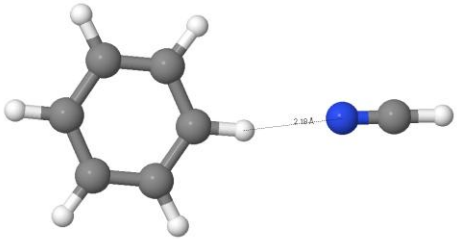
6.2.3.3.2. M06-2X/6-311++G(d,p) level calculations

In order to validate the B3LYP/6-311++G(d,p) calculation level, we used the M06-2X method which is known to be very reliable functional especially in non covalent interactions.⁶¹ The results are shown in Table 29.

The lowest energy isomer for $C_6H_6^+(HCN)$ has the expected bifurcated structure, in which HCN bonding to two CH aromatic hydrogen atoms by 2.4 Å and 2.5 Å bonds. This structure is very similar to that predicted by the B3LYP/6-311+G(d,p). Although the predicted corrected energy is a 1.4 kcal/mol higher in the case of M06-2X functional than in the B3LYP functional case, the relatively large uncertainty in the experimental value (± 1 kcal/mol) rules out any meaningful discussion of the accuracy of the calculated binding energies using the B3LYP and the M06-2X functions. The excellent agreement of B3LYP/6-311+G(d,p) predicted binding energy values with experimental values suggest that M06-2X/6-311+G(d,p) level overestimates the binding energies. B3LYP/6-311+G(d,p) is more suitable for our calculations.

The second lowest energy isomer (1-b) is only 0.2 kcal/mol higher in energy than the most stable isomer (1-a). It has a symmetric structure in which the Nitrogen pole of HCN molecule is bonded to the $C_6H_6^+$ ring by ion-dipole interaction forces. The distance between the N-atom and any aromatic C-atom is 3.2 Å.

The hydrogen bonding isomer for $C_6H_6^+(HCN)$ was predicted to be 0.8 kcal/mol higher in energy than (1-a) at the M06-2X/6-311++G(d,p); as displayed as structure (1-c) in Table 29. It shows the HCN molecule to be hydrogen bonded to an aromatic hydrogen atom via 2.2 Å hydrogen bond.

Name	Optimized Structure	Relative Energy ^a	Binding energy ^a
1-a		0.0	10.8 (*10.6)
1-b		0.2	10.6 (*10.2)
1-c		0.8	9.8 (*9.5)

^a M06-2X/6-311++G(d,p) results in kcal/mol(corrected for ZPE) * corrected for BSSE and ZPE

Table 29. $[C_6H_6]^+$ (HCN) predicted structures at the M06-2X/6-311++G(d,p) level. Binding energies are corrected for ZPE and BSSE

6.2.4. Benzene⁺/CH₃CN reaction study

6.2.4.1. Mass-Spectra

For comparison, solvation study of the benzene radical cation by acetonitrile (CH₃CN) was carried out in our laboratory and reported here. CH₃CN has only one bonding site and thus, it can't form linear hydrogen bonded chains due to the presence of the methyl group.⁷³ Figure 34 displays a comparison of the product distribution at different reaction cell temperatures. These spectra are obtained upon injecting C₆H₆⁺ in the mass-selection mode into the drift cell which contains pure acetonitrile vapor. The product distribution of [C₆H₆⁺ (CH₃CN)_n] was shifted from n=1 at 419 K to be n=3,4 at 226 K, following the usual association trends.

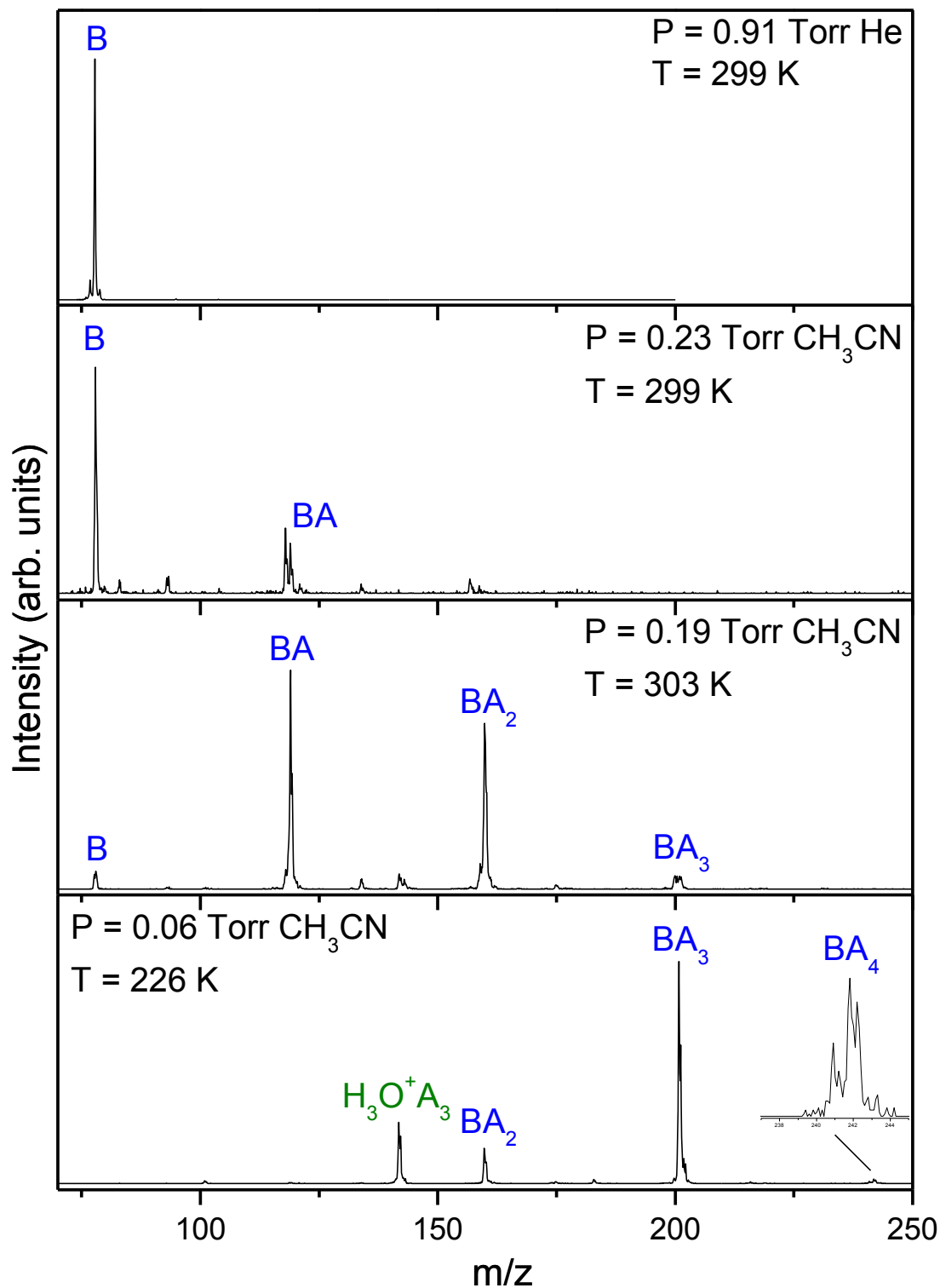
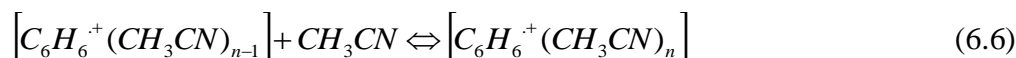


Figure 34. Mass-spectra obtained upon injecting benzene radical cation in the mass selection mode using injection energy of 16 eV (lab. frame) and 5 V/cm drift cell field. The reaction cell temperature and pressure are varied as indicated

6.2.4.2. Thermochemistry measurements and structural implications:

The association reaction under investigation is:



Thermochemical studies were carried out upon injecting the mass-selected $C_6H_6^+$ into 0.06-0.23 Torr of pure CH_3CN vapor in the reaction cell upon applying weak field of 3-5 V/cm. Equilibrium state is ensured to be established as the intensity ratio $[C_6H_6^+(CH_3CN)_n]/C_6H_6^+(CH_3CN)_{n-1}$ is constant regardless the reaction time, which is controlled by the applied field. Equilibrium constants, K_{eq} , were measured at different temperatures using equation (6.7), which yielded van't-Hoff plots shown in Figure 35. van't-Hoff plots resulted in ΔH° and ΔS° values obtained from the slope and intercept, respectively.

$$K_{eq} = \frac{I[C_6H_6^+(CH_3CN)_n]}{I[C_6H_6^+(CH_3CN)_{n-1}] \cdot P_{CH_3CN}} \quad (6.7)$$

Table 30 provides the experimentally measured ΔH° and ΔS° values. The consecutive binding energies follow the usual decreasing trends which can be expected for association reactions as a result of charge delocalization and the repulsion among added CH_3CN molecules.²² Moreover, the entropy loss values (18-22 cal. mol⁻¹. K⁻¹) are expected for the formation of hydrogen bonds where internal rotation and low frequency vibrations are retained.^{22,84} Theoretically calculated values for the lowest energy isomers employing B3LYP/6-311++G(d,p) level are shown in Table 30 as well.

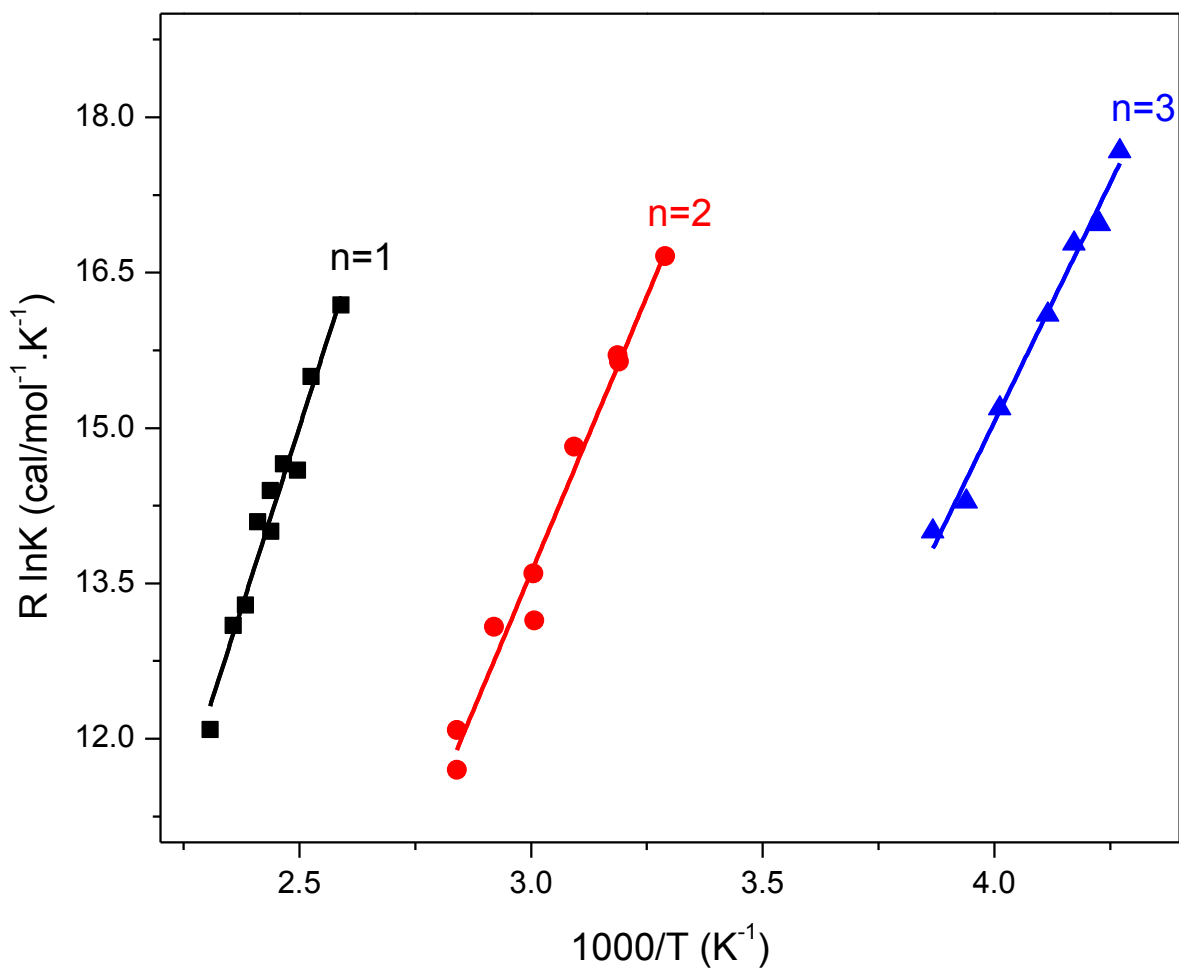


Figure 35. van't-Hoff plots for the association equilibria (6.6) obtained by injecting mass-selected benzene radical cations $C_6H_6^+$ into pure acetonitrile (CH_3CN) vapor. The reaction cell temperature was varied between 234 K and 428 K. Thermochemical measured values are shown in Table 30

n	$-\Delta H^\circ$ ^a	$-\Delta S^\circ$ ^b	BE ^c	BE ^d
1	14.0	19.9	13.0	12.7
2	10.7	18.4	10.5	10.6
3	9.2	21.8	9.2	9.7

^a $\Delta H^\circ_{n-1,n}$ units are kcal/mol, ^b $\Delta S^\circ_{n-1,n}$ units are cal/mol.K, ^c Binding energy calculated by B3LYP/6-311++G(d,p). Units are kcal/mol, and ^d Binding energy calculated by B3LYP/6-311++G(d,p). Units are kcal/mol (with BSSE counterpoise correction included)

Table 30. Measured Thermochemistry ($-\Delta H^\circ_{n-1,n}$ and $-\Delta S^\circ_{n-1,n}$) of the formation of $C_6H_6^+.(CH_3CN)_n$ cluster ions; with n=1-3 and the corresponding calculated binding energy values

6.2.4.3. Theoretical Calculations of the solvated benzene radical cations by CH_3CN molecules

6.2.4.3.1. B3LYP/6-311++G(d,p) level calculations

Tables (31-33) display the optimized structures of the most stable solvated benzene isomers, $C_6H_6^+(CH_3CN)_n$, with n=1-3, calculated by the hybrid DFT B3LYP/6-311++G(d,p) method. Moreover, they include the resulting binding energies corrected for zero-point vibrational energy (ZPVE) and for basis-set superposition error (BSSE) corrected by counterpoise procedure.¹²²

$C_6H_6^+(CH_3CN)$: The lowest energy isomer has a bifurcated structure with CH_3CN bonding to two aromatic CH hydrogen atoms by 2.4 Å and 2.5 Å bonds as shown as structure (1-a) in Table

31. This geometry is very similar to that previously predicted for $C_6H_6^+(H_2O)$ and $C_6H_6^+(HCN)$.^{20,33}

The second most stable (1-b) isomer shown in Table 31 is nearly degenerate with 1-a; it shows the CH_3CN molecule to be nearly perpendicular to the benzene cation plane by 78.4° angle and it binds to an aromatic carbon by 2.6 \AA bond.

The third most stable isomer is (1-c). This structure shows the CH_3CN molecule's nitrogen atom bonding to an aromatic hydrogen atom via a hydrogen bond of 2.1 \AA . Moreover, the calculation at B3LYP/6-311++G (d,p) level shows (1-c) to be higher in energy than (1-a) by about 0.7 kcal/mol.

$C_6H_6^+(CH_3CN)_2$: Upon addition of the second CH_3CN molecule, the most stable structure at the B3LYP/6-311++G(d,p) level shows dominance of internal solvation which can be attributed to the blocked structure of CH_3CN .^{73,78} The most stable theoretically predicted isomer for $C_6H_6^+(CH_3CN)_2$ is (2-a). In (2-a), the second CH_3CN molecule is hydrogen bonded to the $C_6H_6^+$ aromatic hydrogen atom in the β - position from the first binding site. The new hydrogen bond is 2.2 \AA as shown in Table 32.

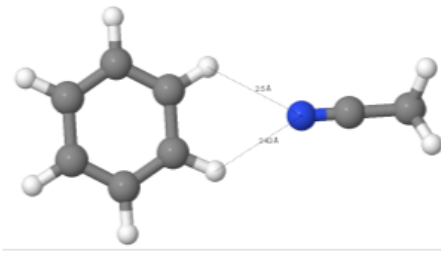
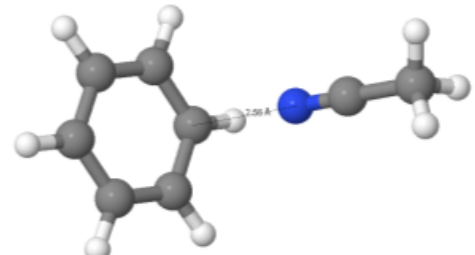
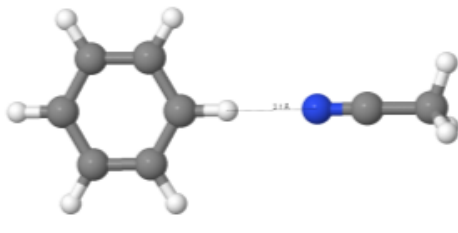
(2-b) isomer is 1.0 kcal/mol higher in energy with respect to (2-a). (2-b) has the second CH_3CN molecule hydrogen bonded to the $C_6H_6^+$ aromatic hydrogen atom in the α -position from the first aromatic binding site. The hydrogen bond is predicted to be of 2.2 \AA length.

The third most stable $[C_6H_6^+(CH_3CN)_2]$ isomer (2-c) is 1.2 kcal/mol less stable than (2-a). As shown in Table 32, (2-c) shows two bifurcated bonds to CH-aromatic hydrogen atoms of benzene⁺. The second CH_3CN molecule is bound to aromatic hydrogen atoms by 2.4 \AA and 2.7 \AA .

C₆H₆⁺(CH₃CN)₃: As displayed in Table 33, the third CH₃CN molecule addition shows dominance of the internal solvation where the third CH₃CN molecule's nitrogen atom binds to two aromatic hydrogen atoms forming a bifurcated structure via 2.6 Å and 2.5 Å hydrogen bonds, as shown in structure (3-a).

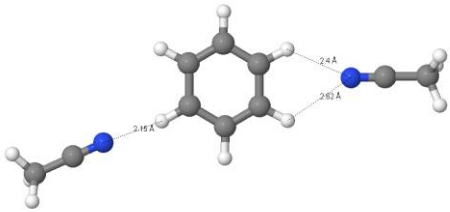
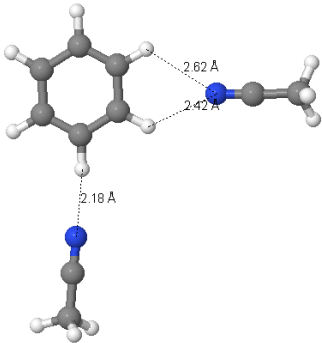
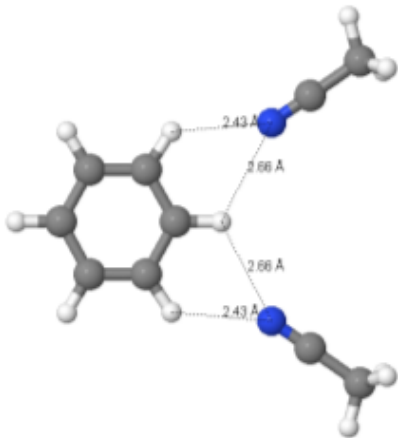
The second most stable isomer, (3-b); displayed in Table 33 has a bifurcated structure as well. This structure is about 0.5 kcal/mol higher in energy than (3-a). The third CH₃CN molecule is hydrogen bonded to the CH aromatic hydrogen by 2.2 Å hydrogen bonds.

In (3-c) structure, the third CH₃CN molecule adds to CH aromatic hydrogen atom by a 2.2 Å hydrogen bond. This isomer is 0.6 kcal/ mol higher in energy than (3-a).

Name	Optimized Structure	Relative Energy ^a	Binding energy ^b
1-a		0.0	13.0 (*12.7)
1-b		0.0	13.0 (*12.4)
1-c		0.7	12.3 (*12.0)

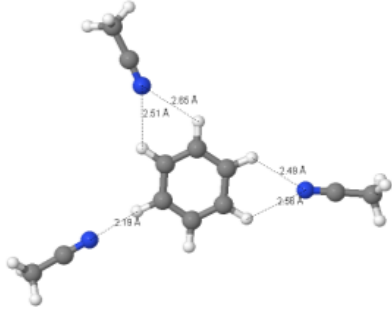
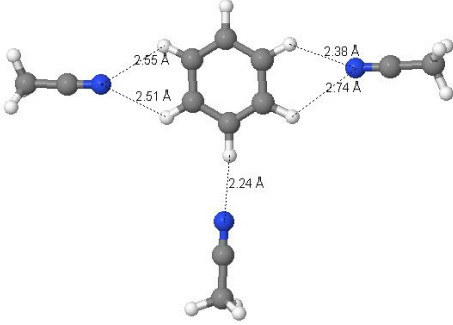
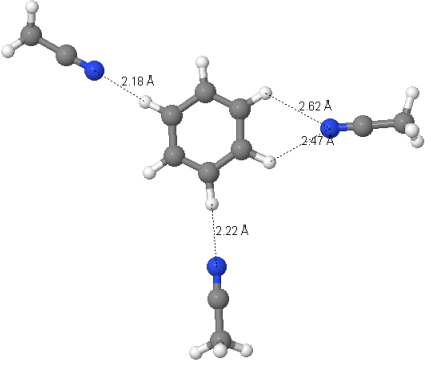
^a in kcal/mol (corrected for ZPE) ^b in kcal/mol (*corrected for ZPE and BSSE)

Table 31. Theoretically optimized structures using B3LYP/6-311++G(d,p) of $[C_6H_6^+(CH_3CN)]$

Name	Optimized Structure	Relative Energy ^a	Binding energy ^b
2-a		0.0	10.5 (*10.6)
2-b		1.0	9.5 (*9.5)
2-c		1.2	9.3 (*9.1)

^a in kcal/mol (corrected for ZPE) ^b in kcal/mol (*corrected for ZPE and BSSE)

Table 32. Theoretically optimized structures using B3LYP/6-311++G(d,p) of $[\text{C}_6\text{H}_6^+(\text{CH}_3\text{CN})_2]$

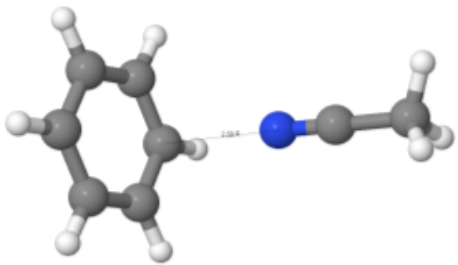
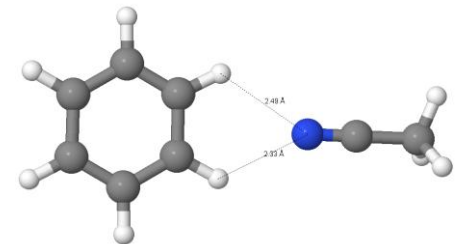
Name	Optimized Structure	Relative Energy ^a	Binding energy ^b
3-a		0.0	9.2 (*9.7)
3-b		0.6	8.6 (*9.2)
3-c		0.6	8.6 (*8.3)

^a in kcal/mol (corrected for ZPE) ^b in kcal/mol (*corrected for ZPE and BSSE)

Table 33. Theoretically optimized structures using B3LYP/6-311++G(d,p) of $[C_6H_6^+(CH_3CN)_3]$

6.2.4.3.2. M06-2X/6-311++G(d,p) level calculations

In order to validate the B3LYP/6-311++G(d,p), we used the M06-2X method which is recognized to be very reliable functional especially in non covalent interactions.⁶¹ M06-2X/6-311++G(d,p) calculations of $C_6H_6^+(CH_3CN)$ have resulted in the optimized structures and energies displayed in Table 34. In the lowest energy isomer (1-a), the CH_3CN binds nearly perpendicular (80°) on the $C_6H_6^+$ plane by a 2.6 Å bond. The bifurcated structure was predicted to be 1.0 kcal/mol higher in energy than (1-a); the CH_3CN molecule binds to two aromatic CH hydrogen atoms via 2.3 Å and 2.5 Å hydrogen bonds in (1-b).

Name	Optimized Structure	Relative Energy ^a	Binding energy ^a
1-a		0.0	15.1 (*14.4)
1-b		1.0	14.2 (*13.8)

^a M06-2X/6-311++G(d,p) results in kcal/mol(corrected for ZPE) * corrected for BSSE and ZPE

Table 34. [$C_6H_6^+(HCN)$] predicted structures at the M06-2X/6-311++G(d,p) level. Binding energies are corrected for ZPE and BSSE

6.2.4.3.3. Charge transfer from benzene⁺ to (RCN)_n

The evolution of the charge distribution on the C₆H₆⁺ moiety versus the solvent moiety (HCN)_n is monitored by employing the natural bond orbital (NBO) charge distribution from Gaussian 03 package.¹¹⁹ As displayed in Figure 36, minor charge is transferring from the C₆H₆⁺ to HCN molecules. It shows that the very little charge is transmitted from the C₆H₆⁺ moiety to the solvent moiety slowly as the charge intensity on the cation core is reduced slightly to 98% after additions of four HCN molecules; which reflects the weakness of the interaction while the charge goes to 97% for C₆H₆⁺(CH₃CN)₃.

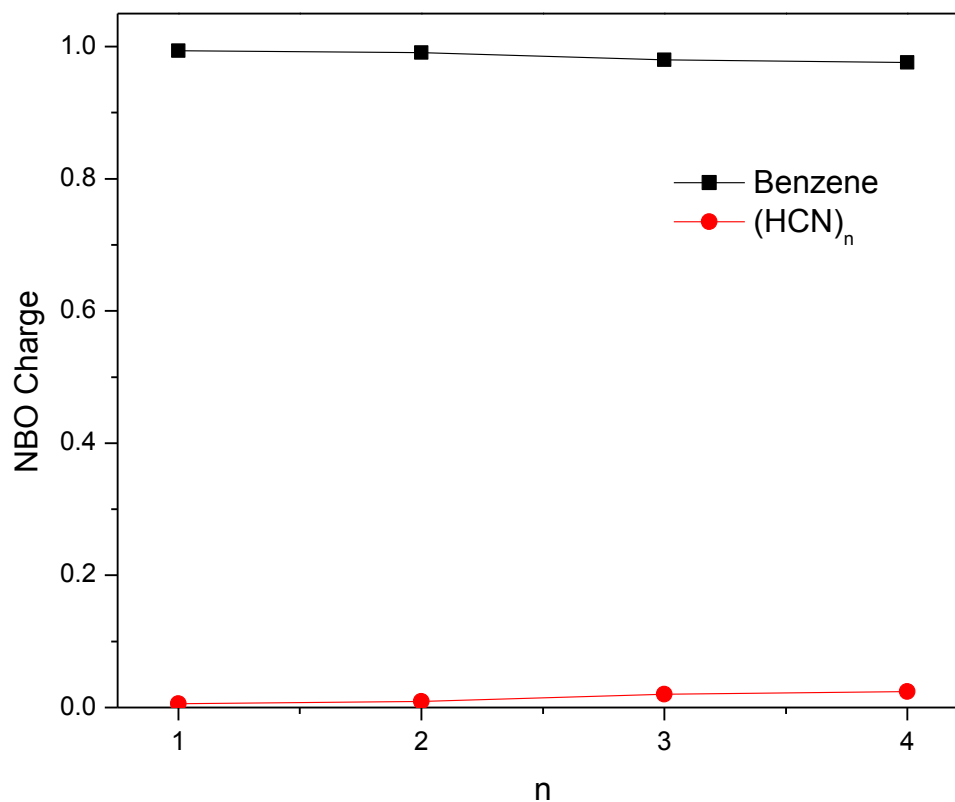


Figure 36. Charge distribution on both benzene⁺ versus (HCN)_n as solvation degree *n* is proceeding

6.3. Stepwise Solvation of Phenyl acetylene⁺ by HCN molecules in the gas-phase. Binding energies and structures of [Phenyl acetylene⁺ (HCN)_n] clusters

6.3.1. Introduction

Phenyl acetylene represents the simplest multifunctional molecule to investigate the competitive hydrogen bonding among the π -acceptors of benzene ring and the activated acetylenic C—H bond which acts as a σ -donor.¹²⁴ Therefore, in order to investigate the competitive solvation by HCN molecules of benzene versus acetylene, it is of paramount importance to examine the stepwise solvation of phenyl acetylene radical cation by several HCN molecules. In this study, the stepwise solvation of phenyl acetylene radical cations ($C_8H_6^+$) on a molecular level by several HCN molecules is reported. Thermochemical equilibrium studies have been utilized to measure the enthalpy and entropy changes accompanying the individual solvation steps. The solvation products of the form $[C_8H_6^+ (HCN)_n]$ were observed with $n=1-4$.

6.3.2. Experimental Section

The molecular ions of ($C_8H_6^+$) were formed by electron impact ionization using electron energy of 50-70 eV following the supersonic expansion of 40 psi (2.8 bar) of ultra high pure helium seeded with about 1-4% of phenyl acetylene vapor. The expansion occurs through a pulsed supersonic nozzle (500 μ m) to the source chamber which has 10^{-7} mbar background pressure. The phenyl acetylene sample was heated to 360 K to increase its vapor pressure.¹⁶⁶ $C_8H_6^+$ is mass-selected by the first quadrupole mass-filter and injected in (30-50 μ s pulses) into the drift cell which contains the neutral hydrogen cyanide gas (HCN) mostly in a mixture with helium buffer gas.⁷³ The temperature of the drift cell can be controlled better than ± 1 K using

four temperature controllers. The pressure can be controlled in the drift cell by using mass flow controllers (MKS # 1479A) within ± 1 mTorr.

6.3.3. Theoretical Calculations

Density functional theory (DFT) calculations have been utilized via the hybrid functional (B3LYP) using Gaussian03 package.¹¹⁹ All the geometry optimizations and energy calculations were performed using a 6-311++G(d,p) basis set. Frequency calculations have been performed for all the optimized geometries at the same level of theory to obtain the zero point vibrational energy (ZPVE) and to verify the absence of any imaginary frequencies. Therefore, all the calculated energies are corrected for ZPVE. In addition, the total spin $\langle s^2 \rangle = 0.75-0.76$ which confirms the lack of any spin contamination.⁶² Moreover, the counterpoise procedure has been used to correct the calculated energies for the basis-set superposition error (BSSE).¹²²

6.3.4. Results and Discussion

6.3.4.1. Thermochemistry measurements and structural implications

This study is interested in the association reaction between the mass-selected phenyl acetylene radical cations ($C_8H_6^+$) and hydrogen cyanide (HCN) molecules under equilibrium conditions (6.8). Thus, this study aims to measure the binding energies and the corresponding entropy changes accompanying the formation of the product ions of the form $C_8H_6^+(HCN)_n$ experimentally. DFT calculations at the B3LYP/6-311++G(d,p) level have been used to predict the lowest energy isomers and their corresponding binding energies.

Equilibrium establishment in association reaction (6.8) is verified when a constant ratio of the integrated intensity of the product to the reactant is maintained even if the residence time is varied at constant pressure and temperature. Moreover, equilibrium establishment could be

verified qualitatively when ATDs of the reactant and product ions are identical indicating equal residence times.



Thermochemical measurements were done at different temperatures upon injecting the mass-selected phenyl acetylene radical cation ($C_8H_6^+$) into the drift cell using low injection energy of 14 eV (laboratory frame). This injection energy is just enough to introduce the injected cations against the escaping flow of HCN gas from the entrance aperture of the drift cell. The resulting mass-spectra at different temperatures are shown below in Figure 37. The study has been stopped at 184 K because of hydrogen cyanide freezing temperature was reached. As displayed in Figure 37, at 298 K, the only observed ions are $C_8H_6^+(HCN)_n$; where $n=0,1$. At 194 K, the intensity is shifted to higher clusters; to $C_8H_6^+(HCN)_n$; where $n=1-4$; following the usual association reactions trends.

In order to check for equilibrium establishment, good test is to check for the matching among the ATDs of both the reactants and adducts indicating equal residence times. Good matching was found as can be seen in Figure 38.

Upon measuring the relative integrated intensities of the reactants and products for each sequential addition at different temperatures, the equilibrium constants have been measured, using equation (6.9):

$$K_{eq} = \frac{I[C_8H_6^+(HCN)_n]}{I[C_8H_6^+(HCN)_{n-1}] \cdot P_{HCN}} \quad (6.9)$$

where, $I[C_8H_6^+.(HCN)_{n-1}]$ and $I[C_8H_6^+.(HCN)_n]$ are the integrated intensities of ATDs of the reactant and product cluster ions, respectively and P_{HCN} is the pressure of HCN in atmosphere. The measured equilibrium constants were subsequently used to plot the van't-Hoff plots. The binding energies and entropy changes are obtained from the slope and intercept of van't-Hoff plots as can be seen in Figure 39 and Table 35.

The binding energy values and entropy changes follow the usual trends of decreasing as the degree of the solvation increases within the experimental accuracy.^{22,25} The measured binding energies (7- 10 kcal/mol) agree with the expected range for $CH^{\delta+} \cdots NCH$ interaction. In addition, these bond strengths are similar to that measured for phenyl acetylene hydration. Whereas, the entropy loss values (20-25 cal/mol.K) are expected for the formation of hydrogen bonds where internal rotation and low frequency vibrations are retained.^{18,22}

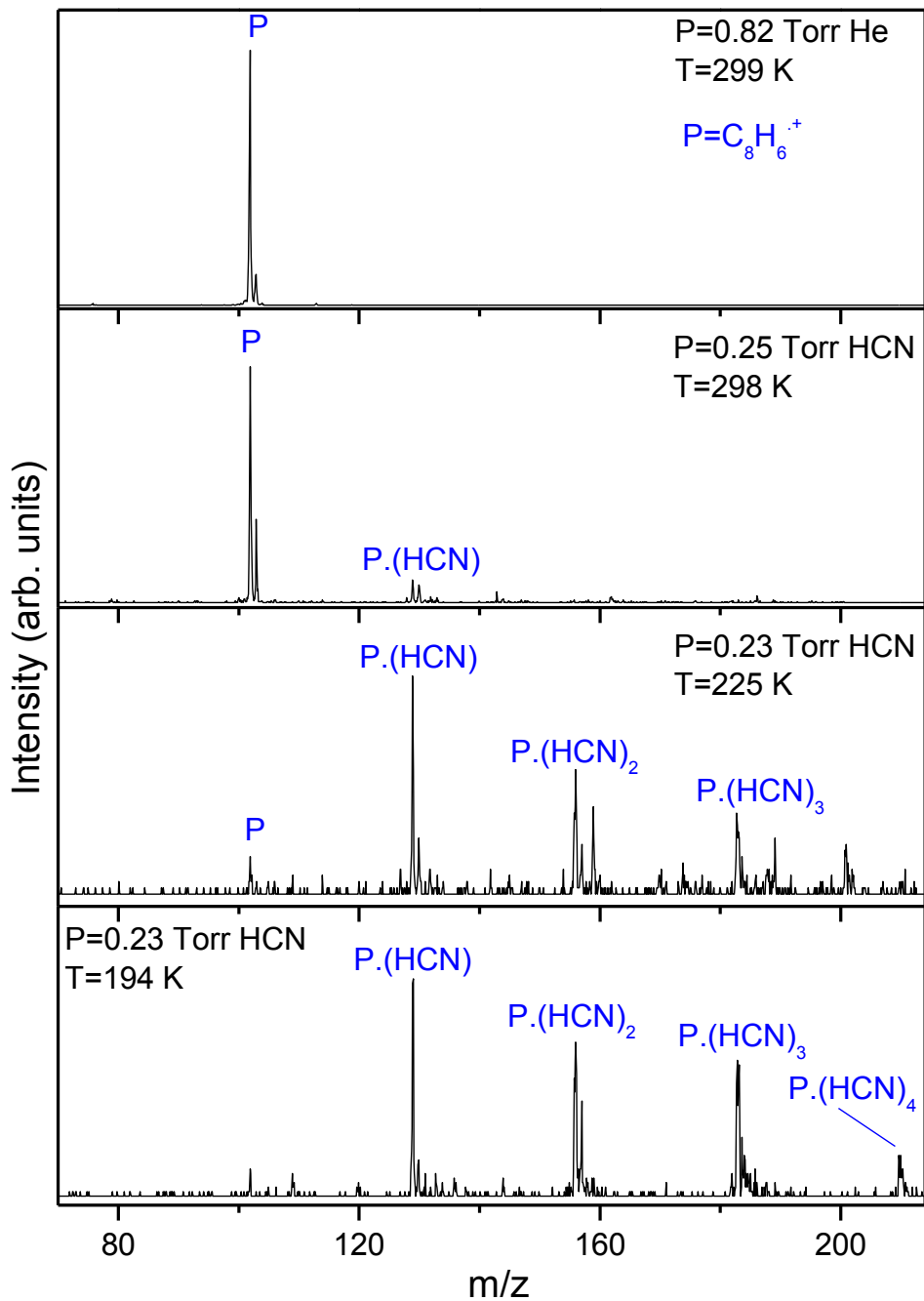


Figure 37. Mass-spectra resulting from injecting the phenyl acetylene radical cations into the drift cell containing different concentrations of hydrogen cyanide, the drift field is 4 V/cm while the injection energy was 14.4 eV (lab.). The drift cell temperature and pressure were varied as indicated

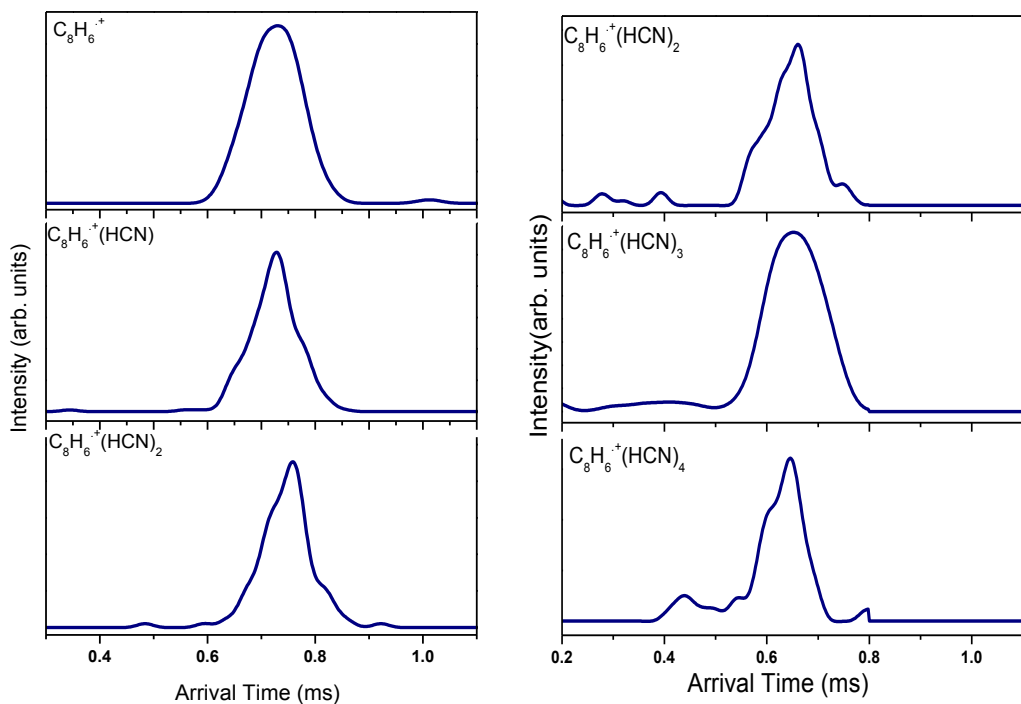


Figure 38. ATDs of [phenyl acetylene⁺(HCN)_n] (**Left**) where n=0-2; collected at 293 K with the drift cell containing 0.25 Torr of hydrogen cyanide. (**Right**) where n=2-4; collected at 194 K with the drift cell containing 0.23 Torr of hydrogen cyanide. The cell field and the injection energy were maintained at 4 V/cm and 14.4 (lab.), respectively

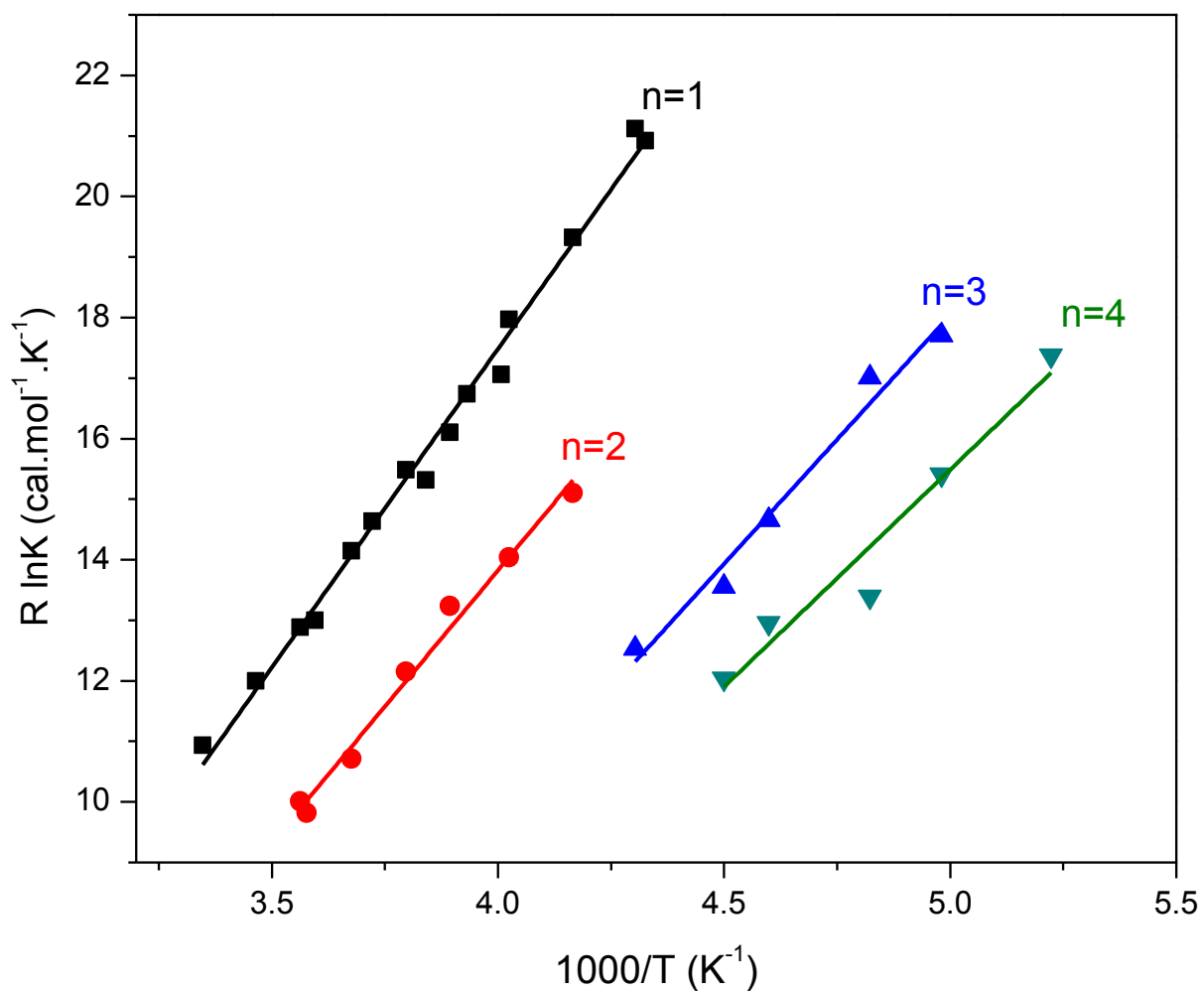


Figure 39. van't- Hoff plots for injecting C_8H_6^+ into HCN gas using an injection energy of 12.4 eV (lab.) and applied field of 4 V/cm. The drift cell temperature was varied between 184 K and 298 K

n	$-\Delta H^\circ$ ^a	$-\Delta S^\circ$ ^b	BE ^c	BE ^d
1	10.5	24.6	9.5	9.3
2	9.0	22.1	7.6	7.4
3	8.2	23.0	6.9	6.7
4	7.2	20.4	6.9	6.8

^a $\Delta H^\circ_{n-1,n}$ units are kcal/mol (± 1 kcal/ mol), ^b $\Delta S^\circ_{n-1,n}$ units are cal/mol.K (± 2 cal/mol. K), ^c Binding energy in kcal/ mol calculated by B3LYP/6-311++G(d,p) with ZPE included, and ^d Binding energy in kcal/ mol calculated by B3LYP/6-311++G(d,p) (with BSSE correction)

Table 35. Measured Thermochemistry ($-\Delta H^\circ_{n-1,n}$ and $-\Delta S^\circ_{n-1,n}$) of the formation of phenyl acetylene.(HCN)_n clusters; with n=1-4 and the corresponding calculated binding energy values

6.3.4.2. Theoretical Calculations of the solvated phenyl acetylene radical cations

The lowest energy isomers calculated structures at the B3LYP/6-311++G (d,p) for $[C_8H_6^+ (HCN)_{1-4}]$ clusters are shown in Tables (36-39). In addition, charge delocalization is tracked as the solvation (*n*) increases, as displayed in Figure 40, which shows that the charge stays on phenyl acetylene⁺ even upon addition of four HCN molecules.

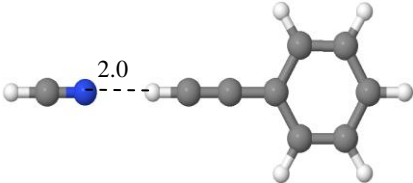
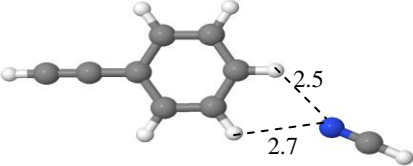
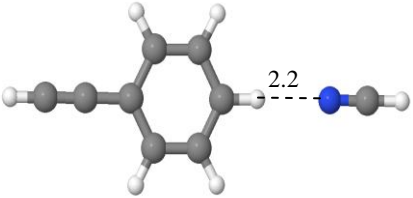
For the monosolvated phenyl acetylene cation $[C_8H_6^+ (HCN)]$, the lowest energy isomer (1-a). In which the N-atom of the HCN molecule is bound to the acetylenic CH by 2.0 Å hydrogen bond. (1-b) isomer is predicted to be at 1.7 kcal/mol higher level in energy than (1-a). It has the HCN molecule to be hydrogen bonded to two aromatic CH hydrogen atoms by 2.5 Å and 2.7 Å hydrogen bonds. The third stable isomer (1-c) is predicted at the B3LYP/6-311++G(d,p) to be at 1.8 kcal/mol higher energy level than the most stable $C_8H_6^+(HCN)$ isomer

(1-a). (1-c) has HCN to be hydrogen bonded to an aromatic hydrogen atom in the para position from the acetylenic group.

The addition of the second HCN molecule showed preference for external solvation; in (2-a) the second HCN molecule is bound to the first HCN molecule by 2.1 Å hydrogen bond. Noteworthy, the internal solvation structure (2-b) is only at 0.5 kcal/mol higher level in energy than the lowest energy isomer (see Table 37). (2-b) has the two HCN molecules are hydrogen bonded in the para position from each other to the $C_8H_6^+$ core ion via two hydrogen bonds of 2.0 Å and 2.3 Å. The third most stable isomer (2-c) is 0.9 kcal/mol higher in energy than the most stable $[C_8H_6^+(HCN)_2]$ isomer (2-a). In (2-c) the second HCN molecule forms a bifurcated structure in which the newly added HCN molecule is hydrogen bonded to two aromatic hydrogen atoms via 2.3 Å and 3.7 Å.

As shown in Table 38, the lowest energy isomer for $[C_8H_6^+(HCN)_3]$ (3-a) has showed internal solvation pattern. The third HCN molecule binds to the phenyl ring forming a bifurcated where it binds to CH aromatic hydrogen atoms by 2.5 Å and 2.7 Å hydrogen bonds. The second most stable isomer of $[C_8H_6^+(HCN)_3]$ (3-b) expresses internal solvation in which the newly added HCN molecule is hydrogen bonded to the para position of the first two HCN molecule. (3-b) is only 0.1 kcal/mol higher in energy than (3-a) as theoretically predicted at the B3LYP/6-311++G(d,p) level of the theory. (3-c) shows external solvation in which all the three HCN molecules are hydrogen bonded to each other forming a linear chain rather than to the $C_8H_6^+$ core ion. Noteworthy, (3-c) is only at 0.3 kcal/mol higher level in energy than the most stable isomer (3-a).

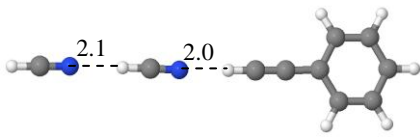
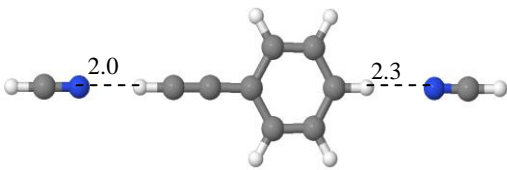
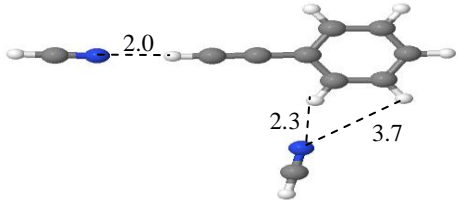
In $[\text{C}_8\text{H}_6^+(\text{HCN})_4]$, the lowest energy isomer (4-a) has the fourth HCN molecule bound to the third molecule by 2.1 Å hydrogen bond. The second most stable $\text{C}_8\text{H}_6^+(\text{HCN})_4$ isomer shows a symmetric structure in which the four HCN molecules are symmetrically hydrogen bonded to the C_8H_6^+ core ion, two from each side as displayed in (4-b) structure in Table 39. Interestingly, (4-b) is only 0.1 kcal/mol higher in energy than (4-a). The third most stable isomer is (4-c) is predicted to be 0.4 kcal/mol higher in energy than (4-a) at the B3LYP/6-311++G(d,p) level. (4-c) has three HCN molecules on one side while the fourth HCN molecule binds through a 2.3 Å hydrogen bond to an aromatic hydrogen atom.

Isomer	Optimized Structure	Relative Energy ^a	Binding Energy ^a
1-a		0.0	9.5 (*9.3)
1-b		1.7	7.8 (*7.7)
1-c		1.8	7.7 (*7.6)

^a calculated by DFT at the B3LYP/6-311++G(d,p) (corrected for ZPE)

*(corrected for ZPE and BSSE)

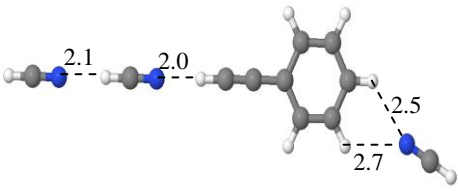
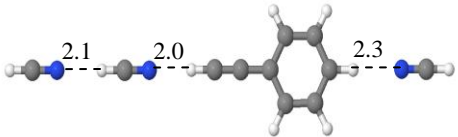
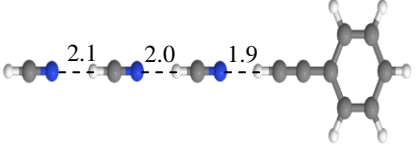
Table 36. Structures of $[C_8H_6^+ (HCN)]$ calculated by DFT at the B3LYP/6-311++G (d,p) corrected for zero-point energies and basis-set super position errors. Energies are in kcal/mol. Distances are in Angstroms

Isomer	Optimized Structure	Relative Energy ^a	Binding Energy ^a
2-a		0.0	7.6 (*7.4)
2-b		0.5	7.1 (*6.9)
2-c		0.9	6.7 (*6.5)

^a calculated by DFT at the B3LYP/6-311++G(d,p) (corrected for ZPE)

*(corrected for ZPE and BSSE)

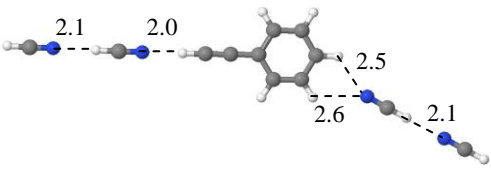
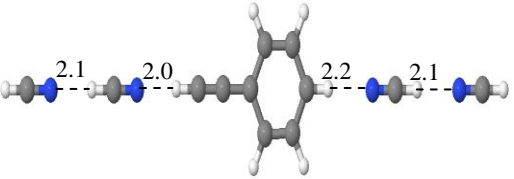
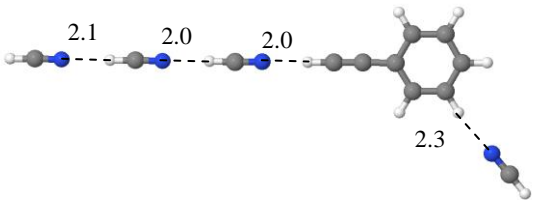
Table 37. Structures of $[C_8H_6^+ (HCN)_2]$ calculated by DFT at the B3LYP/6-311++G (d,p) corrected for zero-point energies and basis-set super position errors. Energies are in kcal/mol. Distances are in Angstroms

Isomer	Optimized Structure	Relative Energy ^a	Binding Energy ^a
3-a		0.0	6.9 (*6.7)
3-b		0.1	6.8 (*6.7)
3-c		0.3	6.6 (*6.4)

^a calculated by DFT at the B3LYP/6-311++G(d,p) (corrected for ZPE)

*(corrected for ZPE and BSSE)

Table 38. Structures of $[\text{C}_8\text{H}_6^+(\text{HCN})_3]$ calculated by DFT at the B3LYP/6-311++G (d,p) corrected for zero-point energies and basis-set super position errors. Energies are in kcal/mol. Distances are in Angstroms

Isomer	Optimized Structure	Relative Energy ^a	Binding Energy ^a
4-a		0.0	6.9 (*6.8)
4-b		0.1	6.8 (*6.6)
4-c		0.4	6.5 (*6.3)

^a calculated by DFT at the B3LYP/6-311++G(d,p) (corrected for ZPE)

*(corrected for ZPE and BSSE)

Table 39. Structures of $[\text{C}_8\text{H}_6^+ (\text{HCN})_4]$ calculated by DFT at the B3LYP/6-311++G (d,p) corrected for zero-point energies and basis-set super position errors. Energies are in kcal/mol. Distances are in Angstroms

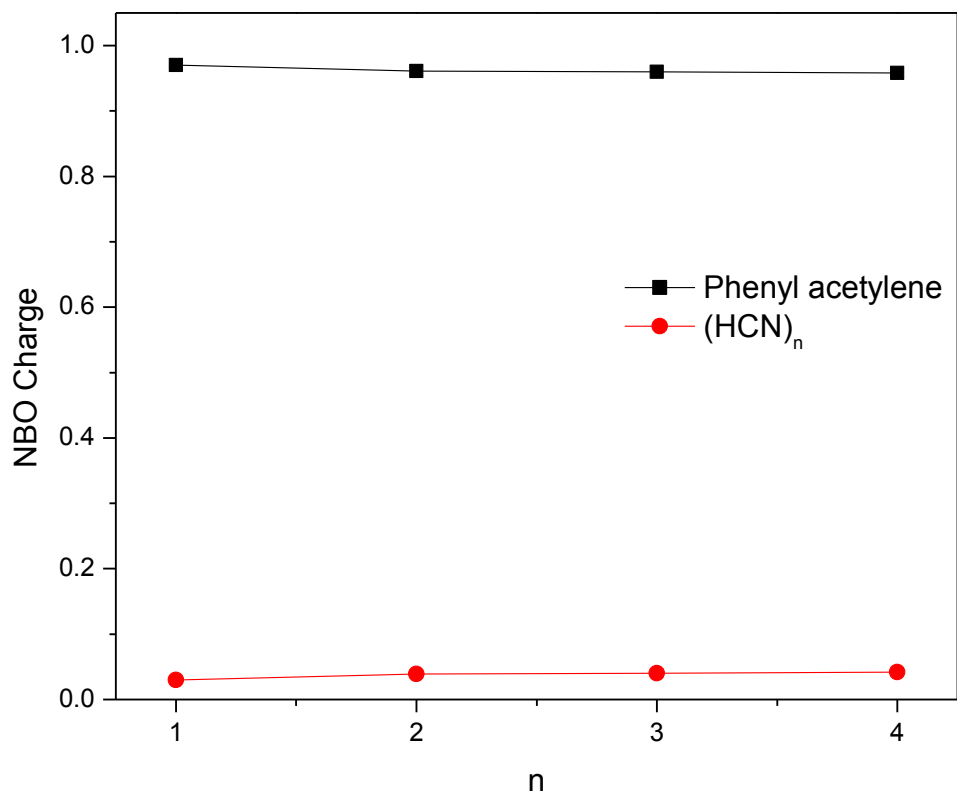


Figure 40. Charge evolution as a function of solvation degree n which shows that the charge stays on phenyl acetylene⁺ in [phenyl acetylene⁺(HCN)_n] clusters

6.4. Summary and Conclusions

Thermochemical equilibrium measurements have been utilized to investigate the binding energies and entropy changes involved in the stepwise additions of HCN and CH₃CN molecules into the mass-selected benzene radical cation resulting in the formation of C₆H₆⁺(HCN)_m and C₆H₆⁺(CH₃CN)_n; where $m=1-4$ and $n=1-3$.¹⁶⁴

The measured binding energy values follow the usual descending trend for association reactions. Moreover, the experimentally measured entropy values fall in the usual range for hydrogen bonding where internal rotations and low-frequency vibrations are retained. In

addition, theoretical studies of the structures and binding energies have been done using DFT at the B3LYP and M06-2X levels. Excellent agreement could be seen among the measured and calculated values. Thus, the employed theory levels are satisfactory for the current studies.

Theoretical frequency calculations of the lowest energy structures identify that $C_6H_6^+$ prefers external solvation in the first two HCN steps. The internal solvation requires more than two solvent molecules. This behavior is very similar to that observed in the hydration of $C_6H_6^+$.²⁰ However, internal solvation was preferred in the solvation via CH_3CN molecules starting from the second addition. This discrepancy can be attributed to the blocked structure of CH_3CN molecules which prevents solvent chains formation.^{78,164}

For comparison, the solvation of phenyl acetylene radical cations by several hydrogen cyanide molecules in the gas-phase was investigated and reported. Thermochemical equilibrium measurements have been utilized. The binding energies and entropy changes involved in the stepwise additions of the first four HCN molecules onto the mass-selected phenyl acetylene radical cation resulting in the formation of $C_8H_6^+ (HCN)_n$; where $n=1-4$ are measured. The measured binding energies (7-10 kcal/mol) reflect weak hydrogen bonding interactions where HCN molecule is hydrogen bound to the hydrogen of the acetylene group of the phenyl acetylene cation as predicted by the theory to be the most stable isomer. In fact, the measured binding energy values follow the usual descending trend for association reactions. In addition, the measured values are correlated with the calculated lowest energy isomers. Good agreement has been seen among the measured and calculated values. Thus, the used theory level is satisfactory for the current study.

Moreover, a theoretical investigation of the charge distribution upon stepwise solvation of the phenyl acetylene radical cation with the HCN molecules showed the charge on the $C_8H_6^+$ in $[C_8H_6^+ (HCN)_4]$ reached 96% at the B3LYP/6-311++G(d,p).

In fact, theoretical frequency calculations of the lowest energy structures identify that $C_8H_6^+$ prefers external solvation in the first two HCN steps. The internal solvation requires more than two HCN molecules. This behavior is very similar to that observed in the hydration and HCN solvation of $C_6H_6^+$.

Chapter 7: Sequential Association of HCN molecules with Pyridine^{·+}, Pyrimidine^{·+} and H⁺Pyridine. Binding Energies and Structures

7.1. Introduction

The formation of the complex polycyclic aromatic nitrogen containing hydrocarbons (PANHs) was theoretically predicted to be feasible through the reaction of benzene radical cation and hydrogen cyanide molecules as well as through the reaction of pyridine radical cation with acetylene molecules.¹⁶³ Therefore, the interaction of aromatic organic cations with HCN is of fundamental experimental and theoretical importance. In this work, we report the stepwise solvation of pyridine radical cations on a molecular level by several HCN molecules. Thermochemical equilibrium measurements have been utilized to measure the enthalpy and entropy changes accompanying the individual solvation steps yielding pyridine^{·+} (HCN)_n; with n=1- 4. The main goal is to compare the solvation binding energies and structures with those previously measured and theoretically predicted for pyridine radical cation hydration, where the distonic ions were formed and stabilized.¹⁷ The distonic ions behave very similarly to the protonated species. Therefore, to further check the possibility of formation of distonic ions, the solvation of protonated pyridine cation by several HCN molecules was investigated under equilibrium conditions.

For comparison purposes, gas-phase stepwise solvation of pyrimidine radical cation via HCN molecules was investigated under equilibrium measurements. Enthalpy and entropy

changes were measured experimentally for pyrimidine (HCN)_n; where n=1-4. Moreover, thermochemistry measurements have been employed to examine the identity of C₄H₄N₂⁺ formed through the reaction of C₂H₂⁺ with two HCN molecules and pyrimidine-like structure is proposed.

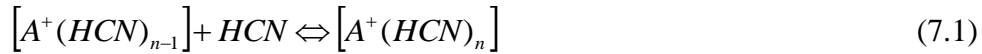
7.2. Experimental Section

The molecular ions of pyridine (C₅H₅N⁺), pyrimidine (C₄H₄N₂⁺) are formed by electron impact ionization using electron energy of 60-80 eV following the supersonic expansion of 40 psi (2.8 bar) of ultra high pure helium seeded with about 0.5-2% of pyridine or pyrimidine vapor. The expansion occurs through a pulsed supersonic nozzle (500 μm) to the source chamber which has 10⁻⁷ mbar background pressure. In order to form the H⁺pyridine (C₅H₅NH⁺), 10% H₂ in helium was used as carrier gas. C₅H₅N⁺, C₅H₅NH⁺ or C₄H₄N₂⁺ ions were mass-selected by the first quadrupole mass-filter according to their (m/z) ratios. The ions of interest are injected in (30-50 μs pulses) into the drift cell which contains the neutral pre-prepared HCN gas mostly in a mixture with helium buffer gas. The temperature of the drift cell is controlled better than ±1 K using four temperature controllers. The pressure can be controlled in the drift cell by using mass flow controllers (MKS # 1479A) within ±1 mTorr. The product and unreacted ions were then scanned using the second quadrupole mass-filter and detected by electron multiplier detector. Arrival time distributions (ATDs) of the ions were collected by monitoring their intensities as a function of time.

HCN is prepared by firstly adding 8 g of sodium cyanide (NaCN) (Sigma-Aldrich, 97%) into a 500 ml stainless steel bubbler. The bubbler is tightly closed and evacuated off air under liquid nitrogen temperature. Then 4 ml of ultra high pure sulfuric acid (H₂SO₄) (Aldrich, 99.999%) are added through a 4 cm stainless steel tube extension of the inlet valve of the

bubbler. Then, the sulfuric acid is allowed to get into the bubbler as a result of pressure difference and to react with the sodium cyanide salt. HCN evolves when the bubbler is allowed to warm up to room temperature. The pressure in the HCN line is monitored by a baratron (MKS-626A).¹⁶⁴

For the following association reaction:



where $A^+ = C_5H_5N^+$, $C_5H_5NH^+$ or $C_4H_4N_2^+$ for pyridine, protonated pyridine and pyrimidine cations, respectively.

Equilibrium establishment is verified when:

- (1) A constant ratio of the integrated intensity of the product to the reactant ions is maintained when the residence time is varied at constant pressure and temperature.
- (2) ATDs of the reactant and product ions are identical indicating equal residence times.

If the equilibrium conditions are well-established, the equilibrium constant, K_{eq} , can be measured using equation (7.2):

$$K_{eq} = \frac{[A^+(HCN)_n]}{[A^+(HCN)_{n-1}][HCN]} = \frac{I[A^+(HCN)_n]}{I[A^+(HCN)_{n-1}] \cdot P_{HCN}} \quad (7.2)$$

where $I[A^+(HCN)_{n-1}]$, $I[A^+(HCN)_n]$ are the integrated intensities of ATDs of the reactant and product cluster ions, respectively and P_{HCN} is the pressure of HCN in atmosphere. The equilibrium constant is measured at different reaction cell temperatures. From van't-Hoff plots,

ΔH° and ΔS° values are obtained from the slope and intercept, respectively.^{18,34,60} The reported values are at least three measurements average.

7.3. Theoretical Calculations

Density functional theory (DFT) calculations have been used at the B3LYP hybrid functional level using Gaussian 03 package.¹¹⁹ DFT at this calculation level has been widely used efficiently in the literature and showed great reliability in such studies.^{37,121,123,165} All the geometry optimizations and energy calculations were performed using a 6-311++G(d,p) basis set, where all the electrons are included.³⁷ Frequency calculations have been performed for all the optimized geometries at the same level of theory to obtain the zero point vibrational energy (ZPVE) and to verify the absence of any imaginary frequencies. Therefore, all the calculated energies are corrected for ZPVE. In addition, the total spin $\langle s^2 \rangle$ was 0.75-0.76 which confirms the lack of any spin contamination for the unrestricted calculations.⁶² Moreover, the counterpoise method has been used to correct the calculated energies for the basis-set superposition error (BSSE).¹²²

7.4. Results and discussion

7.4.1. Solvation of Pyridine⁺ and H⁺pyridine by HCN molecules

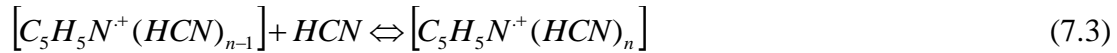
7.4.1.1. Thermochemistry measurements and structural implications of Pyridine⁺/HCN reaction

Pyridine, the simplest of the azasubstituted benzenes or azines, has been the subject of numerous experimental and theoretical investigations over the last few decades.¹⁶⁷ In fact, pyridine and its derivatives were detected in the heavy petroleum and they are emitted into the atmosphere as a result of coal combustion.^{168,169} Moreover, the protonated ions of pyridine and

its derivatives have been observed at significant levels in measurements of the background ion composition of the lower troposphere.¹⁷⁰

The mass-spectra shown in Figure 41 display the solvation of the injected pyridine radical cations in the mass-selection mode under different drift cell temperatures. The clusters are shifted to bigger cluster sizes as the temperature of the drift cell is reduced following the usual association reaction trends. The lowest attainable drift cell temperature was 194 K to avoid HCN freezing.

This study investigated association reaction:



Reaction (7.3) was investigated under weak field conditions of 4 V/cm and low injection energy. The used injection energy was slightly above the required energy to introduce the $C_5H_5N^+$ against the outflow of the reactant gas. Equilibrium conditions were confirmed quantitatively via verifying that a constant ratio of the integrated intensity of the product to the reactant ions is maintained when the residence time is varied at constant pressure and temperature. Qualitative verification was achieved when ATDs of the reactant and product ions are identical indicating equal residence times. This can be seen obviously in Figure 42, where the ATDs of pyridine⁺(HCN)_n; n=0-3 are in excellent matching. Equilibrium constant was measured at different temperatures utilizing equation (7.4):

$$K_{eq} = \frac{[C_5H_5N^+(HCN)_n]}{[C_5H_5N^+(HCN)_{n-1}][HCN]} = \frac{I[C_5H_5N^+(HCN)_n]}{I[C_5H_5N^+(HCN)_{n-1}] \cdot P_{HCN}} \quad (7.4)$$

where $I[C_5H_5N^+(HCN)_{n-1}]$, $I[C_5H_5N^+(HCN)_n]$ are the integrated intensities of ATDs of the reactant and product cluster ions of reaction (7.3), respectively and P_{HCN} is the pressure of HCN

in atmosphere. van't-Hoff plots were then obtained by plotting the $R \ln K_{eq}$ versus $1000/T$, as displayed in Figure 43. From equation (7.5), ΔH° and ΔS° can be readily obtained from the slope and intercept of Figure 43, respectively.

$$R \ln K_{eq} = \frac{-\Delta H^\circ}{T} + \Delta S^\circ \quad (7.5)$$

The binding energies and entropy changes involved in the association reaction (7.3), are tabulated in Table 40 along with theoretically calculated binding energies assigned for the lowest energy isomers. The very good agreement among the experimentally measured and theoretically calculated binding energies within the experimental uncertainty ($\Delta H^\circ = \pm 1$ kcal/mol) verifies the adequacy of the employed calculation levels.

Distonic ions formation possibility can be ruled out since distonic ions are expected to have strong hydrogen bonds which can be of similar strength to that formed with the protonated pyridine cation; as a result of the similarity among the structures of the distonic pyridine radical cations with that of protonated pyridine cation.¹⁷

In addition, to further investigate that possibility in depth, solvation of protonated pyridine was studied under similar conditions. The resulting thermochemistry values are compared with those obtained in the pyridine radical cation case as well as with the theoretically obtained energies. The mass-spectra obtained for protonated pyridine study are shown in Figure 44. All the experimentally measured thermochemistry values and calculated binding energies of $[H^+ \text{pyridine} (\text{HCN})_n]$ clusters formation are shown in Table 45. van't-Hoff plots for $H^+ \text{pyridine} (\text{HCN})_n$ are depicted for $n=1-4$ in Figure 45. In addition, the theoretically predicted structures of $H^+ \text{pyridine} (\text{HCN})_n$; $n=1-4$ are tabulated in Tables (46-48).

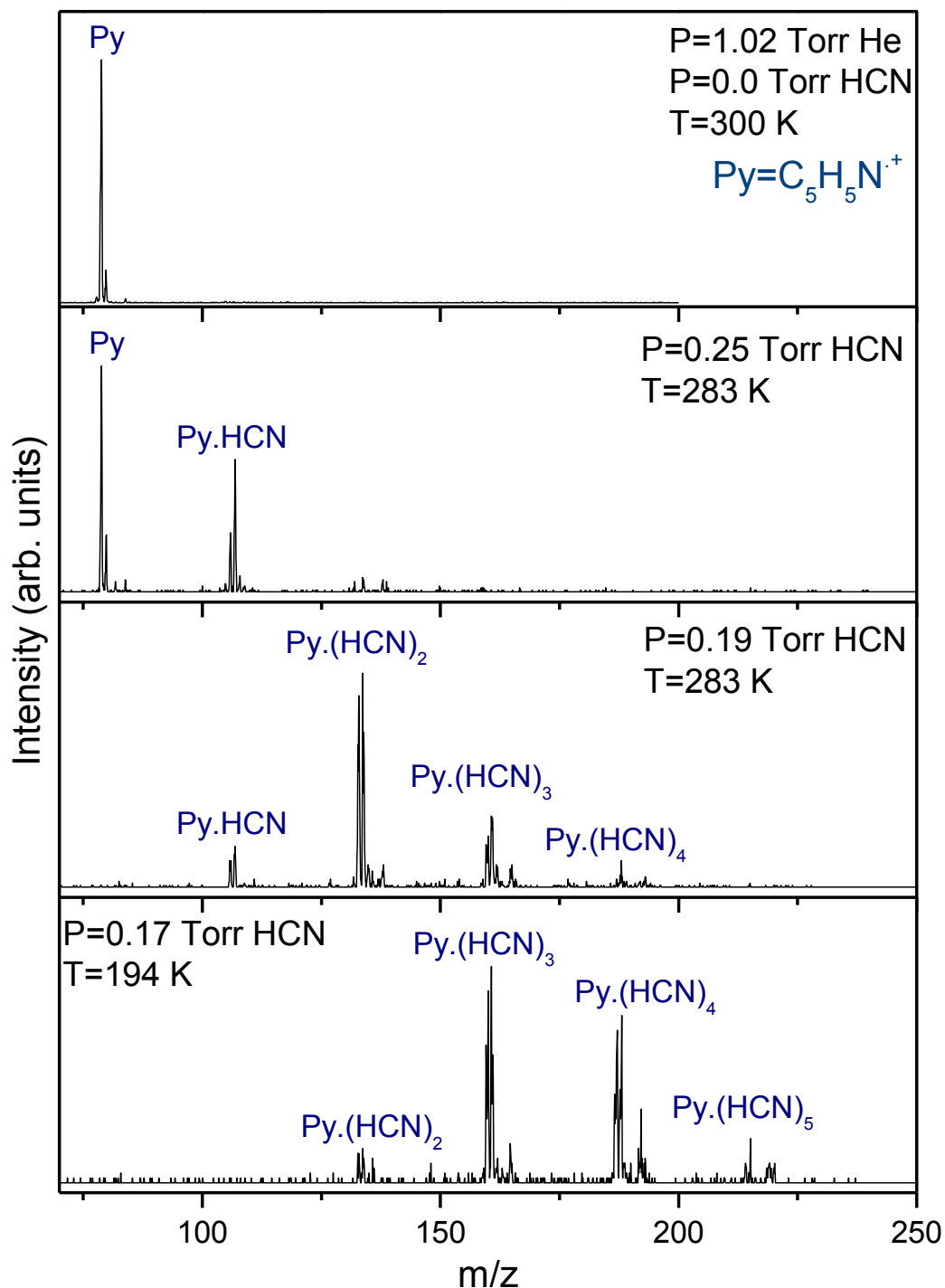


Figure 41. Mass-spectra resulting from injecting pyridine radical cation in the mass-selection mode using injection energy of 13.8 eV (lab) and on applying a drift field of 4 V/cm. The drift cell temperature and pressure are varied as indicated

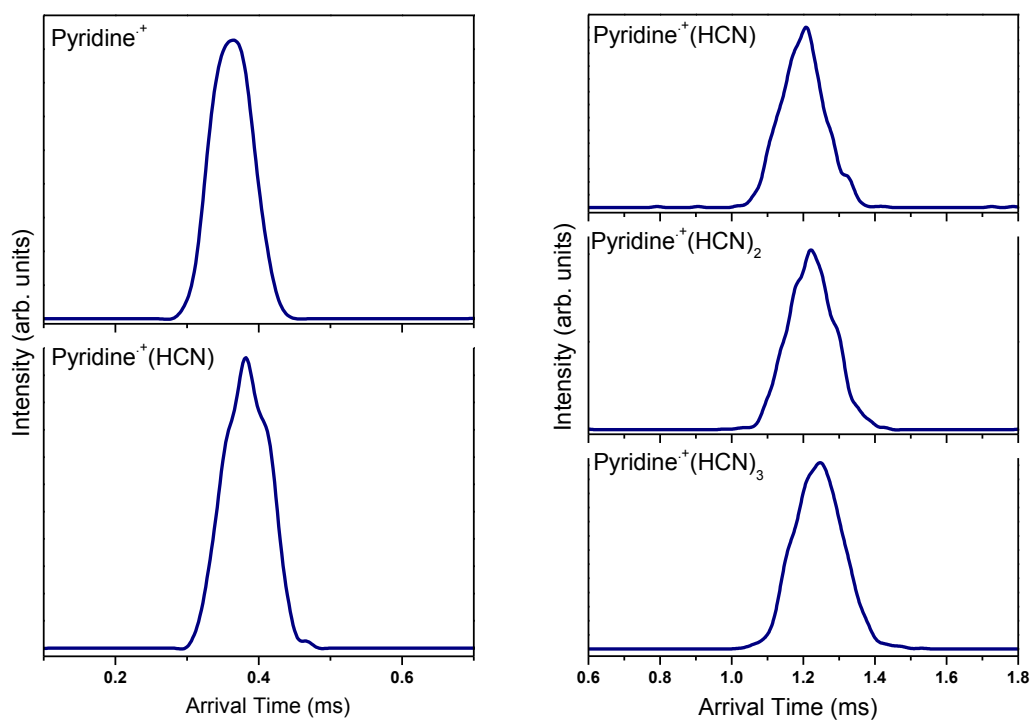


Figure 42. ATDs of $\text{pyridine}^+(\text{HCN})_n$; $n=0-3$ collected upon injecting mass-selected pyridine radical cations into the drift cell which contains hydrogen cyanide gas mixed with helium buffer gas using an injection energy of 13.8 eV (lab.) and by applying a drift field of 4 V/cm (**Left**) ATDs matching of $n=0,1$ collected at 263 K, the concentration of hydrogen cyanide was 0.27 Torr. (**Right**) ATDs matching of $n=1-3$, collected at 255 K, the concentration of hydrogen cyanide was 0.22 Torr

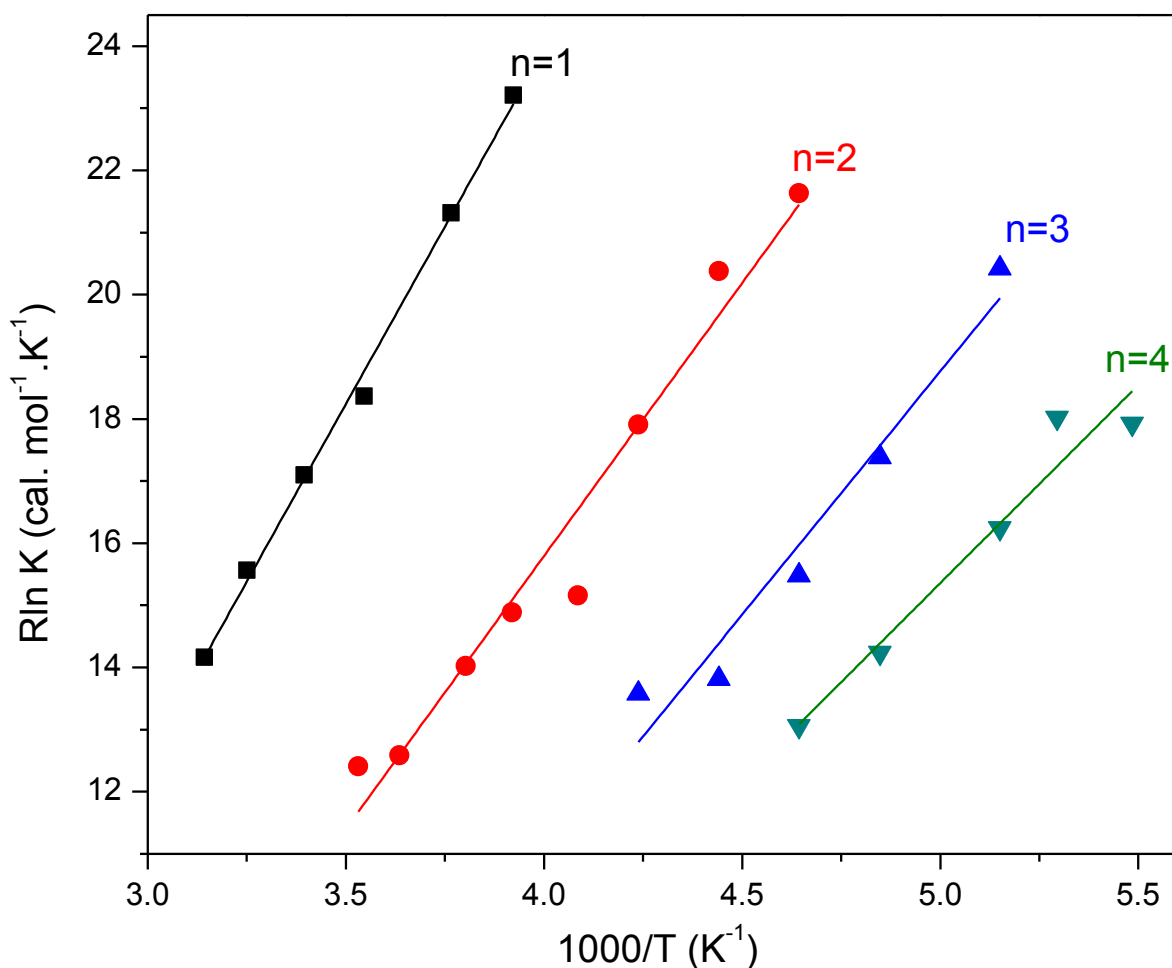


Figure 43. van't-Hoff plots for the association reaction yielding $\text{C}_5\text{H}_5\text{N}^+(\text{HCN})_n$; with $n=1-4$. The drift cell temperature was varied between 182 K and 322 K. The injection energy and drift field were maintained at 14 eV (laboratory frame) and 4 V/cm, respectively

n	$-\Delta H^\circ$	$-\Delta S^\circ$	BE ^c	BE ^d
1	11.4	21.8	11.0	10.6
2	8.8	19.3	9.4	9.2
3	7.8	20.4	7.7	7.5
4	6.4	16.5	7.3	7.1

^a $\Delta H^\circ_{n-1,n}$ units are kcal/mol (± 1 kcal/mol), ^b $\Delta S^\circ_{n-1,n}$ units are cal/mol.K (± 2 cal/mol.K), ^c BE_{n-1,n} in kcal/mol calculated by B3LYP/6-311++G(d,p) with ZPE included, and ^d BE_{n-1,n} in kcal/mol calculated by B3LYP/6-311++G(d,p) (with BSSE correction)

Table 40. Thermochemistry values measured for the association reaction resulting in $C_5H_5N^+(HCN)_n$; where n=1-4. The study was done in the drift cell temperature range of 182 K-322 K. The injection energy was 13.8 eV (lab. frame) while the applied drift field was 4 V/cm. Theoretically calculated binding energies are shown as well, from B3LYP/6-311++G(d,p) calculations

7.4.1.2. Theoretical Calculations of the solvated pyridine radical cations by HCN molecules

Tables (41-44) display the optimized structures of the most stable HCN solvated pyridine radical cation isomers by 1-4 HCN molecules. $[C_5H_5N^+(HCN)_n]$ isomers are calculated by the hybrid DFT B3LYP method, using the standard basis-set of 6-311++G(d,p). Moreover, Table 40 displayed the resulting binding energies corrected for zero-point vibrational energy (ZPVE) and for basis-set superposition error (BSSE).¹²² It is obvious that the theoretically calculated binding energy values are in very good agreement with the experiment within the experimental accuracy

($\Delta H_{n-1,n}^{\circ} \pm 1.0 \text{ kcal mol}^{-1}$). Therefore, we consider this level of theory to be enough for our computational jobs.

$C_5H_5N^+(HCN)$: As displayed in Table 41, the lowest energy isomer for $C_5H_5N^+(HCN)$ is (1-a). (1-a) has ion-dipole nature of interaction in which the N-atom of HCN molecule binds weakly to the N-atom of the $C_5H_5N^+$ ion via 2.4 Å bond. This structure is possible as a result of the difference in charge signs between the pyridine and HCN nitrogen atoms. The N-atom of $C_5H_5N^+$ has a positive charge while that of HCN molecule has a negative charge.

The second lowest energy [$C_5H_5N^+(HCN)$] is (1-b). Isomer (1-b) has 2.0 Å hydrogen bonding interaction between the N-atom of the HCN molecule and the ortho-aromatic hydrogen atom. This isomer was predicted at the B3LYP/6-311++G (d,p) level to be 0.4 kcal/mol higher in energy than (1-a).

The third most stable isomer at the B3LYP/6-311++G (d,p) level was predicted to have the structure (1-c) shown in Table 41 and to be 2.3 kcal/mol higher in energy. (1-c) has the HCN molecule to bind to the para-aromatic hydrogen atom via 2.2 Å hydrogen bond.

$C_5H_5N^+(HCN)_2$: As displayed in Table 42, the lowest energy isomer for [$C_5H_5N^+(HCN)_2$] is (2-a). In which head to tail hydrogen bonded linear chain where the second HCN molecule binds to the first one via 2.0 Å hydrogen bond. Noteworthy, (2-a) expresses external solvation in which the HCN molecules bind to each other rather than binding to the core $C_5H_5N^+$ ion. This behavior was observed in the solvation of several cations with HCN molecules, such as, benzene⁺ and phenyl acetylene⁺.

The second lowest energy isomer for $[\text{C}_5\text{H}_5\text{N}^+(\text{HCN})_2]$ was predicted to be at only 0.3 kcal/mol higher energy level than (2-a). Internal solvation was predicted for (2-b) in which the two HCN molecules bind through 2.1 Å hydrogen bonds to the ortho aromatic hydrogen atoms.

(2-c) is the third most stable $[\text{C}_5\text{H}_5\text{N}^+(\text{HCN})_2]$ isomer at the B3LYP/6-311++G(d,p) level of the theory and it was predicted to be 0.9 kcal/mol higher in energy than (2-a). The second HCN molecule binds to the $\text{C}_5\text{H}_5\text{N}^+$ core ion forming a bifurcated structure in which the N-atom of the secondly added HCN molecule forms two hydrogen bonds with two CH- aromatic hydrogen atoms. The hydrogen bonds were of 2.2 Å and 3.7 Å length.

$\text{C}_5\text{H}_5\text{N}^+(\text{HCN})_3$: As displayed in Table 43, the most stable $[\text{C}_5\text{H}_5\text{N}^+(\text{HCN})_3]$ isomer is (3-a) which has internal solvation pattern to be more energetically favorable. Thus, three HCN molecules were required to get the internal solvation pattern as predicted for benzene⁺ and phenyl acetylene⁺ before. The third HCN molecule forms a bifurcated structure in which the N-atom of HCN molecule binds to two CH-aromatic hydrogen atoms through 2.2 Å and 3.6 Å hydrogen bonds.

The second most stable $[\text{C}_5\text{H}_5\text{N}^+(\text{HCN})_3]$ isomer is (3-b) which has external solvation pattern. External solvation was predicted to be only 0.3 kcal/mol higher in energy than (3-a) at the B3LYP/6-311++G(d,p) level of the theory. The three HCN molecules form a linear hydrogen bonded chain in which the third HCN molecule is hydrogen bonded to the second one via 2.1 Å hydrogen bond.

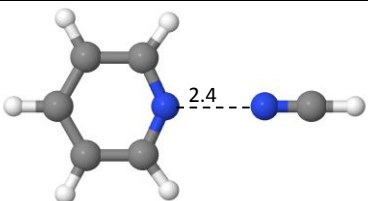
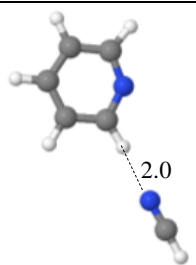
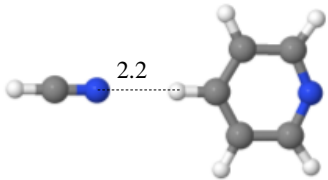
(3-c) is the third lowest energy $[\text{C}_5\text{H}_5\text{N}^+(\text{HCN})_3]$ isomer; it is predicted to be 0.6 kcal/mol higher in energy than the (3-a) isomer. In (3-c), the third HCN molecule binds to the core $\text{C}_5\text{H}_5\text{N}^+$ via

2.3 Å hydrogen bond between the N-atom of the HCN molecule and the meta CH-aromatic hydrogen atom.

$C_5H_5N^+(HCN)_4$: The lowest energy isomer (4-a) shows internal solvation in which the fourth HCN molecule binds to the third one via 2.1 Å hydrogen bond, See (4-a) in Table 44.

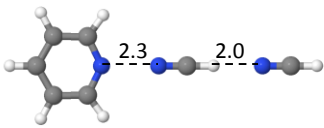
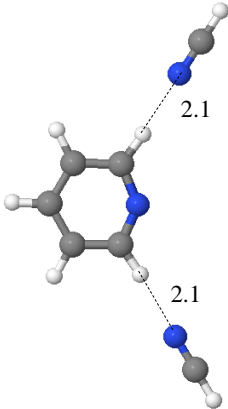
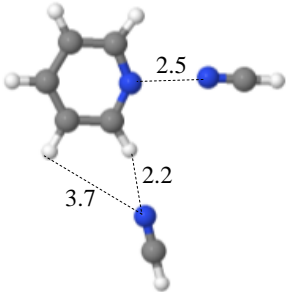
The second stable isomer (4-b) was predicted at the B3LYP/6-311++G(d,p) level to be only 0.1 kcal/mol higher in energy than (4-a). In (4-b), the fourth HCN molecule binds to the first two HCN molecules via 2.1 Å hydrogen bond forming a linear hydrogen bonded chain.

(4-c), the third most stable $C_5H_5N^+(HCN)_4$ isomer has the fourth HCN molecule formed a symmetrically bifurcated structure in which the N-atom of the HCN molecule forms two hydrogen bonds with two CH-aromatic hydrogen atoms using 2.3 Å and 3.6 Å hydrogen bonds.

Name	Optimized Structure	Relative Energy ^a	Binding energy ^b
1-a		0.0	11.0 (*10.6)
1-b		0.4	10.6 (*10.4)
1-c		2.3	8.7 (*8.5)

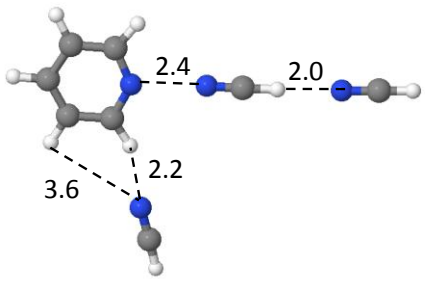
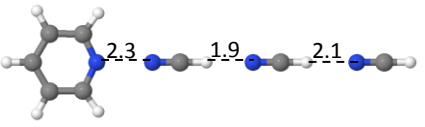
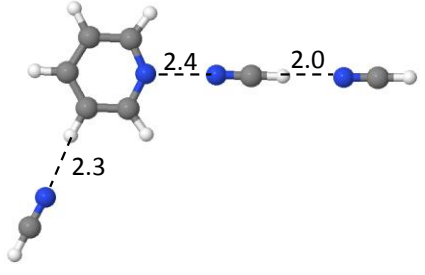
^a in kcal/mol (corrected for ZPE) ^b in kcal/mol *(corrected for ZPE and BSSE)

Table 41. Theoretically optimized structures using B3LYP/6-311++G(d,p) of $[C_5H_5N^+(HCN)]$. Distances are in Angstrom

Name	Optimized Structure	Relative Energy ^a	Binding energy ^b
2-a		0.0	9.4 (*9.2)
2-b		0.3	9.1 (*9.1)
2-c		0.9	8.5 (*8.3)

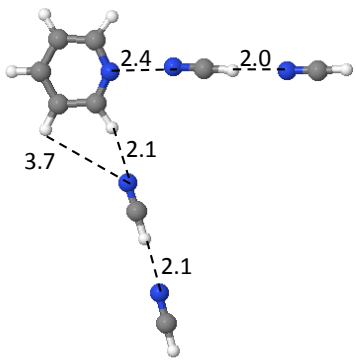
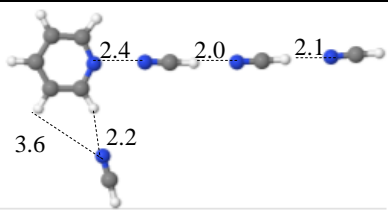
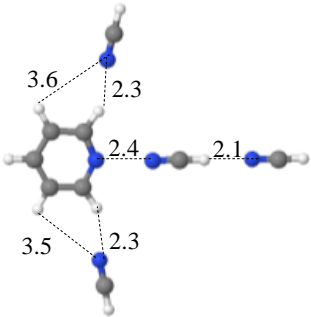
^a in kcal/mol (corrected for ZPE) ^b in kcal/mol *(corrected for ZPE and BSSE)

Table 42. Theoretically optimized structures using B3LYP/6-311++G(d,p) of $[C_5H_5N^+(HCN)_2]$. Distances are in Angstroms

Name	Optimized Structure	Relative Energy ^a	Binding energy ^b
3-a		0.0	7.7 (*7.5)
3-b		0.3	7.4 (*7.2)
3-c		0.6	7.1 (*6.9)

^a in kcal/mol (corrected for ZPE) ^b in kcal/mol *(corrected for ZPE and BSSE)

Table 43. Theoretically optimized structures using B3LYP/6-311++G(d,p) of $[C_5H_5N^+(HCN)_3]$. Distances are in Angstroms

Name	Optimized Structure	Relative Energy ^a	Binding energy ^b
4-a		0.0	7.3 (*7.1)
4-b		0.1	7.2 (*7.0)
4-c		0.3	7.0 (*6.9)

^a in kcal/mol (corrected for ZPE) ^b in kcal/mol *(corrected for ZPE and BSSE)

Table 44. Theoretically optimized structures using B3LYP/6-311++G(d,p) of $[C_5H_5N^+(HCN)_4]$. Distances are in Angstroms

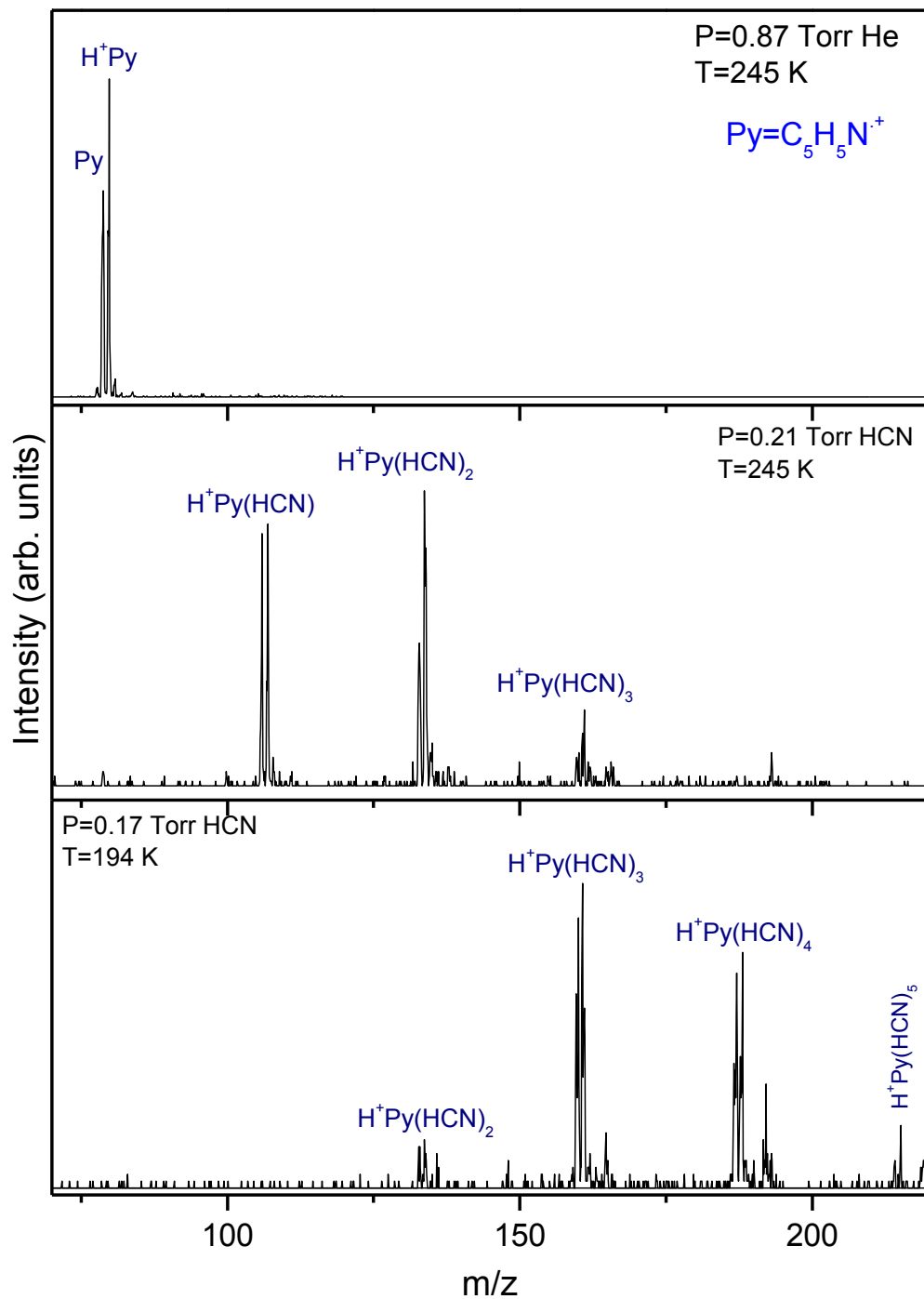


Figure 44. Mass-spectra obtained upon injecting H⁺pyridine in the mass-selection mode into the drift cell using injection energy of 15.8 eV (laboratory frame) and by applying a weak electric field of 4 V/cm. The drift cell temperature and HCN concentrations are varied as indicated

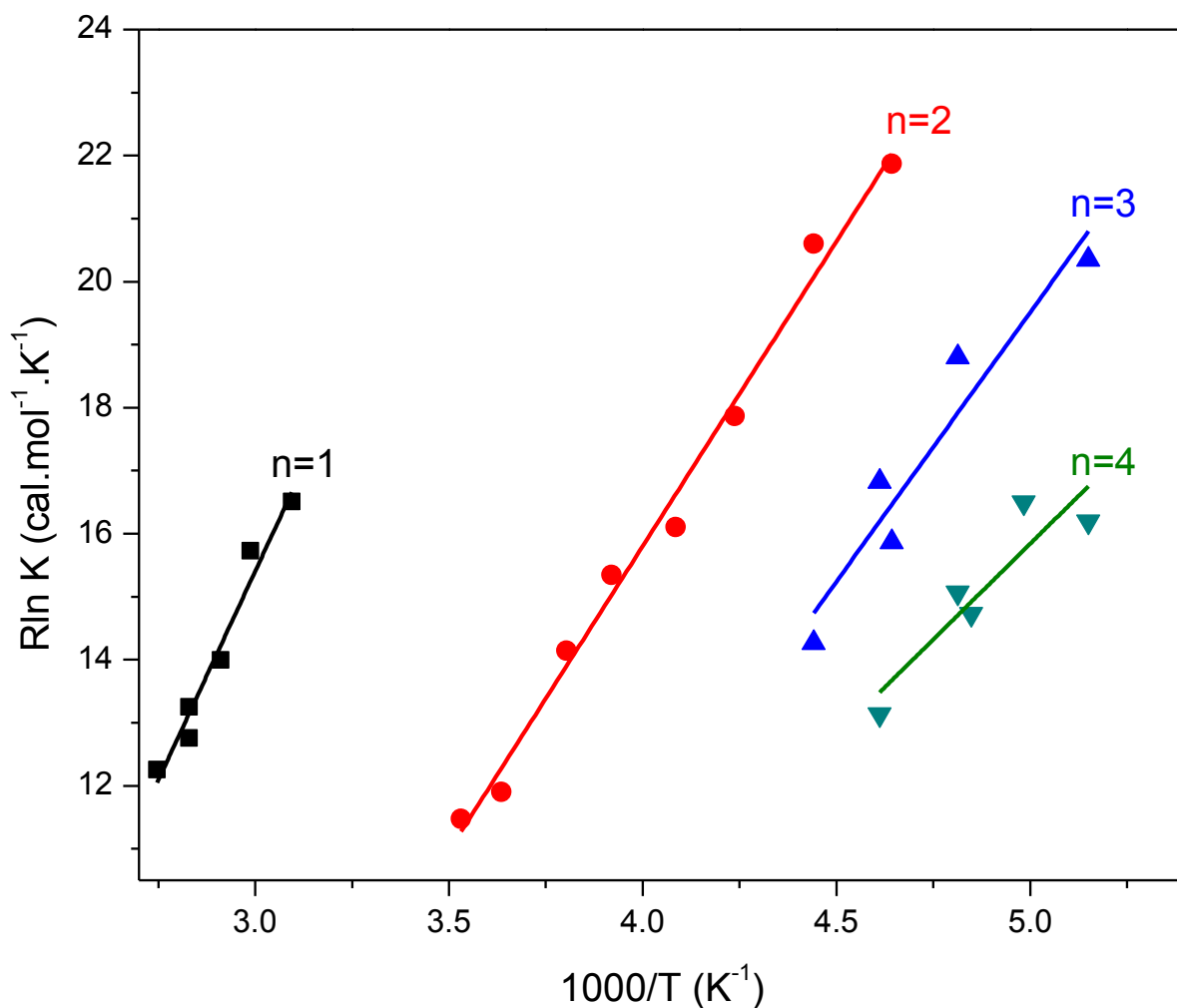


Figure 45. van't-Hoff plots for the association reaction yielding $\text{C}_5\text{H}_5\text{NH}^+(\text{HCN})_n$; with $n=1-4$. The drift cell temperature was varied between 194 K and 364 K. The injection energy and drift field were maintained at 16 eV (laboratory frame) and 4 V/cm, respectively

n	$-\Delta H^\circ$ ^a	$-\Delta S^\circ$ ^b	BE ^c	BE ^d
1	13.2	24.3	15.6	15.3
2	9.7	22.9	9.5	9.3
3	8.5	23.2	7.4	7.2
4	6.1	14.5	6.9	6.7

^a $\Delta H^\circ_{n-1,n}$ units are kcal/mol (± 1 kcal/ mol), ^b $\Delta S^\circ_{n-1,n}$ units are cal/mol.K (± 2 cal/mol. K), ^c

Binding energy in kcal/ mol calculated by B3LYP/6-311++G(d,p) with ZPE included, and ^d

Binding energy in kcal/ mol calculated by B3LYP/6-311++G(d,p) (with BSSE correction)

Table 45. Thermochemistry values measured for the association reaction resulting in $[\text{C}_5\text{H}_5\text{NH}^+(\text{HCN})_n]$; where $n=1-4$. The study was done in the drift cell temperature range of 194 K-364 K. The injection energy was 15.8 eV (lab. frame). The applied drift field was 4 V/cm. Theoretically calculated binding energies are shown as well, from B3LYP/6-311++G(d,p)

7.4.1.3. Theoretical Calculations of the solvated protonated pyridine cations by HCN molecules

Tables (46-48) display the optimized structures of the most stable solvated H^+ pyridine isomers by 1-4 HCN molecules. $[\text{C}_5\text{H}_5\text{NH}^+(\text{HCN})_n]$ are calculated by the hybrid DFT B3LYP method, using a standard basis-set of 6-311++G(d,p). Moreover, Table 45 displayed the resulting binding energies corrected for zero-point vibrational energy (ZPVE) and for basis-set superposition error (BSSE) which has been corrected by counterpoise procedure.¹²² It is obvious that the theoretically calculated binding energy values are in good agreement with the experiment within the experimental accuracy ($\Delta H^\circ_{n-1,n} \pm 1.0$ kcal mol⁻¹). Therefore, we consider this level of theory to be enough for our computational jobs.

C₅H₅NH⁺(HCN): The protonation of pyridine occurs exclusively on the N-atom at the B3LYP/6-311++G(d,p) calculation level. This is expected because the N-atom is the most basic center in pyridine.¹⁷¹ The lowest energy isomer for [C₅H₅NH⁺(HCN)], as displayed in Table 46 is (1-a). (1-a) has hydrogen bonding nature of interaction in which the N-atom of HCN molecule binds strongly to the proton of the C₅H₅NH⁺ ion via 1.8 Å bond.

C₅H₅NH⁺(HCN)₂: (2-a) is the most stable [C₅H₅NH⁺(HCN)₂] isomer. The second HCN molecule binds through a 2.0 Å hydrogen atom to the first one following the external solvation regime.

Internal solvation pattern was expressed in the isomer (2-b) where the second HCN molecule forms a bifurcated structure in which the N-atom binds to two CH aromatic hydrogen atoms through 2.2 Å and 3.9 Å hydrogen bonds. However, (2-b) is 1.9 kcal/mol higher in energy than the lowest energy [C₅H₅NH⁺(HCN)₂] (2-a).

C₅H₅NH⁺(HCN)₃: The lowest energy [C₅H₅NH⁺(HCN)₃] is isomer (3-a). It has the external solvation pattern in contrast to all the previously investigated cations. The third HCN molecule forms a linear hydrogen bonded chain with the first two HCN molecules via 2.1 Å hydrogen bond as displayed in Table 47.

The second lowest energy isomer (3-b) follows the internal solvation regime. The third HCN molecule forms a bifurcated structure with two CH-aromatic hydrogen atoms through 2.3 Å and 3.8 Å hydrogen bonds. (3-b) is 0.3 kcal/mol higher in energy than the lowest energy [C₅H₅NH⁺(HCN)₃] isomer.

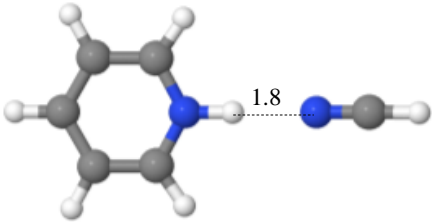
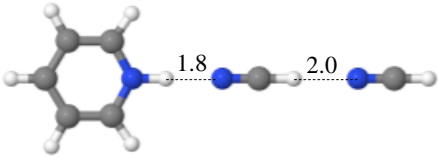
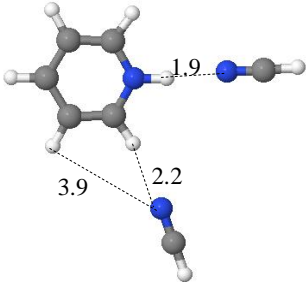
The third more stable isomer is (3-c) which was predicted at the B3LYP/6-311++G(d,p) to be 0.8 kcal/mol higher in energy than the most stable isomer (3-a). The third HCN molecule binds to

the $C_5H_5NH^+$ core ion in the para position from the N-atom via 2.3 Å hydrogen bond to the aromatic hydrogen atom.

$C_5H_5NH^+(HCN)_4$: As displayed in Table 48, the lowest energy isomer for $[C_5H_5NH^+(HCN)_4]$ has internally solvated pattern; see (4-a). The fourth HCN molecule binds through bifurcated structure in which the N-atom of the HCN molecule through two hydrogen bonds to two CH-aromatic hydrogen atoms via 2.3 Å and 3.8 Å hydrogen bonds.

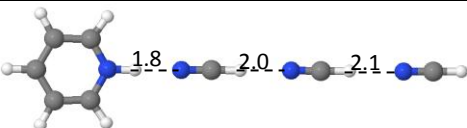
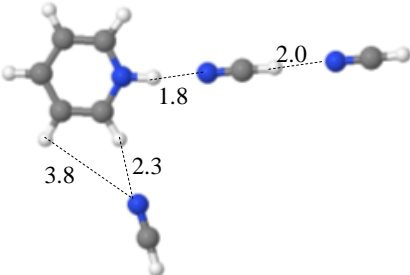
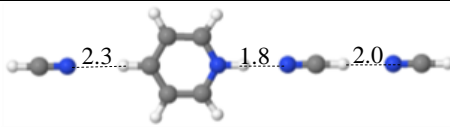
The second lowest energy isomer (4-b) was predicted to be 0.2 kcal/mol higher in energy than (4-a). Moreover, (4-b) has the fourth HCN molecule hydrogen bound to the third HCN molecule via 2.1 Å hydrogen bond.

Interestingly, the third lowest energy isomer (4-c) has externally solvated structure in which all the four HCN molecules form a linearly hydrogen bonded chain. The fourth HCN molecule is hydrogen bonded to the third HCN molecule via 2.1 Å hydrogen bond. (4-c) is only 0.4 kcal/mol higher in energy than (4-a) as predicted at the B3LYP/6-311++G(d,p) level of theory.

Name	Optimized Structure	Relative Energy ^a	Binding energy ^b
1-a		0.0	15.6 (*15.3)
2-a		0.0	9.5 (*9.3)
2-b		1.9	7.6 (*7.4)

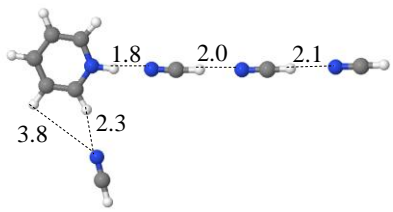
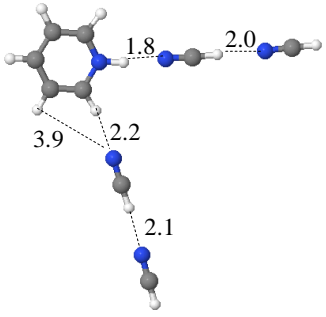
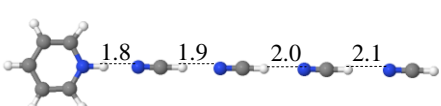
^a in kcal/mol (corrected for ZPE) ^b in kcal/mol *(corrected for ZPE and BSSE)

Table 46. Theoretically optimized structures using B3LYP/6-311++G(d,p) of $[C_5H_5NH^+(HCN)_n]$; $n=1,2$. Distances are in Angstroms

Name	Optimized Structure	Relative Energy ^a	Binding energy ^b
3-a		0.0	7.4 (*7.2)
3-b		0.3	7.1 (*6.9)
3-c		0.8	6.5 (*6.4)

^a in kcal/mol (corrected for ZPE) ^b in kcal/mol *(corrected for ZPE and BSSE)

Table 47. Theoretically optimized structures using B3LYP/6-311++G(d,p) of $[\text{C}_5\text{H}_5\text{NH}^+(\text{HCN})_3]$. Distances are in Angstroms

Name	Optimized Structure	Relative Energy ^a	Binding energy ^b
4-a		0.0	6.9 (*6.7)
4-b		0.2	6.7 (*6.6)
4-c		0.4	6.5 (*6.3)

^a in kcal/mol (corrected for ZPE) ^b in kcal/mol *(corrected for ZPE and BSSE)

Table 48. Theoretically optimized structures using B3LYP/6-311++G(d,p) of $[\text{C}_5\text{H}_5\text{NH}^+(\text{HCN})_4]$. Distances are in Angstroms

7.4.2. Solvation of Pyrimidine Radical cations by HCN molecules

Pyrimidine ($C_4H_4N_2$) represents the main constituent of cytosine and thymine DNA nucleotides.^{37,130} It possesses two different proton acceptor sites: the ring π -cloud and the lone pairs of the heteroatoms.^{62,134,136,172,173} Therefore, pyrimidine solvation can be regarded as a prototype for the solvation of heterocyclic aromatic rings containing nitrogen heteroatoms. In fact, the hydrogen-bonded clusters resulting from supersonic expansion of the pyrimidine/water and pyrimidine/methanol mixtures have been investigated experimentally using laser photoionization time of flight mass spectrometry technique.^{62,134} In addition, hydration of pyrimidine radical cation was investigated under equilibrium conditions where binding energies along with the entropy changes were measured in our laboratory. Moreover, high level theoretical calculations were utilized and compared with the experimentally determined values. The current study aims to investigate the association reaction between the injected pyrimidine radical cations and HCN molecules under equilibrium conditions. The binding energies and the corresponding entropy changes accompanying their formation are measured experimentally.

Pyrimidine⁺ can bind to HCN molecules via two different types of hydrogen bonds. One via $CH^{\delta+} \cdots N$ hydrogen bonds, which would be relatively weak as reported in benzene⁺ hydration example^{20,33} or via $NH^+ \cdots N$ hydrogen bonds, which are stronger than the former case; such as, in protonated pyridine example.¹⁷ In order to check experimentally and theoretically which binding site is favored by hydrogen cyanide molecules, this reaction study results will be compared to the corresponding results obtained in the cases of benzene and protonated pyridine cations solvation with HCN molecules.

7.4.2.1. Mass-spectra

Mass-spectra obtained from injecting $C_4H_4N_2^+$ into the drift cell which has HCN gas at various drift cell temperatures are shown in Figure 46. The cluster distribution is shifted to bigger clusters as the drift cell temperature is reduced following the usual association reaction trends. The major observed ions at 274 K were $[Pyrimidine^+(HCN)_n]$; where $n=0,1$. At 188 K, the observed ions were $[Pyrimidine^+(HCN)_n]$ where $n=2,3$. The study has been stopped at 184 K because of hydrogen cyanide freezing temperature was reached.

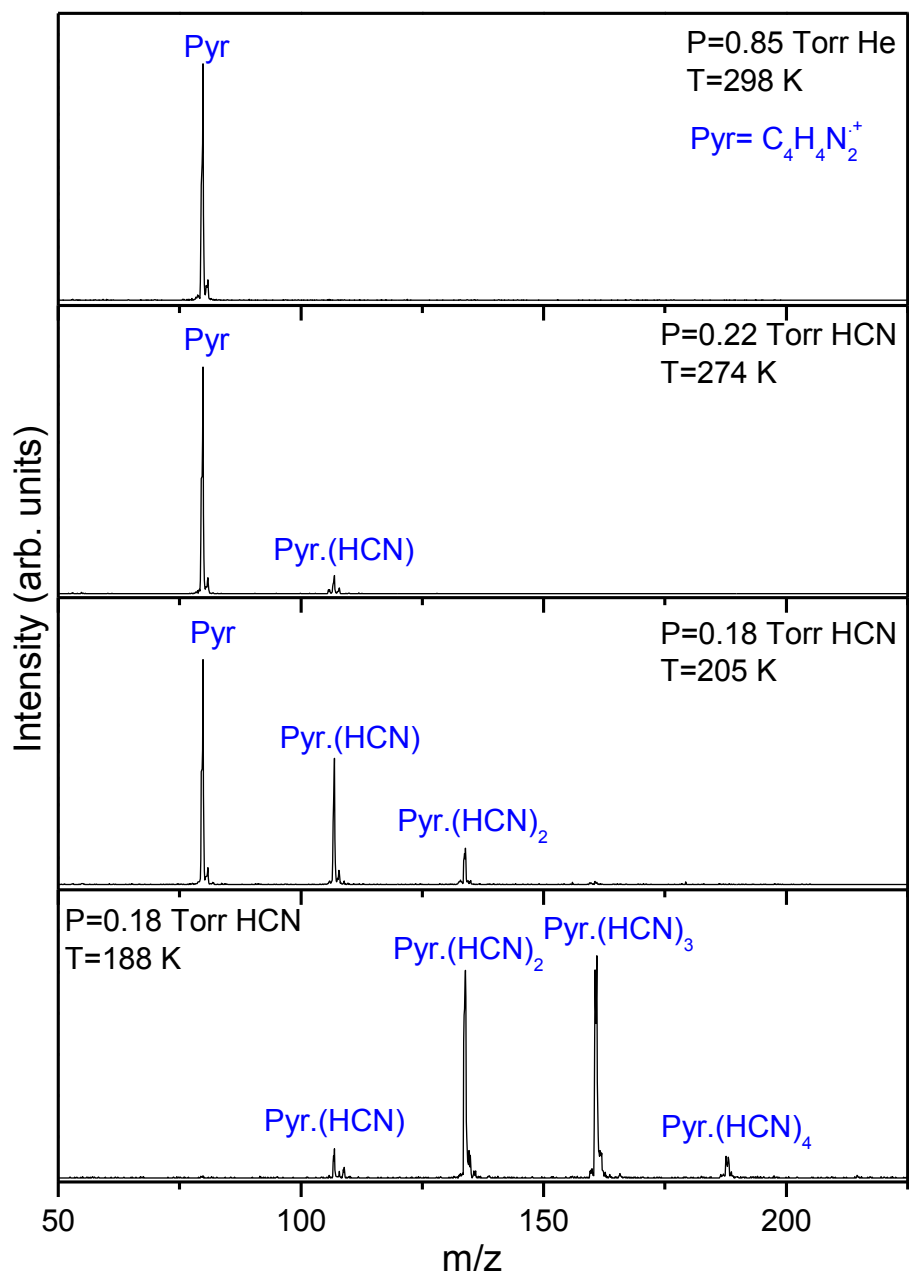


Figure 46. Mass-spectra resulting from injecting the pyrimidine radical cations into the drift cell containing different concentrations of hydrogen cyanide. The applied drift field was 4V/cm while the injection energy was 12.4 eV (lab. frame). The drift cell temperature and pressure were varied as indicated

7.4.2.2. Thermochemistry measurements and structural implications

The investigated association reaction in this study is:



The reaction (7.6) was investigated under weak field conditions of 4 V/cm and low injection energy of 12.4 eV (laboratory frame). This injection energy is slightly above the required energy to introduce the $C_4H_4N_2^+$ against the outflow of the drift gas into the drift cell.

Equilibrium conditions were verified quantitatively via verifying that a constant ratio of the integrated intensity of the product to the reactant ions is maintained when the residence time is varied at constant pressure and temperature. Qualitative verification was carried out since ATDs of the reactant and product ions are identical indicating equal residence times. This can be seen through Figure 47, where the ATDs of pyrimidine⁺(HCN)_n; n=0-4 are matching.

Equilibrium constant was measured at different temperatures following equation (7.7):

$$K_{eq} = \frac{[C_4H_4N_2^+(HCN)_n]}{[C_4H_4N_2^+(HCN)_{n-1}][HCN]} = \frac{I[C_4H_4N_2^+(HCN)_n]}{I[C_4H_4N_2^+(HCN)_{n-1}] \cdot P_{HCN}} \quad (7.7)$$

where $I[C_4H_4N_2^+(HCN)_{n-1}]$, $I[C_4H_4N_2^+(HCN)_n]$ are the integrated intensities of ATDs of the reactant and product cluster ions of reaction (7.6), respectively and P_{HCN} is the pressure of HCN in atmosphere. van't-Hoff plots are then obtained by plotting the $R \ln K_{eq}$ versus $1000/T$, as displayed in Figure 48. From equation (7.5), ΔH° and ΔS° are readily obtained from the slope and intercept of Figure 48, respectively.

The binding energies and entropy changes involved in the association reaction (7.6) are tabulated in Table 49 which also includes the theoretically calculated binding energies. The good agreement among the experimentally measured and theoretically calculated binding energies verifies the adequacy of the used calculation level.

The binding energy values follow the usual descending trends as the degree of the solvation (n) increases which can be attributed to the repulsion of the HCN molecules and the delocalization of the positive charge.²² The entropy loss values (20-23 cal/mol. K) agree with the expected entropy loss accompanying the hydrogen bonds formation.^{22,25} Moreover, the measured binding energies fall in the usual range of the hydrogen bonding with aromatic hydrogen atoms rather than forming any stronger hydrogen bonds with distonic ions. Moreover, the measured binding energies of [Pyrimidine⁺(HCN) _{n}] (7-12 kcal/mol) are very similar to those measured in the solvation of benzene⁺, phenyl acetylene⁺ and pyridine⁺ rather than stronger hydrogen bonds observed in the solvated [H⁺pyridine(HCN) _{n}] clusters.

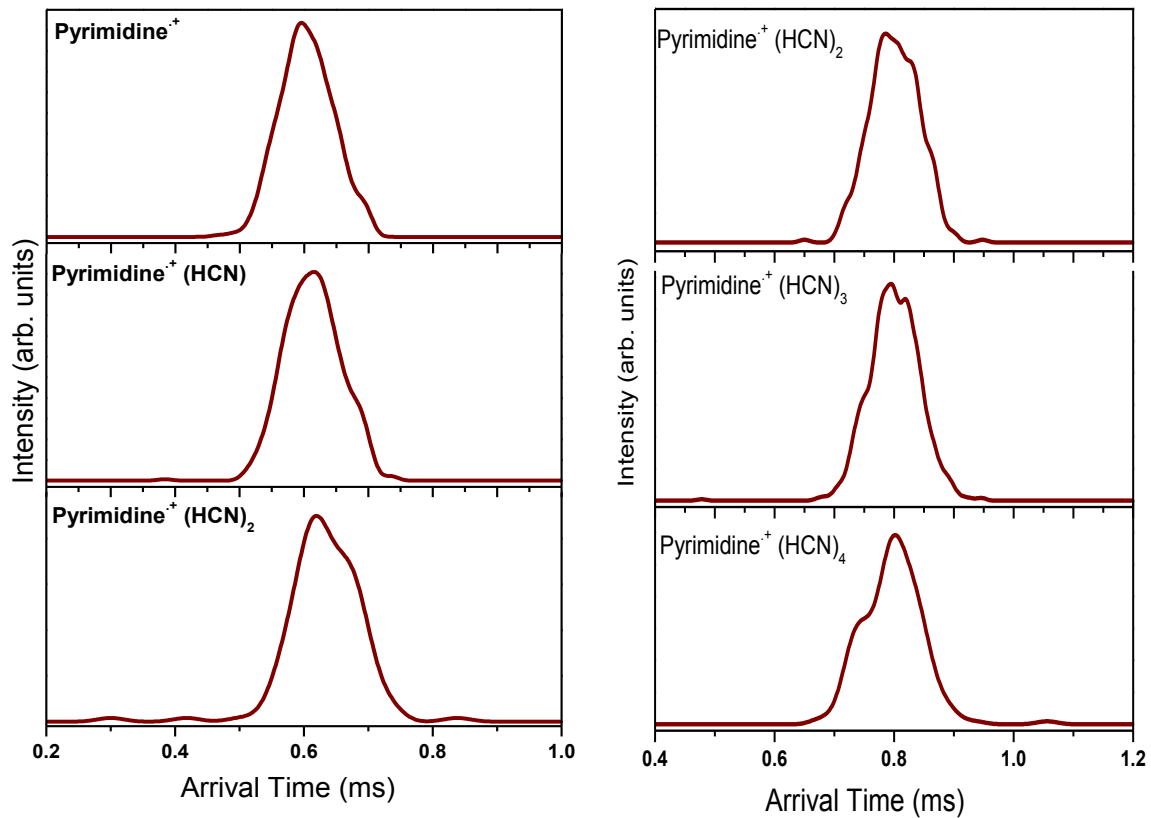


Figure 47. ATDs of [Pyrimidine⁺ (HCN)_n] (**Left**) where n=0-2; collected at 298 K with the drift cell containing 0.23 Torr of hydrogen cyanide. (**Right**) where n=2-4; collected at 213 K with the drift cell containing 0.16 Torr of hydrogen cyanide. The applied cell field and the injection energy were maintained at 4 V/cm and 12.4 (lab. frame), respectively

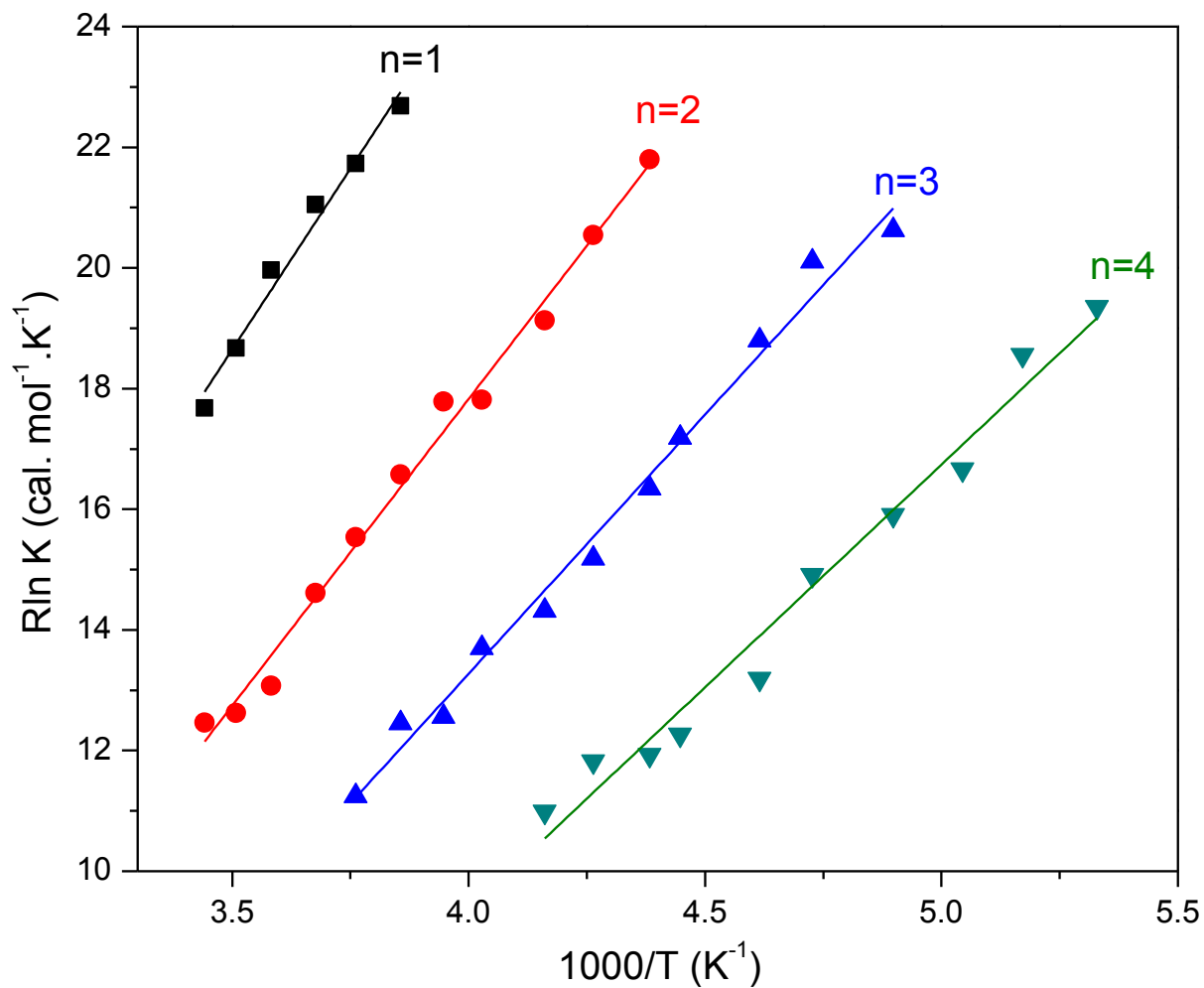


Figure 48. van't- Hoff plots for injecting pyrimidine radical cations into hydrogen cyanide (7.6) using an injection energy of 12.4 eV (lab.) and applied field of 4 V/cm. The drift cell temperature was varied between 184 K and 298 K

n	$-\Delta H^{\circ a}$	$-\Delta S^{\circ b}$	BE ^c	BE ^d
1	12.0	23.3	10.8	10.6
2	10.2	22.8	9.5	9.3
3	8.6	21.1	8.5	8.3
4	7.4	20.2	7.5	7.3

^a $\Delta H^{\circ}_{n-1,n}$ units are kcal/mol (± 1 kcal/ mol), ^b $\Delta S^{\circ}_{n-1,n}$ units are cal/mol.K (± 2 cal/mol. K), ^c Binding energy in kcal/ mol calculated by B3LYP/6-311++G(d,p) with ZPE included, and ^d Binding energy in kcal/ mol calculated by B3LYP/6-311++G(d,p) (with BSSE correction)

Table 49. Binding energy and entropy loss values for the association reaction (7.6) yielding $C_4H_4N_2^+(HCN)_n$; where n=1-4

7.4.2.3. Theoretical Calculations of the solvated pyrimidine radical cations by HCN molecules

Tables (50-53) display the optimized structures of the most stable solvated pyrimidine isomers $C_4H_4N_2^+(HCN)_n$; where n=1-4, calculated by the hybrid DFT B3LYP method, using the standard basis-set of 6-311++G(d,p).¹²³ Moreover, Table 49 displays the resulting binding energies corrected for zero-point vibrational energy (ZPVE) and for basis-set superposition error (BSSE).¹²² It is obvious that the theoretically calculated binding energy values are in good agreement with the experiment within the experimental accuracy ($\Delta H^{\circ}_{n-1,n} \pm 1.0$ kcal mol⁻¹). Therefore, we consider this level of theory to be enough for our computational jobs.

$C_4H_4N_2^+(HCN)$: The lowest energy isomer for $[C_4H_4N_2^+(HCN)]$ as displayed in Table 50 is (1-

a). (1-a) has hydrogen bonding nature of interaction in which N-atom of HCN molecule binds to

an aromatic H-atom (H_2) of the $C_4H_4N_2^+$ ion via 2.1 Å hydrogen bond. This site was expected to have the strongest bond between the N-center of the dipolar HCN molecule and the pyrimidine radical cation since (H_2) was predicted to have the most intense positive charge on $C_4H_4N_2^+$ at the B3LYP/6-311++G(d,p) calculation level (see Table 4).

The second lowest energy isomer (1-b) is another hydrogen bonded complex. The interaction of the N-center occurs with the CH-aromatic hydrogen atom (H_1) via 2.1 Å hydrogen bond. (1-b) was predicted to be only 0.4 kcal/mol higher in energy than the lowest energy isomer (1-a).

The third lowest energy isomer is (1-c) which has hydrogen bonded complex via 2.2 Å hydrogen bond between the aromatic H-atom (H_4) and the N-atom of the HCN molecule. (1-c) is higher than (1-a) by about 1.0 kcal/mol as predicted by the B3LYP/6-311++G(d,p) level of calculations.

$C_4H_4N_2^+(HCN)_2$: As displayed in Table 51, the lowest energy isomer predicted by B3LYP/6-311++G(d,p) calculations is (2-a) which has a symmetric hydrogen bonded structure. (2-a) has the two HCN molecules to be hydrogen bonded through their N-atoms to both of aromatic hydrogen atoms (H_2) via 2.1 Å hydrogen bonds. Therefore, internal solvation is preferred in $[C_4H_4N_2^+(HCN)_2]$, in contrast to the previously investigated cations, benzene, phenyl acetylene, pyridine and H^+ pyridine, which all required three HCN molecules or more to have internal solvation energetically favored over the external solvation pattern.

The second lowest energy isomer has the structure of (2-b) in which the two HCN molecules are hydrogen bonding to two CH-aromatic hydrogen atoms in the meta position to each other via 2.1 Å hydrogen bonds. This isomer was predicted to be at only 0.2 kcal/mol higher level in energy than the lowest energy $C_4H_4N_2^+(HCN)_2$ isomer.

The externally solvated isomer is predicted to be at 1.1 kcal/mol higher in energy than (2-a), as displayed in structure (2-c) in Table 51. In (2-c), the second HCN molecule binds through a 2.1 Å hydrogen bond to the first one.

C₄H₄N₂⁺(HCN)₃ : As displayed in Table 52, (3-a) is the lowest energy isomer predicted to have a symmetrically hydrogen bonded complex with 2.1 Å hydrogen bonds. The three HCN molecules are hydrogen bonded to three CH-aromatic hydrogen atoms in the meta-position to each other.

The second lowest energy isomer (3-b) is predicted to be 0.6 kcal/mol higher in energy than (3-a) at the B3LYP/6-311++G(d,p) level of theory. Internal solvation pattern is expressed in (3-b) where the third HCN molecule is hydrogen bonded to an ortho-HCN molecule forming a linear hydrogen bonded chain via 2.1 Å hydrogen bond.

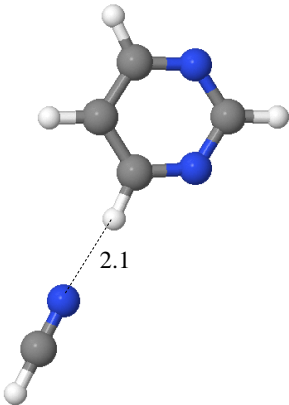
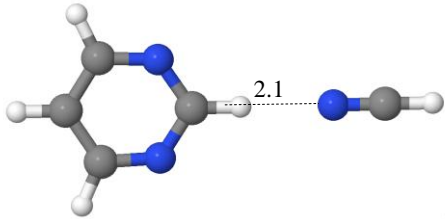
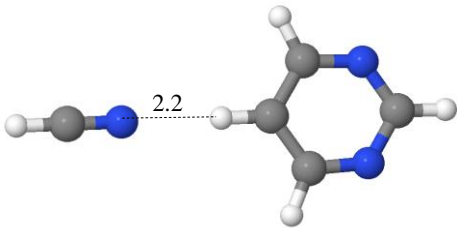
(3-c) isomer is the third lowest energy C₄H₄N₂⁺(HCN)₃ isomer, in which the three HCN molecules are hydrogen bonded to three different CH-aromatic hydrogen atoms, namely, to (H₂ and H₃) of the core C₄H₄N₂⁺. (3-c) is predicted to be 1.5 kcal/mol higher in energy than the lowest energy isomer (3-a).

C₄H₄N₂⁺(HCN)₄ : As displayed in Table 53, the lowest energy isomer (4-a) has the fourth HCN molecule to be hydrogen bonded to another HCN molecule forming a linear hydrogen bonded chain via 2.1 Å hydrogen bond.

The second lowest energy isomer (4-b) has very similar structure to (4-a). However, the fourth HCN molecule was predicted to be hydrogen bonded to the HCN molecule hydrogen bonded to another aromatic hydrogen atom (H₁) forming a linear hydrogen bonded chain via 2.1 Å

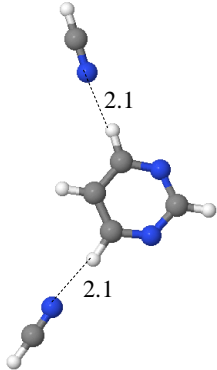
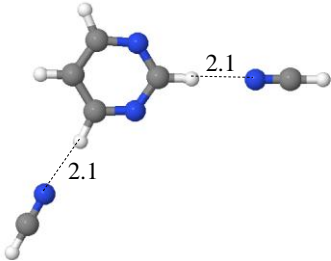
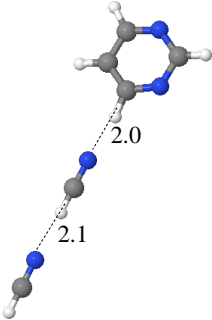
hydrogen bond. Due to the similarity in structures between (4-a) and (4-b), the latter is less stable than the former by only 0.3 kcal/mol.

The third lowest energy $[C_4H_4N_2^+(HCN)_4]$ isomer has the structure displayed in Table 53 for (4-c). In (4-c) all the four HCN are hydrogen bonded to all the available four CH-aromatic hydrogen atoms filling the first solvation shell of the pyrimidine radical cation. (4-c) is 1.2 kcal/mol higher in energy than (4-a) as predicted from the B3LYP/6-311++G(d,p) calculations.

Name	Optimized Structure	Relative Energy ^a	Binding energy ^b
1-a		0.0	10.8 (*10.6)
1-b		0.4	10.4 (*10.2)
1-c		1.0	9.8 (*9.6)

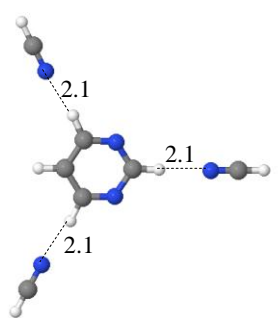
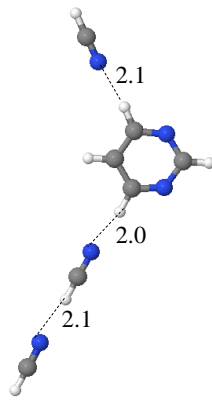
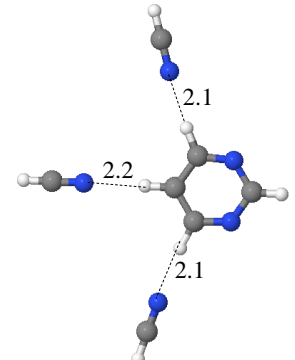
^a in kcal/mol (corrected for ZPE) ^b in kcal/mol *(corrected for ZPE and BSSE)

Table 50. Theoretically optimized structures using B3LYP/6-311++G(d,p) of $[C_4H_4N_2^+(HCN)]$. Distances are in Angstroms

Name	Optimized Structure	Relative Energy ^a	Binding energy ^b
2-a		0.0	9.5 (*9.3)
2-b		0.2	9.3 (*9.1)
2-c		1.1	8.4 (*8.2)

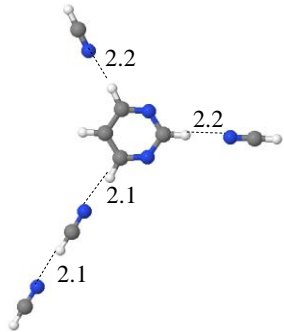
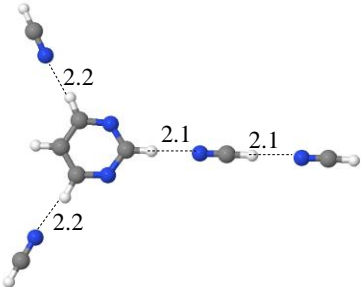
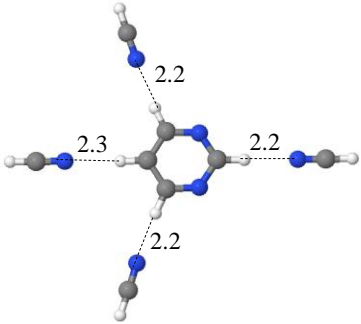
^a in kcal/mol (corrected for ZPE) ^b in kcal/mol *(corrected for ZPE and BSSE)

Table 51. Theoretically optimized structures using B3LYP/6-311++G(d,p) of $[C_4H_4N_2^+(HCN)_2]$. Distances are in Angstroms

Name	Optimized Structure	Relative Energy ^a	Binding energy ^b
3-a		0.0	8.5 (*8.3)
3-b		0.6	7.9 (*7.7)
3-c		1.5	7.0 (*6.8)

^a in kcal/mol (corrected for ZPE) ^b in kcal/mol *(corrected for ZPE and BSSE)

Table 52. Theoretically optimized structures using B3LYP/6-311++G(d,p) of $[\text{C}_4\text{H}_4\text{N}_2^+(\text{HCN})_3]$. Distances are in Angstroms

Name	Optimized Structure	Relative Energy ^a	Binding energy ^b
4-a		0.0	7.5 (*7.3)
4-b		0.3	7.2 (*7.0)
4-c		1.2	6.3 (*6.2)

^a in kcal/mol (corrected for ZPE) ^b in kcal/mol *(corrected for ZPE and BSSE)

Table 53. Theoretically optimized structures using B3LYP/6-311++G(d,p) of $[C_4H_4N_2^+(HCN)_4]$. Distances are in Angstroms

7.5. Reaction of Acetylene radical cation and Hydrogen cyanide molecules in the gas phase

7.5.1. Introduction

HCN is a commonly observed molecule in the interstellar clouds. In fact, after N_2 , HCN is one of the most common nitrogen containing interstellar species.¹⁶³ Moreover, HCN is formed in combustion processes and therefore HCN reactions can be involved in soot formation by either neutral or cationic reactions.¹⁶³

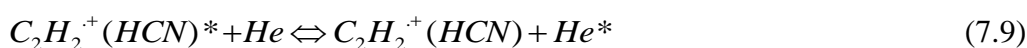
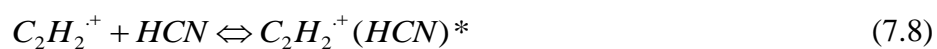
Rotational and rovibrational spectroscopy have been used to identify more than 150 molecular species in space. Some direct attempts to find interstellar pyrimidine haven't conclusively proved its presence.¹⁷⁴ A line fits nicely to pyrimidine spectrum was located but it is not yet enough to prove the presence of pyrimidine in space.¹⁷⁵ However, pyrimidine was detected in the meteorites and new experiments verified pyrimidine to be a possible source of uracil RNA bases under space like conditions.¹⁴⁴

Ion-molecule reactions represent one of the main sources of the large molecules' formation. They occur in faster rates than neutral-neutral reactions due to the electrostatic nature of the interaction between the ions and the molecular electron clouds. Moreover, ion-molecule reactions don't typically include reaction barriers.^{11,174}

The presence of high energy isomers was proven in the interstellar medium. Isomers rather than the global minimum can be formed and take a part in subsequent reactions.¹⁷⁴ For example, hexapentaenyldiene (C_6H_2) has been detected in space although it is less stable than the corresponding global minimum by more than 50 kcal/mol. Therefore, thermodynamic considerations may be irrelevant in low temperature interstellar chemistry.¹⁷⁴

The $C_2H_2^+$ and HCN reaction has been experimentally investigated to get the rate constants for the various production channels. For instance, McEwan and co-workers, have reported a rate constant of $3.6 \times 10^{-10} \text{ cm}^3 \text{ molecule}^{-1} \text{ s}^{-1}$ and the reaction expressed two major channels. Namely the proton transfer channel (66%) leading to H_2CN^+ and the adduct formation channel (34%) leading to $C_3H_2N^+$.¹⁷⁶ Moreover, Schiff and Bohme have reported a similar rate constant of $3.9 \times 10^{-10} \text{ cm}^3 \cdot \text{molecule}^{-1} \cdot \text{s}^{-1}$ but the association adduct $[C_2H_2^+ \cdot HCN]$ was formed at a branching ratio of 0.9 in the presence of He as a third body. The collisions with He atoms have stabilizing effect that leads to the predominance of the adduct formation. In addition, Knight et al. have reported a similar rate of that reaction of $3.7 \times 10^{-10} \text{ cm}^3 \cdot \text{molecule}^{-1} \cdot \text{s}^{-1}$. However, they estimated the branching ratios to be (80% for $[C_2H_2^+ \cdot HCN]$, 15% for $H_2C_3N^+$, and 5% for H_2CN^+)¹⁷⁷

From the previously reported studies, the reaction of HCN with $C_2H_2^+$ can be represented by the following mechanism:



In the second step of the mechanism, the excited adduct formed in the first step is stabilized by helium atom collisions against unimolecular dissociation.

A fast ion-dipole reaction between $C_2H_2^+$ and HCN occurs to yield $C_3H_3N^+$. $C_3H_3N^+$ was presumed to yield the acrylonitrile ion. However, acrylonitrile is more than 45 kcal/mol less stable than the global minimum.¹⁷⁴ Bera et al. have studied theoretically the reaction of $C_2H_2^+$ with HCN molecule extensively. Their study showed that although HCC(H)NCH isomer is about 18 kcal/mol higher in energy than the global minimum, it can be formed in the interstellar

conditions since it represents the product of the direct association reaction of acetylene ion with hydrogen cyanide.³¹

In the current study, we examine the interaction of HCN molecules with the injected acetylene radical cation ($C_2H_2^+$). Such an experimental study can shed light on the possible formation of pyrimidine which can be formed from $C_2H_2^+$ and two HCN molecules. HCN^+ reaction with C_2H_2 was not examined because the ionization potential of HCN is higher (13.6eV) than that of C_2H_2 (11.2 eV). Therefore, charge transfer is expected to be the exclusive reaction channel.^{31,176} Although HCN^+ can be formed by cosmic ray ionization of HCN, the reactions of HCN^+ are insignificant in the interstellar reactions because its rapid removal through reactions with the predominant H_2 molecules which has a rate constant of $9 \times 10^{-10} \text{ cm}^3 \cdot \text{molecule}^{-1} \cdot \text{s}^{-1}$.¹⁷⁸



7.5.2. Results and discussion

$C_2H_2^+$ reacts with HCN molecules to give $H^+(HCN)$ through proton transfer channel and $C_3H_3N^+$ through the adduct formation channel which is greatly favored in the presence of buffer gas as shown in the bottom panel of Figure 49. This agrees with the previous studies reported by Schiff and Bohme, which estimated 90% of the product to be the association adduct ($C_2H_2^+ \cdot HCN$).¹⁷⁹

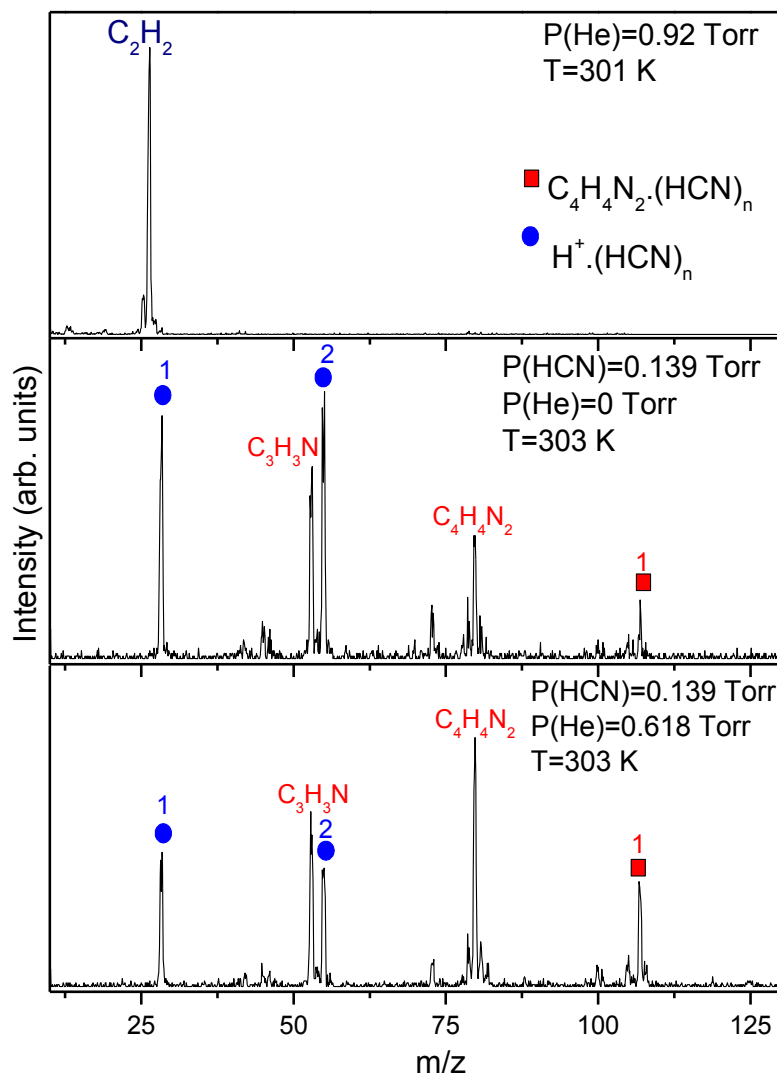


Figure 49. Mass-spectra obtained upon injecting acetylene radical cation in the mass-selection mode into the drift cell which contains a mixture of hydrogen cyanide (HCN) and helium buffer gas using injection energy of 11.8 eV(lab. frame) at room temperature and by applying a drift field of 6 V/cm

$C_2H_2^+$ reacts with HCN molecules to give $C_3H_3N^+$ through the adduct formation channel which further reacts with an additional HCN molecules and results in $C_4H_4N_2^+$ as shown in Figure 50. $C_4H_4N_2^+$ reacts once again with HCN molecule to form $[C_4H_4N_2^+ \cdot (HCN)]$ adduct which doesn't survive at higher drift cell temperatures as shown in the bottom channel of Figure

50 and it dissociates to yield $C_4H_4N_2^+$. However, $C_4H_4N_2^+$ shows exceptional thermal stability as it survives at high temperatures such as 625 K. Therefore, aromatic nature is claimed for $C_4H_4N_2^+$ adduct rather than $[C_4H_4N_2^+ \cdot (HCN)]$. However, further evidence is required to prove the identity of $C_4H_4N_2^+$.

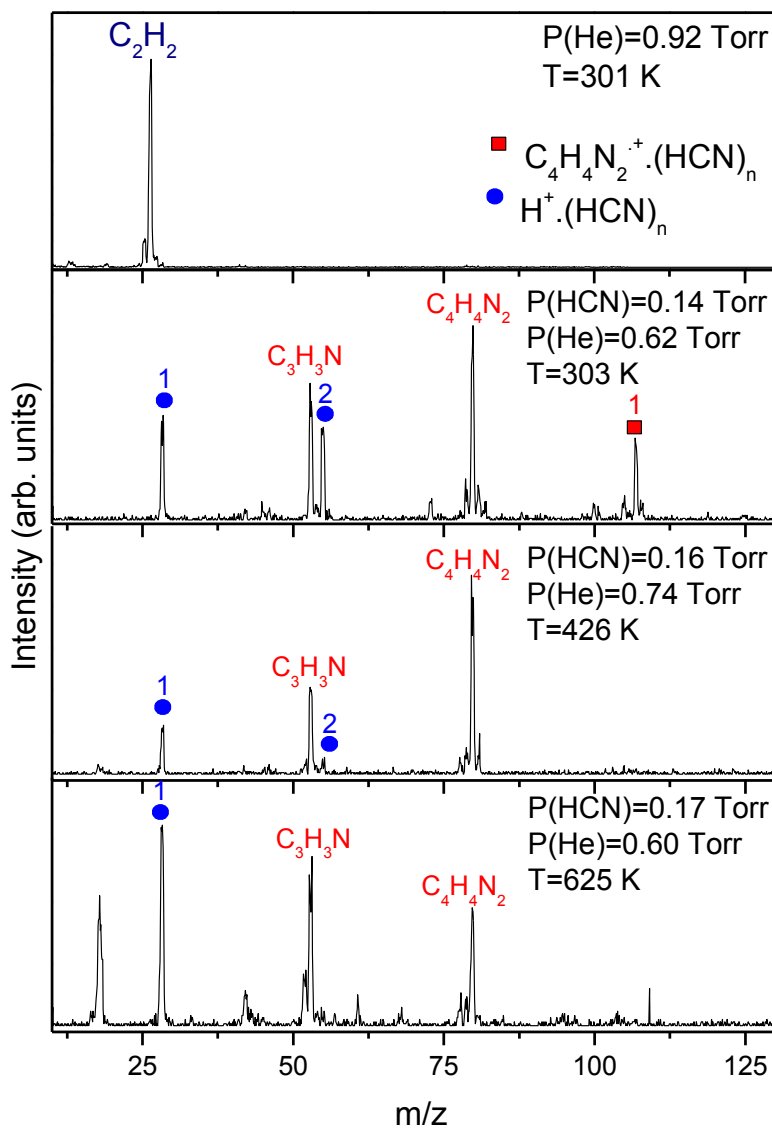


Figure 50. Mass-spectra resulting from the injection of acetylene radical cation ($C_2H_2^+$) in the mass-selection mode into hydrogen cyanide gas mixed with helium buffer gas in the drift cell at different temperatures using injection energy of 11.8 eV(lab.) and by applying a drift field of 6V/cm

7.5.2.1. Thermochemistry measurements

In order to investigate the identity of the $C_4H_4N_2$ radical cation, thermochemical measurements have been carried. The results are then compared with the previous results that we have obtained from solvation of the pyrimidine radical cation reaction with HCN molecules (section 7.4.2.)

As shown below in Figure 51, the addition trend looks very similar to what was observed in the pyrimidine case displayed above in Figure 46. Moreover, the binding energy and entropy loss have been experimentally measured by measuring the equilibrium constant of the reaction (7.11) at different temperatures.



Moreover, as a good check for equilibrium state establishments, the overlap in ATDs of the $C_4H_4N_2^+/C_4H_4N_2^+(HCN)$ couple can be used. An excellent matching between the ATDs can be seen in Figure 52. Equation (7.12) has been used to get the equilibrium constant at different temperatures. By using the resultant K_{eq} values, van't-Hoff plot was constructed and it is displayed below in Figure 53 and Table 54.

$$K_{eq} = \frac{[C_2H_2^+(HCN)_3]}{[C_2H_2^+(HCN)_2][HCN]} = \frac{I[C_2H_2^+(HCN)_3]}{I[C_2H_2^+(HCN)_2] \cdot P_{HCN}} \quad (7.12)$$

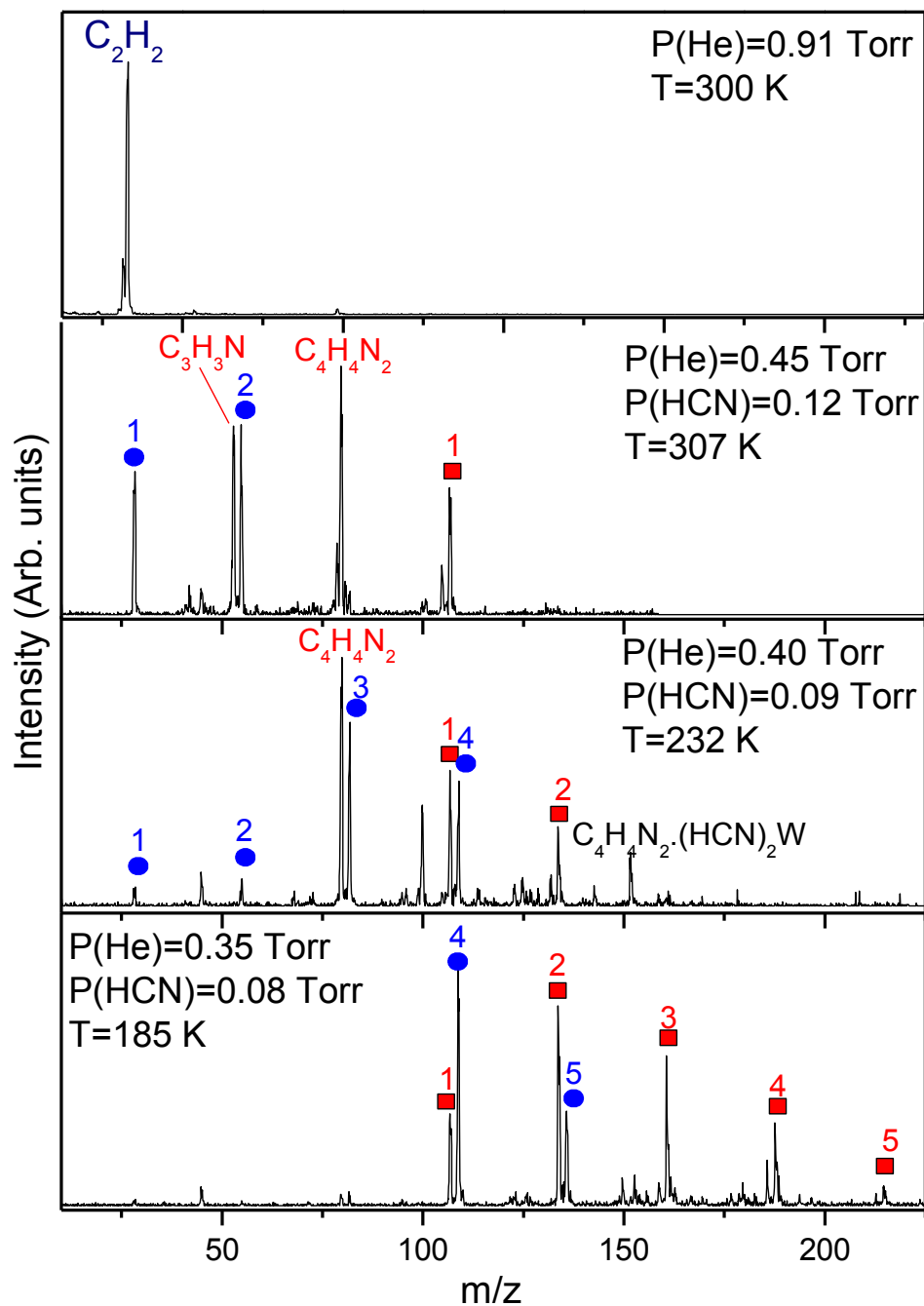


Figure 51. Mass-spectra obtained through thermochemistry measurements of association reaction (7.11) upon injecting acetylene radical cation in the mass-selection mode into a mixture of HCN and helium gases at different temperatures

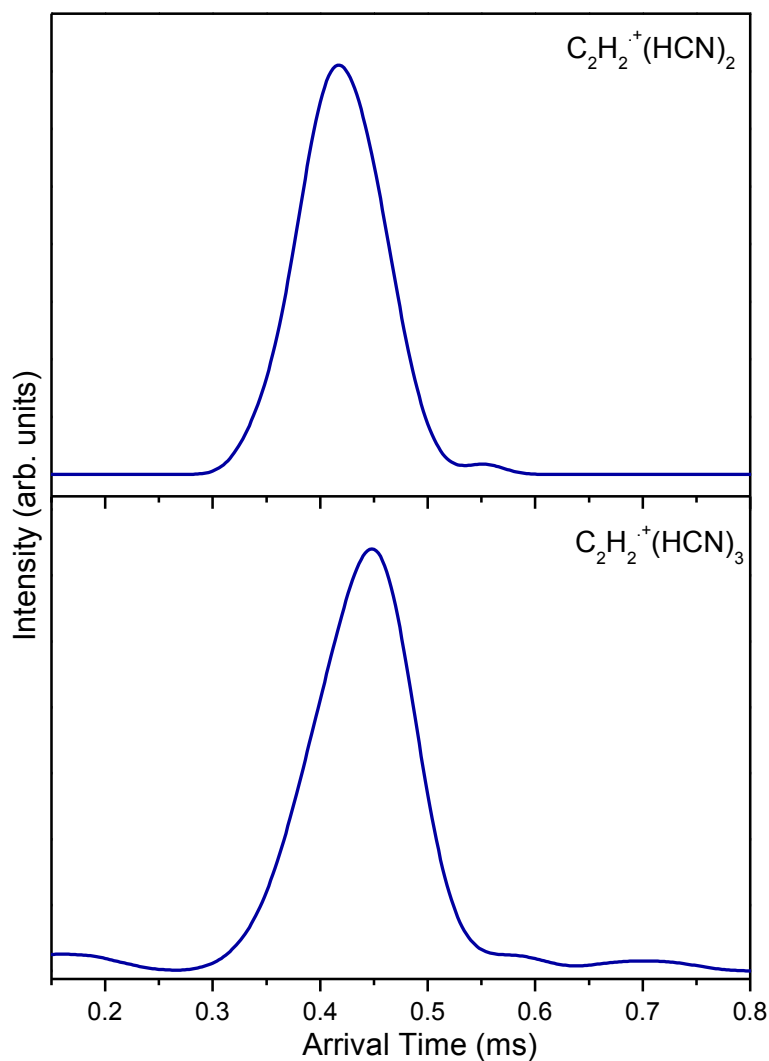


Figure 52. ATDs matching of $C_2H_2^+(HCN)_2$ and $C_2H_2^+(HCN)_3$ obtained at 309 K by applying a drift field of 4 V/cm and using an injection energy of 11.8 eV (lab. frame)

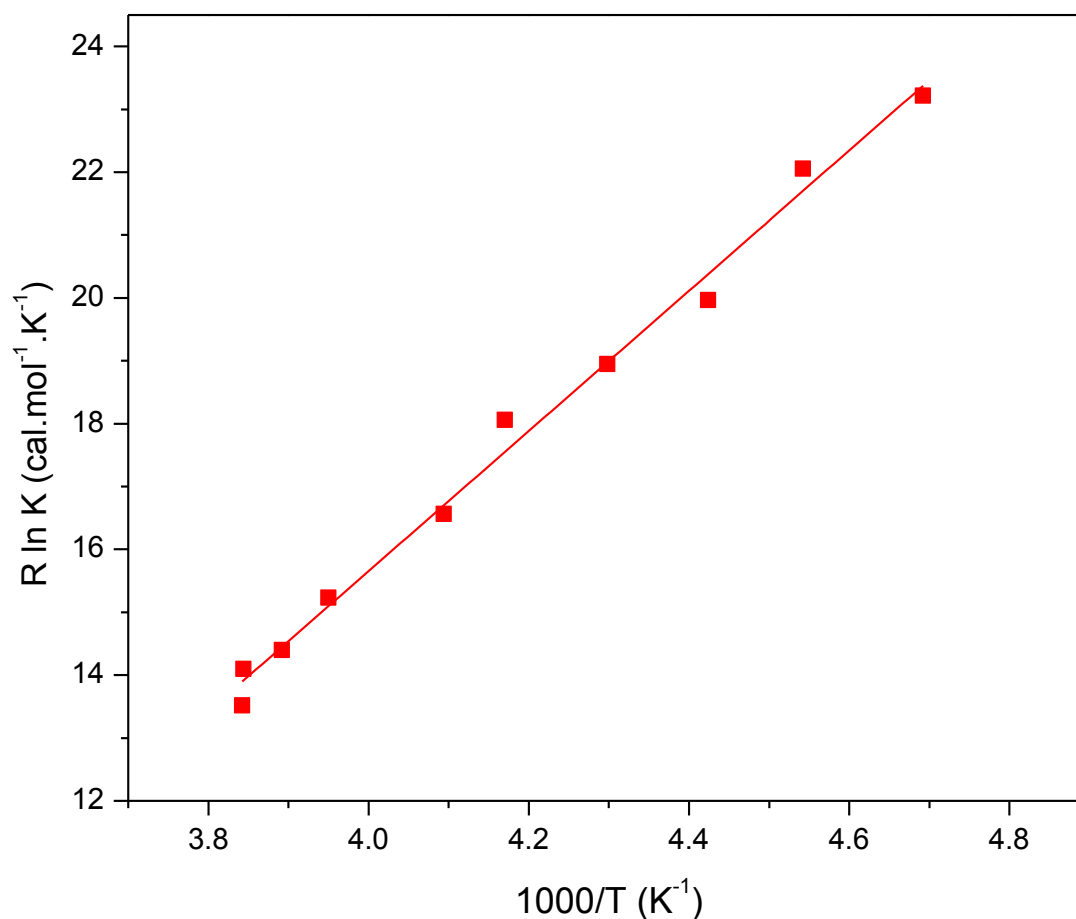


Figure 53. van't-Hoff plot for reaction (7.11) obtained upon injecting acetylene radical cation into the drift cell which contains HCN and He mixture at different drift cell temperatures

Source	Investigated ion	$-\Delta H^{\circ a}$	$-\Delta S^{\circ b}$
$C_2H_2(HCN)_2$	$C_2H_2(HCN)_3$	11.2	28.9
Pyrimidine	$C_4H_4N_2.(HCN)$	12.0	23.3

^a $\Delta H^{\circ}_{n-1,n}$ units are kcal/mol (± 1 kcal/mol), ^b $\Delta S^{\circ}_{n-1,n}$ units are cal/mol.K (± 2 cal/mol.K)

Table 54. Comparison of the thermochemistry values obtained for formation of $C_4H_4N_2^+(HCN)$ complex from two different sources

7.5.2.2. Coexpansion of acetylene and hydrogen cyanide mixture

As a further check for the aromatic identity for the preformed $C_4H_4N_2^+$ through the $C_2H_2^+/HCN$ reaction, coexpansion of the two gases has been launched and it resulted in the mass-spectrum displayed in Figure 54. Exceptional stability of the peak at $m/z=80$ amu; $[C_4H_4N_2^+]$ can be inferred from its abundance in the mass-spectrum and it implies its aromatic nature. Moreover, the base peaks observed at $m/z=159$ amu; $[C_4H_4N_2 \cdot C_5H_5N]^+$ which is expected to have an aromatic nature, similar to that observed in the previously reported stable benzene-pyridine adduct.¹⁶ Other peaks are observed as a result of acetone stabilizer that is mixed with acetylene.

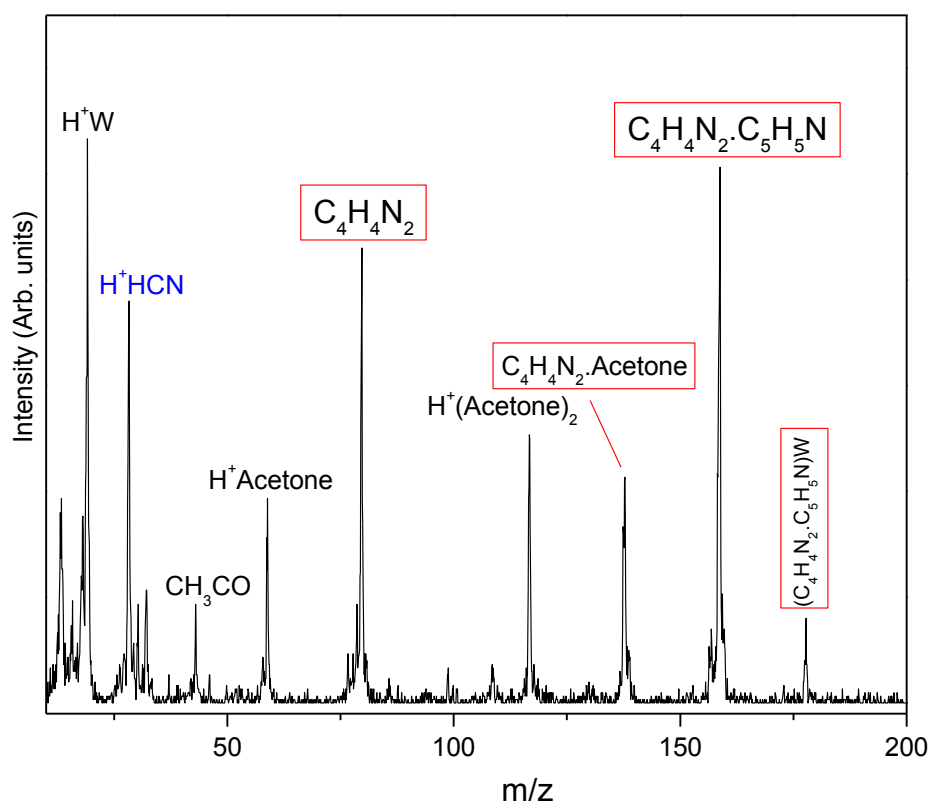


Figure 54. A representative mass-spectrum obtained upon injecting hydrogen cyanide in the RF-mode after coexpansion of HCN and C_2H_2 (from 1% C_2H_2/He) at 335 K. The drift cell contains 4.4 Torr of helium buffer gas

7.6. Summary and Conclusions

Equilibrium measurements have been utilized to investigate the association reactions of HCN molecules with pyridine, protonated pyridine and pyrimidine cations in the gas phase. Pyridine radical cation can bind to HCN molecules either through weak $\text{CH}^{\delta+}\cdots\text{N}$ or $\text{NH}^+\cdots\text{N}$ stronger hydrogen bonds forming distonic ions. Binding energies and entropy changes were measured for pyridine radical cation sequential interactions with four HCN molecules showed that weak ion-dipole interaction between HCN molecule's N-atom and the aromatic N-atom is formed. In contrast, the binding of HCN with protonated pyridine cation occurs through stronger $\text{NH}^+\cdots\text{N}$ hydrogen bonds. The difference in binding energies of HCN molecules with pyridine and H^+ pyridine cations reflects the variation of the solvated structures. Therefore, pyridine radical cation is not expected to have a distonic ion structure in the resulting $[\text{C}_5\text{H}_5\text{N}^+(\text{HCN})_n]$.

In addition, the binding energies and entropy changes of the association reaction of four HCN molecules with pyrimidine radical cation were measured for the individual solvation steps in the gas phase. Similar binding strength of the formed hydrogen bonds between HCN and pyrimidine radical cations with benzene and phenyl acetylene was noticed. Moreover, thermochemistry measurements have been employed to examine the identity of $\text{C}_4\text{H}_4\text{N}_2^+$ yielded through the reaction of C_2H_2^+ with HCN molecules and pyrimidine-like structure is proposed.

DFT calculations were employed to investigate the theoretically predicted structures. The calculated binding energies of the step wisely added HCN molecules are compared with the corresponding measured values. Very good agreement among the theoretically predicted values and the corresponding experimentally measured values verifies the adequacy of our calculation level of the theory.

Chapter 8: Conclusions and future outlooks

The research covered in this dissertation focuses on two dimensional study of different ion-molecule reactions. Experimental mobility and thermochemistry measurements and theoretical calculations have been combined to comprehend the parameters that can control the interaction process clearly. The first route examined the interaction of three different solvents in interaction with the same cation. Namely, experimental and theoretical studies investigated the interaction of water, methanol and acetonitrile solvents with the mass-selected protonated pyrimidine cation. The ion was selected to be protonated pyrimidine because it biological significance where pyrimidine constitutes base blocks of DNA bases. Thus, its interaction with polar solvents is of fundamental interest from chemical and biochemical points of view. These experiments showed that the proton affinity controls the ion-molecule binding energies and thus increases in the order of water<methanol<acetonitrile. Moreover, these studies accounted for the protonated solvent clusters observed in both of water and methanol cases, with clear size dependence. In contrast, they weren't observed in the acetonitrile study at all. Theoretical studies accounted for the observed protonated clusters where water or methanol molecules bind to each other forming a cluster with higher proton affinities than pyrimidine. The formed solvent clusters are able to abstract the proton yielding the observed protonated solvent cluster ion and neutral pyrimidine following dissociative proton transfer reaction scheme.

The second investigation route was based on examination of the ion-molecule starting from various ions in their interactions with the same solvent. Namely, the interactions of HCN molecules with benzene, phenyl acetylene, pyridine, protonated pyridine, and pyrimidine cations in the gas-phase have been investigated.¹⁶⁴ HCN molecule has been chosen due to its presence in interstellar medium and its possible involvement in the prebiotic synthesis. These studies employed theoretical calculations to support and account for the experimentally observed results through thermochemistry measurements. Weak hydrogen bonds were formed between the HCN molecule and the investigated cation in most of the cases implying the formation of hydrogen bonds with the aromatic hydrogen atoms. Whereas, strong hydrogen bond interaction was employed in the protonated pyridine interaction with HCN molecules, similar to its hydration study. Also, ion-dipole interaction was observed in pyridine radical cation solvation by HCN molecules. Moreover, thermochemistry measurements and high temperatures studies have been employed to examine the identity of $C_4H_4N_2^+$ ion resulting from the reaction of $C_2H_2^+$ with two HCN molecules; pyrimidine like structure possibility was verified.

The electrostatic nature of the ion-molecule complexes investigated in the current research promotes further studies to be launched. One study will examine the electrostatic portion of the ion-molecule interaction in detail where an ion with various charge intensities will interact with the same molecule and the interaction energy is expected to vary in direct proportionality with the charge state of the investigated ion. Such study was initiated for phenyl acetylene cation in different charge intensities. Namely, the charge is considered to be controlled by the size of the specified ion; assuming even distribution of charges. The study includes the interaction of $[(\text{phenyl acetylene})_n]^+$ with HCN molecules where $n=1-4$. This study is expected to shed light not only on the electrostatic nature of the ion-molecule interaction but also, the other

parameters that impact such a process such as the steric effects. A representative mass-spectrum of the addition of HCN molecules onto injected [phenyl acetylene)_n]⁺ is shown in Appendix A. Such a study will provide an extra dimension for the previously covered two dimensions through this dissertation.

List of References

- (1) Armentrout, P. B. In *Ion Mobility Spectrometry - Mass Spectrometry: Theory and Applications*; Wilkins, C. L., Trimpin, S., Eds.; CRC Press: Boca Raton, FL, 2011, p 31-52.
- (2) Ibrahim, Y.; Alsharaeh, E.; Mabrouki, R.; Momoh, P.; Xie, E.; El-Shall, M. S. *J. Phys. Chem. A* **2008**, *112*, 1112-1124.
- (3) Kim, S. K.; Lee, W.; Herschbach, D. R. *J. Phys. Chem.* **1996**, *100*, 7933-7937.
- (4) Dugourd, P.; Hudgins, R. R.; Clemmer, D. E.; Jarrold, M. F. *Rev. Sci. Instrum.* **1997**, *68*, 1122-1129.
- (5) Donald, W. A.; Leib, R. D.; Demireva, M.; Negru, B.; Neumark, D. M.; Williams, E. R. *J. Phys. Chem. A* **2011**, *115*, 2-12.
- (6) Zwier, T. S. *Ann. Rev. Phys. Chem.* **1996**, *47*, 205-241.
- (7) Kebarle, P. *Ann. Rev. Phys. Chem.* **1977**, *28*, 445-476.
- (8) Belau, L.; Wilson, K. R.; Leone, S. R.; Ahmed, M. *J. Phys. Chem. A* **2007**, *111*, 10075-10083.
- (9) Enomoto, S.; Miyazaki, M.; Fujii, A.; Mikami, N. *J. Phys. Chem. A* **2005**, *109*, 9471-9480.
- (10) Miyazaki, M.; Fujii, A.; Ebata, T.; Mikami, N. *Chem. Phys. Lett.* **2004**, *399*, 412-416.
- (11) Garver, J. M.; Fang, Y.-r.; Eyet, N.; Villano, S. M.; Bierbaum, V. M.; Westaway, K. C. *J. Amer. Chem. Soc.* **2010**, *132*, 3808-3814.
- (12) Harada, M.; Watanabe, I.; Watarai, H. *Chem. Phys. Lett.* **1999**, *301*, 270-274.
- (13) Petersen, P. B.; Saykally, R. J. *Annu. Rev. Phys. Chem.* **2006**, *57*, 333-364.
- (14) Kebarle, P.; Searles, S. K.; Zolla, A.; Scarborough, J.; Arshadi, M. *J. Amer. Chem. Soc.* **1967**, *89*, 6393-9.
- (15) Gao, B.; Wyttenbach, T.; Bowers, M. T. *J. Am. Chem. Soc.* **2009**, *131*, 4695-4701.
- (16) El-Shall, M. S.; Ibrahim, Y. M.; Alsharaeh, E. H.; Meot-Ner, M.; Watson, S. P. *J. Am. Chem. Soc.* **2009**, *131*, 10066-10076.
- (17) Ibrahim, Y.; Mabrouki, R.; Meot-Ner, M.; El-Shall, M. S. *J. Phys. Chem. A* **2007**, *111*, 1006-1014.
- (18) Momoh, P. O.; El-Shall, M. S. *Phys. Chem. Chem. Phys.* **2008**, *10*, 4827-4834.
- (19) Momoh, P. O.; Hamid, A. M.; Abrash, S. A.; El-Shall, M. S. *J. Chem. Phys.* **2011**, *134*, 204315-13.
- (20) Ibrahim, Y. M.; Meot-Ner, M.; Alshraeh, E. H.; El-Shall, M. S.; Scheiner, S. J. *Am. Chem. Soc.* **2005**, *127*, 7053-7064.
- (21) Meot-Ner, M. *J. Am. Chem. Soc.* **1979**, *101*, 2396-403.

- (22) Meot-Ner, M. *Chem. Rev.* **2005**, *105*, 213-284.
- (23) Meot-Ner, M.; Speller, C. V. *The Journal of Physical Chemistry* **1989**, *93*, 3663-3666.
- (24) Bowers, M. T.; Marshall, A. G.; McLafferty, F. W. *J. Phys. Chem.* **1996**, *100*, 12897-12910.
- (25) Meot-Ner, M. *J. Phys. Chem.* **1987**, *91*, 417-26.
- (26) Froyd, K. D.; Lovejoy, E. R. *J. Phys. Chem. A* **2012**.
- (27) Chiang, C.-T.; Freindorf, M.; Furlani, T.; DeLeon, R. L.; Richard, J. P.; Garvey, J. *F. J. Phys. Chem. A* **2007**, *111*, 6068-6076.
- (28) Nagy, A.; Fulara, J.; Maier, J. P. *Journal of the American Chemical Society* **2011**, *133*, 19796-19806.
- (29) Bohme, D. K.; Wodek, S.; Zimmerman, J. A.; Eyler, J. R. *Formation of C₁₀H₈⁺ from the benzene radical cation: a case for the growth of polycyclic aromatic hydrocarbon ions by ion/molecule reactions in the gas phase*, Dep. Chem., Univ. Florida, Gainesville, FL, USA., 1991.
- (30) Richter, H.; Howard, J. B. *Progress in Energy and Combustion Science* **2000**, *26*, 565-608.
- (31) *NIST Chemistry WebBook*.
- (32) El-Shall, M. S.; Ibrahim, Y. M.; Mabrouki, R. M.; Meot-Ner, M. *Abstracts of Papers, 229th ACS National Meeting, San Diego, CA, United States, March 13-17, 2005* **2005**, PHYS-442.
- (33) Ibrahim, Y.; Alsharaeh, E.; Dias, K.; Meot-Ner, M.; El-Shall, M. S. *J. Am. Chem. Soc.* **2004**, *126*, 12766-12767.
- (34) Momoh, P. O.; Hamid, A. M.; Abrash, S. A.; El-Shall, M. S. *J. Chem. Phys.* **2011**, *134*, 204315.
- (35) Soliman, A. R.; Hamid, A. M.; Abrash, S. A.; El-Shall, M. S. *J. Chem. Phys. Lett.* **2011**, *in press*.
- (36) Gao, B.; Wytttenbach, T.; Bowers, M. T. *J. Phys. Chem. B* **2009**, *113*, 9995-10000.
- (37) Liu, D.; Wytttenbach, T.; Bowers, M. T. *J. Am. Chem. Soc.* **2006**, *128*, 15155-15163.
- (38) Wytttenbach, T.; Gidden, J.; Bowers, M. T. In *Ion Mobility Spectrometry - Mass Spectrometry: Theory and Applications*; Wilkins, C. L., Trimpin, S., Eds.; CRC Press: Boca Raton, FL, 2011, p 3-30.
- (39) Wytttenbach, T.; Bowers, M. T. *Chem. Phys. Lett.* **2009**, *480*, 1-16.
- (40) Rusyniak, M.; Ibrahim, Y.; Alsharaeh, E.; Meot-Ner, M.; El-Shall, M. S. *J. Phys. Chem. A* **2003**, *107*, 7656-7666.
- (41) Rusyniak, M. J.; Ibrahim, Y. M.; Wright, D. L.; Khanna, S. N.; El-Shall, M. S. *J. Am. Chem. Soc.* **2003**, *125*, 12001-12013.
- (42) Momoh, P. O.; Xie, E.; Abrash, S. A.; Meot-Ner, M.; El-Shall, M. S. *J. Phys. Chem. A* **2008**, *112*, 6066-6073.

- (43) Keesee, R. G.; Castleman, A. W., Jr. *J. Phys. Chem. Ref. Data* **1986**, *15*, 1011-71.
- (44) Kanu, A. B.; Dwivedi, P.; Tam, M.; Matz, L.; Hill, H. H., Jr. *J. Mass Spectrom.* **2008**, *43*, 1-22.
- (45) Mabourki, R.; Ibrahim, Y.; Xie, E.; Meot-Ner, M.; El-Shall, M. S. *Chem. Phys. Lett.* **2006**, *424*, 257-263.
- (46) Desiraju, G. R. *Nature* **2001**, *412*, 397-400.
- (47) Meot-Ner, M. *Chem. Rev. (Washington, DC, U. S.)* **2005**, *105*, 213-284.
- (48) Mabrouki, R.; Ibrahim, Y.; Xie, E.; Meot-Ner, M.; El-Shall, M. S. *J. Phys. Chem. A* **2006**, *110*, 7334-7344.
- (49) Ben-Naim, A. *Hydrophobic interactions*; Plenum: New York, 1980.
- (50) Han, F.; Du, Y.; Cheng, S.; Zhou, Q.; Chen, C.; KeyongHou; Wang, W.; Li, H. *Int. J. Mass Spectrom.* **2012**, *309*, 13-21.
- (51) Cooks, R. G.; Ouyang, Z.; Takats, Z.; Wiseman, J. M. *Science* **2006**, *311*, 1566-1570.
- (52) Smith, J. N.; Keil, A.; Likens, J.; Noll, R. J.; Cooks, R. G. *Analyst* **2010**, *135*.
- (53) Krylov, E. V.; Nazarov, E. G. *Int. J. Mass Spectrom.* **2009**, *285*, 149-156.
- (54) Chen, L.; Gao, Y. Q.; Russell, D. H. *J. Phys. Chem. A* **2011**, *116*, 689-696.
- (55) Kemper, P. R.; Dupuis, N. F.; Bowers, M. T. *Int. J. Mass Spectrom.* **2009**, *287*, 46-57.
- (56) Clemmer, D. E.; Hudgins, R. R.; Jarrold, M. F. *Journal of the American Chemical Society* **1995**, *117*, 10141-10142.
- (57) Clemmer, D. E.; Jarrold, M. F. *Journal of Mass Spectrometry* **1997**, *32*, 577-592.
- (58) Mesleh, M. F.; Hunter, J. M.; Shvartsburg, A. A.; Schatz, G. C.; Jarrold, M. F. *J. Phys. Chem.* **1996**, *100*, 16082-16086.
- (59) Momoh, P. O.; Abrash, S. A.; Mabrouki, R.; El-Shall, M. S. *J. Am. Chem. Soc.* **2006**, *128*, 12408-12409.
- (60) Momoh, P. O.; El-Shall, M. S. *Chem. Phys. Lett.* **2007**, *436*, 25-29.
- (61) Zhao, Y.; Truhlar, D. G. *Acc. Chem. Res.* **2008**, *41*, 157-167.
- (62) Zhang, B.; Cai, Y.; Mu, X.; Lou, N.; Wang, X. *J. Chem. Phys.* **2002**, *117*, 3701-3710.
- (63) Dunning, T. H., Jr. **2000**, *104*, 9062-9080.
- (64) Mohajeri, A.; Shakerin, N. **2004**, *711*, 167-172.
- (65) Agarwal, J.; Turney, J. M.; Schaefer, H. F. *J. Phys. Chem. Lett.* **2011**, *2*, 2587-2592.
- (66) Yamabe, S.; Fukuda, T.; Yamazaki, S. *J. Phys. Chem. A* **2012**, *116*, 1289-1297.
- (67) Herbst, E. *Annu. Rev. Phys. Chem.* **1995**, *46*, 27-54.
- (68) Ard, S.; Garrett, W. R.; Compton, R. N.; Adamowicz, L.; Stepanian, S. G. *Chem. Phys. Lett.* **2009**, *473*, 223-226.
- (69) Mayer, P. M. *J. Phys. Chem. A* **1999**, *103*, 5905-5909.
- (70) Hirao, K.; Yamabe, S.; Sano, M. *The Journal of Physical Chemistry* **1982**, *86*, 2626-2632.

- (71) Horn, R.; Mestl, G.; Thiede, M.; Jentoft, F. C.; Schmidt, P. M.; Bewersdorf, M.; Weber, R.; Schlogl, R. *Phys. Chem. Chem. Phys.* **2004**, *6*, 4514-4521.
- (72) Huntress, W. T.; Baldeschwieler, J. D.; Ponnampereuma, C. *Nature* **1969**, *223*, 468-471.
- (73) Meot-Ner, M. *J. Amer. Chem. Soc.* **1978**, *100*, 4694-4699.
- (74) De La Haye, V.; Waite Jr, J. H.; Cravens, T. E.; Robertson, I. P.; Lebonnois, S. *Icarus* **2008**, *197*, 110-136.
- (75) Wincel, H. *Chem. Phys. Lett.* **2010**, *488*, 219-222.
- (76) Matthews, C. N.; Minard, R. D. *Faraday Discuss.* **2006**, *133*, 393-401.
- (77) Matthews, C. N.; Moser, R. E. *Nature* **1967**, *215*, 1230-1234.
- (78) Deakynne, C. A.; Meot-Ner, M.; Campbell, C. L.; Hughes, M. G.; Murphy, S. P. *J. Chem. Phys.* **1986**, *84*, 4958-69.
- (79) Momoh, P. O.; Hamid, A. M.; Soliman, A.-R.; Abrash, S. A.; El-Shall, M. S. *J. Phys. Chem. Lett.*, *2*, 2412-2419.
- (80) Alsharaeh, E. H.; Ibrahim, Y. M.; El-Shall, M. S. *J. Am. Chem. Soc.* **2005**, *127*, 6164-6165.
- (81) Rusyniak, M. J.; Ibrahim, Y. M.; Wright, D. L.; Khanna, S. N.; El-Shall, M. S. *J. Am. Chem. Soc.* **2003**, *125*, 12001-12013.
- (82) Rusyniak, M.; Ibrahim, Y.; Alsharaeh, E.; Meot-Ner, M.; El-Shall, M. S. *J. Phys. Chem. A* **2003**, *107*, 7656-7666.
- (83) El-Shall, M. S. *Acc. Chem. Res.* **2008**, *41*, 783-792.
- (84) A.W. Castleman, J.; Keese, R. G. *Clusters: Properties and Formation*, 1986.
- (85) Stein, G. D. *The Physics Teacher* **1979**, *17*, 503-512.
- (86) Bernstein, E. R. *Atomic and Molecular Clusters*, 1990; Vol. 68.
- (87) Yaws, C. L.; McGraw-Hill: 1999.
- (88) Smith, R. A.; Ditmire, T.; Tisch, J. W. G. *Review of Scientific Instruments* **1998**, *69*, 3798-3804.
- (89) Hagen, O. F.; Obert, W. *The Journal of Chemical Physics* **1972**, *56*, 1793-1802.
- (90) Fenn, J. B. *Int. J. Mass Spectrom.* **2000**, *200*, 459-478.
- (91) Kappes, M.; Leutwyler, S. *Molecular beams of clusters*.
- (92) Bush, M. F.; Forbes, M. W.; Jockusch, R. A.; Oomens, J.; Polfer, N. C.; Saykally, R. J.; Williams, E. R. *J. Phys. Chem. A* **2007**, *111*, 7753.
- (93) Ng, C. Y. In *Advances in Chemical Physics*; John Wiley & Sons, Inc.: 1982, p 263-362.
- (94) Vestal, M. L. *Chem. Rev.* **2001**, *101*, 361-375.
- (95) Evans, E. H.; Pretorius, W.; Ebdon, L.; Rowland, S. *Anal. Chem.* **1994**, *66*, 3400-3407.
- (96) Rejoub, R.; Morton, C. D.; Lindsay, B. G.; Stebbings, R. F. *J. Chem. Phys.* **2003**, *118*, 1756-1760.
- (97) Miller, P. E.; Denton, M. B. *J. Chem. Ed.* **1986**, *63*, 617.

- (98) Reuben, A. J.; Smith, G. B.; Moses, P.; Vagov, A. V.; Woods, M. D.; Gordon, D. B.; Munn, R. W. *Int. J. Mass Spectrom. and Ion Processes* **1996**, *154*, 43-59.
- (99) Campana, J. E.; Jurs, P. C. *Int. J. Mass Spectrom. and Ion Physics* **1980**, *33*, 119-137.
- (100) Campana, J. E. *Int. J. Mass Spectrom. and Ion Physics* **1980**, *33*, 101-117.
- (101) Tunstall, J. J.; Voo, A. C. C.; Taylor, S. *Rapid Communications in Mass Spectrometry* **1997**, *11*, 184-188.
- (102) Pedder, A. E.; Schaeffer, R. A. In *44th ASMS conference on Mass Spectrometry and Allied Topics* 1996.
- (103) Kemper, P. R.; Bowers, M. T. *J. Am. Soc. Mass Spectrom.* **1990**, *1*, 197-207.
- (104) Howdle, M. D.; Eckers, C.; Laures, A. M. F.; Creaser, C. S. *Int. J. Mass Spectrom.* **2010**, *298*, 72-77.
- (105) Krishnamurthy, M.; de Gouw, J. A.; Bierbaum, V. M.; Leone, S. R. *J. Phys. Chem.* **1996**, *100*, 14908-14913.
- (106) E. A. Mason, E. W. M. *Transport properties of ions in gases*; John Wiley & Sons, 1988.
- (107) Hourdakis, E.; Simonds, B. J.; Zimmerman, N. M. *Rev. Sci. Instrum.* **2006**, *77*, 034702-4.
- (108) Revercomb, H. E.; Mason, E. A. *Analytical Chemistry* **1975**, *47*, 970-983.
- (109) Mason, E. A.; McDaniel, E. W. **1988**.
- (110) Mason, E. A.; McDaniel, E. W. **1973**.
- (111) Baykut, G.; Halem, O. v.; Franzen, J.; Raether, O. In *Ion Mobility Spectrometry - Mass Spectrometry: Theory and Applications*; Wilkins, C. L., Trimpin, S., Eds.; CRC Press: Boca Raton, FL, 2011, p 53-74.
- (112) Shvartsburg, A. A.; Hudgins, R. R.; Dugourd, P.; Jarrold, M. F. *Chemical Society Reviews* **2001**, *30*, 26-35.
- (113) Wyttenbach, T.; Helden, G. v.; Batka, J. J. J.; Carlat, D.; Bowers, M. T. *J. Am. Soc. Mass Spectrom.* **1997**, *8*, 275-282.
- (114) Shvartsburg, A. A.; Jarrold, M. F. *Chemical Physics Letters* **1996**, *261*, 86-91.
- (115) Viehland, L. A.; Mason, E. A.; Morrison, W. F.; Flannery, M. R. *At. Data Nucl. Data Tables* **1975**, *16*, 495-514.
- (116) Mesleh, M. F.; Hunter, J. M.; Shvatsburg, A. A.; Schatz, G. C.; Jarrold, M. F. *J. Phys. Chem.* **1996**, *100*, 16082.
- (117) Armentrout, P. B. *J. Am. Soc. Mass Spectrom.* **2002**, *13*, 419-434.
- (118) Frisch, M. J. T., G. W.; Schlegel, H. B.; Scuseria, G. E.; Robb, M. A.; Cheeseman, J. R.; Scalmani, G.; Barone, V.; Mennucci, B.; Petersson, G. A.; Nakatsuji, H.; Caricato, M.; Li, X.; Hratchian, H. P.; Izmaylov, A. F.; Bloino, J.; Zheng, G.; Sonnenberg, J. L.; Hada, M.; Ehara, M.; Toyota, K.; Fukuda, R.; Hasegawa, J.; Ishida, M.; Nakajima, T.; Honda, Y.; Kitao, O.; Nakai, H.; Vreven, T.; Montgomery, Jr., J. A.; Peralta, J. E.; Ogliaro, F.; Bearpark, M.; Heyd, J. J.; Brothers, E.; Kudin, K. N.; Staroverov, V. N.; Kobayashi, R.; Normand, J.; Raghavachari, K.; Rendell, A.; Burant, J. C.; Iyengar, S. S.; Tomasi, J.; Cossi, M.; Rega, N.;

Millam, N. J.; Klene, M.; Knox, J. E.; Cross, J. B.; Bakken, V.; Adamo, C.; Jaramillo, J.; Gomperts, R.; Stratmann, R. E.; Yazyev, O.; Austin, A. J.; Cammi, R.; Pomelli, C.; Ochterski, J. W.; Martin, R. L.; Morokuma, K.; Zakrzewski, V. G.; Voth, G. A.; Salvador, P.; Dannenberg, J. J.; Dapprich, S.; Daniels, A. D.; Farkas, Ö.; Foresman, J. B.; Ortiz, J. V.; Cioslowski, J.; Fox, D. J. Gaussian, Inc., Wallingford CT, 2009. 2009.

(119) Gaussian 03 Revision C.02 Frisch, M. J. T., G. W.; Schlegel, H. B.; Scuseria, G. E.; Robb, M. A.; Cheeseman, J. R.; Montgomery, Jr., J. A.; Vreven, T.; Kudin, K. N.; Burant, J. C.; Millam, J. M.; Iyengar, S. S.; Tomasi, J.; Barone, V.; Mennucci, B.; Cossi, M.; Scalmani, G.; Rega, N.; Petersson, G. A.; Nakatsuji, H.; Hada, M.; Ehara, M.; Toyota, K.; Fukuda, R.; Hasegawa, J.; Ishida, M.; Nakajima, T.; Honda, Y.; Kitao, O.; Nakai, H.; Klene, M.; Li, X.; Knox, J. E.; Hratchian, H. P.; Cross, J. B.; Bakken, V.; Adamo, C.; Jaramillo, J.; Gomperts, R.; Stratmann, R. E.; Yazyev, O.; Austin, A. J.; Cammi, R.; Pomelli, C.; Ochterski, J. W.; Ayala, P. Y.; Morokuma, K.; Voth, G. A.; Salvador, P.; Dannenberg, J. J.; Zakrzewski, V. G.; Dapprich, S.; Daniels, A. D.; Strain, M. C.; Farkas, O.; Malick, D. K.; Rabuck, A. D.; Raghavachari, K.; Foresman, J. B.; Ortiz, J. V.; Cui, Q.; Baboul, A. G.; Clifford, S.; Cioslowski, J.; Stefanov, B. B.; Liu, G.; Liashenko, A.; Piskorz, P.; Komaromi, I.; Martin, R. L.; Fox, D. J.; Keith, T.; Al-Laham, M. A.; Peng, C. Y.; Nanayakkara, A.; Challacombe, M.; Gill, P. M. W.; Johnson, B.; Chen, W.; Wong, M. W.; Gonzalez, C.; and Pople, J. A.; Gaussian, Inc., Wallingford CT, 2004.

(120) Kanawati, B.; Joniec, S.; Winterhalter, R.; Moortgat, G. K. **2007**, *266*, 97-113.

(121) Lavorato, D.; Terlouw, J.; McGibbon, G.; Dargel, T.; Koch, W.; Schwarz, H. *Int. J. Mass Spectrom.* **1998**, *179-180*, 7-14.

(122) Boys, S. F.; Bernardi, F. *Mol. Phys.* **1970**, *19*, 553-566.

(123) Wright, J. S.; Rowley, C. N.; Chepelev, L. L. *Mol. Phys.* **2005**, *103*, 815-823.

(124) Sedlak, R.; Hobza, P.; Patwari, G. N. *J. Phys. Chem. A* **2009**, *113*, 6620-6625.

(125) Sundararajan, K.; Viswanathan, K. S.; Kulkarni, A. D.; Gadre, S. R. *Journal of Molecular Structure* **2002**, *613*, 209-222.

(126) Bowers, M. T.; Marshall, A. G.; McLafferty, F. W. *J. Phys. Chem.* **1996**, *100*, 12897-12910.

(127) Sharma, P.; Attah, I.; Momoh, P.; El-Shall, M. S. **2010**, *300*, 81- 90.

(128) Gillis, E. A. L.; Rajabi, K.; Fridgen, T. D. *J. Phys. Chem. A* **2009**, *113*, 824-832.

(129) Ito, S.; Shen, L.; Dai, Q.; Wu, S. C.; Collins, L. B.; Swenberg, J. A.; He, C.; Zhang, Y. *Science* **2011**, *333*, 1300-1303.

(130) Watson, J. D.; Crick, F. H. C. *Nature* **1953**, *171*, 737-8.

(131) Nguyen, V. Q.; Turecek, F. *J. Am. Chem. Soc.* **1997**, *119*, 2280-2290.

(132) Franklin, R. E.; Gosling, R. G. *Acta Crystallographica* **1953**, *6*, 673-677.

(133) Liu, M.; Li, T. T.; Amegayibor, F. S.; Cardoso, D. S.; Fu, Y. L.; Lee, J. K. *J. Org. Chem.* **2008**, *73*, 9283-9291.

(134) Zhang, B.; Cai, Y.; Mu, X.; Lou, N.; Wang, X. *J. Phys. Chem. A* **2001**, *105*, 10800-10806.

(135) Demeter, A.; Weber, C.; Brlik, J. *J. Am. Chem. Soc.* **2003**, *125*, 2535-2540.

(136) Marzzacco, C. *J. Am. Chem. Soc.* **1973**, *95*, 1774- 1777.

- (137) Nagy, P. I.; Durant, G.; Smith, D. A. *J. Am. Chem. Soc.* **1993**, *115*, 2912-2922.
- (138) Melandri, S.; Sanz, M. E.; Caminati, W.; Favero, P. G.; Kisiel, Z. *J. Am. Chem. Soc.* **1998**, *120*, 11504-11509.
- (139) Fernholt, L.; Romming, C. *Acta Chem. Scand., Ser. A* **1978**, *A32*, 271-3.
- (140) Modelli, A.; Bolognesi, P.; Avaldi, L. *J. Phys. Chem. A*, *115*, 10775-10782.
- (141) Alparone, A.; Millefiori, A.; Millefiori, S. *Chem. Phys.* **2005**, *312*, 261-274.
- (142) Danilov, V. I.; Les, A.; Alderfer, J. L. *Pol. J. Chem.* **2001**, *75*, 1039-1049.
- (143) Danilov, V. I.; Les, A.; Alderfer, J. L. *J. Biomol. Struct. Dyn.* **2001**, *19*, 179-191.
- (144) Nuevo, M.; Milam, S. N.; Sandford, S. A.; Elsila, J. E.; Dworkin, J. P. *Astrobiology* **2009**, *9*, 683-695.
- (145) Zhang, B.; Cai, Y.; Mu, X.; Lou, N.; Wang, X. *J. Chem. Phys.* **2002**, *276*, 277-292.
- (146) Zhang, B.; Cai, Y.; Mu, X.; Lou, N.; Wang, X. *J. Chem. Phys. Lett.* **2002**, *351*, 335-340.
- (147) Pithawalla, Y. B.; Covington, C.; McComish, I.; Germanenko, I. N.; El-Shall, M. S. *Int. J. Mass Spectrom.* **2002**, *218*, 49-62.
- (148) Mahmoud, H.; Germanenko, I. N.; Ibrahim, Y.; El-Shall, M. S. *Chem. Phys. Lett.* **2002**, *356*, 91-100.
- (149) Lozynski, M.; Rusinska-Roszak, D.; Mack, H.-G. *J. Phys. Chem. A* **1998**, *102*, 2899-2903.
- (150) Chiang, C.-T.; Shores, K. S.; Freindorf, M.; Furlani, T.; DeLeon, R. L.; Garvey, J. F. *J. Phys. Chem. A* **2008**, *112*, 11559-11565.
- (151) Ibrahim, Y.; Mabrouki, R.; Meot-Ner, M.; El-Shall, M. S. *J. Phys. Chem. A* **2007**, *111*, 1006-1014.
- (152) Mandal, A.; Prakash, M.; Kumar, R. M.; Parthasarathi, R.; Subramanian, V. *The Journal of Physical Chemistry A* **2010**, *114*, 2250-2258.
- (153) Laura, B.; Javier, C.; José, L. G. d. P. *International Journal of Quantum Chemistry* **2003**, *91*, 432-437.
- (154) Barrio, L.; Catalán, J.; de Paz, J. L. G. *International Journal of Quantum Chemistry* **2003**, *91*, 432-437.
- (155) El-Shall, M. S.; Daly, G. M.; Wright, D. *J. Chem. Phys.* **2002**, *116*, 10253-10266.
- (156) Bauschlicher, C. W.; Ricca, A.; Rosi, M. *Chem. Phys. Lett.* **2002**, *355*, 159-163.
- (157) Honma, K.; Sunderlin, L. S.; Armentrout, P. B. *J. Chem. Phys.* **1993**, *99*, 1623-32.
- (158) Waite, J. H.; Young, D. T.; Cravens, T. E.; Coates, A. J.; Crary, F. J.; Magee, B.; Westlake, J. *Science* **2007**, *316*, 870-875.
- (159) Jobst, K. J.; Terlouw, J. K. *Chem. Phys. Lett.* **2010**, *497*, 7-11.
- (160) Jobst, K. J.; Hanifa, M. R.; Ruttink, P. J. A.; Terlouw, J. K. *Chem. Phys. Lett.* **2009**, *473*, 257-262.
- (161) Ervasti, H. K.; Jobst, K. J.; Gerbaux, P.; Burgers, P. C.; Ruttink, P. J. A.; Terlouw, J. K. *Chem. Phys. Lett.* **2009**, *482*, 211-216.
- (162) Jobst, K. J.; Hasan, S. A.; Terlouw, J. K. *Chem. Phys. Lett.* **2008**, *450*, 243-247.

- (163) Ricca, A.; Bauschlicher, C. W.; Rosi, M. *Chem. Phys. Lett.* **2001**, *347*, 473-480.
- (164) Hamid, A. M.; Soliman, A. R.; El-Shall, M. S. *J. Phys. Chem.* **2012**, *submitted*
- (165) Karpfen, A. *J. Phys. Chem.* **1996**, *100*, 13474-13486.
- (166) Linstrom, P. J.; Mallard, W. G.; National Institute of Standards and Technology: 2001.
- (167) Doering, J. P.; Moore, J. J. H. *The Journal of Chemical Physics* **1972**, *56*, 2176-2178.
- (168) Minderhoud, J. K.; van Veen, J. A. R. *Fuel Processing Technology* **1993**, *35*, 87-110.
- (169) Kolczewski, C.; Puttner, R.; Plashkevych, O.; Agren, H.; Staemmler, V.; Martins, M.; Snell, G.; Schlachter, A. S.; Sant'Anna, M.; Kaindl, G.; Pettersson, L. G. M. *The Journal of Chemical Physics* **2001**, *115*, 6426-6437.
- (170) Zhao, Z.; Huskey, D. T.; Olsen, K. J.; Nicovich, J. M.; McKee, M. L.; Wine, P. H. *Physical Chemistry Chemical Physics* **2007**, *9*, 4383-4394.
- (171) Nguyen, V. Q.; Turek, F. e. *Journal of the American Chemical Society* **1997**, *119*, 2280-2290.
- (172) Lipkind, D.; Chickos, J. *Structural Chemistry* **2009**, *20*, 49-58.
- (173) Franks, K. J.; Li, H.; Kong, W. *The Journal of Chemical Physics* **1999**, *110*, 11779-11788.
- (174) Bera, P. P.; Lee, T. J.; Schaefer, H. F. *Journal of Chemical Physics* **2009**, *131*.
- (175) Fondren, L. D.; McLain, J.; Jackson, D. M.; Adams, N. G.; Babcock, L. M. *Int. J. Mass Spectrom.* **2007**, *265*.
- (176) McEwan, M. J.; Anicich, V. G.; Huntress, W. T., Jr. *Interstellar molecules; Proceedings of the Symposium, Mont Tremblant, Quebec, Canada, August 6-10, 1979. (A81-27676 11-90) Dordrecht, D. Reidel Publishing Co., 1980, p. 299-302; Discussion, p. 302, 303.* **1980**, 299-302.
- (177) Knight, J. S.; Freeman, C. G.; McEwan, M. J.; Adams, N. G.; Smith, D. *Mon. Not. R. Astron. Soc.* **1986**, *219*, 89-94.
- (178) McEwan, M. J.; Anicich, V. G.; Huntress Jr, W. T. *Int. J. Mass Spectrom. Ion Phys.* **1981**, *37*, 273-281.
- (179) Schiff, H. I.; Bohme, D. K. *Astrophys. J.* **1979**, *232*, 740-746.

Appendix A

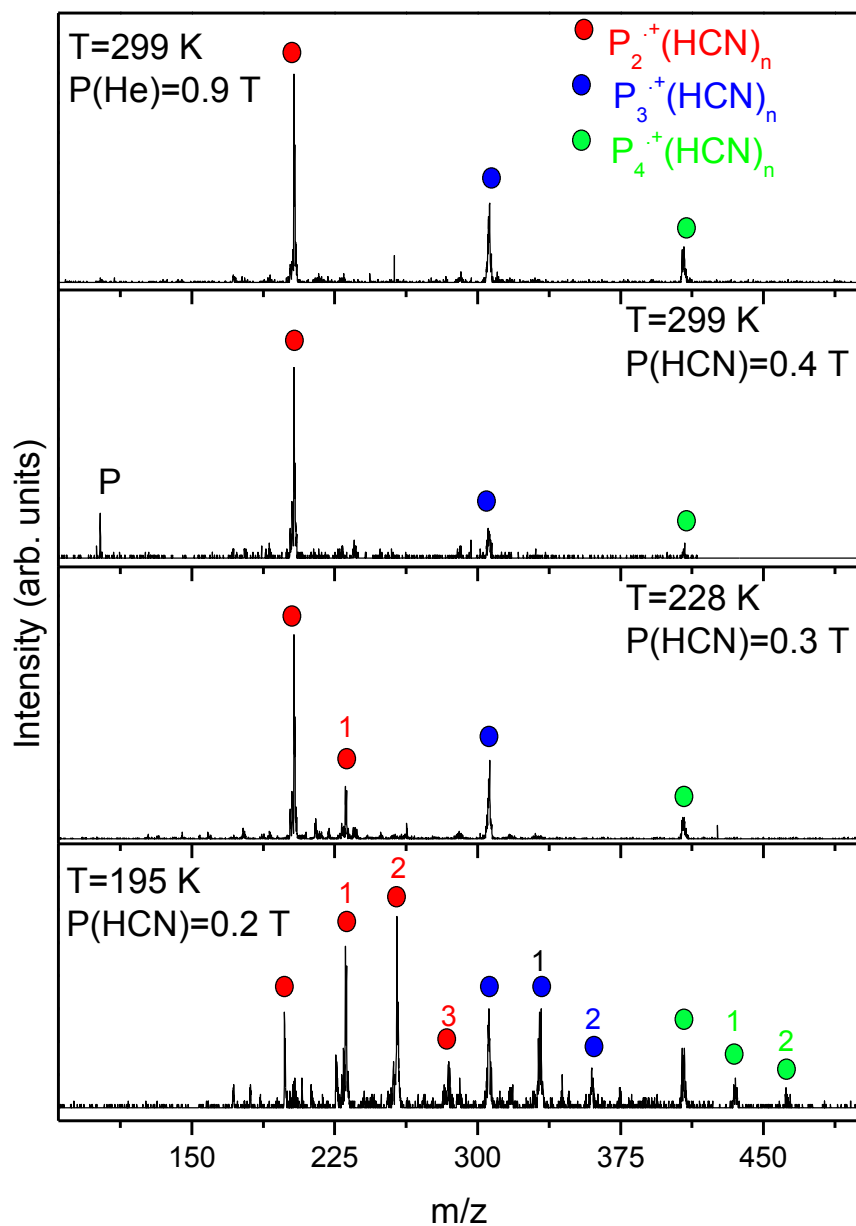


Figure 55. Spectrum of phenyl acetylene clusters $(P_n)^+$ reacting with HCN molecules and different temperatures. They are obtained after injecting phenyl acetylene dimer in the RF-selection mode using 13 eV (lab. frame) injection energy

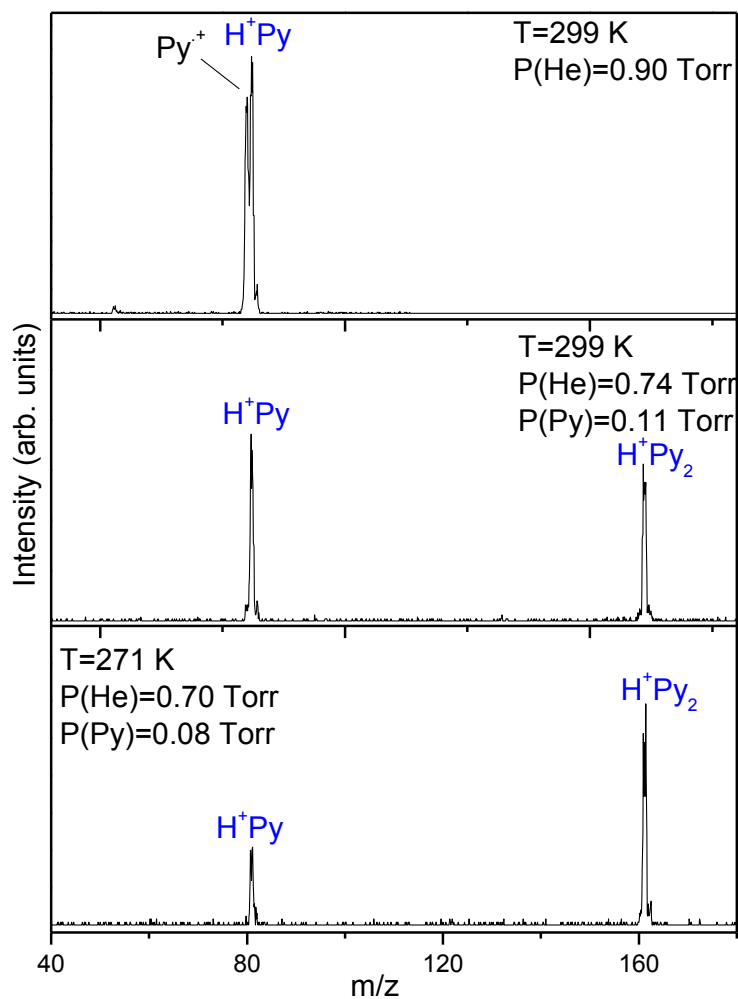


Figure 56. Spectrum of injecting protonated pyrimidine (H^+py) into pyrimidine vapor (py) in the mass-selection mode using 14 eV (lab. frame) injection energy

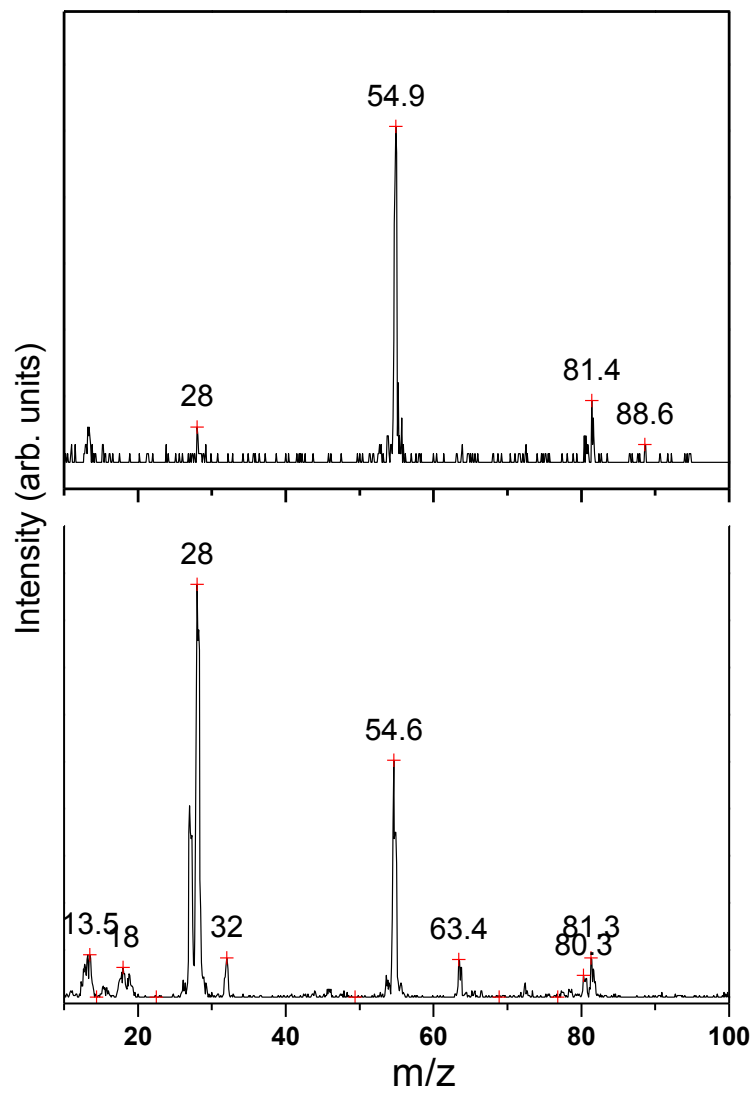


Figure 57. Mass-spectra for $H^+(HCN)_n$ clusters

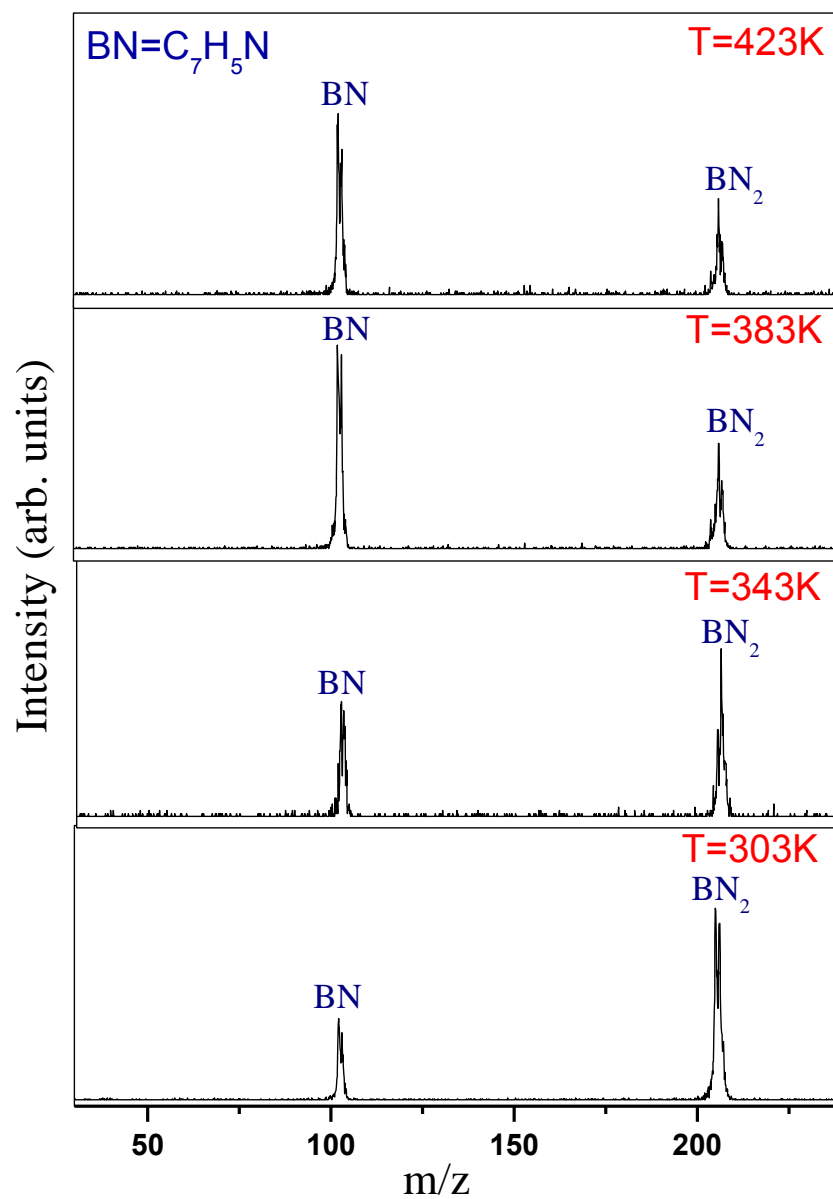


Figure 58. Mass-spectra of thermal dissociation of benzonitrile dimer collected via injecting mass-selected benzonitrile dimer, BN_2 , into drift cell which has 0.89 Torr pure helium only using 9 eV injection energy (lab. frame) and 3V/cm as drift field

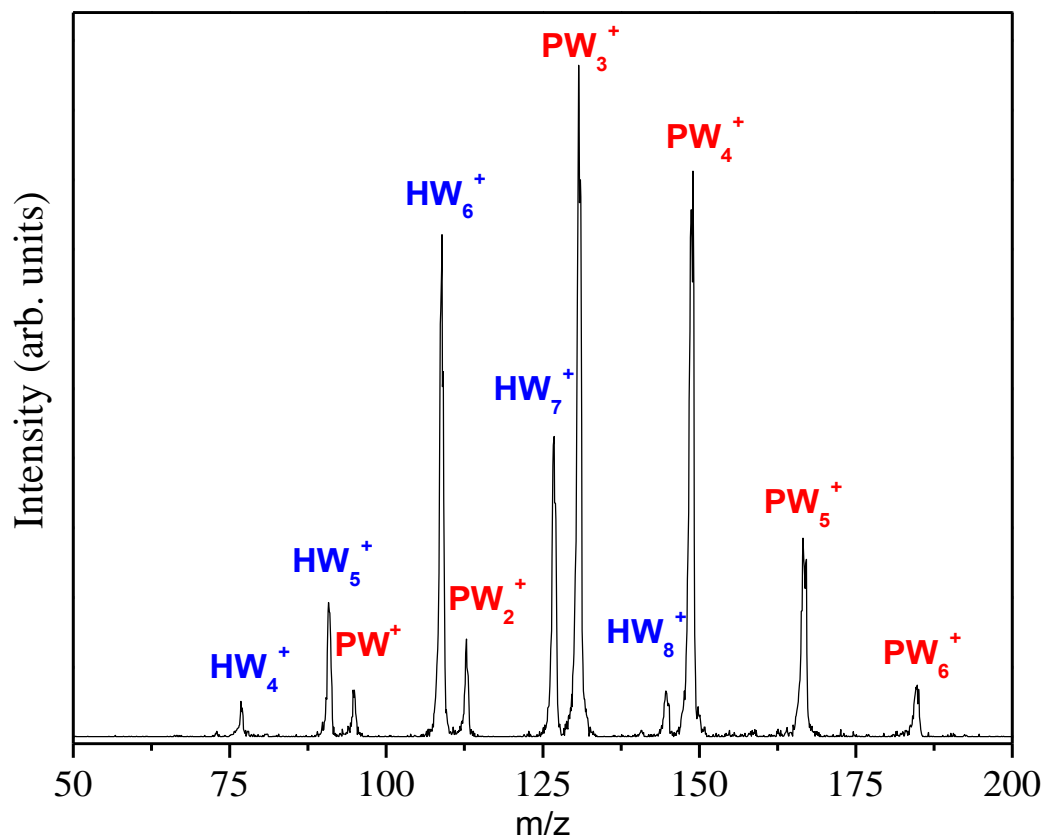


Figure 59. Mass-spectrum collected when the phenyllium cation ($P=C_6H_5^+$) was injected into 0.12 Torr water (W) only at 234 K at 12.9 eV injection energy (lab. frame) and 5 V/cm drift field

Appendix B: Preliminary studies of Benzonitrile-water clusters

Ion mobility and collision cross sections of benzonitrile radical cation-water clusters

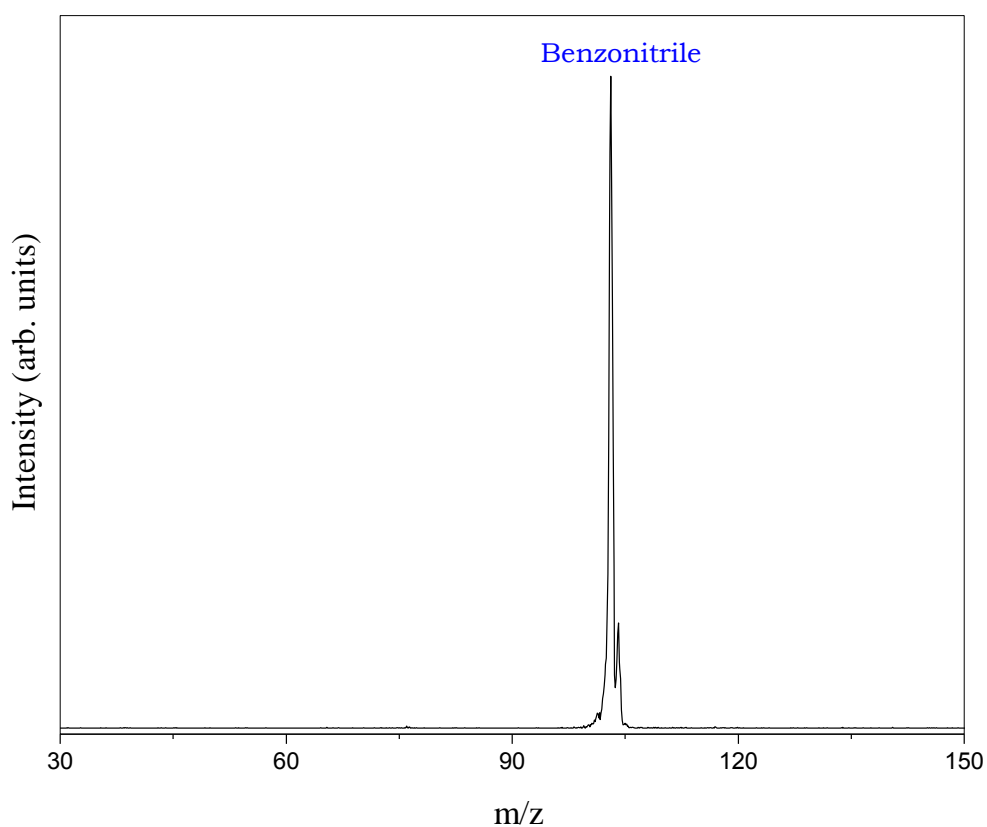


Figure 60. Mass-spectrum of mass-selected benzonitrile injected onto the drift cell contains 0.75 Torr of pure He using an injection energy of 14eV (lab.frame), the temperature of the drift cell=299 K, drift field=6V/cm

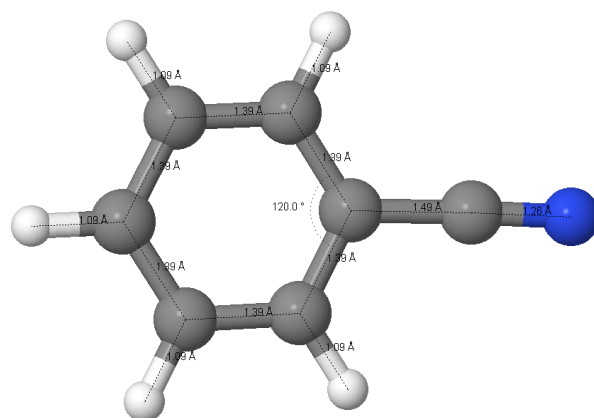
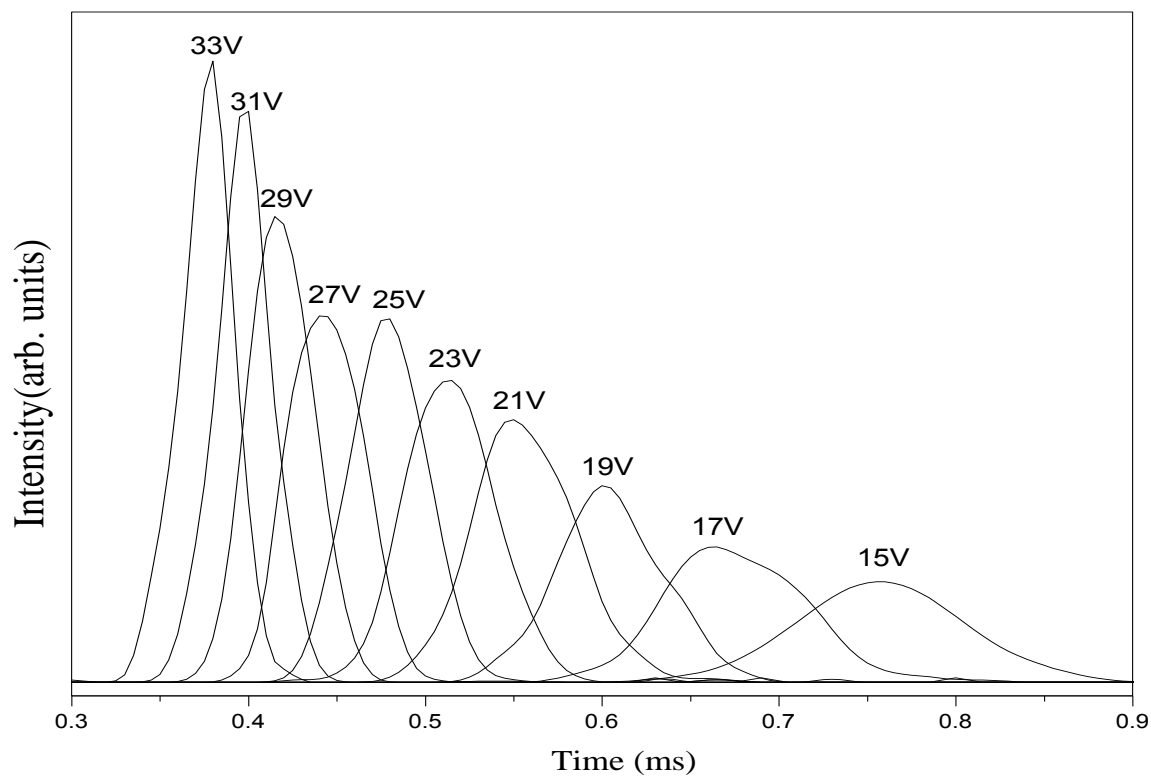


Figure 61. (Top) Arrival time distributions (ATDs) of benzonitrile monomer, $m/z=103$, the drift voltage was varied between 15 V and 33 V at 300 K with the drift cell contains 3.6 Torr of helium buffer gas **(Bottom)** The calculated structure of Benzonitrile using B3LYP/6-311++G(d,p)

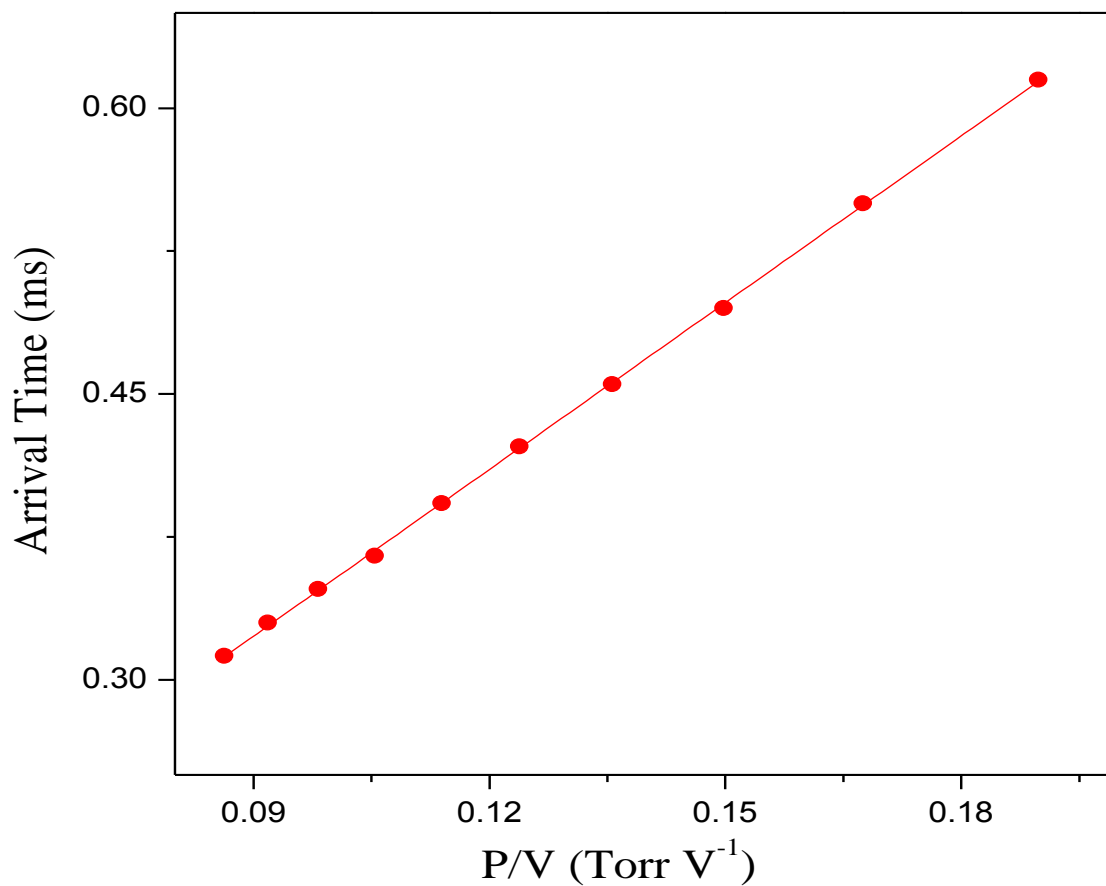


Figure 62. A plot of the mean arrival time of benzonitrile as a function of P/V (Torr.V⁻¹), $R^2=0.9997$

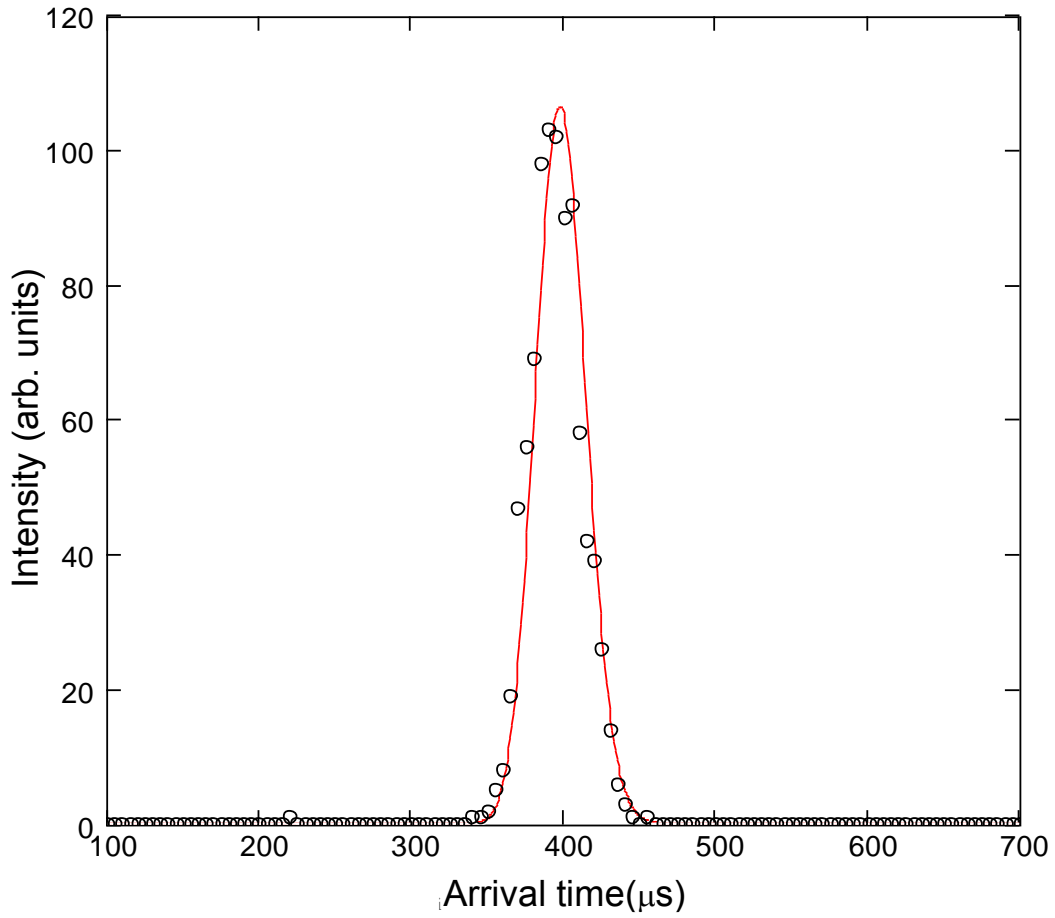


Figure 63. An example to Fitting of the experimental (open circles) to the transport theory (solid line). The measurement conditions were 300 K, 2.85 Torr and 5 V/cm

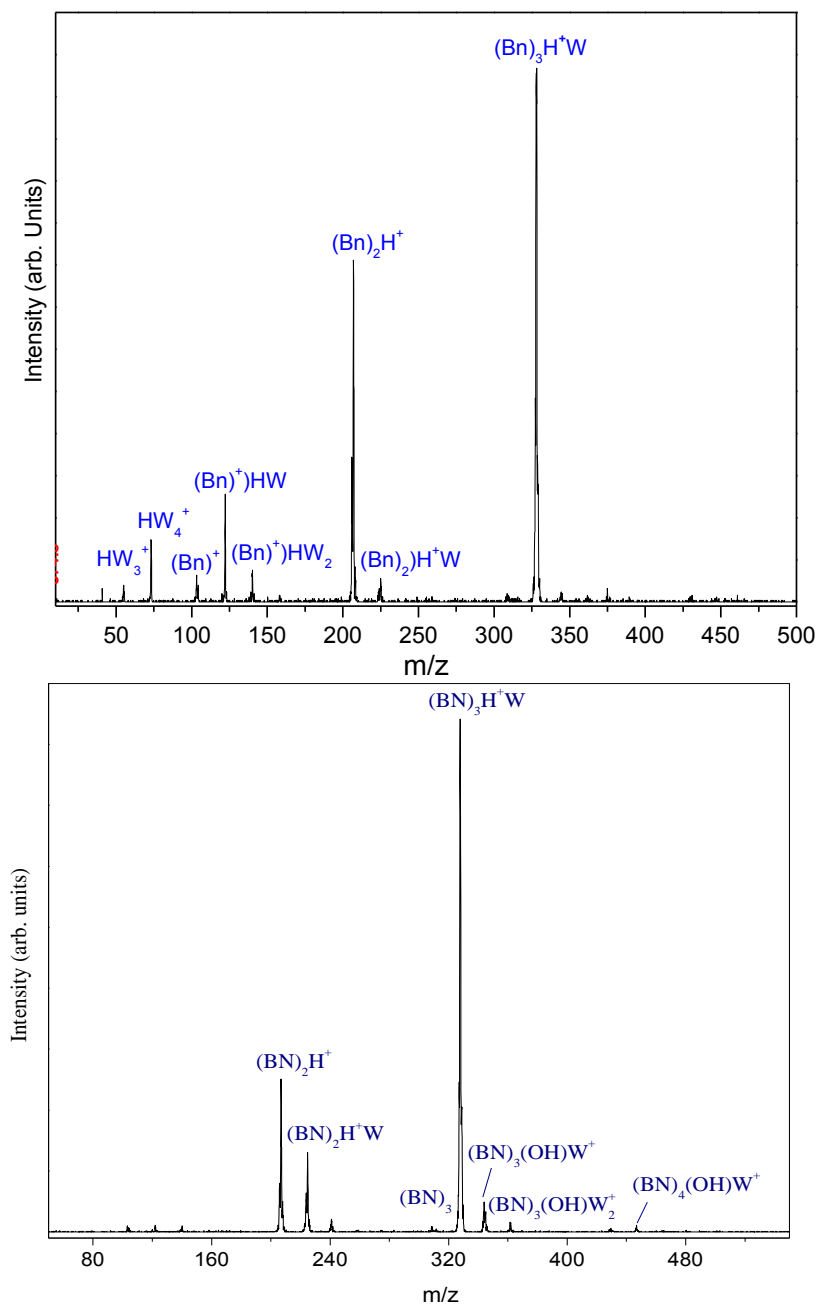


Figure 64. Mass-spectrum resulting from expanding both benzonitrile and water using He as a carrier gas, selecting (**Top**) Benzonitrile dimer in the RF-mode, the drift cell contains 0.76 Torr pure helium, the temperature of the drift cell=300 K, using 14 eV as injection energy (lab. frame) and 7 V/cm as drift field. (**Bottom**) Protonated hydrated benzonitrile trimer in the RF-mode, the drift cell contains 0.71 Torr pure helium, the temperature of the drift cell=301K, using 10 eV as injection energy (lab. frame) and 6 V/cm as drift field

Cluster	T K	$K_{o(\text{exp})}$	$K_{o(\text{calc})}$	$\Omega_{(\text{exp})}$	$\Omega_{(\text{calc})}$
Benzonitrile Monomer (BN^+) ($m/z=103$)	300	10.22	9.91	53.3	54.9
	121	11.98	12.15	71.0	70.6
Benzonitrile dimer (BN^+) ₂ ($m/z=206$)	301	5.89	6.53	91.4	82.4
	226	6.42	7.17	96.9	86.7
	121	7.88	8.43	107.7	100.7
Benzonitrile protonated dimer (BN^+) ₂ H^+ ($m/z=207$)	301	5.34		100.9	
Benzonitrile protonated hydrated dimer (BN^+) ₂ H^+W ($m/z=225$)	301	4.26	5.05	126.3	106.5
Benzonitrile protonated hydrated trimer (BN^+) ₃ H^+W ($m/z=328$)	301	3.51		152.8	

Table 55. Reduced mobilities of various benzonitrile-water binary clusters and their corresponding collision cross-section values. K_o results are expressed in $\text{cm}^2 \cdot \text{V}^{-1} \cdot \text{s}^{-1}$ while Ω values are expressed in \AA^2 units. Calculated results from Mobcal program using B3LYP/6-311++G (d,p) optimized structures

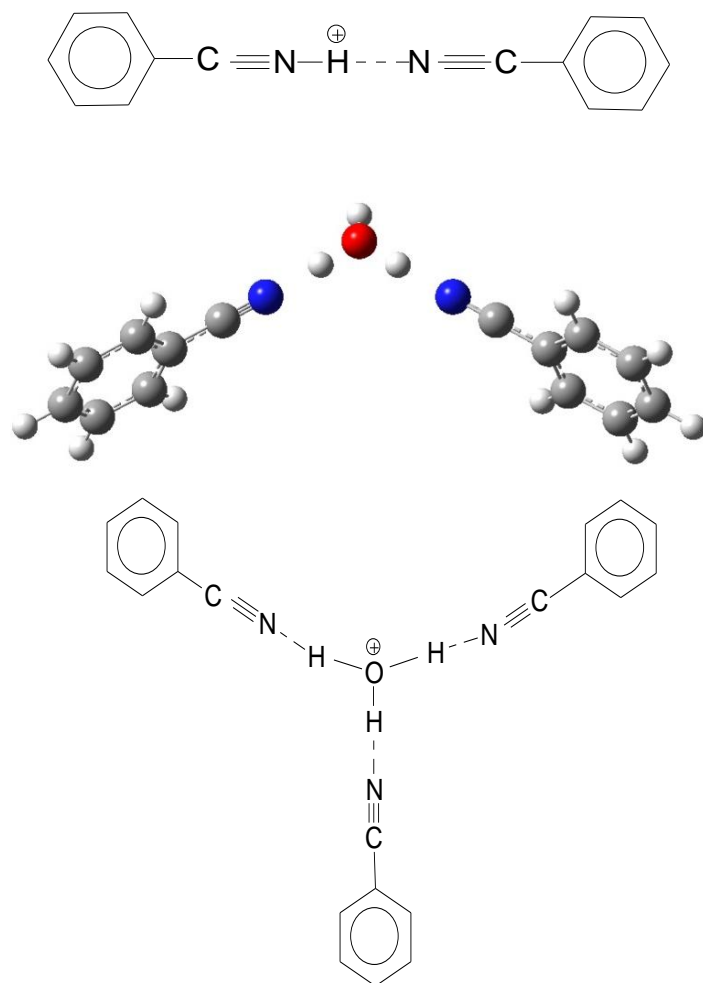


Figure 65. (Top) The suggested structure of the protonated benzonitrile dimer, $[\text{BN}_2\text{H}^+]$. (Middle) Optimized structure for $[\text{BN}_2\text{H}(\text{H}_2\text{O})^+]$. (Bottom) The suggested structure of the protonated hydrated benzonitrile dimer, $[\text{BN}_2\text{H}^+(\text{H}_2\text{O})]$

Thermochemistry studies of the hydration of Benzonitrile Radical Cation in the gas phase

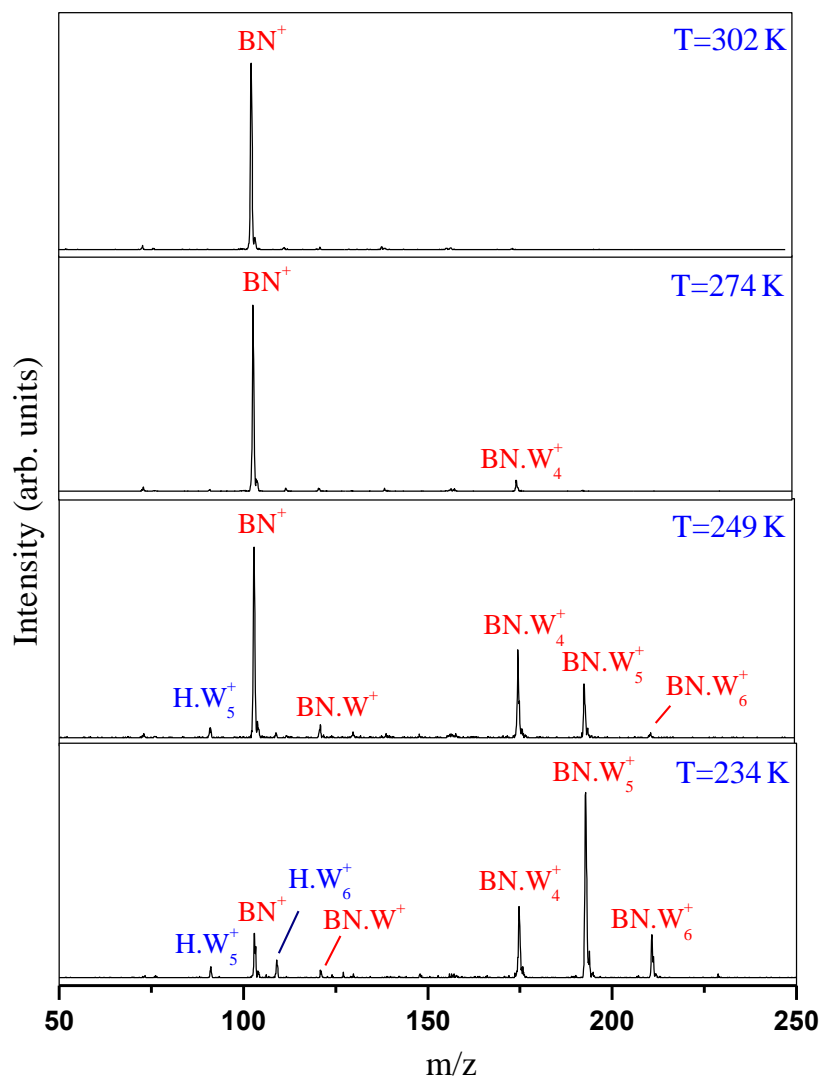


Figure 66. Mass-spectra obtained following injecting mass-selected benzonitrile monomer, $\text{BN}^{\cdot+}$ ($m/z=103$), into 0.90 Torr of pure water in a drift cell temperature range of 234 K and 302 K via 13.9 eV as injection energy, and 6V/cm as drift field. Drift cell temperatures are varied as indicated

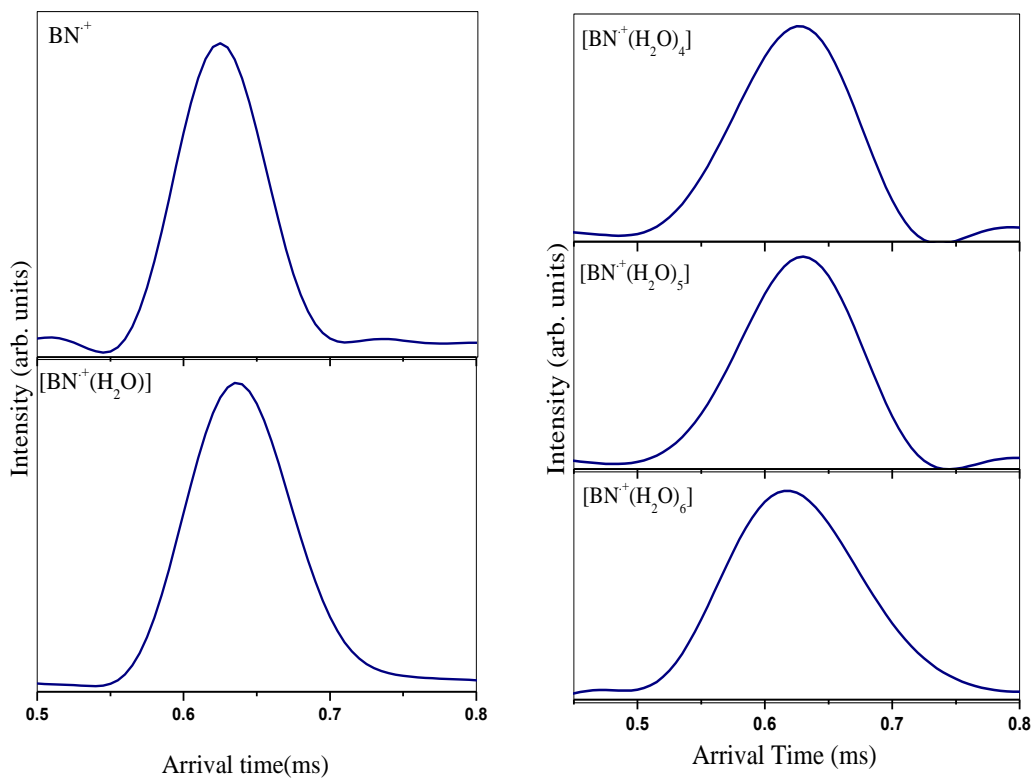


Figure 67. ATDs of $[\text{BN}^+(\text{H}_2\text{O})_n]$ clusters obtained by injection of benzonitrile cation, BN^+ , at 14 eV injection energy and 6V/cm drift field into **(Left)** 0.78 Torr of pure water at 245 K and **(Right)** 0.84 Torr of pure water at 234 K

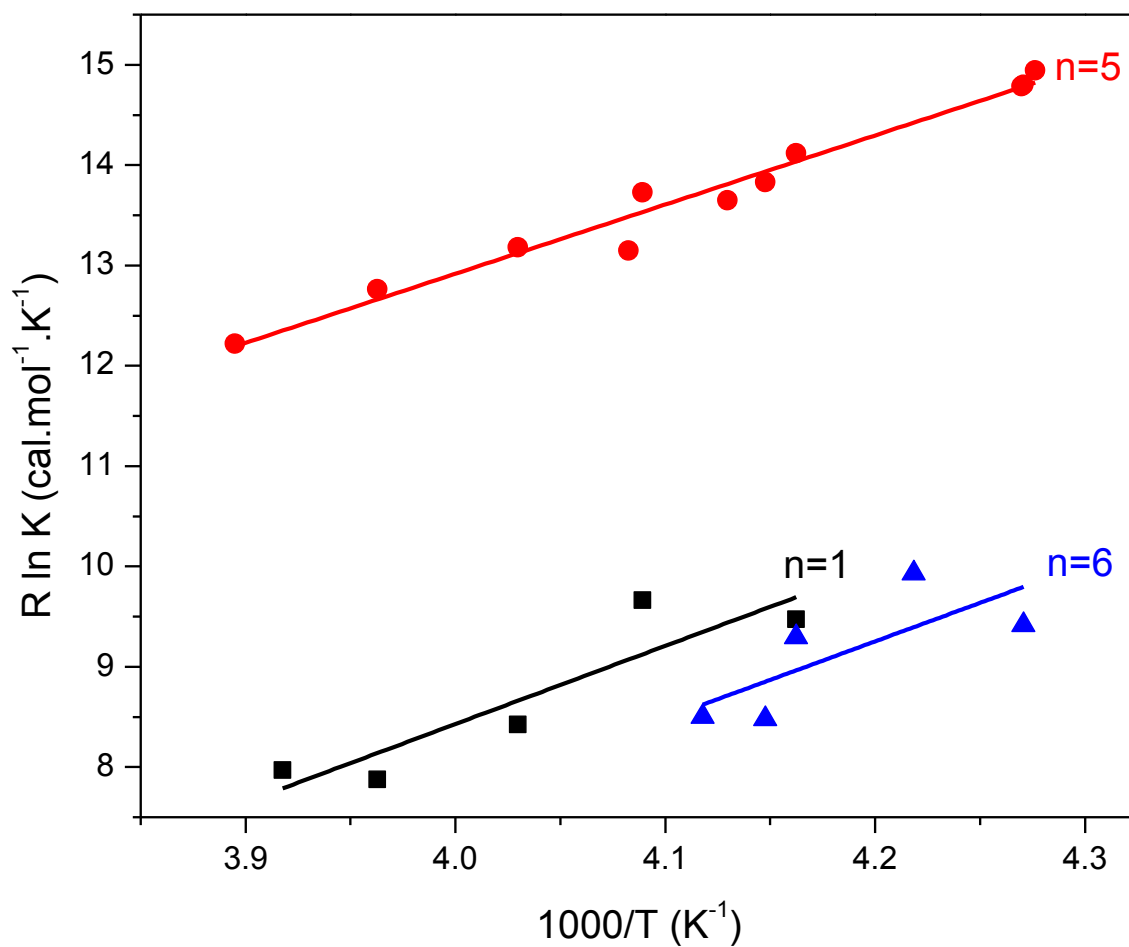


Figure 68. van't Hoff plots for the equilibria yielding $[\text{BN}^+(\text{H}_2\text{O})_n]$ for n values as indicated. The drift field was 4V/cm while the injection energy was 13.9 eV (lab. frame)

Name	$-\Delta H^\circ$ ^a	$-\Delta S^\circ$ ^b	BE ^c
BN ⁺ W	7.8	22.7	9.2 (*8.4)
BN ⁺ W ₂	N/A	N/A	8.9 (*8.0)
BN ⁺ W ₃	N/A	N/A	
BN ⁺ W ₄	N/A	N/A	
BN ⁺ W ₅	6.9	14.7	
BN ⁺ W ₆	7.7	23.0	

^a $\Delta H^\circ_{n-1,n}$ units are kcal/mol , ^b $\Delta S^\circ_{n-1,n}$ units are cal/mol.K and ^c calculated by B3LYP/6-311+G(d,p) (* including BSSE correction)

Table 56. Measured thermochemistry of benzonitrile⁺ (water)_n clusters along with the corresponding theoretical values

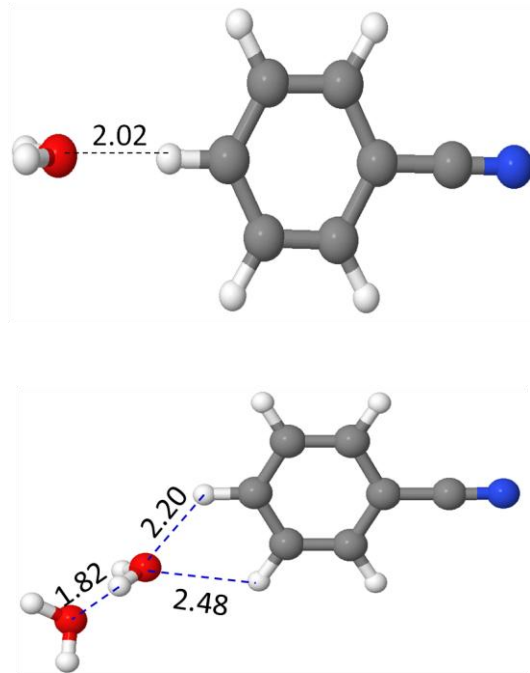


Figure 69. B3LYP/6-311+G(d,p) structures of [Benzonitrile⁺ (H₂O)_n]; n=1-2

Vita

Ahmed Mohamed Kotb Hamid was born at June, 15, 1983, in Behira, Egypt, and is an Egyptian citizen. He graduated from high school in 2000 and then joined faculty of Science at Alexandria University in Alexandria, Egypt from which he graduated in May 2004 in excellence with honors from the Chemistry department. He has pre-M.Sc. diploma in Inorganic and Physical Chemistry earned in 2006 from faculty of Science, Alexandria University with a very good final grade. He joined the Chemistry department at Virginia Commonwealth University in Fall semester of 2007 and since then, he is working for Dr. M. Samy El-Shall. Ahmed has accepted an offer from Purdue University to work as a postdoctoral fellow for Dr. R. Graham Cooks on biological mass spectrometry.